An experimental and theoretical investigation into the break-up of curved liquid jets in the prilling process

by

Lucy Partridge

A thesis submitted to
The University of Birmingham
for the degree of
Doctor of Philosophy

School of Mathematics
The University of Birmingham
November 2006

Abstract

A pilot scale study of the dynamics of the break-up of curved liquid jets is presented. This work is motivated by an industrial process called prilling which is used in the manufacture of pellets. In this process a sieve-like cylindrical can spins rapidly on its central vertical axis. Molten liquid is pumped into the top of the can and flows from the holes in the form of curved liquid jets.

Experiments are described which were carried out on a pilot scale rig. Some differences between the break-up modes observed in this study and previous work using a small laboratory scale rig are discussed.

Previous theories describing break-up mechanisms of curved liquid jets were extended to include viscosity and gravity. Break-up lengths and drop sizes were obtained theoretically and compared with experimental results.

Experiments were carried out using insonification, a process where sound waves are fired at the jet to control satellite drop formation. Three different frequencies of wave were used, 10, 100 and 200 Hz at four different rotation rates. It was observed that insonification was successful at eliminating satellite drops at low rotation rates and when frequencies of 100 or 200 Hz were used. Insonification was included in the theory. The theory predicted that insonification eliminated satellite drops for a large range of frequencies in the experimental regimes for sufficiently large acoustic volume. The theory also predicted that satellite drops were eliminated in parameter regimes outside the experimental regimes.

The trajectory of the jet was allowed to become unsteady, in a rotating frame of reference. Simulations were carried out in inviscid and viscous regimes.

Acknowledgements

I would like to thank my supervisors Professor Stephen Decent and Dr Mark Simmons for their guidance during this project. I would also like to thank Dr Emilian Părău for his assistance with the theoretical aspects of the project. Dr David Wong provided me with invaluable advice on the experimental aspects of the project.

I am grateful to Tom Whateley and Ben Caine for helping with some of the experiments as well as taking some of the photographs in this thesis.

I would like to thank Dr Simon Goodwin for helping me with general computer difficulties and latex problems. I am also indebted to my parents for their encouragement and support.

I acknowledge financial support from EPSRC which made this work possible.

Contents

List of Figures

List of Tables

s	Arc-length
t	Time
(n, ϕ)	Polar coordinates in any cross section of the jet
$\mathbf{r}$	Position vector
I	Metric tensor
$R(s, \phi, t)$	Radius of the jet
$\mathbf{n}$	Unit normal pointing away from the jet
$f(\mathbf{r}, t)$	Free surface position of the jet
ρ	Density
σ	Surface tension
μ	Dynamic viscosity
ν	Kinematic viscosity
Ω	Rotation rate in $\mathrm{rad\,s^{-1}}$
$\mathbf{u}$	Velocity vector
u, v, w	Components of the velocity vector
$\mathbf{e}_s$, $\mathbf{e}_n$, $\mathbf{e}_\phi$	Unit vectors in the new coordinate system
$X(s,t)$, $Y(s,t)$, $Z(s,t)$	Coordinates of the centreline
U	Jet exit speed
$\boldsymbol{\omega}$	Angular velocity vector
ω	Component of angular velocity vector
K (chapter 5), κ (chapters 6, 7, 8 and 9)	Wavenumber
$\boldsymbol{\sigma}$	Stress tensor
λ	Wavelength
δ	Amplitude of the initial perturbation
a	Radius of the orifice
s_0	Radius of can
D	Diameter of can
H	Height of liquid in can
α	Amplitude of the sound wave
β	Frequency of the sound wave
$\epsilon = a/s_0$	Aspect ratio
$Re = \rho U a/\mu$	Reynolds number
$Rb = U/s_0\Omega$	Rossby number
$We = \rho U^2 a/\sigma$	Weber number
$F = U/\sqrt{s_0 g}$	Froude number
$Fr = U/\sqrt{gH}$	Modified Froude number
$Oh = \mu/\sqrt{\sigma a \rho}$	Ohnesorge number

Table 1: Nomenclature

Chapter 1

Introduction

The prilling process is used to produce solid pellets from molten materials such as fertiliser and magnesium. In this process the molten fluid is pumped into a perforated cylindrical can which is suspended at the top of a tower. The can rotates about its vertical axis. Due to centrifugal forces, the molten liquid is forced outwards to the wall of the can and flows out through the perforations, forming liquid jets. Each jet follows a curved trajectory and breaks up into droplets due to the growth of surface tension driven instabilities on the surface of the liquid jet. These droplets cool and solidify as they fall to the bottom of the tower, forming pellets. At the bottom of the tower the pellets are removed on a conveyer belt and sorted for quality, including a check on the size of the pellets.

1.1 The industrial problem

The prilling process currently produces pellets of a non-uniform size causing waste. There is a need to minimise the formation of fine particles formed by the creation of small satellite drops during the break-up of the jets to save money and energy.

Figure 1.1 is a photograph of a typical prilling can, which is 1 m high and 0.5 m in diameter. This would be suspended from the top of a tower, typically 30 m high and 24 m in diameter. The curved side of the can is perforated with approximately 2000 holes with a diameter of around 4 mm, near the base. Hot molten urea is pumped into the can. The can is rotated at a rate of 320-450 revolutions per minute (rpm) and the liquid is forced out of the holes into the atmosphere as jets. Capillary forces cause the jets to

Figure 1.1: Photograph of a prilling can, courtesy of GEA Niro A/S.

break-up into drops. Figure 1.2 is a photograph of jets emanating from a prilling can at a production facility at Norsk Hydro, Porsgrunn, Norway used to make fertiliser pellets used by farmers. The can is rotating in an anti-clockwise direction. Hundreds of jets can be seen emanating from the can as well as some drops. The jets break-up at a distance of the order of hundreds of times of the radius of the orifice, [42].

Some theoretical and experimental work has already been carried out on the break-up of curved liquid jets during this process. This study extends investigations to develop an understanding of break-up mechanisms on a larger scale than previously considered. The results of experimental work are used to test existing theory and to develop a model to include more physical effects.

1.2 Aims and objectives

This thesis extends the work on the behaviour of liquid jet break-up and drop formation from the laboratory scale to the pilot scale to achieve a better understanding of the problem on scale closer to the industrial scale. The objectives are:

- To determine the break-up behaviour of curved jets in parameter regimes closer to the industrial case than previous experiments using a pilot scale facility and compare the results to previous laboratory scale experiments.
- To develop the theory from previous attempts to include other parameters such as viscosity and gravity.
- To carry out novel work on insonification to attempt to control drop formation.
- To allow the trajectory of the jet to become unsteady in the rotating reference frame and obtain simulations of the jet in more complex situations.

1.3 Thesis outline

The introduction sets out the background to the problem. In section 1.1 the industrial problem is introduced and section 1.2 presents the aims and objectives for the thesis.

In chapter 2 a literature review is presented along with previous theoretical work carried out by Wallwork *et al.* [42] and previous experimental work carried out by Wong *et al.* [44].

In chapter 3 the pilot scale experiments are described and experimental values for the laboratory, pilot and industrial scales are compared. A detailed exposition of the experimental procedure is given in section 3.1. A list of experimental assumptions is presented. Results are given in the form of flow maps and drop size distributions.

In chapter 4 results from the pilot and laboratory scale experiments are compared. Section 4.1 compares the break-up regime and the break-up modes on the pilot and laboratory scale. Section 4.2 compares the effect of rotation rate and viscosity on both the

laboratory and pilot scales. Section 4.3 examines the effect of rotation rate on exit velocity. Section 4.4 compares the different drop size distributions obtained on the pilot and laboratory scales. Drop sizes obtained on the pilot scale were plotted against experimental parameters. Section 4.5 presents break-up lengths obtained on the pilot scale plotted against experimental parameters.

In chapter 5 the non-linear analysis developed by Părău *et al.* [34] is examined in more detail. Break-up lengths obtained experimentally on the pilot scale are compared to break-up lengths obtained using the theory. A parametric study is carried out where surface tension, rotation rate and the amplitude of the disturbance at the orifice are varied and trends in the break-up length are observed.

In chapter 6 viscosity is included in the mathematical model. The scaling used in the inviscid case is different from the scaling used in the viscous case. Break-up lengths and drop sizes obtained using the viscous theory are compared to experimental results obtained on the pilot scale. A parametric study is carried out where surface tension, rotation rate, viscosity and the amplitude of the disturbance at the orifice are varied and trends in break-up length and drop size are obtained.

In chapter 7 gravity is included in the non-linear analysis. Simulations of the jet breaking up are obtained; side and plan views of the jet are given. Theoretically obtained break-up lengths and drop sizes are compared to experimental results obtained on the pilot scale. The parametric study is continued to include gravity.

In chapter 8 a process called insonification is used to control satellite drop formation is discussed. During this process sound waves are fired at the jet from a sub-aqua speaker situated within the can. Three different wave frequencies each at four different rotation rates are used. The resulting drop sizes are measured and drop size distributions are given. These are compared to drop size distributions obtained when no insonification was used.

In chapter 9 the centreline of the jet is allowed to become time-dependent. The deviation of the centreline from the steady-state is calculated in inviscid and viscous cases. Simulations of the jet in this more complicated situation are obtained.

In chapter 10 we discuss the results obtained in this thesis. Conclusions are made and ideas for future work are presented.

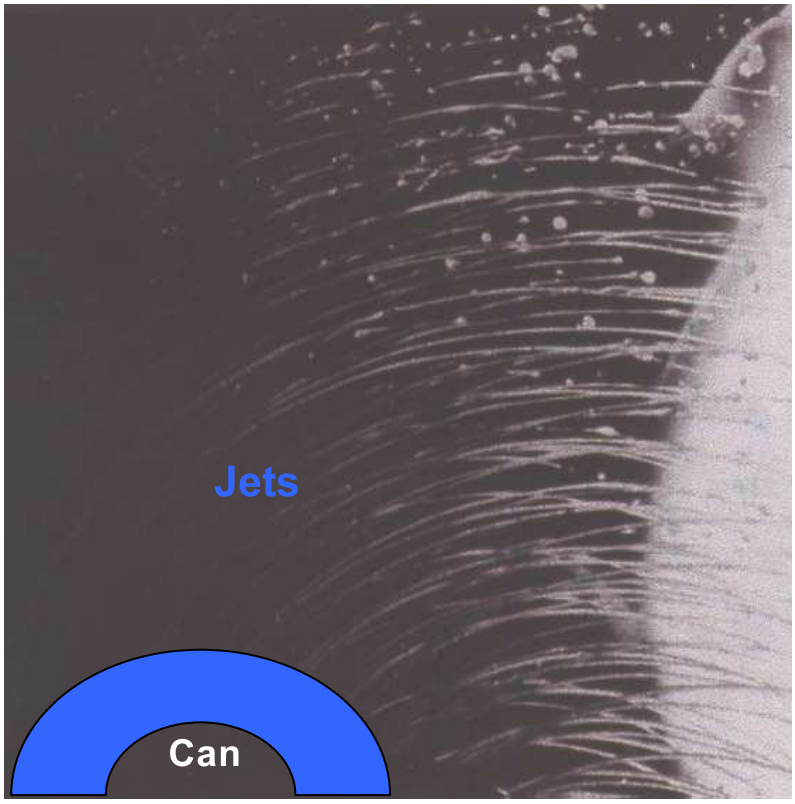

Figure 1.2: Photograph of jets emanating from the prilling can.

Chapter 2

Literature review and previous work

2.1 Literature review

A great deal of literature can be found which focuses on the break-up of straight liquid jets. The earliest jet experiments were carried out by Savart in 1833. These experiments concentrated on the shape of the jet using different orifices [37]. Savart investigated the decay of liquid jets by illuminating the jets using sheets of light. He observed tiny undulations growing on a jet of water as shown in figure 2.1.

Savart offered some fundamental insights into drop formation but he failed to recognise surface tension as the source of the instability despite surface tension being discovered thirty years earlier [17].

It was Lord Rayleigh [36] who noticed that the instabilities leading to break-up resulted from surface tension, by considering the linear stability of an infinite column of incompressible inviscid fluid, with circular cross section that is subjected to small perturbations from its equilibrium. He considered travelling wave modes of the form $\exp(ikx + \alpha t + s\phi)$, where x is the distance along the jet, ϕ is the azimuthal coordinate (in a cylindrical polar coordinate system), t is time, k is the wavenumber, $\mathrm{Re}(\alpha)$ is the growth rate and $\mathrm{Im}(\alpha)$ is the wave frequency. Rayleigh found that disturbances of the radius grow in time according to

$$\alpha^2 = \left(\frac{\sigma}{\rho a^3}\right)\left(\frac{I_s'(ka)(1 - s^2 - k^2a^2)ka}{I_s(ka)}\right) \tag{2.1}$$

Figure 2.1: Definition sketch from Savart's paper [37] of perturbations growing on a water jet.

in a frame of reference moving with the undisturbed jet, where ρ is the density of the fluid, a is the undisturbed jet radius, σ is the surface tension of the fluid and I_s is the modified Bessel function of order s. The integer s is the periodicity of the motion around the jet's circumference. For $s = 0$ the mode is axisymmetric and is stable for $ka > 1$ and unstable for $0 < ka < 1$. For $s > 0$ the modes are not axisymmetric. When $s \geq 1$ the modes neutrally stable. (Note. The velocity of the wave is proportional to $\cos(s\phi)$ where ϕ is the angle associated with the polar coordinates (x, r, ϕ), with the axis at the jet's centre. Therefore $s = 0$ gives axisymmetric modes.) By maximising $Re(\alpha)$ in equation 2.1 for $s = 0$ the most unstable wavenumber corresponds to $ka = 0.697$ [1]. At this wavenumber the perturbation grows fastest and ka governs the size of the drops.

A review of early work was carried out by Bogy [6] and a more recent and extensive review is given by Eggers [17]. Other background references include books by Middleman [29], Anno [2] and Lin [28].

Rayleigh [36] incorporated viscosity into the problem by considering a cylinder of incompressible viscous liquid. Weber [43] also considered the problem of viscous liquid jets. They found that adding viscosity to the problem resulted in an increase in the most unstable wavelength.

Keller and Weitz [25] considered a steady two dimensional sheet with surface tension emerging from a horizontal orifice and then falling under gravity. They found surface tension made the sheets fall more sharply.

Spatial instability of jets was first considered by Keller, Rubinow and Tu [26]. They include the orifice in their formulation. The instability of a circular straight jet in air was considered with the assumption that the wavenumber k is complex while α is purely imaginary. This means that the travelling wave disturbances grow with distance along the jet rather than with time. They found that there were infinitely many unstable modes.

[1] In equation 2.1 k and a are both dimensional quantities, giving that ka is a non-dimensional quantity. Later in this thesis we non-dimensionalise all physical quantities so k becomes relabelled as a non-dimensional quantity.

Surface tension forces acting on the jet are known to cause the jet to break-up into droplets when it comes into contact with air. Early analytical work such as the work by Rayleigh [36] predicted the formation of one drop for a given wavelength. However experimental studies by Chaudhary and Maxworthy [9, 8] and Goedde and Yuen [21] found that two drops were formed; a main drop and a smaller satellite drop.

The stability is highly dependent on the Weber number. The Weber number is a dimensionless group derived from non-dimensionalising the equations of motion and is given by $We = \rho U^2 d/\sigma$ where ρ is the liquid density, U is the liquid jet speed, d is the lengthscale of the problem and σ is the surface tension of the liquid. Several authors have identified $We = 1$ as a singularity when $d = a$, where a the radius of the orifice from which the jet emerges.

Baird and Davidson [3] studied straight annular liquid jets without gravity. They obtained a singularity at $We = 1$. They had some agreement with experiment for long fast jets but not for short jets. They concluded that short jets have a large menisci at the orifice which alters the jet profile. Finnicum *et al.* [20] studied two-dimensional liquid curtains falling under gravity. They found that the singularity at $We = 1$ is removable by including more detail in the model considering the menisci at the orifice. When $We > 1$ jets are are always formed. However when $We < 1$ the exit angle of the jet is crucial. Ramos [35] studied one-dimensional incompressible, inviscid jets with similar results.

Hilbing and Heister [23] investigated the non-linear stability of a straight liquid jet. They developed a boundary element method to describe the non-linear evolution and drop formation of a straight jet emanating from an orifice in the absence of gravity. The sizes of both main and satellite drops were predicted. They found that changing the frequency or amplitude of the perturbation altered the mechanism of break-up.

Kowaleski [27] performed some experiments using imaging to investigate break-up mechanisms. The aim of these investigations was to compare the experimental observations with an asymptotic non-linear model developed by Eggers [16]. Kowaleski found

that just before break-up a long ligament is formed connecting two droplets. The characteristics of this ligament are a function of viscosity, orifice diameter, amplitude of the disturbance causing the jet to break-up and the frequency of the disturbance. The jet breaks up when the ligament approaches a limiting value (approximately 10^{-6} m) and this limiting value appears to be independent of liquid parameters. It was found that increasing the viscosity increases the length of the ligament but the diameter of the ligament remained almost constant.

Kowaleski's experimental results were only in partial agreement with Eggers' model. The shape of the pinch-off region obtained by the theory was in good agreement with the experimental results. The post rupture behaviour predicted by Eggers [16] did not agree very well with Kowaleski's experiments.

Blaisot and Adeline [5] found that for a free straight jet falling under gravity, the break-up length is a function of jet exit velocity. Camelot *et al.* [7] showed that the instability causing jet break-up changed from *varicose* (axisymmetric) to *kink* (non-axisymmetric) with increasing flow rate. Blaisot and Adeline [5] suggested kink instabilities could be due to the increasing influence of aerodynamic effects i.e., wind resistance.

Curved liquid jets without rotational effects have been studied by Vanden-Broeck and Keller [40]; Dias and Vanden-Broeck [14]; Finnicum *et al.* [20]; Cummings and Howell [11]; Entov and Yarin [19] and Hohman *et al.* [24].

Wallwork *et al.* [42] and Wallwork [41] used a mathematical model to describe a jet emanating from an orifice in the curved side of a can spinning on its vertical axis, but only considered linear waves. Some preliminary experiments which involved high speed imaging of jets of Newtonian liquids, emerging from a 0.085 m diameter can, showed some agreement with theory. Following the work of Wallwork *et al.* [42] and Wallwork [41], Decent *et al.* [13] incorporated gravity into the model, again only for linear waves. Use of linear stability theory allowed similar predictions of the break-up length to those developed by Middleman [29] and others for straight jets. Nevertheless, they noted that

non-linear effects were important. Decent *et al.* [12] included viscosity into the linear model.

Wong *et al.* [44] performed a more comprehensive experimental study on the laboratory scale using the same equipment as Wallwork *et al.* [42]. Glycerol-water mixtures of dynamic viscosity ranging from 0.001-0.09 Pa.s were used as the working fluid. Four generic break-up modes were identified and discussed.

A non-linear inviscid model was developed by Părău *et al.* [34, 33]. They presented a non-linear evolution of a travelling wave disturbance on a curved slender inviscid jet emerging from a rotating orifice. Gravity was neglected in the analysis. One dimensional equations were derived using asymptotic methods and solved numerically. The results showed some qualitative agreement with results obtained by Wong *et al.* [44].

2.2 Previous investigations into break-up of curved liquid jets

This section describes work carried out by a post-doctoral research fellow Dr David Wong and a previous doctoral student Dr Iain Wallwork at the University of Birmingham.

2.2.1 Previous theoretical work

This section describes a theoretical study carried out by Wallwork *et al.* [42]. A single jet leaving a rotating orifice of radius a situated on a curved face of a cylindrical can of radius s_0, which is rotating on its axis at a constant rate Ω was considered.

The coordinate system used is an extension of cylindrical polar coordinates (s, n, ϕ), where s is the arc-length along the centreline of the jet and (n, ϕ) are polar coordinates in any cross section of the jet. See figures 2.2 and 2.3. The centreline of the jet is described in the Cartesian coordinate system $(X(s,t), 0, Z(s,t))$ in a rotating frame of reference fixed in the container. The origin is in the centre of the orifice from which the jet emerges. The x-axis points in a line from the central axis of the can towards the centre of the orifice and points away from the can. The x-axis is orthogonal to the central axis of the cylindrical can. The z-axis is orthogonal to the x-axis, lying in the

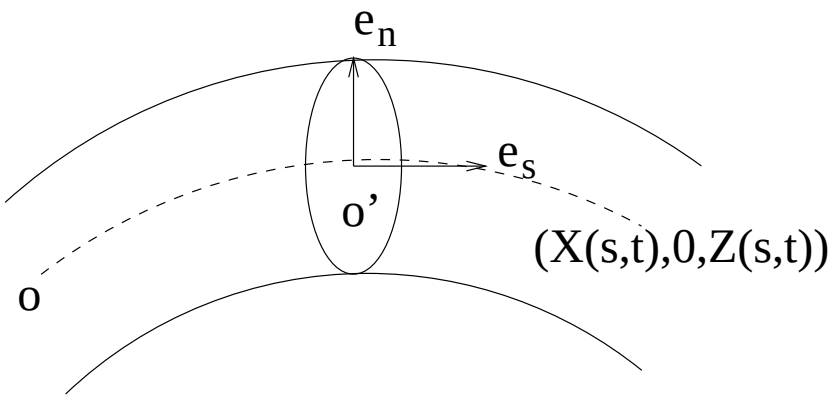

Figure 2.2: Definition sketch of the Cartesian coordinate system describing the centreline of the jet.

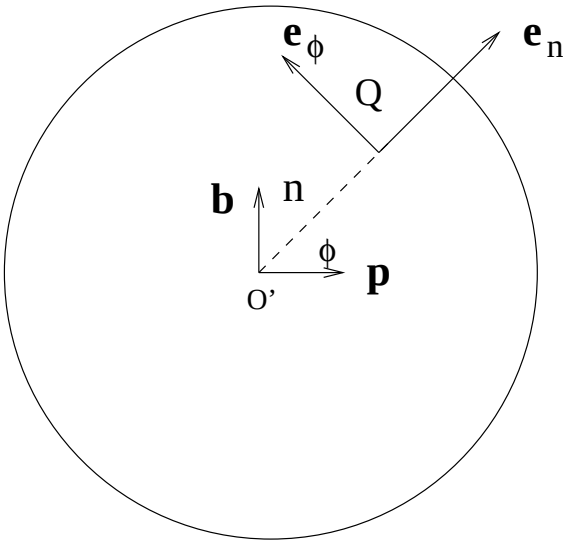

Figure 2.3: Definition sketch of the cross-section of the jet.

plane of the centreline of the jet, pointing in the opposite direction to which the can is rotating. Note t is time. The centreline of the jet can be written as $\mathbf{r}_{cl} = X\mathbf{i} + Z\mathbf{k}$ where $\mathbf{i}$, $\mathbf{j}$ and $\mathbf{k}$ are the unit vectors in the Cartesian coordinate system fixed inside the can. From $ds^2 = dX^2 + dZ^2$ we obtain the standard arc-length condition $X_s^2 + Z_s^2 = 1$. The unit vectors in the jet's coordinate system are determined from the principal unit vector $\mathbf{p}$ and the binormal vector $\mathbf{b}$. See figure 2.3. The vectors $\mathbf{e}_s$, $\mathbf{p}$ and $\mathbf{b}$ are written as,

$$\mathbf{e}_s = X_s\mathbf{i} + Z_s\mathbf{k}, \tag{2.2}$$

$$\mathbf{p} = \frac{\mathbf{e}_{s,s}}{|\mathbf{e}_{s,s}|} = \frac{X_{ss}\mathbf{i} + Z_{ss}\mathbf{k}}{\sqrt{X_{ss}^2 + Z_{ss}^2}} \tag{2.3}$$

and

$$\mathbf{b} = \mathbf{p} \times \mathbf{e}_s = \frac{(Z_{ss}X_s - X_{ss}Z_s)}{\sqrt{X_{ss}^2 + Z_{ss}^2}}\mathbf{j}. \tag{2.4}$$

The two other vectors $\mathbf{e}_n$ and $\mathbf{e}_\phi$ are defined as

$$\mathbf{e}_n = \cos\phi\,\mathbf{p} + \sin\phi\,\mathbf{b} \tag{2.5}$$

and

$$\mathbf{e}_\phi = -\sin\phi\,\mathbf{p} + \cos\phi\,\mathbf{b}. \tag{2.6}$$

After substituting equations (2.3) and (2.4) into equations (2.5) and (2.6) we find that the unit vectors in this coordinate system are

$$\begin{aligned}
\mathbf{e}_s &= X_s\mathbf{i} + Z_s\mathbf{k} \\
\mathbf{e}_n &= \cos\phi Z_s\mathbf{i} - \sin\phi\mathbf{j} - \cos\phi X_s\mathbf{k} \\
\mathbf{e}_\phi &= -\sin\phi Z_s\mathbf{i} - \cos\phi\mathbf{j} + \sin\phi X_s\mathbf{k},
\end{aligned}$$

here subscripts denote differentiation with respect to that subscript. The position vector of any particle Q relative to an origin located at the centre of the orifice O is

$$\mathbf{r} = \int_0^s \mathbf{e}_s ds + n\mathbf{e}_n. \tag{2.7}$$

This analysis is carried out in a more general situation in Wallwork [41].

The liquid is assumed to be inviscid. The model is written down using conservation of mass and Euler's equations,

$$\begin{aligned} \nabla \cdot \mathbf{u} &= 0, & (2.8)\\ \frac{\partial \mathbf{u}}{\partial t} + \mathbf{u} \cdot \nabla \mathbf{u} &= -\frac{1}{\rho}\nabla p - 2\boldsymbol{\omega} \times \mathbf{u} - \boldsymbol{\omega} \times (\boldsymbol{\omega} \times \mathbf{r}'). & (2.9) \end{aligned}$$

The boundary conditions are the kinematic condition and the dynamic condition, namely

$$\frac{\partial f}{\partial t} + \mathbf{u} \cdot \nabla f = 0 \ \text{ on } \ n = R(s, \phi, t) \tag{2.10}$$

and

$$p = \sigma\kappa \ \text{ on } \ n = R(s, \phi, t), \tag{2.11}$$

where σ is the surface tension, ρ is the density, κ is the curvature of the free surface, $\boldsymbol{\omega} = \Omega\mathbf{j}$ is the angular velocity vector in Cartesian coordinates, $\mathbf{r}' = \mathbf{r} + s_0\mathbf{i}$, $f(\mathbf{r}, t) = n - R(s, \phi, t) = 0$ defines the free surface position,

$$\mathbf{u} = u\mathbf{e}_s + v\mathbf{e}_n + w\mathbf{e}_\phi$$

is the velocity vector and p is the liquid pressure. Gravity is neglected; this is perhaps justified because usually the can is rotating quickly enough so that jet break-up occurs before the jet falls significantly due to gravity since $s_0^2\Omega >> g$ in most situations. (This will be generalised in chapter 7.) The arc-length condition $X_s^2 + Z_s^2 = 1$ is also required to close the system. The equations of motion are non-dimensionalised using the following

scales

$$\hat{u} = \frac{u}{U},\ \hat{v} = \frac{v}{U},\ \hat{p} = \frac{p}{\rho U^2},\ \hat{n} = \frac{n}{a},\ \epsilon = \frac{a}{s_0},\ \hat{R} = \frac{R}{a},\ \hat{s} = \frac{s}{s_0},\ \hat{t} = \frac{tU}{s_0},\ \hat{X} = \frac{X}{s_0},\ \hat{Z} = \frac{Z}{s_0} \tag{2.12}$$

where U is the exit speed of the jet at the orifice, $R(s,t)$ is the radius of the jet, a is the radius of the orifice, Ω is the rotation rate of the can, ϵ is the aspect ratio which is small and s_0 is the radius of the can. The hatted variables correspond to non-dimensional quantities. Some very lengthy equations are obtained. These are presented in Wallwork and Wallwork *et al.* [41, 42]. The following non-dimensional groups are obtained

$$We = \frac{\rho U^2 a}{\sigma},\quad Rb = \frac{U}{\Omega s_0},$$

which are the Weber number and Rossby number respectively. Dropping the hats for simplicity and denoting $\mathbf{X} = X\mathbf{i} + Z\mathbf{k}$, Wallwork *et al.* [42] found the steady solutions by posing the asymptotic expansions, namely

$$\left.\begin{aligned} u &= u_0(s) + \epsilon u_1(s,n,\phi) + \cdots \\ v &= \epsilon v_1(s,n,\phi) + \epsilon^2 v_2(s,n,\phi) + \cdots \\ p &= p_0(s,n,\phi) + \epsilon p_1(s,n,\phi) + \cdots \\ R &= R_0(s) + \epsilon R_1(s,\phi) + \cdots \\ X &= X_0(s) + \epsilon X_1(s) + \cdots \\ Z &= Z_0(s) + \epsilon Z_1(s) + \cdots \end{aligned}\right\} \tag{2.13}$$

and substituting (2.13) into the equations of motion as shown in Wallwork *et al.* [42]. In the steady case the trajectory depends on both the Weber number and the Rossby number. The resulting equations are

$$p_0 = \frac{1}{WeR_0}, \tag{2.14}$$

$$u_0 = \left(1 + \frac{1}{Rb^2}(X^2 + 2X + Z^2) + \frac{2}{We}\left(1 - \frac{1}{R_0}\right)\right)^{1/2}, \tag{2.15}$$

$$p_1 = \frac{n}{WeR_0}\cos\phi(X_s Z_{ss} - X_{ss} Z_s) + h_1(s), \tag{2.16}$$

$$v_1 = -\frac{n}{2}\frac{du_0}{ds}, \tag{2.17}$$

$$Z_{ss} = \frac{WeR_0 X_s}{WeR_0 u_0^2 - 1}\left(\frac{2u_0}{Rb} + \frac{ZX_s - (X+1)Z_s}{Rb^2}\right), \tag{2.18}$$

$$R_{0s} = -\frac{WeR_0^2((X+1)X_s + ZZ_s)}{Rb^2(2WeR_0 u_0^2 + 1)} \tag{2.19}$$

and

$$X_s^2 + Z_s^2 = 1 \tag{2.20}$$

where $h_1(s)$ could be found at next order in the expansion. However only the leading order equations are required for the centreline. Equations (2.18), (2.19) and (2.20) are a set of three differential equations for the three unknowns X, Z and R_0. They are solved numerically using a Runge-Kutta-Merson method subject to the initial conditions $X_s = 1$, $X = Z = Z_s = 0$ and $R_0 = u_0 = 1$. The larger the Rossby number the less tightly coiled the trajectory; this is as one would expect as the larger Rossby number corresponds to a lower rotation rate. The smaller the Weber number the more tightly coiled the trajectory. The explanation for this is that low speed jets coil more tightly than high speed jets since low speed jets are more influenced by rotation.

A linear temporal stability analysis is then performed on the steady solutions using a multiple scales approach given by

$$\left.\begin{aligned} \mathbf{u} &= \mathbf{u}(s, n, \phi, \epsilon) + \delta\tilde{\mathbf{u}}(s, \bar{s}, n, \phi, t, \bar{t}), \\ R &= R(s, \phi, \epsilon) + \delta\tilde{R}(s, \bar{s}, \phi, t, \bar{t}) \\ p &= p(s, n, \phi, \epsilon) + \delta\tilde{p}(s, \bar{s}, n, \phi, t, \bar{t}) \\ \mathbf{X} &= \mathbf{X}(s, \epsilon) + \delta\tilde{\mathbf{X}}(s, \bar{s}, t, \bar{t}) \end{aligned}\right\} \tag{2.21}$$

where the leading order part of (2.21) corresponds to the steady solution.

Travelling wave modes of the form $\exp(ik\bar{s}+\lambda\bar{t}+m\phi)$ are considered, where $\bar{s}=s/\epsilon$ and $\bar{t}=t/\epsilon$ gives short perturbations with wavelength $O(\epsilon)$ as required. This means the quantities with a tilde in (2.21) are proportional to $\exp(ik\bar{s}+\lambda\bar{t}+m\phi)$, corresponding to short travelling waves. These are the most general solutions to our stability problem, corresponding to a Fourier decomposition. The steady solutions are perturbed, where δ is a small dimensionless parameter measuring the size of the waves. Note that $\mathbf{u}$, R, p and $\mathbf{X}$ are steady and $\tilde{\mathbf{u}}$, $\tilde{R}$, $\tilde{p}$ and $\tilde{\mathbf{X}}$ are unsteady. This expansion is then substituted into the jet equations given in Wallwork *et al.* [42] and only linear terms in δ are retained. These equations are then solved at leading order in ϵ.

The growth rate and wavelength of the unstable mode is found to be a function of the arc-length, given by

$$(\lambda_m+iku_0)^2=\frac{1}{We}\left(\frac{1}{R_0^2}(1-m^2)-k^2\right)k\frac{I_m'(kR_0)}{I_m(kR_0)} \tag{2.22}$$

where the integer m represents the parameter associated with the azimuthal terms in the Fourier expansion and I_m is the mth order modified Bessel function.

Equation (2.22) can now be interpreted in terms of the temporal stability. Consider an instability mode of the form $\exp(ik\bar{s}+\lambda\bar{t}+m\phi)$ where λ is complex and k is real. For an unstable mode we require $Re(\lambda)>0$. From equation (2.22) we obtain an infinite number of neutrally stable eigenvalues and one unstable eigenvalue. The neutrally stable eigenvalues are

$$\lambda_m=-iku_0\pm\sqrt{\frac{1}{We}\left(\frac{1}{R_0^2}(1-m^2)-k^2\right)k\frac{I_m'(kR_0)}{I_m(kR_0)}}, \tag{2.23}$$

for $m\neq 0$. This mode looks similar to the classic Rayleigh mode given by equation (2.1). But this mode varies with arc-length. The unstable mode, obtained when $m=0$, is given by

$$\lambda_0=-iku_0\pm\sqrt{\frac{1}{We}\left(\frac{1}{R_0^2}-k^2\right)k\frac{I_1(kR_0)}{I_0(kR_0)}}. \tag{2.24}$$

This mode is unstable for $0 < k < 1/R_0$, since $Re(\lambda_0) > 0$. We find the most unstable mode occurs when $k = k^* = 0.697/R_0$. This value of k maximises $Re(\lambda_0)$. The most unstable mode has a wavenumber which grows with s since the undisturbed jet radius $R_0(s)$ decreases with s. This is discussed in more detail in Wallwork *et al.* [42]. Note that (2.24) reduces to the non-dimensional straight jet result when R_0 is a constant. This occurs in equations (2.14) to (2.20) when $Rb = \infty$ which corresponds to zero rotation.

Wallwork *et al.* [42] also derived a theoretical break-up length from the linear theory. Some simple experiments were carried out to compare with the linear theory and some agreement was found. But it was observed that the droplets were of non-uniform size, in the experiments, whereas the linear theory predicts droplets of uniform size.

2.2.2 Previous experimental work

This section describes previous experimental work on curved jets carried out by Wong *et al.* [44]. Laboratory scale experiments were carried out in the Department of Chemical Engineering at the University of Birmingham. The apparatus used consisted of a cylindrical can of diameter $D = 0.085$ m and height 0.115 m. It contained two diametrically opposed orifices with diameters of 0.001 m and 0.003 m. The can was partially filled with liquid to a height H where the aspect ratio (H/D) varied from 2/3 to 5/4. The liquid level H was kept constant by continuously supplying fresh solution to the can using a peristaltic pump (Waltson-Marlow 505s).

The trajectory of the jet was captured using a high speed digital camera (Photron Fastcam Super 10k) which is capable of 10,000 frames per second. Images from the camera were downloaded onto a personal computer for analysis. Measurements accurate to a tenth of a millimetre were made using Image-Pro Express software (Datacell Ltd.,U.K). At least 35 frames were used to ascertain break-up length. The reproducibility of the experiments was checked by repeating each experiment three times.

Use of different fluids allowed the physical properties of the liquids to be altered. In the experiments solutions of water and glycerol (0-80% glycerol by volume) were used

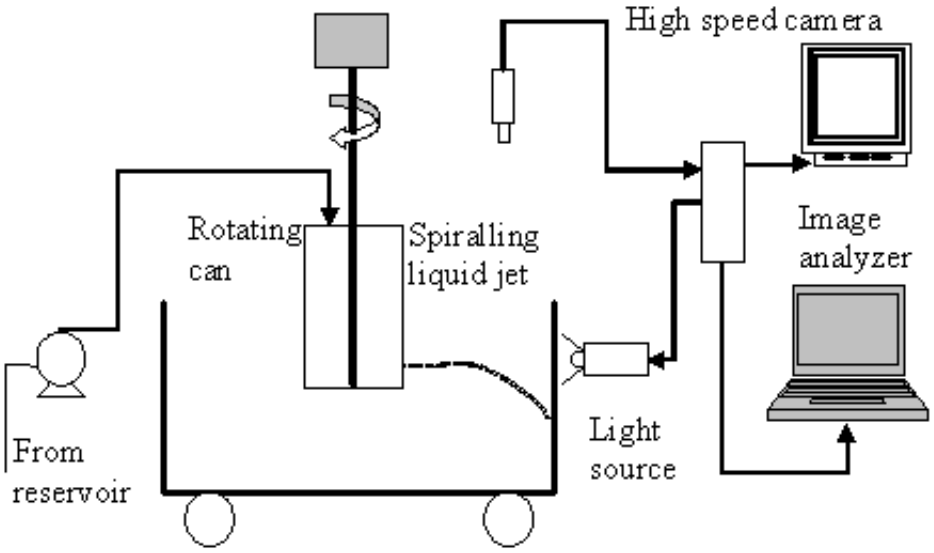

Figure 2.4: Diagram of the experimental set-up for the laboratory scale experiment

which gave dynamic viscosities ranging from 0.001 to 0.09 Pa s. This enabled both viscous and almost inviscid jets to be studied. The rotational speed of the can was varied from 50 to 300 rpm, which corresponds to an angular speed of $\Omega = 5.24 - 31.4$ rad s^{-1}. A diagram of the experimental set-up is shown in figure 2.4 taken from Wong *et al.* [44]. A photograph of the set-up is given in figure 2.5.

Along with Rossby number and Weber number there are three more non-dimensional groups, namely Ohnesorge number $Oh = \mu/\sqrt{\sigma a \rho}$, Reynolds number $Re = \rho U a/\mu$ and Froude number $F = U/(s_0 g)^{1/2}$, where μ is the dynamic viscosity and g is acceleration due to gravity. These non-dimensional groups incorporate effects due to viscosity and gravity and are discussed in more detail later in the thesis.

Over the range of experimental parameters investigated by Wong *et al.* [44], four different modes of break-up (mode 1-mode 4) were observed. These different modes have very different break-up mechanisms and resultant drop size distributions. Each mode is described below and pictures of each mode are shown in figures 2.6 to 2.13, taken from Wong *et al.* [44].

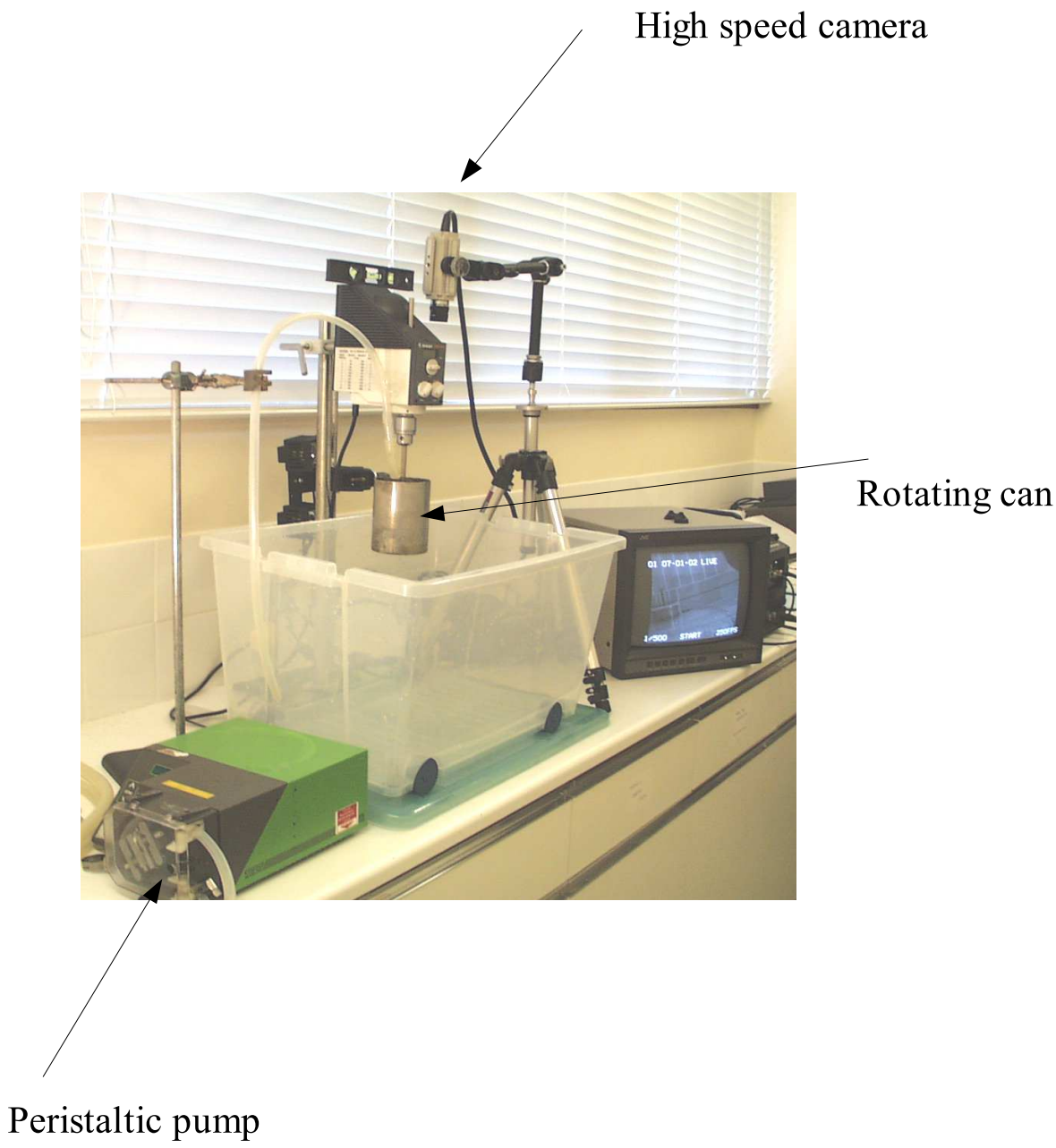

Figure 2.5: Photograph of the experimental set-up for the laboratory scale experiment

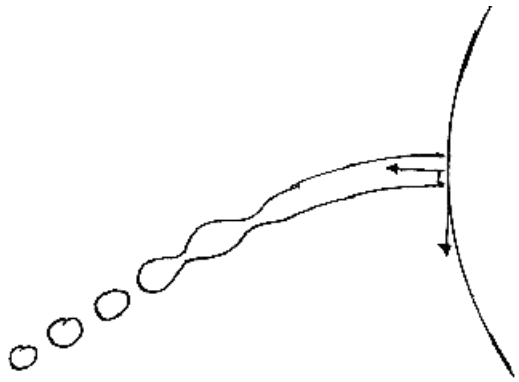

Figure 2.6: Sketch of mode 1 break-up

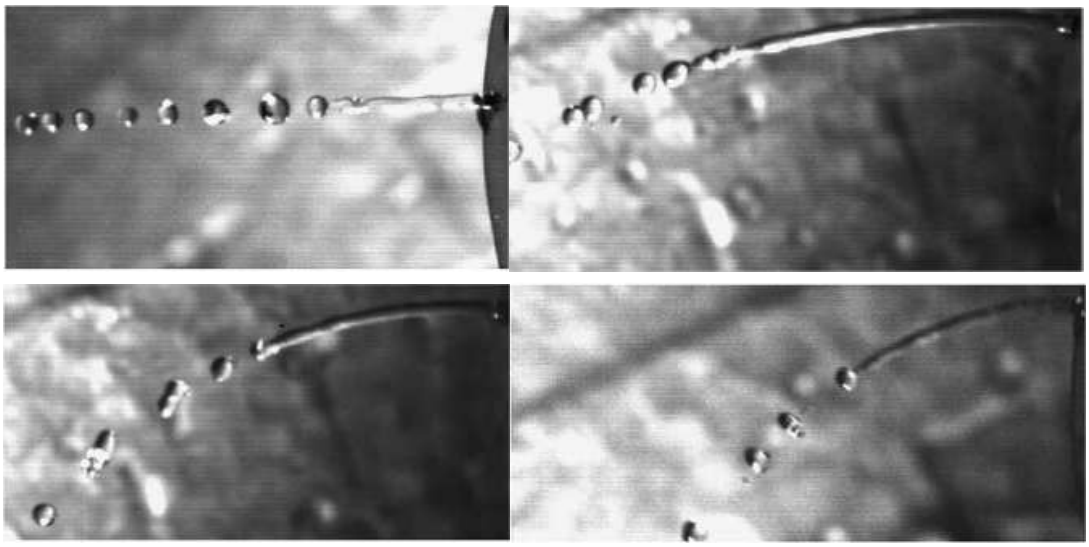

Figure 2.7: Mode 1 break-up for different rotation rates

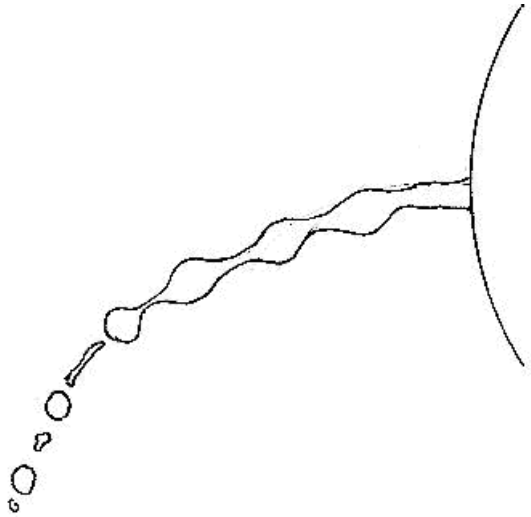

Figure 2.8: Sketch of mode 2 break-up

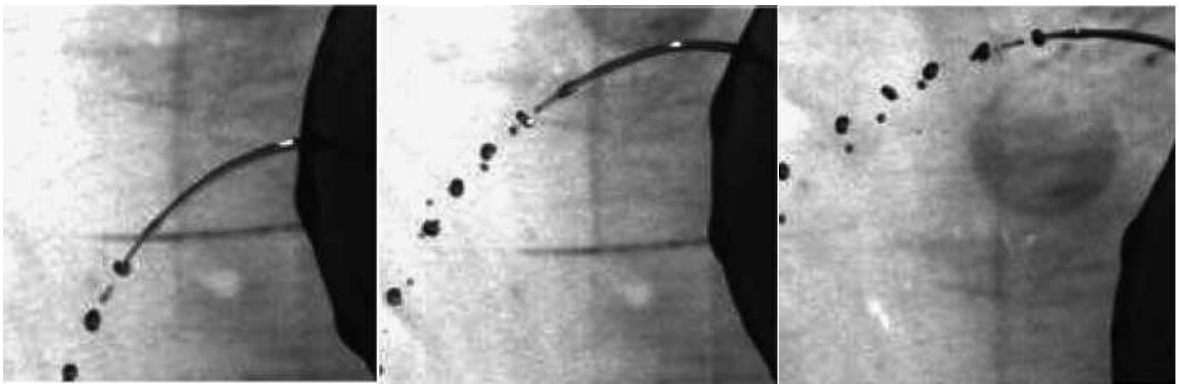

Figure 2.9: Sequence of mode 2 break-up

Mode 1, figure 2.6. Rapid formation of main drops near the orifice with an absence of satellite drops. Surface tension driven disturbances on the jet surface are convected downstream until they are large enough so that main drops form by capillary pinch-off. This mode was observed when the jets were least curved. This occurs for water jets emanating from the 0.001 m diameter orifice at low rotation rates. Figure 2.7 shows the mode 1 break-up sequence.

Mode 2, figure 2.8. Rapid disturbances of short wavelength visible on the surface of the jet. Formation of main drops is due to capillary pinch-off. Satellite drops are formed between the main drops from fragments of fluid created by the break off of the main

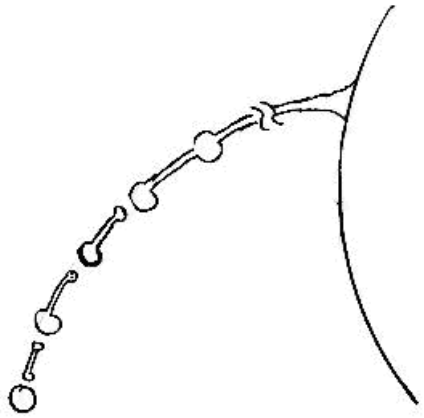

Figure 2.10: Sketch of mode 3 break-up

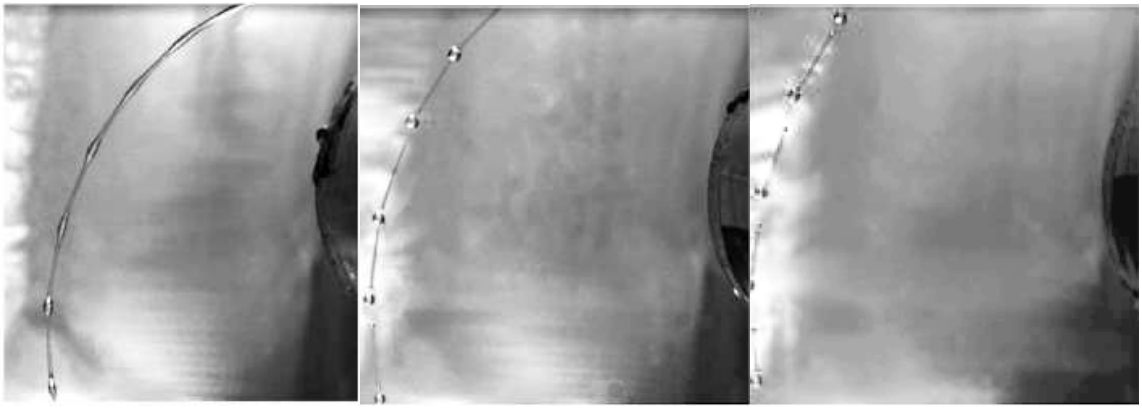

Figure 2.11: Sequence of mode 3 break-up

drop. The break-up mode changed from mode 1 to mode 2 when the jet exit velocity was increased, either by increasing the orifice size or increasing the rotation rate. Figure 2.9 shows the sequence of mode 2 break-up.

Mode 3, figure 2.10. Long wavelength (2-5 times the jet diameter) disturbances are visible on the jet surface. The jet breaks up simultaneously at several points along the curved jet into a continuous stream of droplets. Satellite drops are formed from the contraction of liquid threads connecting the main drops. This mode occurs when jets are created with high exit velocities using fluids with high dynamic viscosities. Figure 2.11 shows a sequence of mode 3 break-up.

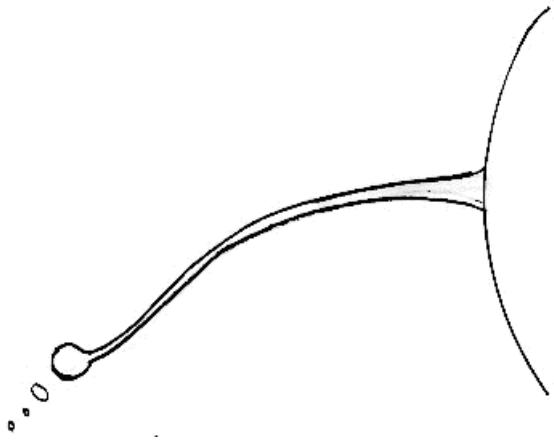

Figure 2.12: Sketch of mode 4 break-up

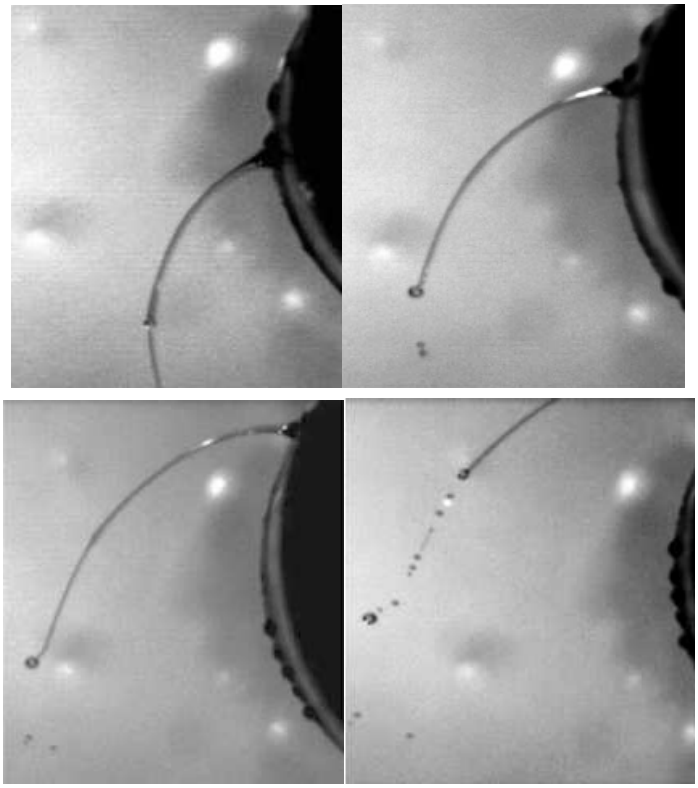

Figure 2.13: Sequence of mode 4 break-up

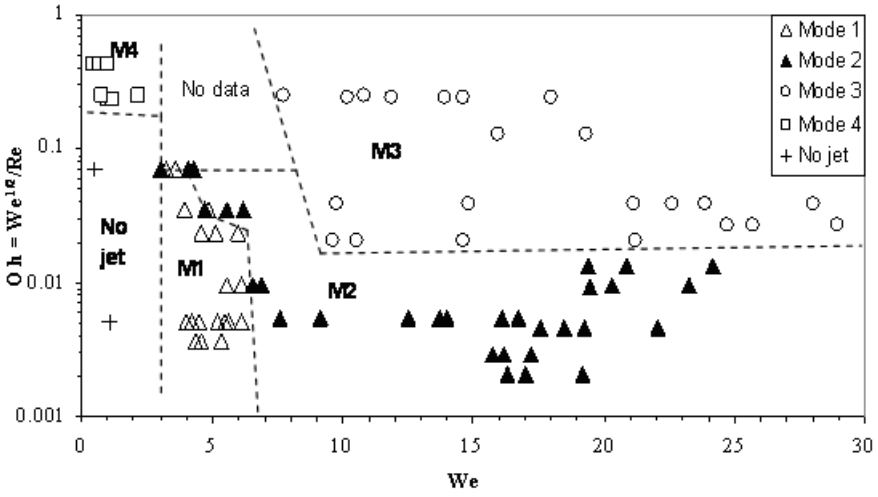

Figure 2.14: Flow map obtained from the laboratory scale experiments. Ohnesorge number against Weber number.

Mode 4, figure 2.12. Highly non-linear disintegration is observed. The jet first elongates and emaciates, then a swell forms at the end of the jet. The inertia of the swell causes the jet to bend away from the can. This causes the trajectory of the jet to change. The jet eventually becomes so tenuous it shatters forming satellite drops and the remaining jet recoils. This mode occurs for high viscosity jets with a low exit velocity. Here the jet elongates because of reduced instability caused by high viscosity. The tip of the jet bends away from the can and causes disturbances to be convected upstream which is a unique feature of this mode. Figure 2.13 shows the sequence of mode 4 break-up.

Variables such as the observed break-up mode, the break-up length, drop size distribution and drop size are dependent upon many different parameters such as liquid viscosity, surface tension, rotation rate of the can, orifice size, density of the liquid and liquid height in the can. Using the non-dimensional groups identified earlier allows the influence of various parameters to be determined.

The break-up mode observed is a strong function of viscosity and exit velocity. A plot of Ohnesorge number and Weber number shown in figure 2.14 groups together data for each mode. Therefore the break-up mode can be predicted from this plot. Introduction

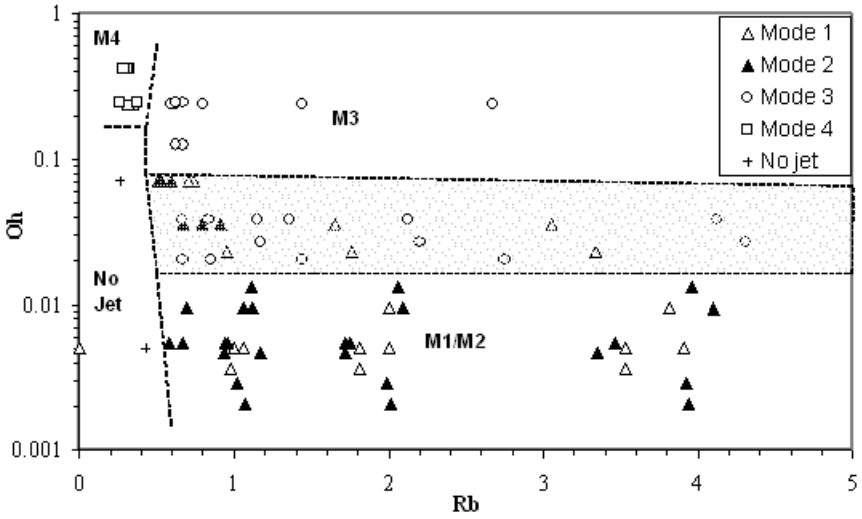

Figure 2.15: Flow map from the laboratory scale experiments. Ohnesorge number against Rossby number.

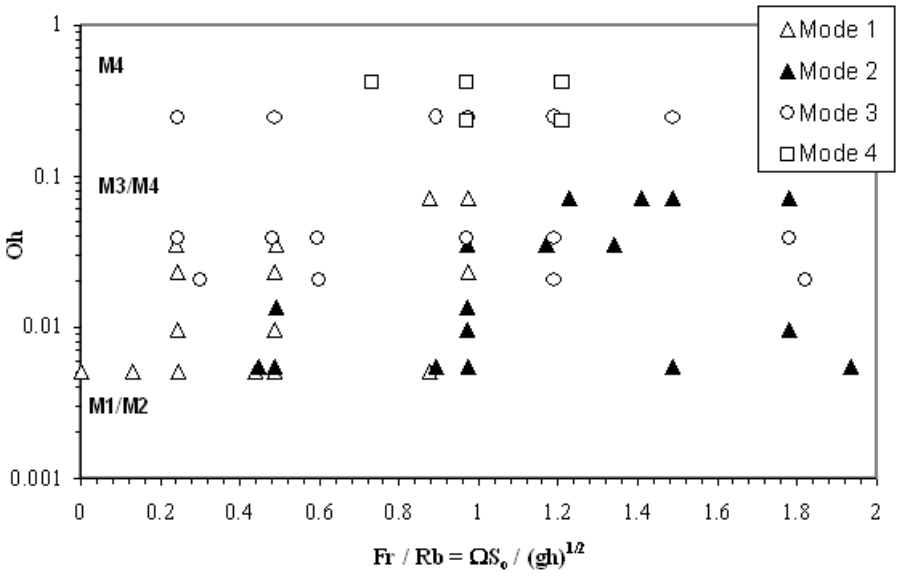

Figure 2.16: Flow maps from the laboratory scale experiments. Ohnesorge number against modified Froude number/Rossby number.

of rotation rate complicates the analysis. The exit velocity is affected by the centrifugal forces generated by the rotation of the can. A plot of Ohnesorge number and Rossby number (figure 2.15) shows regions where there is mode 1 break-up, mode 2 break-up, mode 3 break-up or mode 4 break-up. However we can see that mode 1 and mode 2 break-up overlap therefore we cannot predict break-up mode from this plot. To elucidate the influence of rotation on break-up without considering exit velocity we define another non-dimensional group a modified Froude number, Fr, namely

$$Fr = \frac{U}{\sqrt{gH}},$$

where H is the height of the liquid in the can above the orifice. This modified Froude number compares the exit velocity of the jet under the influence of gravity with the can rotating and the exit velocity of the jet when the can is stationary. Hence dividing the modified Froude number by the Rossby number we obtain,

$$Fr/Rb = \frac{\Omega s_0}{\sqrt{gH}},$$

which is independent of exit velocity. Figure 2.16 shows that the data cannot be grouped using this parameter, but at low Ohnesorge number mode 1 is seen to occur predominately at values of $Fr/Rb < 1$, while mode 2 occurs mainly at $Fr/Rb > 1$. At high Ohnesorge number mode 3 and mode 4 occur over the whole range of Fr/Rb. This is an important result as it shows that break-up mode cannot be predicted from rotation rate and fluid properties alone and that knowledge of exit velocity is essential.

The high speed digital camera was also used to capture images of the drops so that drop size could be measured and image analysis software used to calculate the drop size distribution. Drop size distribution curves were obtained using samples of at least 200 drops. The drop size distributions are plots of the drop diameter normalised against the orifice diameter and $f(n)$. To define $f(n)$ we consider some drops within a sample to

have a normalised diameter of n. The ranges of drop sizes were sub-divided into a finite number of distinct intervals. The number n corresponds to the drop size of the centre of each interval. To find $f(n)$ corresponding to the diameter n we use the following formula

$$f(n) = \frac{\text{The number of drops with diameter } n}{\text{Total number of drops measured}}.$$

This corresponds to the frequency of drops of diameter n (or more exactly, the proportion of drops within the corresponding interval). The drop size distributions obtained in mode 1 are uni-modal corresponding to an absence of satellite drops. This drop size distribution can be found in Wong *et al.* [44].

Figure 2.17 shows drop size distribution curves for mode 2 break-up. The drop size distribution is bi-modal, the smallest peak indicating the size and frequency of the satellite drops. The other peak corresponds to the main drops. Figure 2.18 shows drop size distribution curves for mode 3 break-up. Mode 3 break-up produced a significant number of satellite drops. The sizes of the satellite drops approach the size of the main drops. Figure 2.19 shows that mode 4 (represented by dashed lines) is dominated by satellite drops. These are formed as a result of the jet shattering as it thins, Wong *et al.* [44]. (Note that the dashed lines show higher values of $f(n)$ because a smaller number of intervals were used to sub-divide the data for mode 4.)

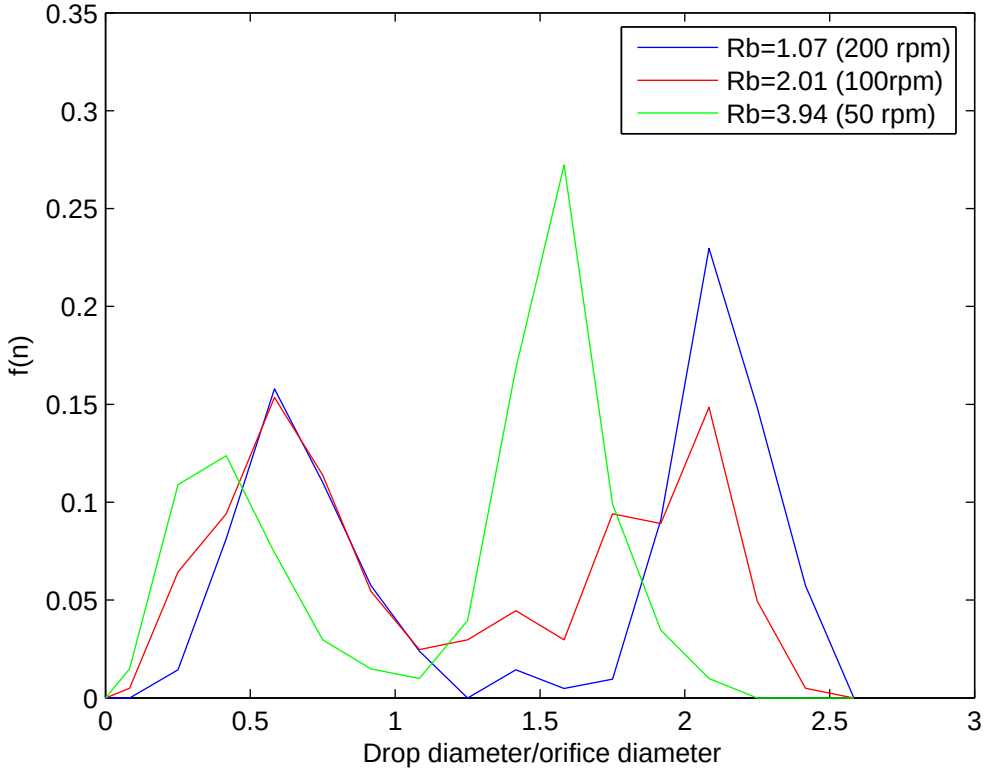

Figure 2.17: Drop size distributions for three rotation rates in break-up mode 2, $Rb = 3.94,\ 2.01$ and 1.07, $Oh = 0.0029$.

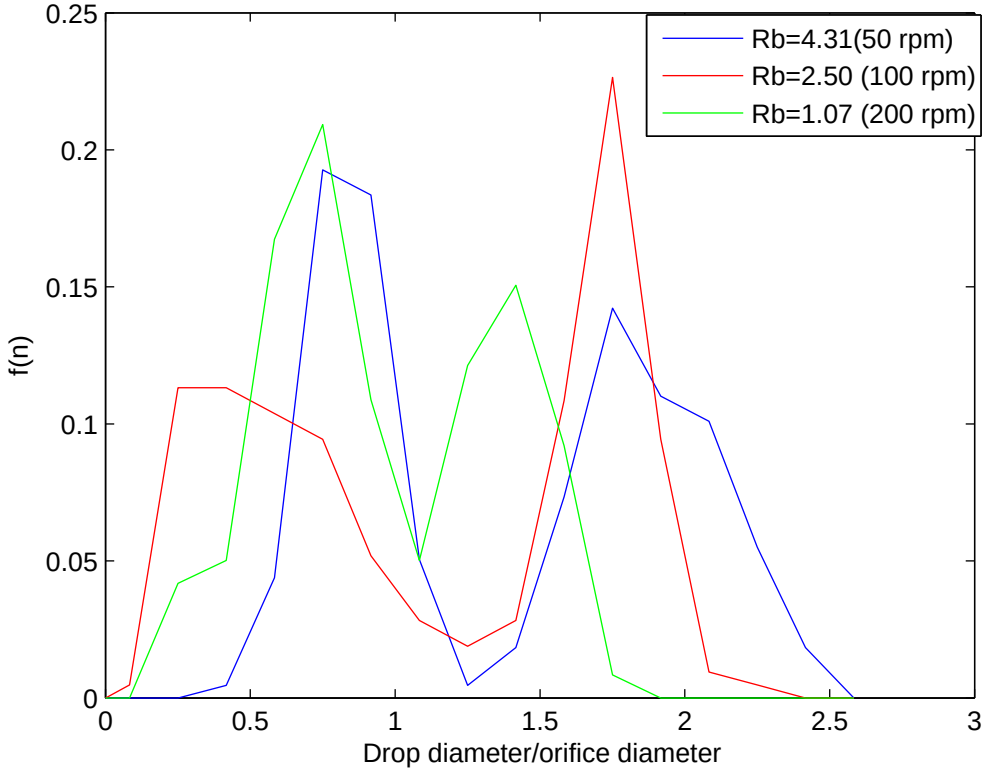

Figure 2.18: Drop size distributions for three rotation rates in break-up mode 3, $Rb = 4.31,\ 2.20$ and 1.17; $Oh = 0.038$.

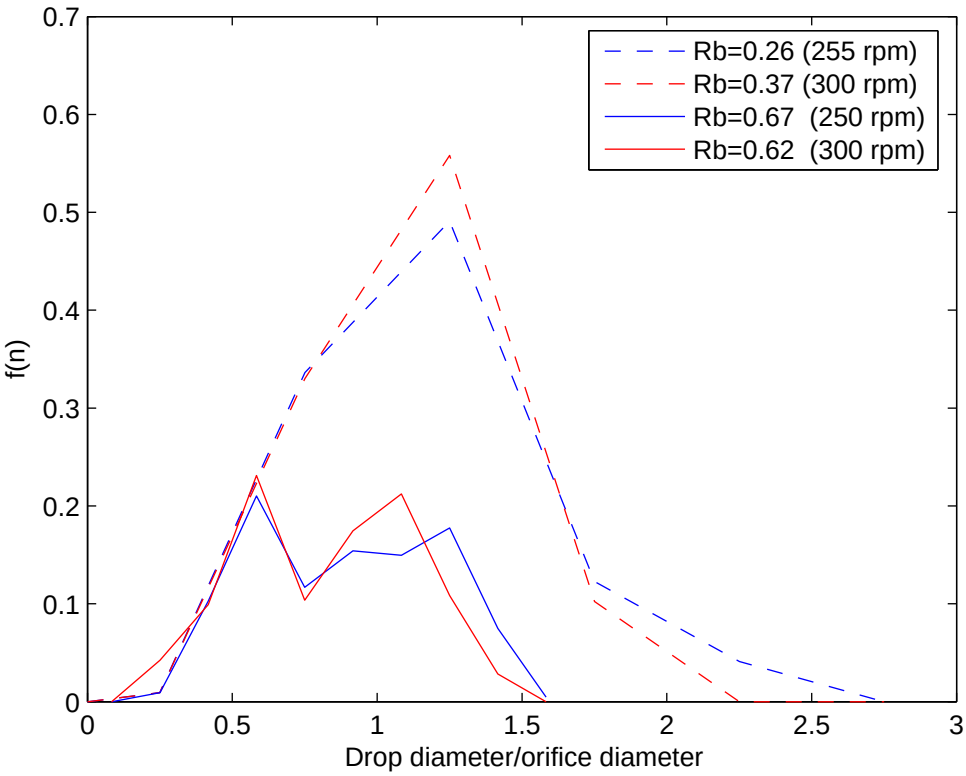

Figure 2.19: Drop size distributions for two rotation rates: (a) break-up mode 3 $Rb = 0.67$ and 0.62; $Oh = 0.178$ with the 0.0015 m orifice; (b) break-up mode 4 $Rb = 0.26$ and 0.37; $Oh = 0.352$ with the 0.0005 m orifice.

Chapter 3

Pilot scale experiments

This chapter describes original experimental investigations carried on the pilot scale rig. Previous work that was carried out on a laboratory scale rig is described in section 2.2.2. Whilst this gave an insight into break-up mechanisms and drop formation we could not approach the typical parameter values obtained in the industrial situation. It was not possible to build an experimental rig with the same dimensions as an industrial prilling tower for use in a laboratory. A pilot scale rig was built; this was larger than the laboratory scale rig but smaller than the industrial scale. This pilot scale rig would provide results closer to the industrial scale. Table 3.1 compares typical parameter values for laboratory, pilot and industrial scales. (The information in table 3.1 was obtained from Wallwork *et al.* [42], Wallwork [41] and Hide [22].) The experiments on the laboratory scale were repeated on the pilot scale; this enabled a larger range of parameters to be studied since a larger exit velocity can be obtained. It was shown on the laboratory scale that exit velocity had a large influence on the break-up behaviour so experiments on the pilot scale would provide a more realistic insight to break-up behaviour on the industrial scale.

Table 3.1: Table showing parameter values on the laboratory, pilot and industrial scales for fertiliser production at Norsk Hydro in Norway.

Parameter	**Laboratory scale**	**Pilot scale**	**Typical industrial scale**
Liquid dynamic viscosity, μ (Pa s)	0.001-0.09	0.001-0.0081	0.00148
Liquid density, ρ (kgm^{-3})	1000-1200	1000-1215	1313
Liquid surface tension, σ (Nm^{-1})	0.047-0.072	0.065-0.072	0.092
Orifice radius, a (m)	0.0005 and 0.0015	0.0005 and 0.0015	0.002
Can rotation rate, Ω (rad s^{-1})	5.2-31.4 (50-300 rpm)	3.14-31.4 (30-300 rpm)	33.5-47.1 (320-450 rpm)
Jet exit velocity (ms^{-1})	0.318-0.985	0.1-6.3	1.3
Can radius, s_0 (m)	0.0425	0.1425	0.25
Rossby number, $Rb = U/s_0\Omega$	0.4-4.0	0.13-7.0	0.11
Reynolds number, $Re = \rho U a/\mu$	1-1000	2-4200	232
Weber number, $We = \rho U^2 a/\sigma$	0.5-25	0.36-170.2	48.29
Ohnesorge number, $Oh = \mu/\sqrt{\sigma a \rho}$	0.005-0.4	0.0031-0.3091	0.03

The pilot scale rig consisted of a rotating can with a diameter, D, of 0.285 m and height 0.5 m. The can was partially filled with liquid to a height H where the aspect ratio (H/D) is 1/4 or 1/2. The can contains one orifice of either 0.001 m or 0.003 m diameter. The image analysis was performed as described in section 2.2.2. A photograph of the rig is shown in figure 3.1 and a sketch of the experimental set-up is given in figure 3.2.

3.1 Methods and materials

In this section we give a detailed description of the methods and materials used in the pilot scale experiments. Initial experiments were carried out by myself. Once the experimental method was well established and repeatable further experiments were carried out by Tom Whateley and Ben Caine, fourth year MEng students, supervised by myself, Dr Mark Simmons, Department of Chemical Engineering and Professor Stephen Decent, School of Mathematics.

The physical properties of each liquid system were altered by using different fluids. In the experiments solutions of water and glycerol (0-80% glycerol by volume) were used which gave dynamic viscosities ranging from 0.001 to 0.09 Pa s. This enabled both viscous and almost inviscid jets to be studied. The solutions were dyed black with nigrosine (BDH Chemical Suppliers, 5% by volume) to give better contrast in the images. The rotational speed of the can was varied from 30 to 300 rpm, which corresponds to an angular speed of $\Omega = 3.14 - 31.4$ rad s^{-1}. The exit velocity was estimated by measuring the difference in liquid height, dH and using the following formula

$$U = \frac{s_0^2 dH}{a^2 t},$$

where U is the jet exit velocity, s_0 is the radius of the can, a is the radius of the orifice and t is the duration of the experiment in seconds. Note that throughout this thesis we refer to the jet exit velocity U; this is taken to be the velocity in the rotating frame of

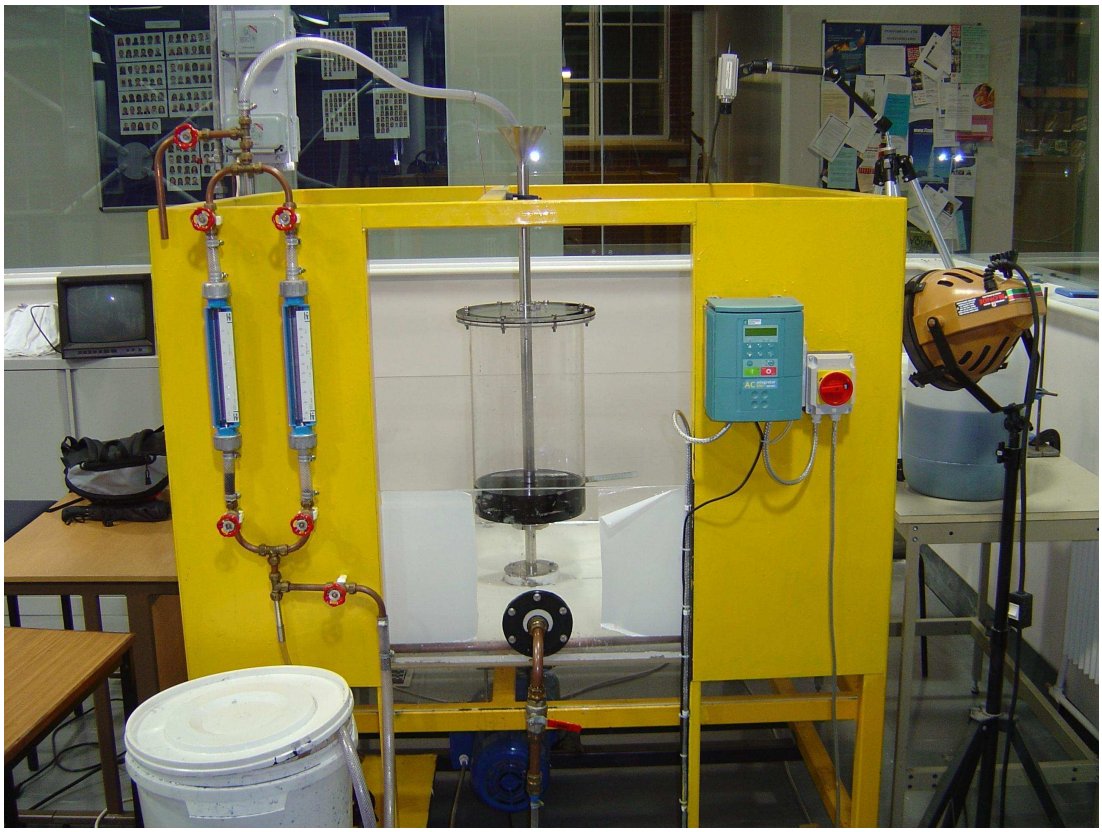

Figure 3.1: Photograph of the pilot scale rig

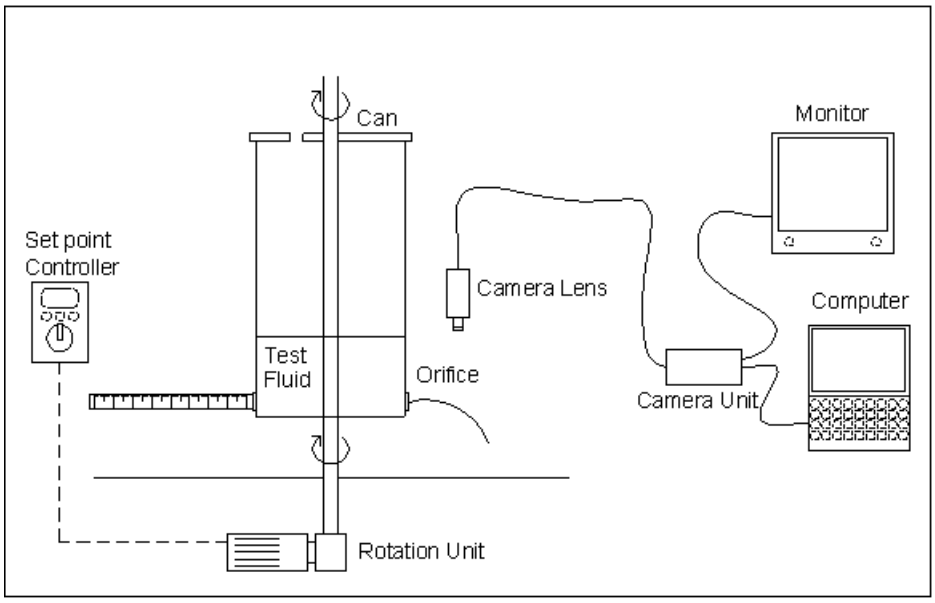

Figure 3.2: Sketch of the pilot scale set-up

reference moving with the can. In the frame fixed in the laboratory the jet exit speed is given by $\sqrt{U^2 + \Omega^2 s_0^2}$.

3.1.1 Experimental method

In this section we give a detailed exposition of the experimental procedure. The desired liquid was prepared as to requirements for each experiment. Nigrosine (BDH Chemical Suppliers) was added and stirred into the mixture. The solution was left overnight to ensure any remaining segregation was removed by molecular diffusion. Next, the desired orifice size was selected and fitted to the can. A bung was used to prevent liquid escaping from the orifice before the experiment. The high speed camera (Photron Fastcam Super 10k) was fitted with a suitable lens and positioned so the jet broke up within the camera's field of view. A 25 mm lens was used for images when the camera is away from the jet, and a 12 mm lens was used for taking close up images. Two high powered lights were used to illuminate the jets.

A ruler was attached to the can on the opposite side to the orifice, as shown in figure 3.2 for calibration purposes. An image of the rule was taken and saved to the

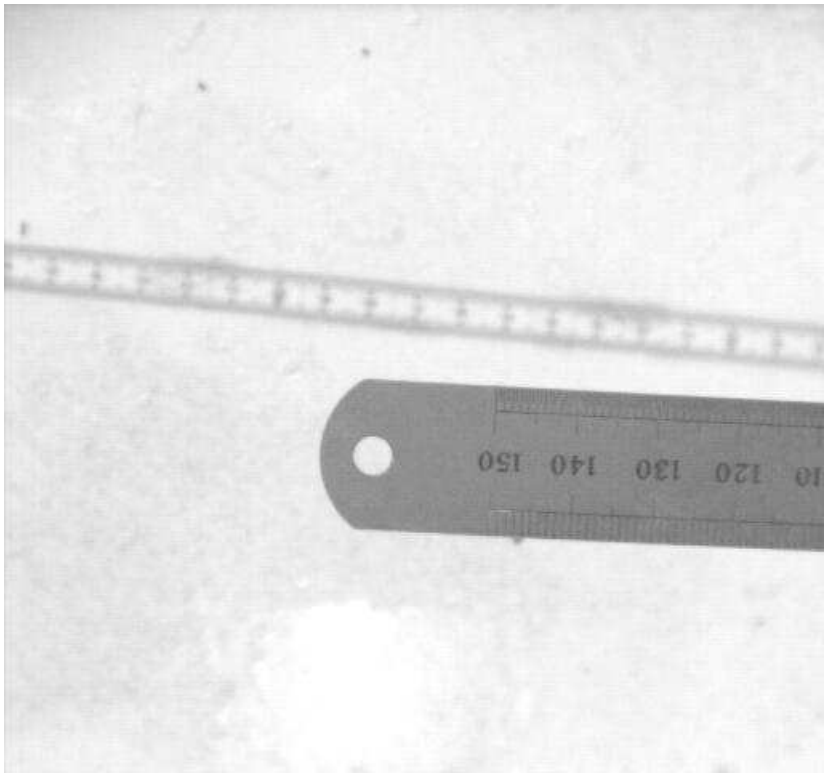

Figure 3.3: An image used for calibration

personal computer, see figure 3.3. This image was used for calibrating the image analysis software for drop size and break-up length measurements. A typical measurement made using the software is shown in figure 3.4. Next the solution was added to the can to the required height and the desired rotation rate was selected.

To start the experiment the bung was removed; the motor to drive the can and the timer were switched on simultaneously. Images of the jet were taken when the liquid in the can was observed to have reached a steady state. When the required time for the test was over the experiment was stopped and the bung was replaced. Next, the drop in liquid level in the can was measured and recorded so that the exit velocity could be calculated. Then the images of the jets were downloaded onto a personal computer for analysis. To ensure reproducibility the experiment was repeated three times. One of the parameters was then altered and the above process repeated.

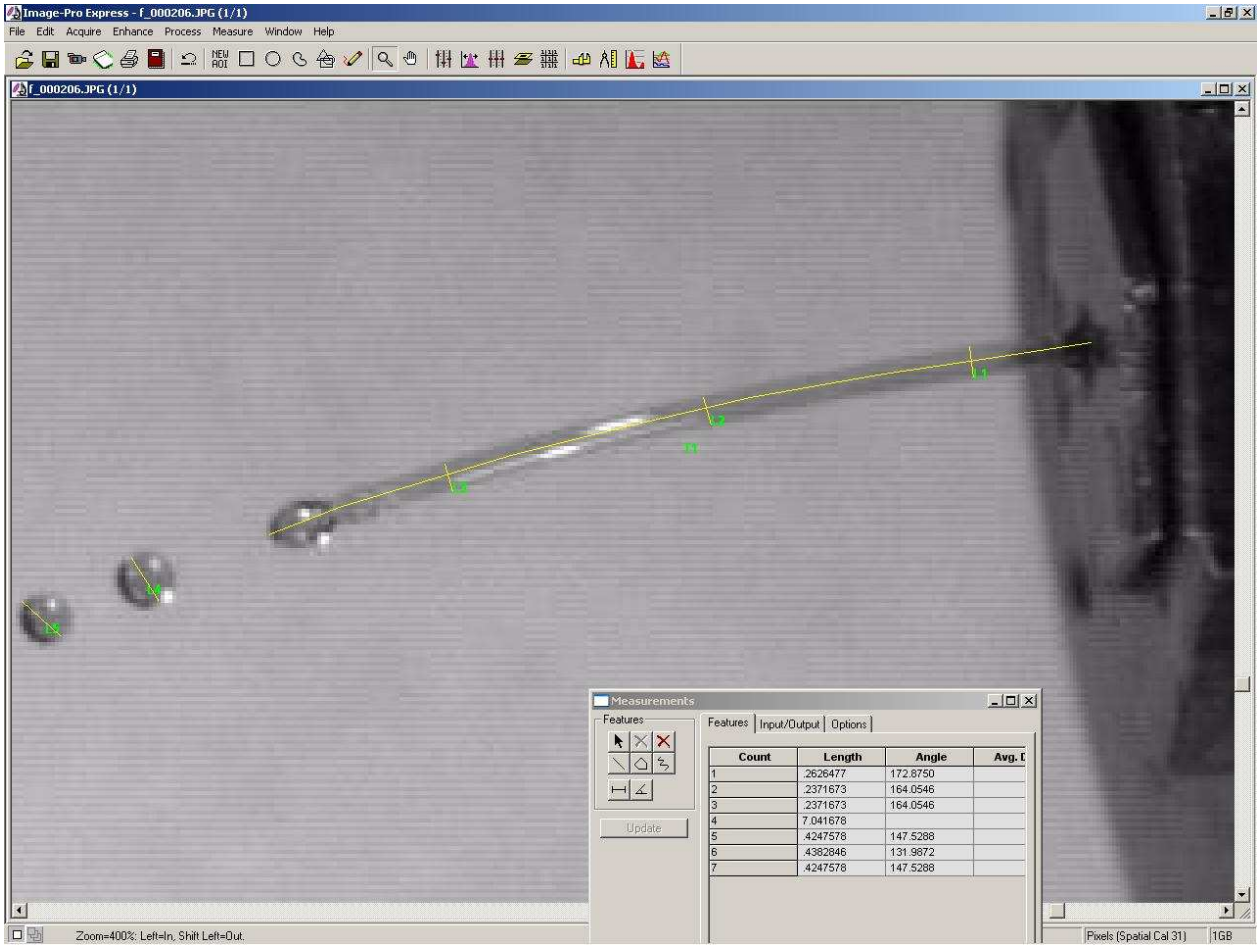

Figure 3.4: Image analysis using Image-Pro Express software (Datacell Ltd., U.K).

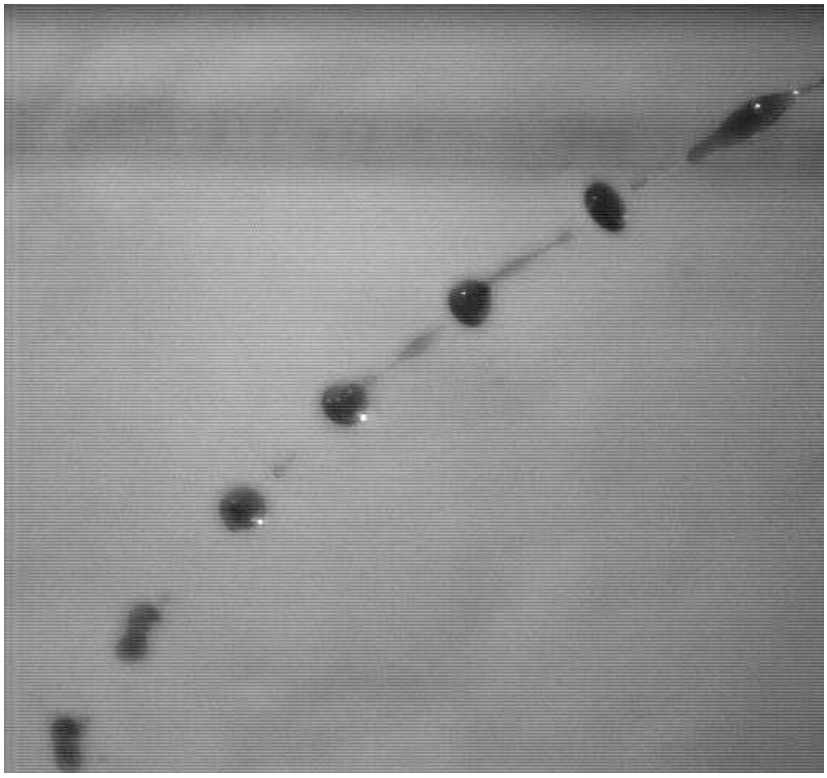

Figure 3.5: Typical image used for measuring drop sizes.

The images were analysed on a personal computer using Image-Pro Express software (Datacell Ltd., U.K). The software program was calibrated using the calibration image recorded before each experiment. This software was used to measure the break-up length and the diameters of the drops formed. To ensure a representative sample of drop size 200 drops were measured, a typical image used for drop size measurements is shown in figure 3.5. The measurements taken were exported to Microsoft Excel where they were tabulated and used for analysis.

3.1.2 Experimental assumptions

In this section the assumptions made to facilitate a realistic analysis of the results are described.

- The exit velocity of the jet is assumed to be constant. This is justified since $dH << H$.

- 200 drop size measurements are sufficient to determine drop size distributions.
- 35 break-up measurements are sufficient to determine average break-up length.

The last two assumptions were verified by Wong *et al.* [44].

Chapter 4

Pilot scale results and comparison with laboratory scale

4.1 Break-up mechanism and prediction of break-up regime

This section discusses the results of the experiments carried on the pilot scale rig and makes comparisons with the laboratory scale work of Wong *et al.* [44]. The data from the pilot scale experiments is shown in figure 4.1, together with the mode boundaries obtained from the laboratory scale experiments.

Wong *et al.* [44] found that the modes of break-up were dependent upon the different influences of liquid inertia, liquid viscosity, surface tension and rotation rate acting upon the jet. They found that the mode of break-up could be predicted from a plot of Oh against We.

The results obtained from the pilot scale rig are generally in good agreement with the previously defined boundaries, but there are some notable differences. Mode 1 was not observed on the pilot scale and satellite drops were always obtained. At the laboratory scale, no satellite formation was observed for mode 1. Furthermore, jets on the pilot scale that displayed characteristics of mode 2 break-up were observed to break-up simultaneously in several places (as usually associated with mode 3), this typically occurred when Ohnesorge number was around 0.01 to 0.02 as shown by the use of both symbols for mode 2/mode 3 in figure 4.1; this is a mode with characteristics of both mode 2 and mode 3.

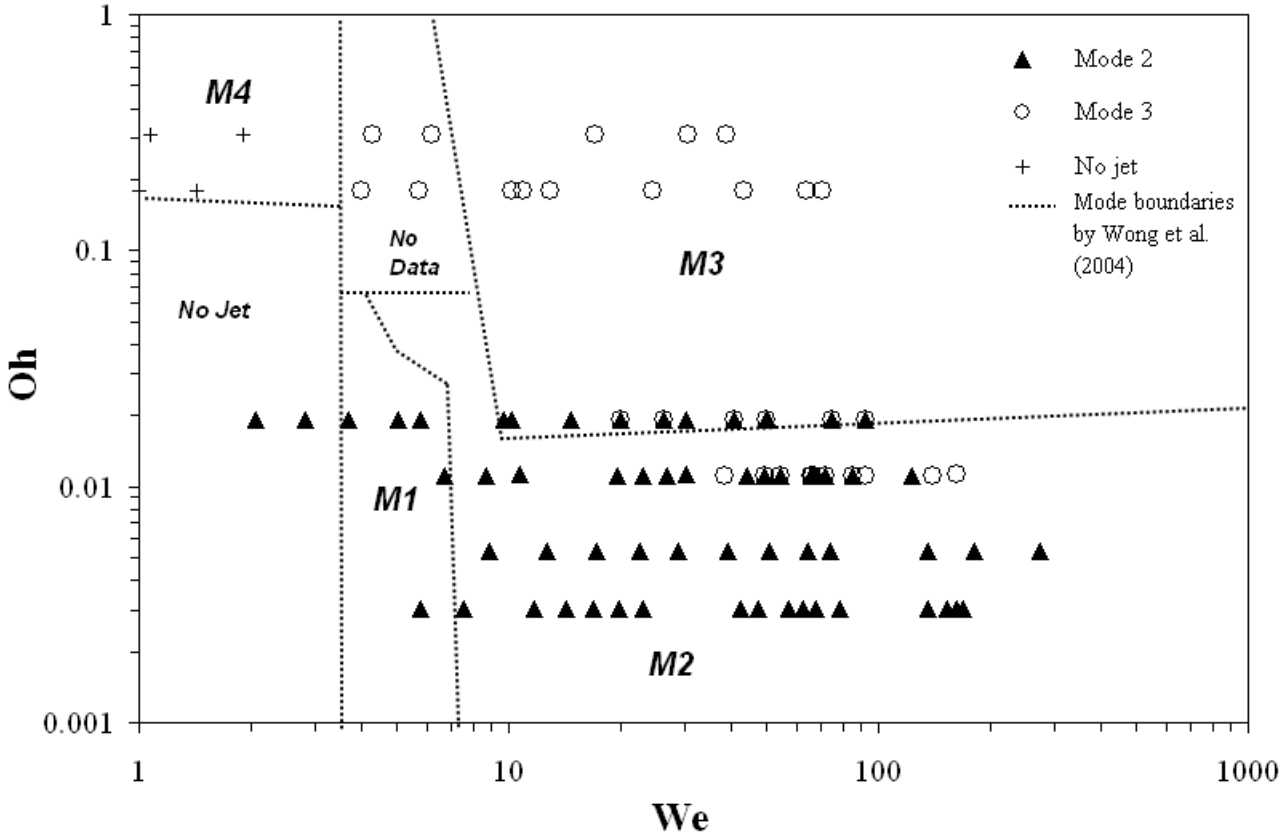

Figure 4.1: Flow-map showing We against Oh. The data points represent data obtained from the pilot scale. The mode boundaries (dashed lines) were obtained from the laboratory scale. Where jets showed characteristics of more than one mode two overlapping symbols are given.

Previous work by Wong *et al.* [44] found this simultaneously occurring break-up in more than one place a feature of only mode 3 and mode 4 break-up on the laboratory scale. Multiple break-up points and the absence of mode 1 break-up may be caused by wind drag, slight vibration in the rig or a combination of both, particularly at higher rotation rates. The break-up mode changed from mode 2 to mode 3 when the fluid viscosity was increased ($Oh > 0.1$), as shown in figure 4.1.

Mode 3 is distinguished by long wavelength disturbances (∼2-5 times the jet diameter) visible on the jet surface (figure 2.11). Considerable elongation of the jet was also observed and there was a difference in the way satellite droplets were created when compared with the laboratory scale. At the laboratory scale, a single satellite droplet was formed in mode 3 from the contraction of the liquid thread between each main drop. However, in this study on the pilot scale, multiple satellite droplets were frequently formed simultaneously from the fragmentation of liquid threads connecting the main droplets, rather than single satellite drops.

Over the range of experimental parameters studied, mode 4 break-up was not observed on the pilot scale; no jets were observed on the pilot scale in the mode 4 region from the laboratory scale. ('No jets' means that direct atomisation occurred at the orifice.) Also jets were obtained in the region where no coherent jets were observed on the laboratory scale at $Oh = 0.02$, see figure 4.1. This could be due to increased exit velocity on the pilot scale. The exit velocity is greater on the pilot scale than the laboratory scale for the same rotation rate and orifice size because the height of the liquid in the can is greater.

Figure 4.2 shows a plot of Rb against Oh for the pilot scale data. Mode 2 break-up generally occurs at low Oh and high Rb, i.e. for low viscosity liquids and low rotation rates. Mode 3 break-up occurs at high Oh and low Rb, i.e. for high rotation rates and high viscosity liquids.

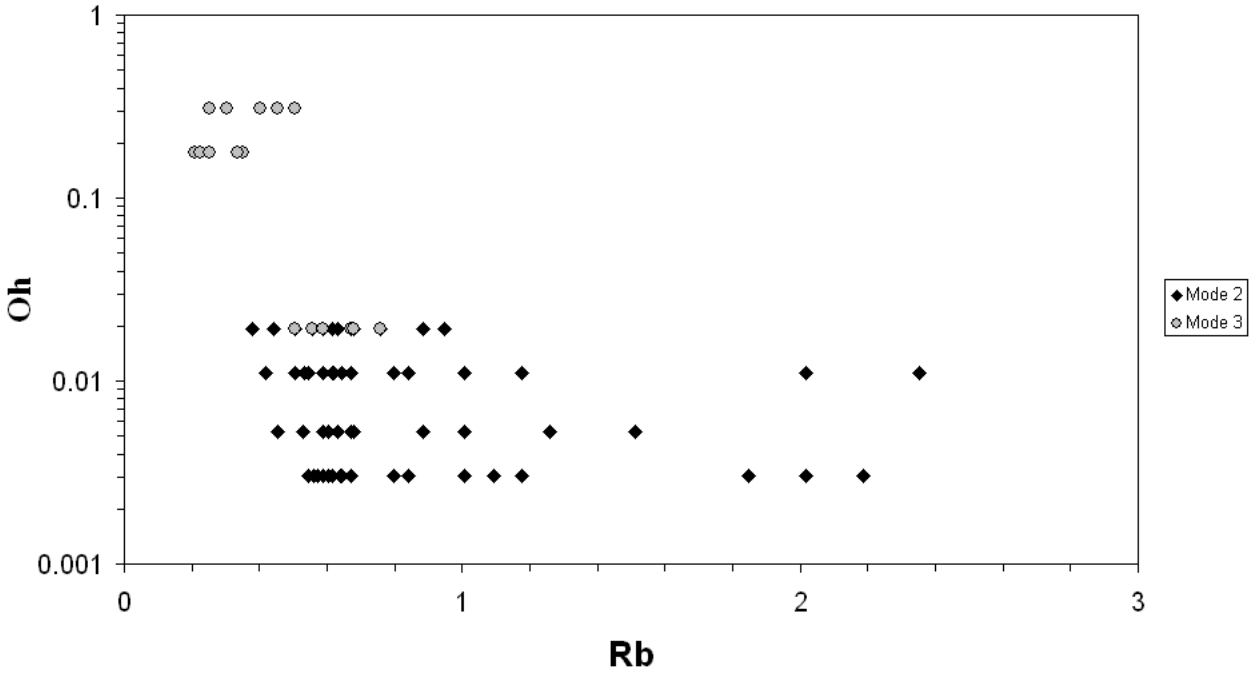

Figure 4.2: Flow-map of Oh against Rb for the pilot scale data.

4.2 Effect of rotation rate and viscosity upon jet break-up

The influence of rotation rate upon the break-up of a curved water jet (μ=0.001 Pa.s) is shown in figure 4.3. The break-up mode is mode 2. Increasing the rotation rate causes the trajectory of the jet to become more curved. Several features of the break-up are different from those observed at the laboratory scale. Break-up of the jet at multiple points occurs on the pilot-scale as shown in Figure 4.3(b); this is not observed at the laboratory scale. This effect is similar to that seen in mode 4 break-up on the laboratory scale, except that no disturbances were seen to propagate upstream. Non-axisymmetric (kink) disturbances are also visible on Figure 4.3(d) (right insert) but only axisymmetric (varicose) disturbances are observed on the laboratory scale in modes 1 to 3. The effect of wind resistance may be observed as the ligands between the primary drops are observed to bend in a direction normal to the curved central axis of the jet. Other possible reasons for the occurrence of multiple break-up points are increased mechanical vibration from the shaft and motor driving the rotation of the can.

4.3 Exit velocity and rotation rate

Figure 4.4 is a plot of rotation rate Ω, against the exit velocity U. The data was obtained on the pilot scale rig and in all cases $Oh = 0.011$. The circles correspond to liquid depth $H = 0.1425$ m and the stars correspond to liquid depth $H = 0.07$ m. We can see that exit velocity increases with the rotation rate within each liquid depth. Also the exit velocity is greater for larger liquid depth, which is expected. This demonstrates that exit velocity in the rotating frame of reference is a function of rotation rate and the depth of the liquid in the can; therefore $U = U(\Omega, H)$. This means that changing the rotation rate not only changes Rossby number but also Weber number, Reynolds number and Froude number. So the parameters in the experimental system are coupled and cannot easily be separated. This is indicative of a complex flow inside the can which is discussed further in chapter 10.

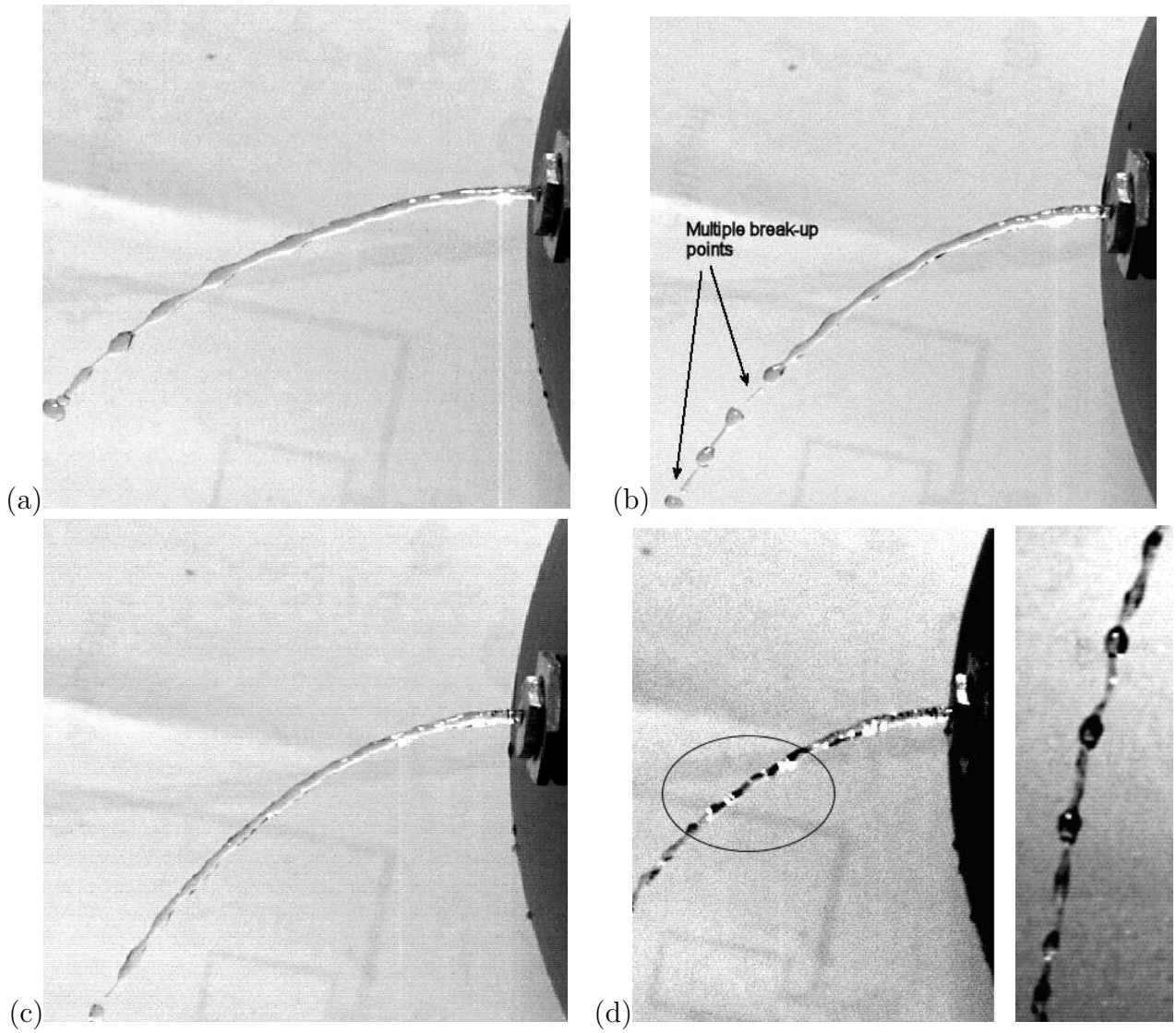

Figure 4.3: Features of break-up mode 2 with increasing rotational speed and orifice radius 0.0015 m (a) $Rb = 3.64$ (60 rpm); (b) $Rb = 2.47$ (120 rpm); (c) $Rb = 1.91$ (180 rpm) (d) $Rb = 1.41$ (300 rpm). $Oh = 0.0053$ ($\mu = 0.001$ Pa.s; $\rho = 997$ kgm^{-3}).

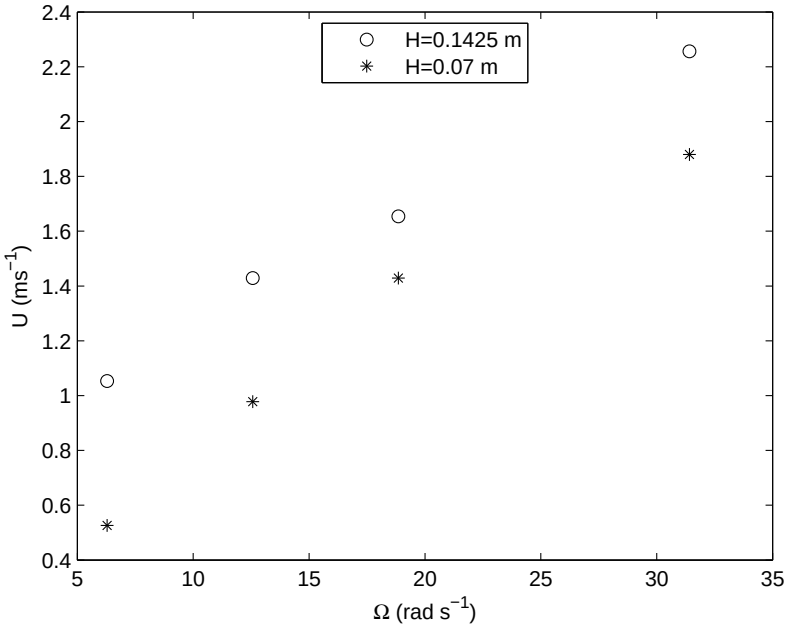

Figure 4.4: A plot of rotation rate, Ω against exit velocity, U. The data was all obtained on the pilot scale and $Oh = 0.011$. The circles correspond to a liquid depth of 0.1425 m and the stars correspond to a liquid depth of 0.07 m.

4.4 Drop sizes

Figure 4.5 is a plot of Rb against exit velocity on the laboratory and pilot scale. At $Rb \sim 1$ the exit velocity is similar on the laboratory and pilot scale. However at higher Rossby numbers the exit velocity on the pilot scale can be much higher than the exit velocity obtained on the laboratory scale because H can be much greater on the pilot scale experiment. The drop size distributions will only be compared qualitatively, since it is not always possible to obtain the same values of Re, We, Rb and F simultaneously at both scales.

Figure 2.17 (taken from Wong *et al.* [44]) shows drop size distributions in mode 2 on the laboratory scale for three rotational rates ($Rb = 3.94$, $Rb = 2.01$, $Rb = 1.07$). The drop size distributions are bi-modal with the smaller peak corresponding to satellite drops. Figure 4.6 shows drop size distributions in mode 2 for three rotational rates ($Rb = 0.84$, $Rb = 0.588$, $Rb = 0.56$) on the pilot scale. The drop size distributions are

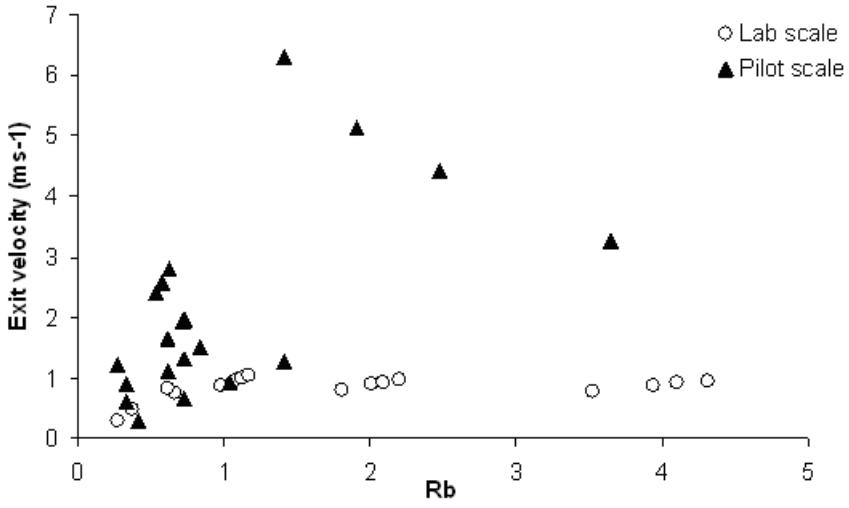

Figure 4.5: A plot of Rb against exit velocity on the pilot and laboratory scale.

bi-modal as expected. There are similar numbers of satellite drops as main drops. This is more like the drop size distributions obtained for mode 3 on the laboratory scale, see figure 2.18. Also extra satellite drops could be formed from the multiple break-up points, which was only observed for mode 3 and mode 4 on the laboratory scale.

Figure 2.18 (taken from Wong *et al.* [44]) shows the drop size distributions in mode 3 for three rotational rates ($Rb = 4.31$, $Rb = 2.20$, $Rb = 1.17$) on the laboratory scale. The drop size distributions are again bi-modal with peaks corresponding to the median sizes of the primary and satellite drops. There are a similar numbers of satellite and primary drops.

Figure 4.7 shows the drop size distributions in mode 3 for three rotational rates ($Rb = 0.336$, $Rb = 0.332$, $Rb = 0.269$) on the pilot scale. The drop size distributions are again bi-modal. The drop size distributions on the pilot scale are reasonably similar to the drop size distributions on the laboratory scale with similar number of satellite and primary drops obtained.

As expected, the drop size distributions obtained at the mode 2/mode 3 boundary for three rotational rates ($Rb = 0.588$, $Rb = 0.546$, $Rb = 0.504$) are also bi-modal (figure

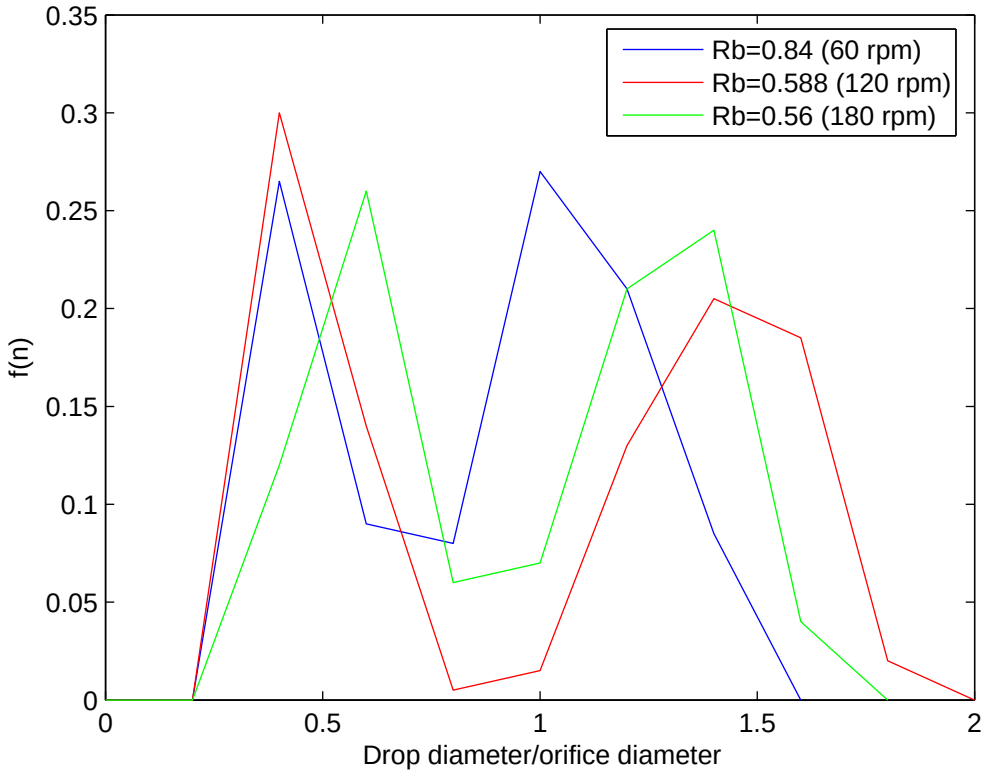

Figure 4.6: Mode 2 drop size distributions for three rotational rates, $Rb = 0.84$, $Rb = 0.588$ and $Rb = 0.56$ (60,120 and 180 rpm) on the pilot scale. ($Oh = 0.0031$)

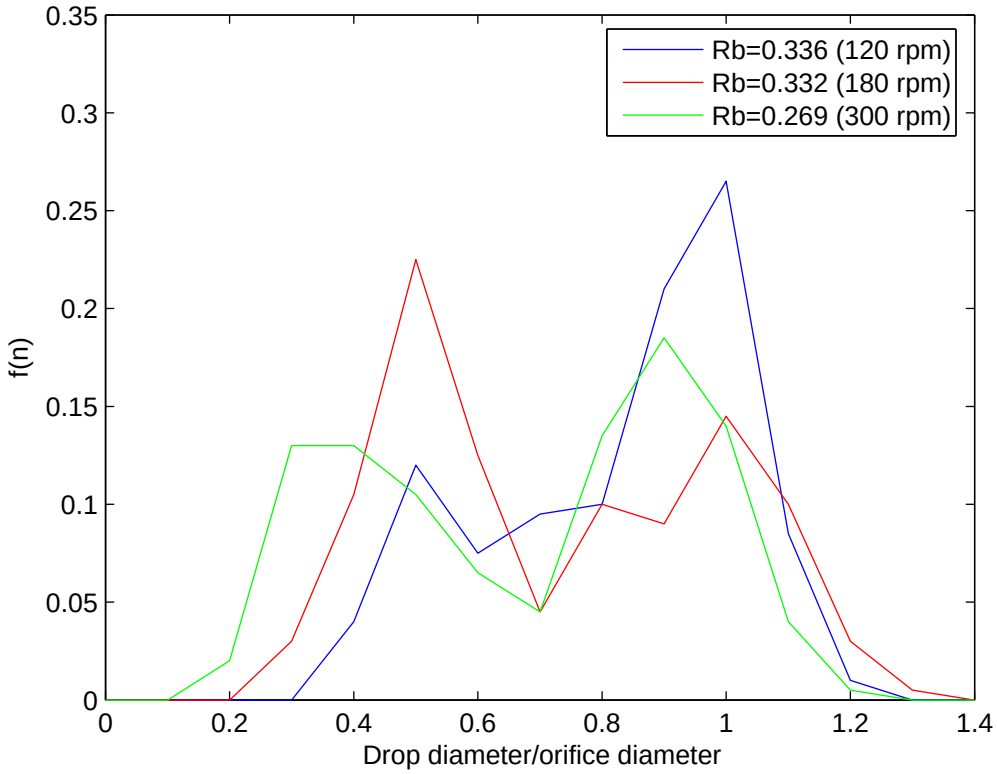

Figure 4.7: Mode 3 drop size distributions for three rotational rates, $Rb = 0.336$, $Rb = 0.332$ and $Rb = 0.269$ (120, 180 and 300 rpm) on the pilot scale, $Oh = 0.1785$.

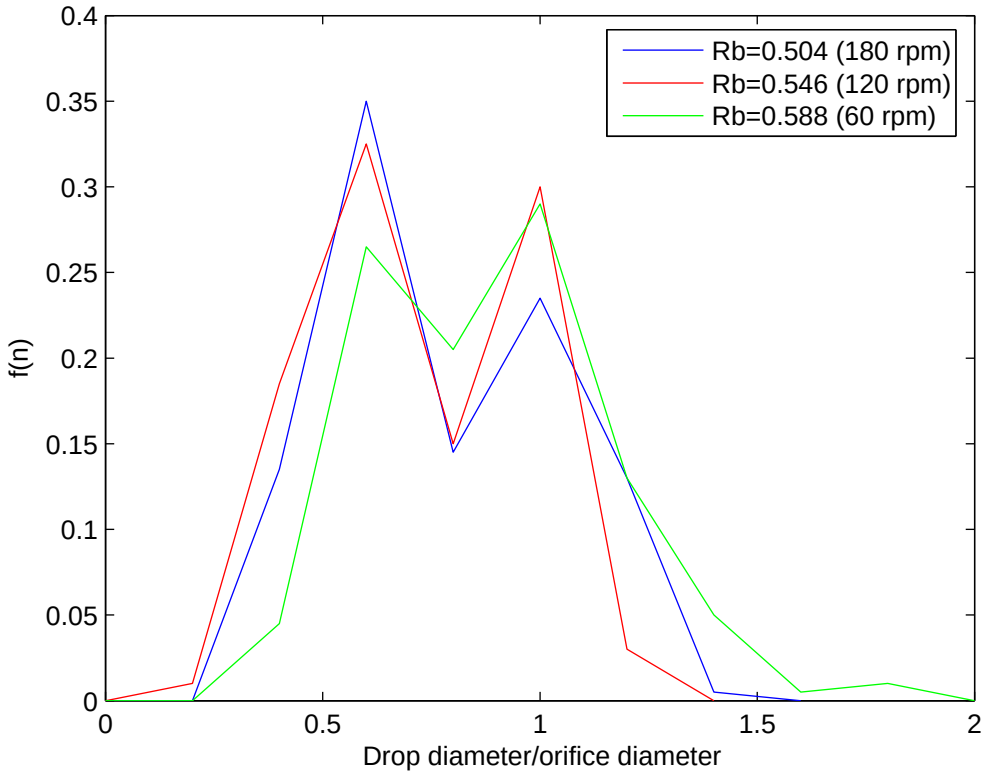

Figure 4.8: Mode 2/mode 3 drop size distributions for three rotational rates, $Rb = 0.588$, $Rb = 0.546$ and $Rb = 0.504$ (180, 120 and 60 rpm), $Oh = 0.011$ on the pilot scale.

4.8). There are similar numbers of satellite and main drops; this means the drop size distributions are more similar to mode 3 than mode 2.

Drop collisions causing the formation of larger drops by coalescence at higher rotation rates were observed in all modes of break-up. On the laboratory scale Wong *et al.* [44] only observed drop collisions during mode 1 and mode 2 break-up. An example of two drops coalescing is given in figure 4.9.

Figures 4.10, 4.11, 4.12 and 4.13 are plots of experimental main and satellite drop size against Weber number, Rossby number, Reynolds number and Froude number for $Oh = 0.0031$ and $Oh = 0.011$. The main and satellite drop sizes were obtained by taking the average normalised drop radius of the main and satellite drops. From figure 4.10 there appears to be a weak decrease in main drop size with increasing Weber number,

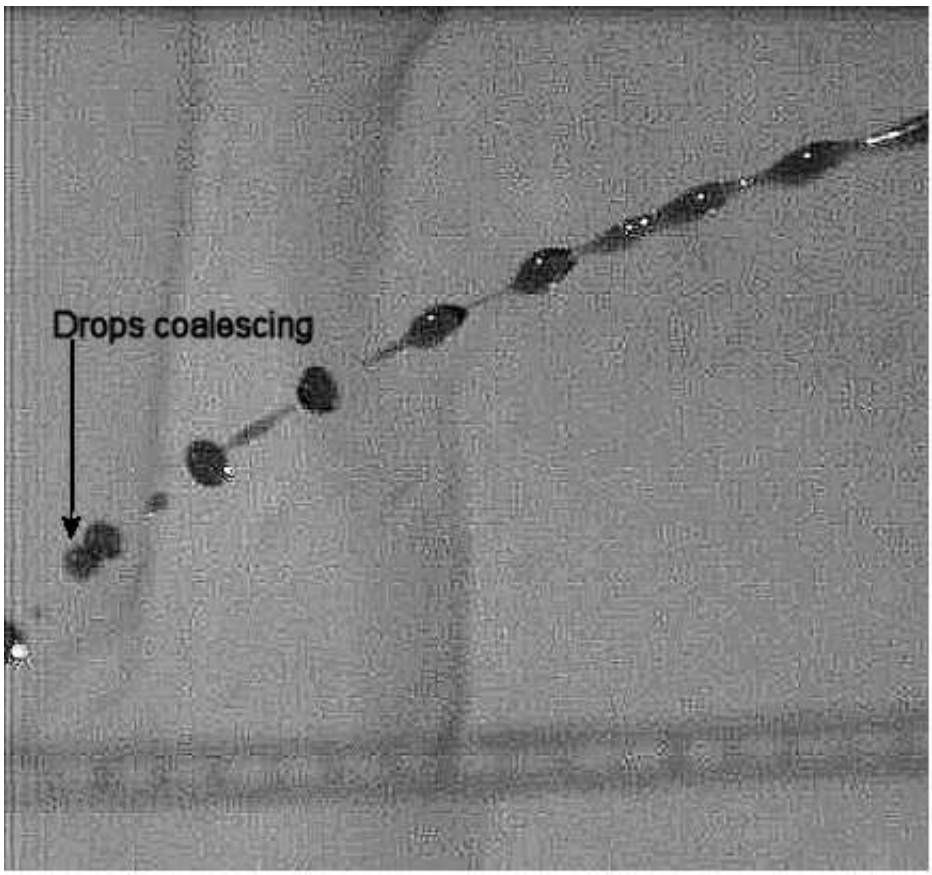

Figure 4.9: Drops coalescing to form one larger drop, $Rb = 1.68$, $We = 47.15$, $Oh = 0.0031$.

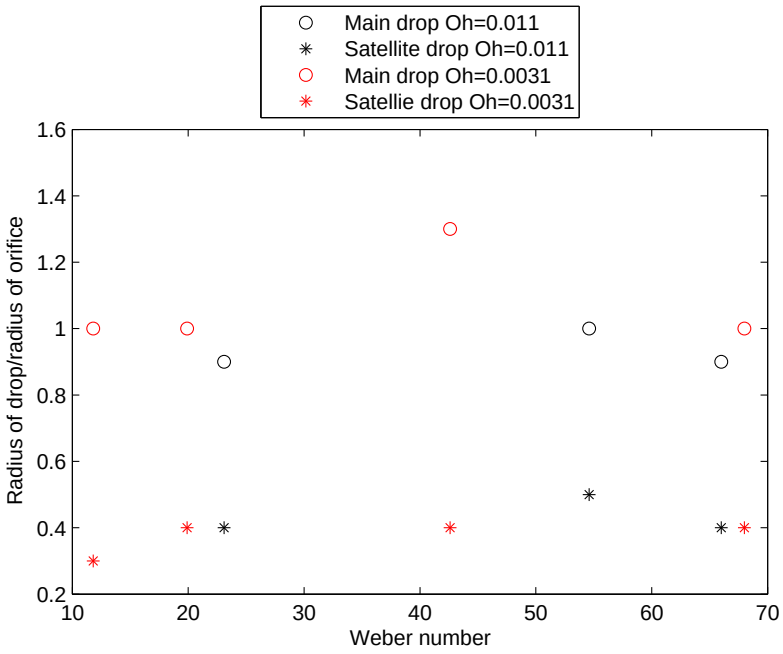

Figure 4.10: A plot of experimental main and satellite drop sizes against Weber number for $Oh = 0.0031$ and $Oh = 0.011$.

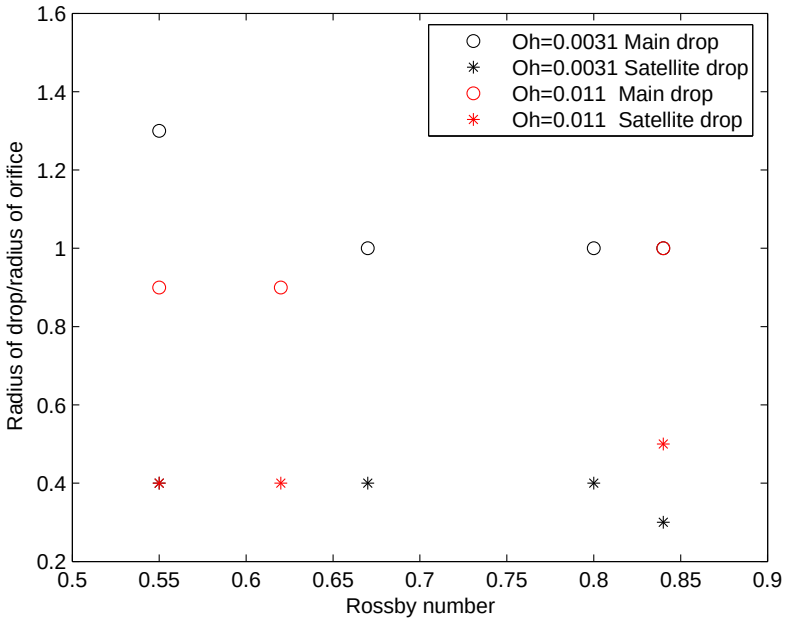

Figure 4.11: A plot of experimental main and satellite drop sizes against Rossby number for $Oh = 0.0031$ and $Oh = 0.011$. At $Rb = 0.55$ the size of the satellite drop for both Ohnesorge number is the same therefore the red and black star correspond to the same point. At $Rb = 0.84$ the size of the main drop is the same for both Ohnesorge numbers therefore the red and black circle correspond to the same point.

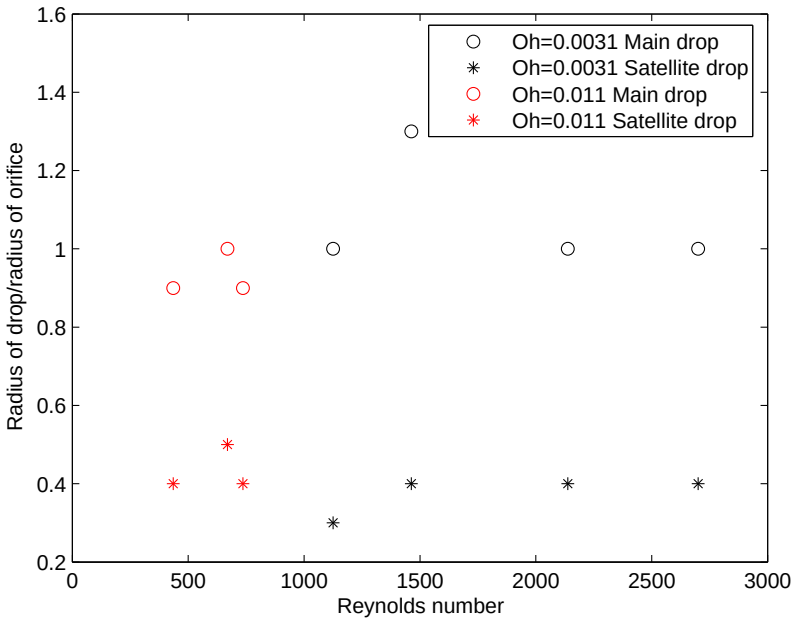

Figure 4.12: A plot of experimental main and satellite drop sizes against Reynolds number for $Oh = 0.0031$ and $Oh = 0.011$.

but the satellite drop size remains almost constant. From figure 4.11 we cannot ascertain a conclusive trend between Rossby number and drop size. In figure 4.12 there is no relation between Reynolds number and main or satellite drop size. In figure 4.13 we can see there is no conclusive trend between Froude number and main drop size and the satellite drop size remains almost constant.

There are clearly great difficulties in ascertaining trends in drop sizes from figures 4.10 to 4.13 since experimentally we cannot vary one parameter while keeping the others fixed, since as we vary one parameter in the experiments the other parameters vary too. From figure 4.4 exit velocity U is a function of rotation rate Ω, hence when Rossby number is varied in the experiments Weber number, Reynolds number and Froude number vary. So figures 4.10 to 4.13 do not give us much information on their own since all parameters are varied in each figure. Also some parameters could be more dominant than others so we cannot be sure that the trends obtained are due to the parameter in question that is plotted. However in chapters 6 and 7 we develop a theory where drop sizes can be

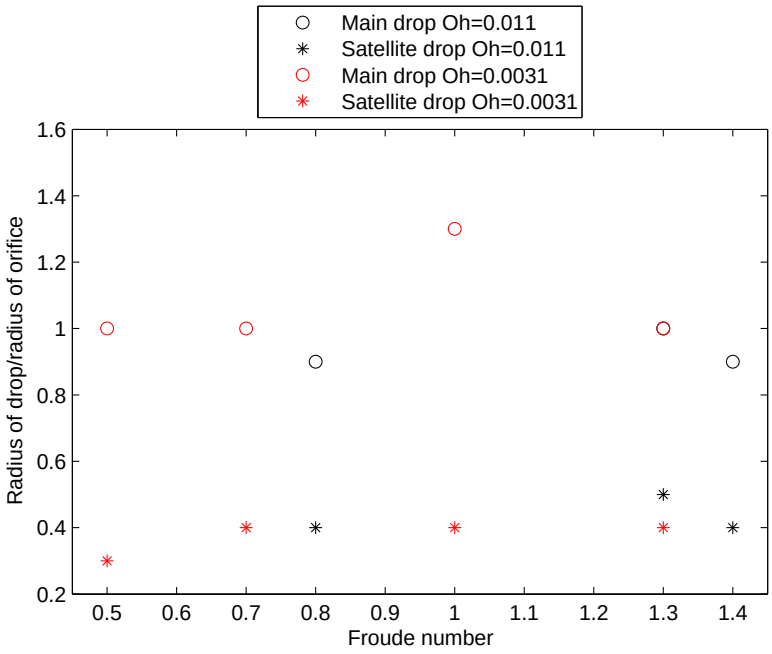

Figure 4.13: A plot of experimental main and satellite drop sizes against Froude number for $Oh = 0.0031$ and $Oh = 0.011$. At $F = 1.3$ the size of the main drop is the main drop is the same for both Ohnesorge numbers. Therefore the red and black circle correspond to the same point.

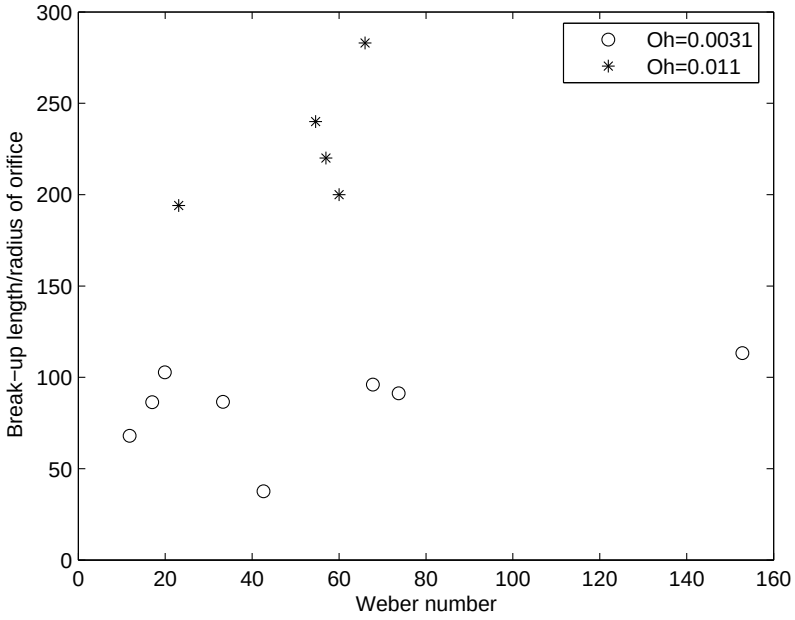

Figure 4.14: Weber number against experimental break-up length for $Oh = 0.011$ and $Oh = 0.0031$.

predicted. We can then decouple the parameters in the theory and find the trend between each parameter and drop size from the theory. These experimental results will then be discussed in more detail in chapters 6 and 7 in light of this theoretical insight.

4.5 Break-up length

In this section we present four plots showing break-up lengths obtained during the pilot scale experiments against Weber number, Rossby number, Reynolds number and Froude number (figures 4.14, 4.15, 4.16 and 4.17). Break-up lengths are obtained for two different Ohnesorge numbers. The normalised break-up lengths presented here are the average value of thirty-five experimentally obtained break-up lengths.

Figure 4.14 is a plot comparing Weber number against the experimental break-up length obtained on the pilot scale for $Oh = 0.011$ and $Oh = 0.0031$. The break-up lengths are longer for the higher Ohnesorge number. The higher Ohnesorge number corresponds to a higher viscosity of liquid. Viscous forces stabilise the jet therefore the jet travels further before breaking up. We can also see within each Ohnesorge number there is a

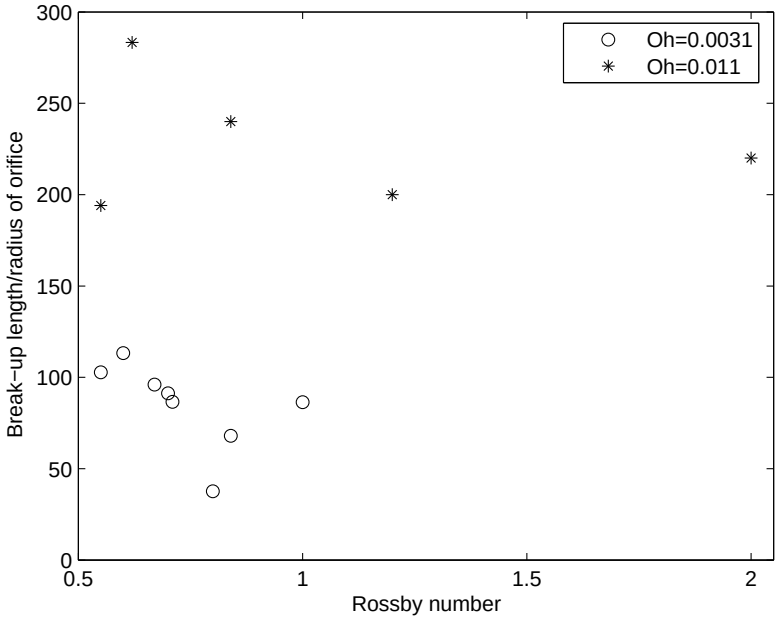

Figure 4.15: Rossby number against experimental break-up length for $Oh = 0.011$ and $Oh = 0.0031$.

clear but slight trend for break-up length to increase with Weber number. This maybe due to higher Weber number corresponding to greater inertia therefore the jet travels further before breaking up. Experimental work carried out on the laboratory scale by Wong *et al.* [44] agrees with this result.

Figure 4.15 shows Rossby number against experimental break-up length for $Oh = 0.011$ and $Oh = 0.0031$. Again the break-up length is longer for higher Ohnesorge number. We can see that within each Ohnesorge number there is a slight trend for the break-up length to decrease with increasing Rossby number.

Figure 4.16 shows a plot of Reynolds number against experimental break-up length for $Oh = 0.011$ and $Oh = 0.0031$. The break-up length is longer for greater Ohnesorge number. Also the jets with the higher Ohnesorge number have the lower Reynolds number, which is expected since Ohnesorge number and Reynolds number are related. Within each Ohnesorge number there is a trend for the break-up length to increase with Reynolds number. If all the fluid properties are the same then increasing Reynolds number is due

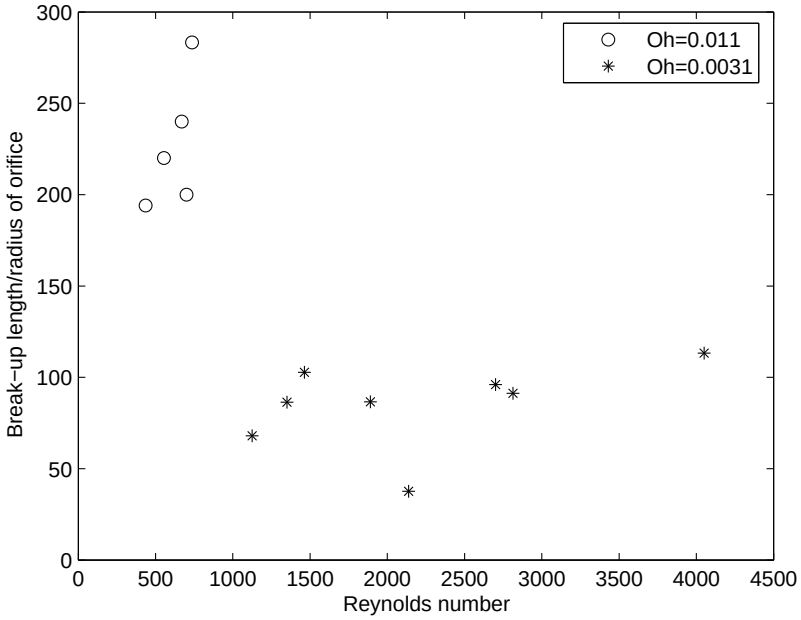

Figure 4.16: Ohnesorge number against experimental break-up length $Oh = 0.011$ and $Oh = 0.0031$.

to increasing inertia, so the jet will travel further before breaking up.

Figure 4.17 is a plot of Froude number against experimental break-up length for $Oh = 0.011$ and $Oh = 0.0031$. Again we can see that the break-up length is longer for higher Ohnesorge number. Within each Ohnesorge number there is a trend for the break-up length to increase with increasing Froude number. It is not clear whether this result is expected and it will be discussed later in light of theoretical results.

The experimental results presented in figures 4.14, 4.15, 4.16 and 4.17 have limitations since we cannot vary one parameter and hold the others constant in experiments. This means it is difficult to ascertain whether the trends obtained in these figures are influenced by the other parameters. In chapters 5, 6 and 7 we carry out a parametric study which allows us to vary one parameter and hold the others constant. This allows us to identify the effects of each parameter on break-up length without other parameters distorting the results. Also it allows us to identify which parameters are more dominant. We will then discuss the experimental results obtained in this section in chapters 5, 6

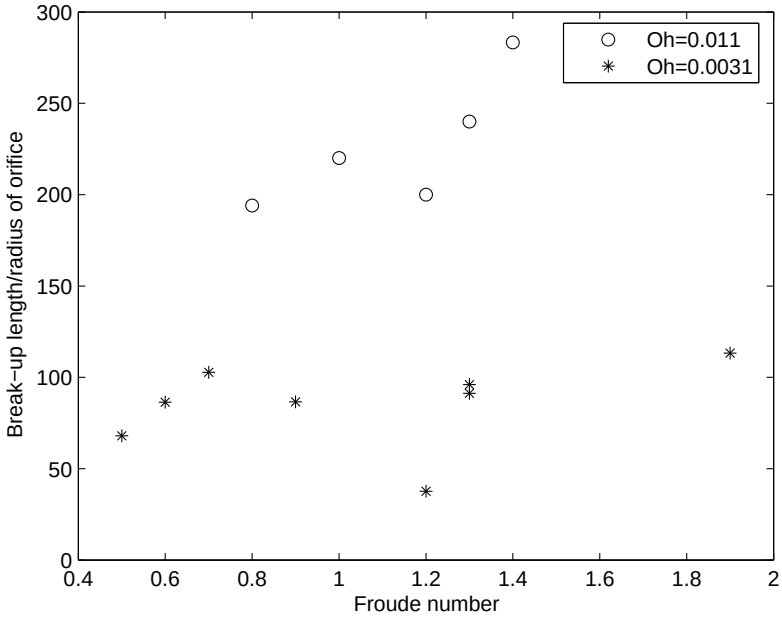

Figure 4.17: Froude number against experimental break-up length for $Oh = 0.011$ and $Oh = 0.0031$.

and 7 in light of theoretical results.

4.6 Summary

In this section results from the pilot scale experiments have been presented. A plot of Ohnesorge number against Weber is given allowing for the prediction of break-up mode. There were some differences with the laboratory scale. Mode 1 and mode 4 break-up were not observed and the boundary between mode 2 and mode 3 break-up was less well defined. However there was still fairly good agreement between the location of the mode 2/mode 3 boundary.

The effect of exit velocity and rotation rate upon jet break-up was discussed and compared to the observations found on the laboratory scale. Some features were different from the laboratory scale, in particular multiple break-up points were observed in mode 2 break-up on the pilot scale. On the laboratory scale this was only observed in mode 3 and mode 4 break-up.

The effect of rotation rate on exit velocity was discussed. It was found that exit velocity increases with rotation rate, changing the rotation rate varies the exit velocity. This means if Rossby number is varied then Weber number, Reynolds number and Froude number will change. The parameters are coupled and experimentally it is very difficult to separate them.

Drop size distributions were obtained for mode 2 break-up, mode 3 break-up and the boundary between mode 2 and mode 3 break-up. These drop size distributions were compared to results obtained on the laboratory scale. All the drop size distributions were bi-modal corresponding to the formation of main and satellite drops. All the drop size distributions on the pilot scale were similar to the mode 3 drop size distributions that were obtained on the laboratory scale. This was unsurprising since the boundary between mode 2 and mode 3 break-up was less well defined on the pilot scale.

Plots of experimental main and satellite drop size and break-up lengths against Weber number, Rossby number, Reynolds number and Froude number were presented for two different Ohnesorge numbers. Some trends were found. This will be discussed in more detail with theoretical results in chapters 5, 6 and 7.

Chapter 5

Inviscid non-linear theory

5.1 Non-linear analysis

In this section the experimental results obtained from the pilot scale are compared with the theoretical work carried out by Părău *et al.* [33, 34]. A parametric study which investigates trends in break-up length is then described.

Părău *et al.* [33, 34] developed a non-linear model using the long length scale over which the jet curves; and a short length scale corresponding to the wavelength of the perturbations that cause the jet to break-up into drops. The wavelength of the perturbation to the jets is $\lambda << s_0$. The short dimensionless lengthscale is given by

$$\bar{s} = \frac{s}{\lambda} = \frac{\gamma}{\epsilon}\hat{s},$$

where $\gamma = a/\lambda$, so that γ is the ratio of the radius of the orifice to the wavelength. A small dimensionless timescale is written as

$$\bar{t} = \frac{\gamma}{\epsilon}\hat{t},$$

where $\bar{s}$ and $\bar{t}$ are dimensionless, s and t are dimensional, $\hat{s}$ and $\hat{t}$ are longer dimensionless scales for length and time. ϵ is the aspect ratio $\epsilon = a/s_0$ which is small, where a is the

radius of the orifice and s_0 is the radius of the can. A slender jet series is given by

$$\begin{aligned}
u &= u_0(s,\bar{s},t,\bar{t}) + \gamma u_1(s,\bar{s},n,\phi,t,\bar{t}) + \gamma^2 u_2(s,\bar{s},n,\phi,t,\bar{t}) + \cdots \\
v &= \gamma v_1(s,\bar{s},n,\phi,t,\bar{t}) + \gamma^2 v_2(s,\bar{s},n,\phi,t,\bar{t}) + \cdots \\
w &= \gamma w_1(s,\bar{s},n,\phi,t,\bar{t}) + \gamma^2 w_2(s,\bar{s},\phi,t,\bar{t}) + \cdots \\
p &= p_0(s,\bar{s},n,\phi,t,\bar{t}) + \gamma p_1(s,\bar{s},n,\phi,t,\bar{t}) + \gamma^2 p_2(s,\bar{s},n,\phi,t,\bar{t}) + \cdots \\
R &= R_0(s,\bar{s},t,\bar{t}) + \gamma R_1(s,\bar{s},n,\phi,t,\bar{t}) + \gamma^2 R_2(s,\bar{s},n,\phi,t,\bar{t}) + \cdots \\
X &= X_0(s) + \gamma^2 X_1(s,t) + \cdots \\
Z &= Z_0(s) + \gamma^2 Z_1(s,t) + \cdots .
\end{aligned}$$

(For simplicity we drop the hats but not the overbars.)

Wallwork *et al.* [42] used multiple scales to determine the linear instability of the steady state by perturbing the curved liquid jets using linear travelling waves. When a weakly non-linear calculation is carried out for large Weber number, an equation is found to describe the variation in the wave amplitude on the long lengthscale s as long as $\gamma^2 \sim \epsilon$, Wallwork [41]. The travelling wave is initially linear near the orifice. It becomes weakly non-linear and then strongly non-linear as it travels away from the orifice. This is a distinguished limit arising from the equations of motion. This result was also obtained by Schulkes [38] for straight jets. We use a long wavelength theory to generalise the linear and weakly non-linear results of Wallwork *et al.* and Wallwork [42, 41] on a strongly non-linear setting. In this case we use the limit $\gamma^2 \sim \epsilon$, as in Părău *et al.* [34].

There is experimental evidence to support this distinguished limit. On the laboratory, pilot and industrial scales, [42, 45, 44, 31], the aspect ratio ϵ is always of the order of 10^{-2} for low viscosity jets. Several experiments have been carried out using different sizes of a and s_0. In all cases an ϵ of the order 10^{-2} was required for a coherent jet to form. If ϵ is an order of magnitude larger then the jet is not particularly slender and is turbulent. If ϵ is an order of magnitude smaller then it is difficult to obtain a jet

with an $O(1)$ break-up length and direct atomisation at the orifice is often observed in experiments. From Wallwork *et al.* [42] the most unstable mode has a wavenumber of the order $k = 0.697/a$, with $\lambda = 2\pi/k$, so $\gamma = a/\lambda$ is of the order 10^{-1} for a low viscosity liquid. This agrees with results obtained in both laboratory and pilot scale experiments. Therefore to obtain coherent jets in experiments $\epsilon \approx \gamma^2$ must hold, Părău *et al.* [34]. (Note that these arguments do not hold for a very viscous jet and a different limit must be used. This is discussed in chapters 6 and 9). Therefore we can write $\epsilon = K\gamma^2$ where K is an $O(1)$ constant.

It is assumed that the position of the centreline is not affected by the perturbations and at leading order is not time dependent. It would be possible to write X_0 and Z_0 as functions of time. This would give rise to an extra equation from the kinematic condition at lower order than the main equation, obtained here, which would describe any temporal translation of the centreline of the jet caused by the waves. This is discussed in chapter 9 where an unsteady centreline is examined with $X_{0t} \neq 0$ and $Z_{0t} \neq 0$. But for now it is assumed $v_0 = w_0 = X_{0t} = Z_{0t} = 0$, where v_0 and w_0 are the leading order terms in the expansions for v and w (not included in the above expansions).

From now on X_0 and Z_0 are written as X and Z for simplicity. The expansions under these scalings are substituted into the inviscid equations of motion. Părău *et al.* [33, 34] obtained the kinematic condition, given by

$$R_{0\bar{t}} + \frac{R_0}{2}u_{0\bar{s}} + u_0 R_{0\bar{s}} = 0 \tag{5.1}$$

and the axial momentum equation, given by

$$u_{0\bar{t}} + u_0 u_{0\bar{s}} = -p_{0\bar{s}} \tag{5.2}$$

where $p_0 = 1/WeR_0$. From the continuity equation, the azimuthal and radial momentum equations, and dynamic boundary condition, we find

$$u_0^2(X_sZ_{ss} - X_{ss}Z_s) - \frac{2u_0}{Rb} + \frac{1}{Rb^2}((X+1)Z_s - ZX_s) - \frac{X_sZ_{ss} - X_{ss}Z_s}{WeR_0} = 0. \tag{5.3}$$

The final equation to close the system is the arc-length condition, which is

$$X_s^2 + Z_s^2 = 1. \tag{5.4}$$

The details are given in Părău *et al.* [33, 34].

As we are assuming the centreline is steady, X and Z are functions of s only. To find the temporal solutions u_0 and R_0 we only need to solve equations (5.1) and (5.2). Equations (5.3) and (5.4) are first of all used in combination with the steady versions of (5.1) and (5.2) to obtain the steady solution; this is used as the initial condition of the flow. Then equations (5.1) and (5.2) are used to integrate this steady solution forward in time along with an unsteady disturbance at the orifice. This then enables (5.1) and (5.2) to simulate how a disturbance at the orifice causes a non-linear travelling wave to propagate down the jet, causing the jet to rupture. Equations (5.3) and (5.4) are only used to provide the initial condition. This procedure is discussed in [33, 34]. This procedure will also be adopted in chapters 6 and 7 when viscosity and gravity are incorporated into the model. In chapter 9 this simplified approach will be verified using a more rigorous approach.

A linear, temporal stability analysis can be performed on the steady solutions $u_0(s)$ and $R_0(s)$ using (5.1)-(5.2), Părău *et al.* [34]. The results of the analysis shows that $p_0 = 1/WeR_0$ has to be replaced with the full curvature, namely

$$\kappa = \frac{1}{We}\left[\frac{1}{R_0(1+\gamma^2R_{0\bar{s}}^2)^{1/2}} - \frac{\gamma^2R_{0\bar{s}\bar{s}}}{(1+\gamma^2R_{0\bar{s}}^2)^{3/2}}\right]$$

to make the system suitable for numerical methods, Eggers [17], otherwise the jet is unstable to infinitesimally short wave modes which is unphysical. This method of using the full expression for curvature has been successfully used by other authors, [30, 18] in the case of straight jets, and is well known. We prefer to carry out the numerical computations using a scaling based on the lengthscale of the problem, arc-length s, rather than the wavelength λ. This is discussed in Părău *et al.* [34]. The equations are rescaled using

$$T = \frac{tU}{a}, \quad S = \frac{s}{a}$$

where s and t are dimensional variables and S and T are non-dimensional variables. Changing the notations $R_0 \to R$ and $u_0 \to u$ it is found that equation (5.1) becomes

$$R_T + \frac{R}{2}u_S + uR_s = 0 \tag{5.5}$$

and equation (5.2) becomes

$$u_T + uu_S = -\frac{1}{We}\frac{\partial}{\partial S}\left(\frac{1}{R(1+R_S^2)^{1/2}} - \frac{R_{SS}}{(1+R_S^2)^{3/2}}\right). \tag{5.6}$$

The initial conditions are provided by the solutions to the steady-state equations along with (5.3) and (5.4) as already discussed.

Equations (5.5) and (5.6) are solved using a finite difference method. The spatial grid is kept fixed and uniform. The time integration is carried out by modifying a technique used by Zhu *et al.* [46] which is based on the Lax-Wendroff method. This is explained in the next section.

5.2 Lax-Wendroff method

The Lax-Wendroff method is a second order in time method used to solve equations of the form

$$\frac{\partial \mathbf{u}}{\partial t} = -\frac{\partial \mathbf{F}(\mathbf{u})}{\partial x}$$

where **F** and **u** are vectors. **F** is called the conserved flux and can depend not only on **u** but on the spatial derivatives of **u**. A detailed exposition can be found in Press *et al.* [32].

For illustrative purposes we consider a scalar version of this equation, namely

$$\frac{\partial u}{\partial t} = \frac{\partial F}{\partial x}.$$

We choose equally spaced points along both the t and x axes, namely

$$x_j = x_0 + j\Delta x, \;\; t_n = t_0 + n\Delta t.$$

Let u_j^n denote $u(t_n, x_j)$. We can denote the time derivative as

$$\frac{\partial u}{\partial t} = \frac{u_j^{n+1} - u_j^n}{\Delta t} + \cdots .$$

For the space derivatives we can use

$$\frac{\partial F}{\partial x} = \frac{F_{j+1}^n - F_{j-1}^n}{2\Delta x} + \cdots .$$

The resulting finite difference approximation is

$$\frac{u_j^{n+1} - u_j^n}{\Delta t} = \frac{F_{j+1}^n - F_{j-1}^n}{2\Delta x}.$$

This system can be unstable, so instead we use

$$u_j^n \to \frac{1}{2}(u_{j+1}^n + u_{j-1}^n).$$

Substituting into the finite difference approximation we arrive at

$$u_j^{n+1} = \frac{1}{2}(u_{j+1}^n + u_{j-1}^n) + \frac{\Delta t}{2\Delta x}(F_{j+1}^n - F_{j-1}^n).$$

For the Lax-Wendroff method we define intermediate points $u_{j+1/2}^{n+1/2}$ at the half time-steps $t_{n+1/2}$ and the half mesh points $x_{j+1/2}$ as

$$u_{j+1/2}^{n+1/2} = \frac{1}{2}(u_{j+1}^{n} + u_{j}^{n}) - \frac{\Delta t}{2\Delta x}(F_{j+1}^{n} - F_{j}^{n}).$$

The new fluxes $F_{j+1/2}^{n+1/2}$ are then calculated and

$$u_{j}^{n+1} = u_{j}^{n} - \frac{\Delta t}{\Delta x}\left(F_{j+1/2}^{n+1/2} - F_{j-1/2}^{n+1/2}\right).$$

This process is repeated for all points.

5.3 Application of the Lax-Wendroff method

We need to apply the Lax-Wendroff method to solve equations (5.5) and (5.6). We denote $A = R^2$ and arrive at the hyperbolic system given by

$$A_T + (Au)_S = 0 \tag{5.7}$$

and

$$u_T + \left(\frac{u^2}{2}\right)_S = -\frac{1}{We}\frac{\partial}{\partial S}\frac{4(2A + A_S^2 - A_{SS})}{(4A + A_S^2)^{3/2}}. \tag{5.8}$$

In this case the vector

$$\mathbf{u} = (A, u)$$

and the conserved flux is

$$\mathbf{F} = \left(Au, \frac{u^2}{2}\right).$$

This system is solved by integrating forward in time using a fixed grid of m equally spaced points where $s = s_0 + ids$ is the numerical length of the jet and $i = 1, m$.

The initial conditions at $T = 0$ are given by the solutions to the steady equations as already discussed. We impose periodic boundary conditions

$$A(0,T) = 1, \quad u(0,T) = 1 + \delta \sin(KT)$$

at the orifice, where δ is the amplitude of the non-linear disturbance at the orifice and the frequency of the perturbation at the orifice is given by $K = 2\pi a/\lambda$, which is non-dimensional.

Decent *et al.* [12] carried out a temporal linear stability analysis on a curved viscous jet. They found that the most unstable mode depends on the viscosity and is given by

$$K^* = \frac{1}{2^{1/4}\sqrt{\sqrt{2} + 3Oh}} \tag{5.9}$$

where K^* is the most unstable wavenumber and Oh is the Ohnesorge number given by $Oh = \mu/\sqrt{\sigma a \rho}$. Here ρ is the density of the liquid, μ is the viscosity of the liquid and a is the radius of the orifice. When the liquid is inviscid $Oh = 0$ and $K^* = 0.7$ to one significant figure therefore we use $K = 0.7$ in all the inviscid calculations so that K is the most unstable mode. (Viscosity is included in the problem in chapter 6).

The solution can then be put on the X-Z plane. For all $S > 0$ we have a steady centreline. By using the numerical method just illustrated we can calculate $R(S,T)$ at a time T. To find the equations on the free surface of the jet we consider that for each point S there is a point on the centreline of the jet $(X(S), Z(S))$ and a point on the radius of the jet at $R(S,T)$. If we move a distance $R(S,T)$ from the point $(X(S), Z(S))$ in the direction normal to the centreline we arrive at the surface of the jet. The normal vector pointing away from the centreline is given by $\mathbf{n} = (-Z'(S), X'(S))$. So one surface of the jet is given by $(X(S), Z(S)) + R(S,T)(-Z'(S), X'(S))$ and the other surface is given by $(X(S), Z(S)) - R(S,T)(-Z'(S), X'(S))$.

In the simulations jet break-up was chosen to occur when the minimum dimensionless radius is less than an arbitrarily chosen value (in this case 5% of the initial radius). Downstream of jet break-up the solution has no physical meaning since the jet would have broken into droplets which cannot be described by this approach. This means after jet break-up the simulation has no meaning. This is also the case for simulations of straight jets using this method. Părău *et al.* [34] checked the numerical accuracy by varying the spatial grid size, number of grid points and and the number of time steps. The method described here was compared with an implicit scheme which was more stable but required more computational effort; very good agreement was found. This shows the method described in this chapter is convergent.

5.4 Results

Figure 5.1 shows a jet with $We = 50$, $Rb = 5$, $\delta = 0.01$ and $K = 0.7$ evolving in time. (When the liquid is inviscid, the most unstable mode will correspond to $K = 0.7$, so this is the frequency that should be used at the orifice; see Middleman [29].) At $T = 0.3$ some small amplitude perturbations can be seen on the surface of the jet. At $T = 0.4$ the amplitude of the perturbations has increased and the perturbations are convected along the jet. At $T = 0.5$ the amplitude of the perturbations has increased further and the beginning of capillary pinch-off can be seen. At $T = 0.7$ the jet finally breaks up in mode 2, since satellite drops will be formed near the break-up point due to the thin thread near the main drop at break-up. The jet shapes shown above the break-up point would not exist in reality, since that part of the jet would have already ruptured.

Figure 5.2 shows the shape of the perturbations which are the variation in $R(s,t)$ along the arc-length s of the jet in figure 5.1. The horizontal axis is the arc-length s and the vertical axis is the radius of the jet $R(s,t)$. We can see that at $T = 0.3$, $R(s,t)$ does not deviate much from the undisturbed radius. At $T = 0.4$, $R(s,t)$ deviates more from the undisturbed state and the deviation continues further along the length of the jet. At $T = 0.5$ the deviation of $R(s,t)$ from the undisturbed radius increases further.

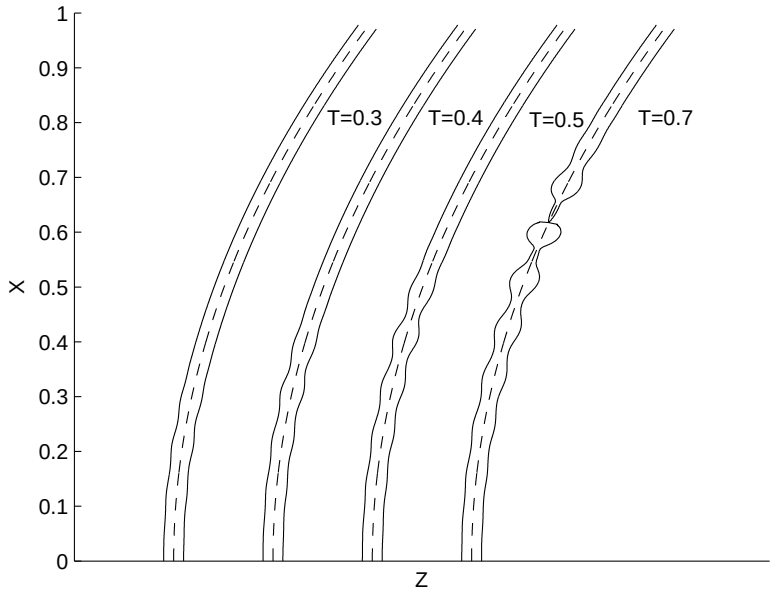

Figure 5.1: An inviscid jet with $We = 50$, $Rb = 5$, $K = 0.7$ at times $T = 0.3,\ 0.4,\ 0.5$ and 0.7. The perturbations develop along the jet causing it to break-up at $T = 0.7$. The orifice has been artificially shifted so that the jets at different times can be viewed more easily. Here $\delta = 0.01$.

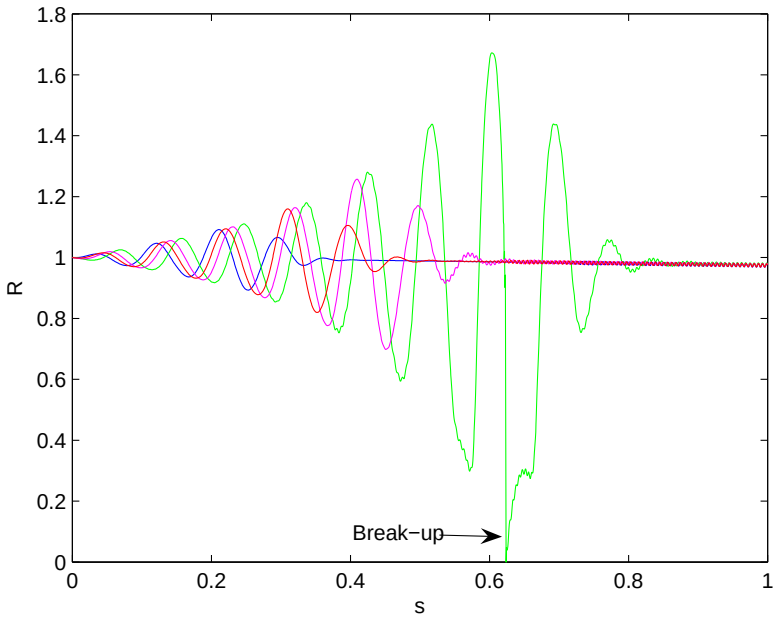

Figure 5.2: The perturbations travelling along the jet presented in figure 5.1. The blue line corresponds to $T = 0.3$, the red line corresponds to $T = 0.4$, the pink line corresponds to $T = 0.5$ and the green line corresponds to $T = 0.7$. The break-up point has been highlighted.

At $T = 0.7$ the jet breaks up. The point of break-up has been highlighted in figure 5.2 as the minimum of $R(s,t)$. It can be seen that $R(s,t)$ does not actually touch zero, and the break-up is chosen once this becomes 5% of the undisturbed radius. This is because there is a singularity in the equations at the break-up point [39] which is impossible to integrate through. Also small numerical instabilities can be seen in figure 5.2 on the green curve close to break-up, where it is difficult to resolve the singularity with the grid.

We attempted to obtain simulations using identical parameter values to those obtained on the pilot scale rig, namely for We=5.31, 23.1 and 47.15. Specifically it was attempted to take a single experimental result and replicate it in the model by solving the equations for identical parameters and selecting δ so the break-up lengths matched. We were unable to obtain a theoretical break-up length using this model that matched the break-up length achieved experimentally for any value of δ no matter what values of δ were chosen. However this investigation is repeated in chapters 6 and 7 where viscosity

is included and it is possible to achieve very good agreement between experimental and theoretical results for break-up lengths.

5.4.1 Parametric Study

In this section a parametric study is carried out using the inviscid theory. This allows us to identify trends in break-up length. This is difficult to carry out experimentally since we cannot vary one parameter and keep the others constant. Wherever possible experimental results will be compared to the theoretical results but this is not the aim of this section, as we might expect the results not to be good at least quantitatively. The variables in the study were Weber number and Rossby number and δ. The spatial grid contained 1501-2001 spaces, $dS = 0.05$, the temporal grid contained 700,000-950,000 spaces, $dT = 0.0001$ and $K = 0.7$ is chosen so that (5.9) is satisfied. We can also use this theory to plot the trajectories of the jets.

Figure 5.3 shows the break-up length obtained theoretically for different Weber numbers (We=1.5, 2, 5, 10, 20, 50, 70, 100 and 150) while keeping the Rossby number and δ fixed ($Rb = 1$, $\delta = 0.01$). We can see that as the Weber number increases the break-up length increases dramatically from 20 to 80 in non-dimensional units. Weber number is a balance between inertia and surface tension forces. Increasing Weber number corresponds to increasing inertia therefore the jet travels further before breaking up. Theoretical results obtained in Wallwork *et al.* [42] and Wallwork [41] agree with this result.

We can compare figure 5.3 with the pilot scale experimental results presented in figure 4.14. In figure 4.14 break-up length increases with Weber number within each Ohnesorge number. However the increase in break-up length is not as marked experimentally as it is theoretically. This might be due to the Rossby number varying for each Weber number in the experimental case.

Figure 5.4 shows the trajectories of three jets with different Weber numbers, We=10, 20 and 50. We can see that as the Weber number decreases the trajectory of the jet be-

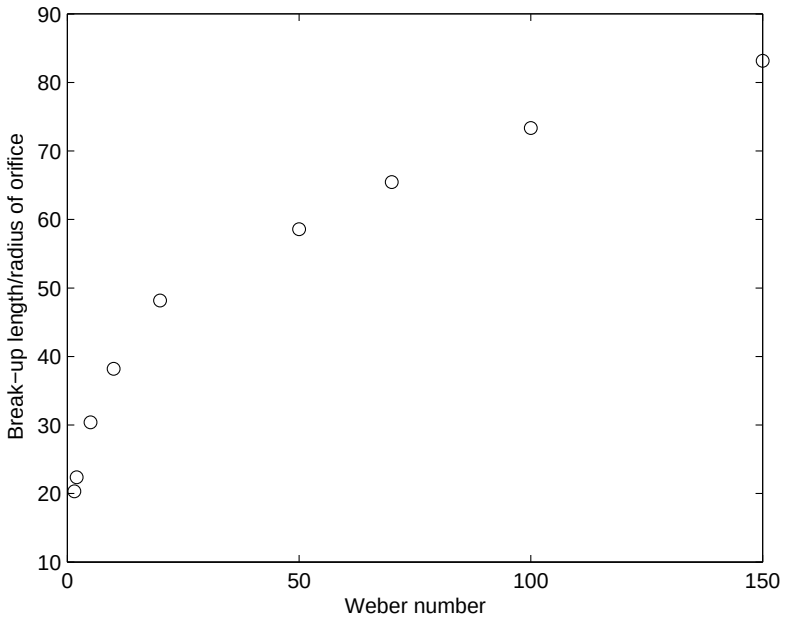

Figure 5.3: Plot of Weber number against break-up length. $Rb = 1$ and $\delta = 0.01$. $We = 1.5, 2, 5, 10, 20, 50, 70, 100$ and 150.

comes more curved since a lower Weber number corresponds to less inertia and the jet is more influenced by rotation; this trend agrees with previous theoretical work carried out by Wallwork *et al.* [42] and Wallwork [41]. Experiments carried out in Wallwork *et al.* [42] show that the trajectory curves more with decreasing Weber number. Therefore, the results obtained in figure 5.4 agree qualitatively with experimental results.

Figure 5.5 shows the normalised break-up length for five different Rossby numbers, $Rb = 0.8$, 1, 2, 3 and 5. Here Weber number and δ are fixed so that $We = 50$ and $\delta = 0.01$. The break-up length varies from 59 to 66 in non-dimensional units which is very small. This difference is caused by jet break-up occurring at the front or back of a travelling wave.

Figure 5.6 shows the trajectories of four jets with Rossby numbers $Rb = 0.8$, 1, 2 and 3. We can see that as the Rossby number increases the trajectory of the jet becomes less curved. Increasing Rossby number corresponds to decreasing rotation rates. Decreasing rotation rate causes the jet to become less curved. Theoretical work carried out by

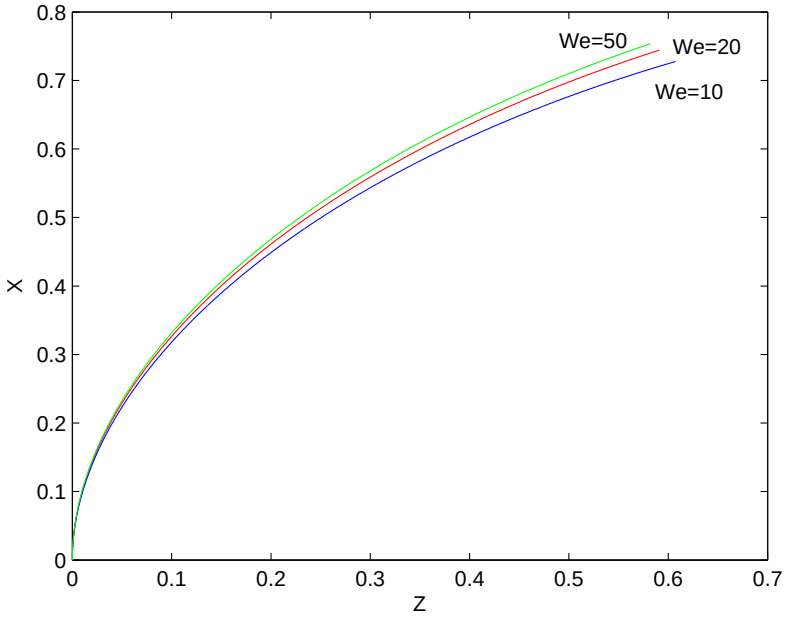

Figure 5.4: The trajectories of three jets with different Weber numbers. $We = 10,\ 20$ and 50 and $Rb = 1$

Wallwork *et al.* [42] and Wallwork [41] is in agreement with this result. Wallwork *et al.* [41] also found quantitative agreement between theoretical and experimental data for trajectories for different rotation rates, by overlaying theoretical curves over experimental photographs of trajectories.

Figure 5.7 shows the break-up length when δ is varied ($\delta = 0.009,\ 0.01,\ 0.02$ and 0.05). Here the Rossby number and Weber number are fixed ($We = 50$ and $Rb = 1$). We can see that break-up length increases with decreasing δ. This is expected since δ is the amplitude of the wave at the orifice. The wave propagates along the jet. The smaller the amplitude of the wave at the orifice the longer it will take for the jet to break-up. The trajectory of the jet is unaffected by δ. There are difficulties in comparing results of varying δ with experimental data as δ is usually unknown in experiments.

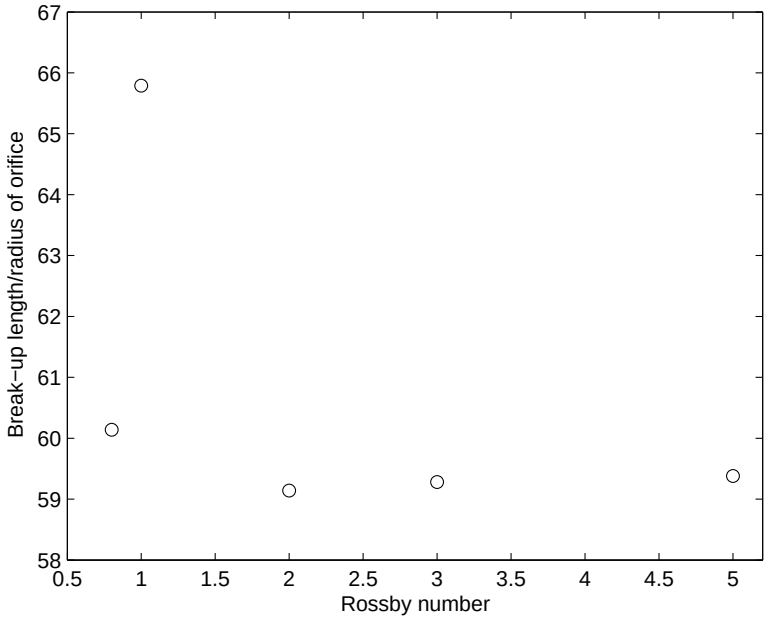

Figure 5.5: A plot of Rossby number against break-up length. $Rb = 0.8,\ 1,\ 2,\ 3$ and 5. $We = 50$ and $\delta = 0.01$

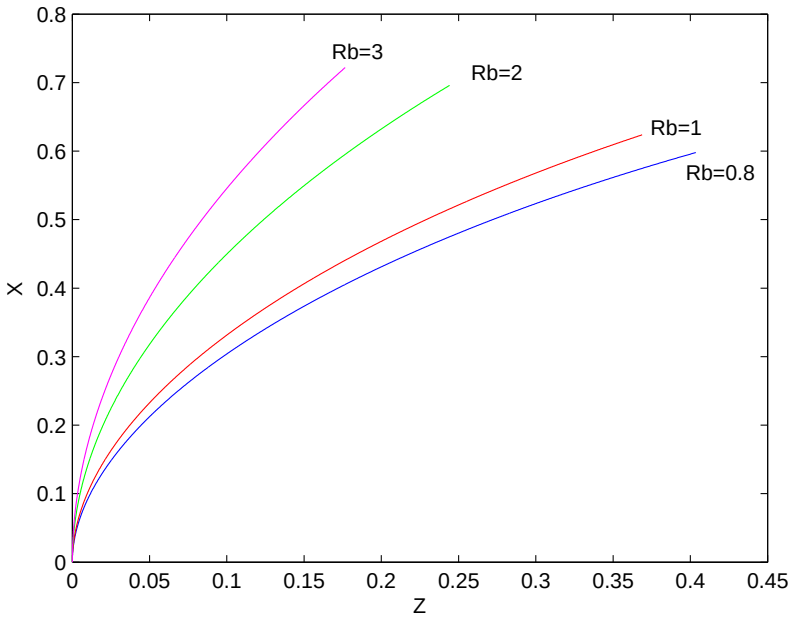

Figure 5.6: The trajectories of four jets with different Rossby numbers, $Rb = 0.8,\ 1,\ 2$ and 3 and $We = 50$.

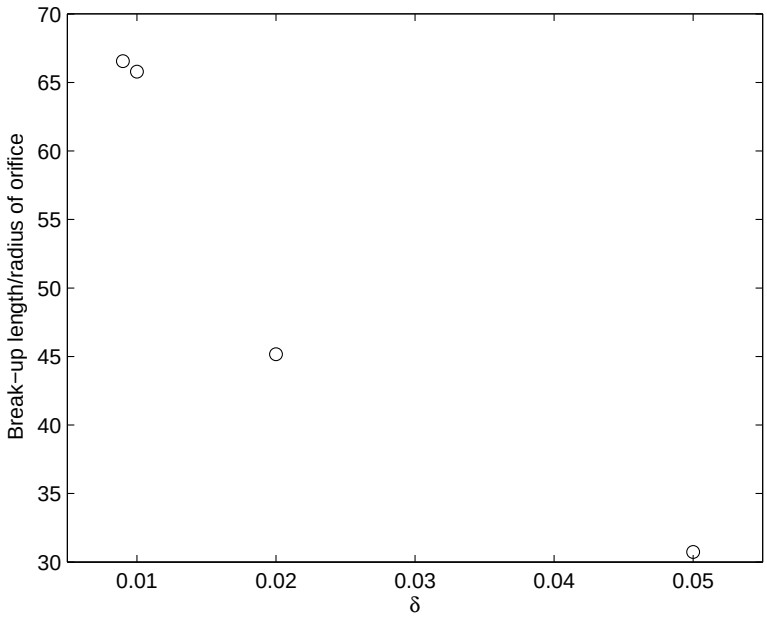

Figure 5.7: A plot of δ against break-up length. $We = 50$ and $Rb = 1$. $\delta = 0.009,\ 0.01,\ 0.02$ and 0.05.

5.5 Summary

In this chapter we presented a non-linear inviscid theory. The theory was developed from Euler's equations. One dimensional equations were derived using asymptotic techniques. These equations were then solved numerically. The equations were solved using a finite difference method where the spatial grid is kept fixed and uniform and the temporal integration was carried out using a technique based on the Lax-Wendroff method.

Some simulations of a jet were carried out at different times allowing us to visualise the disturbance developing along the length of the jet leading to break-up. We also plotted the arc-length of the jet against the radius of the jet for different times. This allowed us see how the amplitude of the disturbance along the jet varied with time.

We attempted to compare theoretical and experimental break-up lengths. We varied δ until the difference between the theoretical and experimental break-up lengths were minimised. However with the inviscid theory we could not obtain a good match between

experimental and theoretical break-up length.

A parametric study was carried out. The parameters were Weber number, Rossby number and δ. One parameter was varied while the others were kept fixed. Trends for break-up lengths were obtained. Also trajectories were plotted. These results were compared to experimental results presented in chapter 4 and some agreement was found.

Chapter 6

Inclusion of viscosity in the non-linear model

6.1 The model

Theoretical work up to this point has been developed considering inviscid fluids. In this chapter viscosity is included in the non-linear model for the first time, and the inviscid and viscous results are compared. The coordinate system described in section 2.2.1 is used.

The equations in the bulk are given by the continuity equation and the Navier-Stokes equations, namely

$$\nabla \cdot \mathbf{u} = 0 \tag{6.1}$$

and

$$\frac{\partial \mathbf{u}}{\partial t} + \mathbf{u} \cdot \nabla \mathbf{u} = -\frac{1}{\rho}\nabla p + \nu \nabla^2 \mathbf{u} - 2\boldsymbol{\omega} \times \mathbf{u} - \boldsymbol{\omega} \times (\boldsymbol{\omega} \times \mathbf{r}'). \tag{6.2}$$

The equations on the free surface $n = R(s, \phi, t)$ are given by the kinematic condition, the tangential stress condition and the normal stress condition, which are

$$\frac{\partial f}{\partial t} + \mathbf{u} \cdot \nabla f = 0, \tag{6.3}$$

$$\mathbf{t} \cdot \boldsymbol{\sigma} \cdot \mathbf{n} = 0, \tag{6.4}$$

$$\mathbf{n} \cdot \boldsymbol{\sigma} \cdot \mathbf{n} = \sigma \nabla \cdot \mathbf{n}, \tag{6.5}$$

where μ is the viscosity, ν is the kinematic viscosity defined by $\nu = \mu/\rho$, $\mathbf{n}$ is the unit normal pointing away from the surface of the jet, $\mathbf{t}$ is the tangent vector to the free surface, $f(\mathbf{r}, t) = n - R(s, \phi, t) = 0$ defines the position of the free surface. The position vector $\mathbf{r}$ is defined as

$$\mathbf{r} = \int_0^s \mathbf{e}_s ds + n\mathbf{e}_n \tag{6.6}$$

where

$$\mathbf{e}_s = X_s\mathbf{i} + Z_s\mathbf{k}, \tag{6.7}$$

$$\mathbf{e}_\phi = -\sin\phi Z_s\mathbf{i} - \cos\phi\mathbf{j} + \sin\phi X_s\mathbf{k} \tag{6.8}$$

and

$$\mathbf{e}_n = \cos\phi Z_s\mathbf{i} - \sin\phi\mathbf{j} - \cos\phi X_s\mathbf{k} \tag{6.9}$$

are unit vectors, this was discussed in section 2.2.1, $\mathbf{r}' = \mathbf{r} + s_0\mathbf{i}$ and $\boldsymbol{\sigma}$ is the stress tensor. From Batchelor [4], we can write down the components of the stress tensor σ_{ij} in an orthogonal curvilinear coordinate system as

$$\sigma_{11} = -p + 2\mu e_{11}$$

and

$$\sigma_{23} = \mu e_{23}$$

where

$$e_{11} = \frac{1}{h_1}\frac{\partial u_1}{\partial x_1} + \frac{u_2}{h_1 h_2}\frac{\partial h_1}{\partial x_2} + \frac{u_3}{h_3 h_1}\frac{\partial h_1}{\partial x_3}$$

and

$$e_{23} = \frac{h_3}{2h_2}\frac{\partial}{\partial x_2}\left(\frac{u_3}{h_3}\right) + \frac{h_2}{2h_3}\frac{\partial}{\partial x_3}\left(\frac{u_2}{h_2}\right).$$

The coordinates of the system are x_1, x_2 and x_3, in this case $x_1 = s$, $x_2 = n$ and $x_3 = \phi$. u_1, u_2 and u_3 are the components of the velocity vector in this case $u_1 = u$, $u_2 = v$ and

$u_3 = w$. h_1, h_2 and h_3 are the scale factors which are defined as

$$h_i = \left| \frac{\partial \mathbf{r}}{\partial x_i} \right|, \quad i = 1, 3.$$

The scale factors in this coordinate system are calculated to be, $h_1 = h_s = 1+n\cos\phi(X_s Z_{ss} - X_{ss} Z_s)$, $h_2 = h_n = 1$ and $h_3 = h_\phi = n$. The components of the stress tensor can be obtained from interchanging the suffixes, therefore

$$\begin{aligned}
\sigma_{ss} &= -p + \frac{2\mu}{h_s}\left(\frac{\partial u}{\partial s} + (v\cos\phi - w\sin\phi)\left(X_s Z_{ss} - X_{ss} Z_s\right)\right) \\
\sigma_{nn} &= -p + 2\mu\frac{\partial v}{\partial n} \\
\sigma_{\phi\phi} &= -p + \frac{2\mu}{n}\left(\frac{\partial w}{\partial \phi} + v\right) \\
\sigma_{sn} &= \mu\left(\frac{1}{h_s}\frac{\partial v}{\partial s} + \frac{\partial u}{\partial n} - \frac{u}{h_s}\cos\phi(X_s Z_{ss} - X_{ss} Z_s)\right) \\
\sigma_{n\phi} &= \mu\left(\frac{\partial w}{\partial n} - \frac{w}{n} + \frac{1}{n}\frac{\partial v}{\partial \phi}\right) \\
\sigma_{s\phi} &= \mu\left(\frac{1}{n}\frac{\partial u}{\partial \phi} + \frac{u}{h_s}\sin\phi(X_s Z_{ss} - X_{ss} Z_s) + \frac{1}{h_s}\frac{\partial w}{\partial s}\right)
\end{aligned}$$

where $\sigma_{sn} = \sigma_{ns}$, $\sigma_{n\phi} = \sigma_{\phi n}$ and $\sigma_{s\phi} = \sigma_{\phi s}$.

We write the normal to the surface of the jet as,

$$\mathbf{n} = \frac{\nabla(n - R(s,\phi,t))}{|\nabla(n - R(s,\phi,t))|} = \frac{1}{E}\left(-\frac{1}{h_s}\frac{\partial R}{\partial s}, 1, -\frac{1}{R}\frac{\partial R}{\partial \phi}\right)$$

(where the components of the vector given in brackets are $\mathbf{e}_s$, $\mathbf{e}_\phi$ and $\mathbf{e}_n$ respectively) and

$$E = \left(1 + \frac{1}{h_s^2}\left(\frac{\partial R}{\partial s}\right)^2 + \frac{1}{R^2}\left(\frac{\partial R}{\partial \phi}\right)^2\right)^{1/2}.$$

The normal stress condition is $\mathbf{n}\cdot\boldsymbol{\sigma}\cdot\mathbf{n}=\sigma\kappa$ on the free surface, where κ is the curvature of the free surface given by

$$\kappa=\nabla\cdot\mathbf{n}=\frac{1}{nh_s}\left(\frac{\partial}{\partial s}\left(\frac{-\frac{n}{h_s}\frac{\partial R}{\partial s}}{E}\right)+\frac{\partial}{\partial n}\left(\frac{nh_s}{E}\right)+\frac{\partial}{\partial\phi}\left(\frac{-\frac{h_s}{n}\frac{\partial R}{\partial\phi}}{E}\right)\right).$$

After some work we find the normal stress condition can be written as

$$\begin{aligned}p-\frac{2\mu}{E^2}\Bigg(&\frac{1}{h_s^3}\left(\frac{\partial R}{\partial s}\right)^2\left(\frac{\partial u}{\partial s}+(v\cos\phi-w\sin\phi)(X_sZ_{ss}-X_{ss}Z_s)\right)\\&+\frac{\partial v}{\partial n}+\frac{1}{R^3}\left(\frac{\partial w}{\partial\phi}+v\right)\left(\frac{\partial R}{\partial\phi}\right)^2-\frac{1}{h_s}\frac{\partial R}{\partial s}\left(\frac{1}{h_s}\frac{\partial v}{\partial s}+\frac{\partial u}{\partial n}-\frac{u}{h_s}\cos\phi(X_sZ_{ss}-X_{ss}Z_s)\right)\\&-\frac{1}{R}\frac{\partial R}{\partial\phi}\left(\frac{\partial w}{\partial n}-\frac{w}{n}+\frac{1}{R}\frac{\partial v}{\partial\phi}\right)+\frac{1}{h_sR}\frac{\partial R}{\partial s}\frac{\partial R}{\partial\phi}\left(\frac{1}{R}\frac{\partial u}{\partial\phi}+\frac{u}{h_s}\sin\phi(X_sZ_{ss}-X_{ss}Z_s)+\frac{1}{h_s}\frac{\partial u}{\partial s}\right)\Bigg)=\sigma\kappa\\&\text{on}\quad n=R(s,\phi,t).\end{aligned}\tag{6.10}$$

The axisymmetric version of the normal stress condition with no azimuthal velocity is

$$p-\frac{2\mu}{\tilde{E}^2}\left(\left(\frac{\partial R}{\partial s}\right)^2\frac{\partial u}{\partial s}+\frac{\partial v}{\partial n}-\frac{\partial R}{\partial s}\left(\frac{\partial v}{\partial s}+\frac{\partial u}{\partial n}\right)\right)=\sigma\tilde{\kappa}\ \text{ on }\ n=R(s,t)\tag{6.11}$$

where

$$\tilde{E}=\left(1+\left(\frac{\partial R}{\partial s}\right)^2\right)^{1/2}$$

and

$$\tilde{\kappa}=\frac{1}{n}\left(\frac{\partial}{\partial s}\left(\frac{-n\frac{\partial R}{\partial s}}{\tilde{E}}\right)+\frac{\partial}{\partial n}\left(\frac{n}{\tilde{E}}\right)\right).$$

The two tangent vectors are

$$\mathbf{t}_1=\left(1,\frac{1}{h_s}\frac{\partial R}{\partial s},0\right)$$

and

$$\mathbf{t}_2=\left(0,\frac{1}{R}\frac{\partial R}{\partial\phi},1\right).$$

The tangential stress condition is $\mathbf{t}\cdot\boldsymbol{\sigma}\cdot\mathbf{n}=0$ on the free surface. This can be written as

$$\left(1-\frac{1}{h_s^2}\left(\frac{\partial R}{\partial s}\right)\right)\left(\frac{1}{h_s}\frac{\partial v}{\partial s}+\frac{\partial u}{\partial n}-\frac{u}{h_s}\cos\phi(X_sZ_{ss}-X_{ss}Z_s)\right)$$
$$+\frac{2}{h_s}\frac{\partial R}{\partial s}\left(\frac{\partial v}{\partial n}-\frac{1}{h_s}\frac{\partial u}{\partial s}-\frac{v\cos\phi-w\sin\phi}{h_s}(X_sZ_{ss}-X_{ss}Z_s)\right)=0 \qquad (6.12)$$
$$\text{on}\ \ n=R(s,\phi,t)$$

corresponding to the stress in the s direction, and

$$\left(1-\frac{1}{R^2}\left(\frac{\partial R}{\partial\phi}\right)^2\right)\left(\frac{\partial w}{\partial n}-\frac{w}{R}+\frac{1}{R}\frac{\partial v}{\partial\phi}\right)+\frac{2}{R}\frac{\partial R}{\partial\phi}\left(\frac{\partial v}{\partial n}-\frac{1}{R}\left(\frac{\partial w}{\partial\phi}+v\right)\right)=0\ \ \text{on}\ \ n=R(s,\phi,t) \qquad (6.13)$$

corresponding to the stress in the ϕ direction. For an axisymmetric jet with no azimuthal velocity the first tangential stress condition (6.12) is

$$\left(1-\left(\frac{\partial R}{\partial s}\right)^2\right)\left(\frac{\partial v}{\partial s}+\frac{\partial u}{\partial n}\right)+2\frac{\partial R}{\partial s}\left(\frac{\partial v}{\partial n}-\frac{\partial u}{\partial s}\right)=0\ \ \text{on}\ \ n=R(s,t) \qquad (6.14)$$

and the second tangential stress condition (6.13) disappears trivially.

The kinematic condition is written as

$$\frac{D}{Dt}(R(s,\phi,t)-n)=0\ \ \text{on}\ \ n=R(s,\phi,t)$$

which is

$$\frac{\partial R}{\partial t}+\frac{\partial R}{\partial s}\frac{\partial s}{\partial t}+\frac{\partial R}{\partial\phi}\frac{\partial\phi}{\partial t}-\frac{\partial n}{\partial t}=0\ \ \text{on}\ \ n=R(s,\phi,t). \qquad (6.15)$$

Substituting equations (6.7), (6.8) and (6.9) into equation (6.6) the position vector becomes

$$\mathbf{r}=(X+n\cos\phi Z_s)\mathbf{i}-\sin\phi\mathbf{j}+(Z-n\cos\phi X_s)\mathbf{k}. \qquad (6.16)$$

The velocity field is

$$\frac{d\mathbf{r}}{dt} = \left(X_s\frac{\partial s}{\partial t} + X_t + \frac{\partial n}{\partial t}\cos\phi Z_s - \frac{\partial \phi}{\partial t}n\sin\phi Z_s + n\cos\phi Z_{ss}\frac{\partial s}{\partial t} + n\cos\phi Z_{st}\right)\mathbf{i} \\ - \left(\frac{\partial n}{\partial t}\sin\phi + \frac{\partial \phi}{\partial t}n\cos\phi\right)\mathbf{j} \\ + \left(Z_s\frac{\partial s}{\partial t} + Z_t - \frac{\partial n}{\partial t}\cos\phi X_s + \frac{\partial \phi}{\partial t}n\sin\phi X_s - n\cos\phi X_{ss}\frac{\partial s}{\partial t} - n\cos\phi X_{st}\right)\mathbf{k}. \quad (6.17)$$

But the velocity field is also equal to

$$\frac{d\mathbf{r}}{dt} = u\mathbf{e}_s + v\mathbf{e}_n = (uX_s + v\cos\phi Z_s - w\sin\phi Z_s)\mathbf{i} - (v\sin\phi + w\cos\phi)\mathbf{j} + (uZ_s - v\cos\phi X_s + w\sin\phi X_s)\mathbf{k}. \quad (6.18)$$

We can equate the **i**, **j** and **k** components of equations (6.17) and (6.18) and we obtain three simultaneous equations to be solved for u, v and w, namely

$$X_s\frac{\partial s}{\partial t} + X_{st} + \frac{\partial n}{\partial t}\cos\phi Z_s - n\sin\phi\frac{\partial \phi}{\partial t}Z_s + n\cos\phi Z_{ss}\frac{\partial s}{\partial t} + n\cos\phi Z_{st} = uX_s - v\cos\phi X_s + w\sin\phi X_s, \quad (6.19)$$

$$\frac{\partial n}{\partial t}\sin\phi + n\cos\phi\frac{\partial \phi}{\partial t} = v\sin\phi + w\cos\phi, \quad (6.20)$$

and

$$Z_s\frac{\partial s}{\partial t} + Z_{st} - \frac{\partial n}{\partial t}\cos\phi X_s + n\sin\phi\frac{\partial \phi}{\partial t}X_s - n\cos\phi X_{ss}\frac{\partial s}{\partial t} - n\cos\phi X_{st} = uZ_s - v\cos\phi X_s + w\sin\phi X_s \quad (6.21)$$

After solving equations (6.19), (6.20) and (6.21) we obtain the following expressions for u, v and w

$$u = \frac{\partial s}{\partial t}(1 + n\cos\phi(X_sZ_{ss} - X_{ss}Z_s)) + X_tX_s + Z_tZ_s + n\cos\phi(X_sZ_{st} - X_{st}Z_s) \quad (6.22)$$

$$v = \frac{\partial n}{\partial t} + \cos\phi(X_tZ_s - X_sZ_t) \quad (6.23)$$

$$w = n\frac{\partial \phi}{\partial t} - \sin\phi(X_tZ_s - X_sZ_t) \quad (6.24)$$

on the free surface. Rearranging (6.22), (6.23) and (6.24) and substituting into (6.15) we have

$$(1+n\cos\phi(X_sZ_{ss}-X_{ss}Z_s))\left(\frac{\partial R}{\partial t}-v+\cos\phi(X_tZ_s+X_sZ_t)+\frac{w}{n}\frac{\partial R}{\partial\phi}+\frac{1}{n}\frac{\partial R}{\partial\phi}\sin\phi(X_tZ_s-X_sZ_t)\right)$$
$$+\frac{\partial R}{\partial s}(u-X_tX_s-Z_tZ_s-n\cos\phi(X_sZ_{st}-X_{st}Z_s))=0, \tag{6.25}$$

which is the kinematic condition on the free surface.

The continuity equation

$$\nabla\cdot\mathbf{u}=0$$

becomes

$$n\frac{\partial u}{\partial s}+h_s\left(v+n\frac{\partial v}{\partial n}+\frac{\partial w}{\partial\phi}\right)+n(X_sZ_{ss}-X_{ss}Z_s)(v\cos\phi-w\sin\phi)=0,$$

and using the scalings from (2.12) we have

$$\epsilon n\frac{\partial u}{\partial s}+h_s\left(v+n\frac{\partial v}{\partial n}+\frac{\partial w}{\partial\phi}\right)+\epsilon n(X_sZ_{ss}-X_{ss}Z_s)(v\cos\phi-w\sin\phi)=0. \tag{6.26}$$

The arclength condition is

$$X_s^2+Z_s^2=1 \tag{6.27}$$

and

$$v=w=0 \ \text{ on } \ n=0. \tag{6.28}$$

We evaluate the Navier-Stokes equations and non-dimensionalise using the scalings from (2.12) and we obtain

$$\begin{aligned}
h_s\left(\epsilon\frac{\partial u}{\partial t}+\epsilon(v\cos\phi-w\sin\phi)(Z_{st}X_s-X_{st}Z_s)+v\frac{\partial u}{\partial n}+\frac{w}{n}\frac{\partial u}{\partial\phi}\right)+\epsilon u\frac{\partial u}{\partial s}\\
+\epsilon u(X_sZ_{ss}-X_{ss}Z_s)(v\cos\phi-w\sin\phi)=\\
-\epsilon\frac{\partial p}{\partial s}+h_s\left(\frac{2\epsilon}{Rb}(v\cos\phi-w\sin\phi)+\frac{\epsilon}{Rb^2}((X+1)X_s+ZZ_s)\right)\\
+\frac{1}{\epsilon Ren}\left(\frac{-\epsilon^3n^2\cos\phi(X_sZ_{sss}-Z_sX_{sss})}{h_s^2}\left(\frac{\partial u}{\partial s}+v\cos\phi(X_sZ_{ss}-Z_sX_{ss})\right.\right.\\
\left.-w\sin\phi(X_sZ_{ss}-Z_sX_{ss})\right)\frac{\epsilon^2n}{h_s}\left(-u(X_sZ_{ss}-Z_sX_{ss})^2+\frac{\partial^2u}{\partial s^2}\right.\\
+2\frac{\partial v}{\partial s}\cos\phi(X_sZ_{ss}-Z_sX_{ss})+(v\cos\phi-w\sin\phi)(X_sZ_{sss}-Z_sX_{sss})\\
\left.\left.-2\frac{\partial w}{\partial s}\sin\phi(X_sZ_{ss}-X_{ss}Z_s)\right)+(1+2\epsilon n\cos\phi(X_sZ_{ss}-X_{ss}Z_s))\frac{\partial u}{\partial n}+nh_s\frac{\partial^2u}{\partial n^2}\right.\\
\left.-\epsilon\frac{\partial u}{\partial\phi}\sin\phi(X_sZ_{ss}-Z_sX_{ss})+\frac{h_s}{n}\frac{\partial^2u}{\partial\phi^2}\right),
\end{aligned}\tag{6.29}$$

$$\begin{aligned}
h_s\left(\epsilon\frac{\partial v}{\partial t}+\epsilon u\cos\phi(X_{st}Z_s-Z_{st}X_s)+v\frac{\partial v}{\partial n}+\frac{w}{n}\frac{\partial v}{\partial\phi}-\frac{w^2}{n}\right)+\epsilon u\frac{\partial v}{\partial s}-\epsilon\cos\phi(X_sZ_{ss}-Z_sX_{ss})u^2\\
=\left(-\frac{\partial p}{\partial n}-\frac{2\epsilon}{Rb}u\cos\phi+\frac{h_s\epsilon\cos\phi}{Rb^2}((X+1)Z_s-ZX_s+\epsilon n\cos\phi)\right)+\\
\frac{1}{\epsilon Ren}\left(\frac{-\epsilon^3n^2\cos\phi(X_sZ_{sss}-Z_sX_{sss})}{h_s^2}\left(\frac{\partial v}{\partial s}-u\cos\phi(X_sZ_{ss}-Z_sX_{ss})\right)\right.\\
+\frac{\epsilon^2n}{h_s}\left(-v\cos^2\phi(X_sZ_{ss}-Z_sX_{ss})^2+\frac{\partial^2v}{\partial s^2}-2\frac{\partial u}{\partial s}\cos\phi(X_sZ_{ss}-Z_sX_{ss})\right.\\
\left.-u\cos\phi(X_sZ_{sss}-Z_sX_{sss})+w\sin\phi\cos\phi(X_sZ_{ss}-Z_sX_{ss})^2\right)\\
+(1+2\epsilon n\cos\phi(X_sZ_{ss}-Z_sX_{ss}))\frac{\partial v}{\partial n}+nh_s\frac{\partial^2v}{\partial n^2}\\
\left.-\epsilon\left(\frac{\partial v}{\partial\phi}-w\right)\sin\phi(X_sZ_{ss}-Z_sX_{ss})+\frac{h_s}{n}\left(\frac{\partial^2v}{\partial\phi^2}-v-2\frac{\partial w}{\partial\phi}\right)\right)
\end{aligned}\tag{6.30}$$

and

$$h_s\left(\epsilon\frac{\partial w}{\partial t}+\epsilon u\sin\phi(Z_{st}X_s-X_{st}Z_s)+v\frac{\partial w}{\partial n}+\frac{w}{n}\frac{\partial w}{\partial\phi}+\frac{wv}{n}\right)+\epsilon u\frac{\partial w}{\partial s}+\epsilon\sin\phi(X_sZ_{ss}-X_{ss}Z_s)u^2$$
$$=h_s\left(-\frac{1}{n}\frac{\partial p}{\partial\phi}+\frac{2\epsilon}{Rb}u\sin\phi+\frac{\epsilon\sin\phi}{Rb^2}(ZX_s-(X+1)Z_s-\epsilon n\cos\phi)\right)$$
$$+\frac{1}{\epsilon nRe}\left(\frac{-\epsilon^3n^2\cos\phi(X_sZ_{sss}-Z_sX_{sss})}{h_s^2}\left(\frac{\partial w}{\partial s}\right.\right.$$
$$\left.+u\sin\phi(X_sZ_{ss}-X_{ss}Z_s)\right)+\frac{\epsilon^2n}{h_s}\left(-w\sin^2\phi(X_sZ_{ss}-X_{ss}Z_s)^2+\frac{\partial^2w}{\partial s^2}\right.$$
$$+2\frac{\partial u}{\partial s}\sin\phi(X_sZ_{ss}-X_{ss}Z_s)+u\sin\phi(X_sZ_{sss}-Z_sX_{sss})$$
$$\left.+v\sin\phi\cos\phi(X_sZ_{ss}-Z_sX_{ss})^2\right)+(1+2\epsilon n\cos\phi(X_sZ_{ss}-Z_sX_{ss}))\frac{\partial w}{\partial n}$$
$$\left.+nh_s\frac{\partial^2w}{\partial n^2}-\epsilon\left(\frac{\partial w}{\partial\phi}+v\right)\sin\phi(X_sZ_{ss}-Z_sX_{ss})+\frac{h_s}{n}\left(\frac{\partial^2w}{\partial\phi^2}-w+2\frac{\partial v}{\partial\phi}\right)\right).\tag{6.31}$$

We obtain three non-dimensional groups

$$Rb=\frac{U}{s_0\Omega},\quad Re=\frac{\rho Ua}{\mu},\quad Oh=\frac{\mu}{\sqrt{\sigma a\rho}}$$

which are Rossby number, Reynolds number and Ohnesorge number respectively. We non-dimensionalise the boundary conditions. The kinematic condition is

$$h_s\left(\epsilon\frac{\partial R}{\partial t}+\cos\phi(X_tZ_s-X_sZ_t)-v+\frac{w}{n}\frac{\partial R}{\partial\phi}+\frac{1}{n}\frac{\partial R}{\partial\phi}\sin\phi(X_tZ_s-X_sZ_t)\right)$$
$$+\epsilon u\frac{\partial R}{\partial s}-\epsilon\frac{\partial R}{\partial s}(X_tZ_s+Z_tX_s+\epsilon n\cos\phi(X_sZ_{st}-X_{st}Z_s))=0\tag{6.32}$$
$$\text{on } n=R(s,\phi,t).$$

The tangential stress conditions are

$$\left(1-\frac{\epsilon^2}{h_s^2}\left(\frac{\partial R}{\partial s}\right)^2\right)\left(\epsilon\frac{\partial v}{\partial s}+h_s\frac{\partial u}{\partial n}-\epsilon u\cos\phi(X_sZ_{ss}-X_{ss}Z_s)\right)+2\epsilon\frac{\partial R}{\partial s}\left(\frac{\partial v}{\partial n}\right.$$
$$\left.-\frac{\epsilon}{h_s}\frac{\partial u}{\partial s}-\frac{\epsilon(v\cos\phi-w\sin\phi)}{h_s}(X_sZ_{ss}-X_{ss}Z_s)\right)=0\tag{6.33}$$

and

$$\left(1-\frac{1}{R^2}\left(\frac{\partial R}{\partial\phi}\right)^2\right)\left(\frac{\partial w}{\partial n}-\frac{w}{R}+\frac{1}{R}\frac{\partial v}{\partial\phi}\right)+\frac{2}{R}\frac{\partial R}{\partial\phi}\left(\frac{\partial v}{\partial n}-\frac{1}{R}\left(\frac{\partial w}{\partial\phi}+v\right)\right)=0 \quad \text{on } n=R(s,\phi,t). \tag{6.34}$$

The normal stress condition is

$$\begin{aligned} p-\frac{2}{ReE^2}\Bigg(&\frac{\epsilon^2}{h_s^3}\left(\frac{\partial R}{\partial s}\right)^2\left(\frac{\partial u}{\partial s}+(v\cos\phi-w\sin\phi)(X_sZ_{ss}-X_{ss}Z_s)\right)\\ &+\frac{1}{\epsilon}\frac{\partial v}{\partial n}+\frac{1}{\epsilon R^3}\left(\frac{\partial R}{\partial\phi}\right)^2\left(\frac{\partial w}{\partial\phi}+v\right)-\frac{\epsilon}{h_s}\frac{\partial R}{\partial s}\left(\frac{\partial v}{\partial s}+\frac{1}{\epsilon}\frac{\partial u}{\partial n}-\frac{u}{h_s}\cos\phi(X_sZ_{ss}-X_{ss}Z_s)\right)\\ &-\frac{1}{\epsilon R}\frac{\partial R}{\partial\phi}\left(\frac{\partial w}{\partial n}-\frac{w}{R}+\frac{1}{R}\frac{\partial v}{\partial\phi}\right)+\frac{\epsilon}{h_sR}\frac{\partial R}{\partial s}\frac{\partial R}{\partial\phi}\left(\frac{1}{\epsilon R}\frac{\partial u}{\partial\phi}+\frac{u}{h_s}\sin\phi(X_sZ_{ss}-X_{ss}Z_s)\right.\\ &\left.+\frac{1}{h_s}\frac{\partial u}{\partial s}\right)\Bigg)=\frac{\kappa}{We},\ \text{on } n=R(s,\phi,t) \end{aligned} \tag{6.35}$$

where

$$\kappa=\frac{1}{h_s}\left(\epsilon^2\frac{\partial}{\partial s}\left(-\frac{1}{h_sE}\frac{\partial R}{\partial s}\right)+\frac{1}{n}\frac{\partial}{\partial n}\left(\frac{nh_s}{E}\right)+\frac{\partial}{\partial\phi}\left(-\frac{h_s}{n^2E}\frac{\partial R}{\partial\phi}\right)\right), \tag{6.36}$$

$$h_s=1+\epsilon n\cos\phi(X_sZ_{ss}-X_{ss}Z_s), \tag{6.37}$$

and

$$E=\left(1+\frac{\epsilon^2}{h_s^2}\left(\frac{\partial R}{\partial s}\right)^2+\frac{1}{n^2}\left(\frac{\partial R}{\partial\phi}\right)^2\right)^{1/2}. \tag{6.38}$$

We obtain another non-dimensional group, the Weber number, which is defined as $We=\rho U^2a/\sigma$. We also have equations (6.27) and (6.28) which are already non-dimensional.

To simplify the analysis we consider all variables to depend on long time and length-scales only. We also use a different scaling to chapter 5 so all the expansions are in ϵ

rather than γ. We pose the expansions

$$\left.\begin{aligned} u &= u_0(s,t) + (\epsilon n)u_1(s,\phi,t) + (\epsilon n)^2 u_2(s,\phi,t) + \cdots \\ v &= (\epsilon n)v_1(s,\phi,t) + (\epsilon n)^2 v_2(s,\phi,t) + \cdots \\ w &= (\epsilon n)w_1(s,\phi,t) + (\epsilon n)^2 w_2(s,\phi,t) + \cdots \\ p &= p_0(s,\phi,t) + (\epsilon n)p_1(s,\phi,t) + \cdots \\ R &= R_0(s,t) + \epsilon R_1(s,\phi,t) + \cdots \\ X &= X_0(s) + \epsilon X_1(s,t) + \cdots \\ Z &= Z_0(s) + \epsilon Z_1(s,t) + \cdots , \end{aligned}\right\} \tag{6.39}$$

where the aspect ratio $\epsilon = a/s_0$ is assumed to be small. We assume that the centreline is not affected by the perturbations and at leading order is not time-dependent. (In chapter 9 we do not make this assumption and allow the trajectory to become unsteady in order to check this assumption.) From now on we write X_0 and Z_0 as X and Z respectively for simplicity and denote $X_s Z_{ss} - X_{ss} Z_s$ as S. We substitute these expansions into the non-dimensionalised continuity equation, Navier-Stokes equations, kinematic, normal and tangential stress conditions and equations (6.27) and (6.28).

From the continuity equation (6.26) we have

$$O(\epsilon n): \; u_{0s} + 2v_1 + w_{1\phi} = 0 \tag{6.40}$$

and

$$O((\epsilon n)^2): \; u_{1s} + 3v_2 + w_{2\phi} + (3v_1 + w_{1\phi})\cos\phi S - w_1 \sin\phi S = 0. \tag{6.41}$$

From the second tangential stress condition (6.34) we have

$$O(\epsilon): \; R_0^3 v_{1\phi} = 0 \tag{6.42}$$

and

$$O(\epsilon^2): \; 3R_0^2 R_1 v_{1\phi} + R_0^4(w_2 + v_{2\phi}) - 2R_0^2 R_{1\phi} w_{1\phi} = 0. \tag{6.43}$$

From equation (6.42) we have

$$v_{1\phi} = 0. \tag{6.44}$$

Differentiating (6.40) with respect to ϕ, we arrive at

$$w_{1\phi\phi} = 0. \tag{6.45}$$

Therefore

$$w_{1\phi} = K$$

where K is a constant. But w_1 must be periodic in ϕ so $K = 0$, which means that $w_1 = w_1(s,t)$ so w_1 does not depend on ϕ. So equation (6.40) becomes

$$u_{0s} + 2v_1 = 0$$

and can be rearranged to give

$$v_1 = -\frac{u_{0s}}{2}. \tag{6.46}$$

Equation (6.43) becomes

$$w_2 + v_{2\phi} = 0. \tag{6.47}$$

From the first tangential stress condition we obtain

$$O(\epsilon) : \ u_1 = u_0 S \cos\phi, \tag{6.48}$$

and

$$O(\epsilon^2) : \ u_2 = \frac{3}{2} u_{0s} \frac{R_{0s}}{R_0} + \frac{u_{0ss}}{4}. \tag{6.49}$$

Differentiating equation (6.47) with respect to ϕ we obtain

$$w_{2\phi} = -v_{2\phi\phi}.$$

We substitute this into equation (6.41) to give

$$v_{2\phi\phi} - 3v_2 = u_{1s} + 3v_1 \cos\phi S - w_1 \sin\phi S. \tag{6.50}$$

Substituting equations (6.46) and (6.48) into (6.50), we obtain

$$v_{2\phi\phi} - 3v_2 = \left(u_0 S_s - \frac{u_{0s}}{2} S\right) \cos\phi - w_1 S \sin\phi. \tag{6.51}$$

The particular solution to equation (6.51) is

$$v_2 = \frac{1}{4}\left(\frac{u_{0s}}{2} S - u_0 S_s\right) \cos\phi + \frac{w_1}{4} S \sin\phi \tag{6.52}$$

and we obtain

$$w_2 = \frac{1}{4}\left(\frac{u_{0s}}{2} S - u_0 S_s\right) \sin\phi - \frac{w_1}{4} S \cos\phi. \tag{6.53}$$

From the second Navier-Stokes equation (6.30) we have

$$-u_0^2 S \cos\phi = -p_1 - \frac{2}{Rb} u_0 \cos\phi + \frac{(X+1)Z_s - ZX_s}{Rb^2} \cos\phi + \frac{1}{Re}\left(-\left(\frac{5}{2} u_{0s} S + u_0 S_s\right) \cos\phi + w_1 S \sin\phi\right) \tag{6.54}$$

at order ϵ which can be rearranged to give

$$p_1 = -\left(-u_0^2 S + \frac{2}{Rb} u_0 - \frac{(X+1)Z_s - ZX_s}{Rb^2} + \frac{1}{Re}\left(\frac{5}{2} u_{0s} S + u_0 S_s\right)\right) \cos\phi - \frac{1}{Re} w_1 S \sin\phi. \tag{6.55}$$

The third Navier-Stokes equation (6.31) gives

$$p_{0\phi} = 0$$

at leading order and

$$u_0^2 S\sin\phi = -p_{1\phi} + \frac{2}{Rb}u_0\sin\phi + \frac{ZX_s-(X+1)Z_s}{Rb^2}\sin\phi + \frac{1}{Re}\left(\left(\frac{5}{2}u_{0s}S+u_0S_s\right)\sin\phi + w_1 S\cos\phi\right) \tag{6.56}$$

at order ϵ which can be written as

$$p_{1\phi} = \left(-u_0^2 S + \frac{2}{Rb}u_0 + \frac{ZX_s-(X+1)Z_s}{Rb^2}\sin\phi + \frac{1}{Re}\left(\frac{5}{2}u_{0s}S+u_0S_s\right)\right)\sin\phi + \frac{1}{Re}w_1 S\cos\phi. \tag{6.57}$$

Note that if we differentiate equation (6.55) with respect to ϕ we obtain equation (6.57) (which is not the case when $w=0$).

From the normal stress condition (6.35) we have

$$p_0 - \frac{2}{Re}v_1 = \frac{1}{R_0 We}. \tag{6.58}$$

Substituting (6.46) into (6.58) we obtain

$$p_0 = -\frac{u_{0s}}{Re} + \frac{1}{R_0 We}. \tag{6.59}$$

At order ϵ we obtain

$$R_0 p_1 - \frac{4}{Re}R_0 v_2 = \frac{1}{We}\left(-\frac{R_{1\phi\phi}+R_1}{R_0^2} + S\cos\phi\right). \tag{6.60}$$

Substituting (6.55) into equation (6.60) we obtain

$$-\frac{R_{1\phi\phi}+R_1}{WeR_0^3} = \left(u_0^2 S - \frac{2}{Rb}u_0 + \frac{(X+1)Z_s - ZX_s}{Rb^2} - \frac{3}{Re}u_{0s}S - \frac{S}{WeR_0}\right)\cos\phi. \tag{6.61}$$

Since R_1 is periodic in ϕ we require the right-hand side of equation (6.61) to vanish, therefore

$$u_0^2 S - \frac{2u_0}{Rb} + \frac{(X+1)Z_s - ZX_s}{Rb^2} - \frac{3}{Re}u_{0s}S - \frac{S}{WeR_0} = 0, \tag{6.62}$$

since a non-zero term on the right-hand side of (6.61) would give rise to $\phi\cos\phi$ and $\phi\sin\phi$ terms in R_1, which are non-periodic and hence unphysical.

The first Navier-Stokes equation (6.29) is

$$u_{0t} + u_0 u_{0s} = -p_{0s} + \frac{(X+1)X_s + ZZ_s}{Rb^2} + \frac{1}{Re}(u_{0ss} + 4u_2 + u_{2\phi\phi}) \tag{6.63}$$

at leading order. Substituting equation (6.49) into equation (6.63) and differentiating equation (6.59) with respect to s and substituting into equation (6.63) we obtain

$$u_{0t} + u_0 u_{0s} = -\frac{1}{We}\left(\frac{1}{R_0}\right)_s + \frac{(X+1)X_s + ZZ_s}{Rb^2} + \frac{3(R_0^2 u_{0s})_s}{ReR_0^2}. \tag{6.64}$$

From the kinematic condition (6.32) we obtain at order ϵ

$$R_{0t} + \frac{u_{0s}}{2}R_0 + u_0 R_{0s} = 0. \tag{6.65}$$

The last equation required to close the system is (6.27). Equations (6.62), (6.64), (6.65) and (6.27) form the system of four equations to be solved for the four unknowns u_0, R_0, X and Z.

To obtain the conditions at the orifice we consider the jet leaving an orifice of radius a with exit velocity U. We assume the exit radius of the jet to be the radius of the orifice. In dimensional variables this gives us $X_s = 1$, $X = Z = Z_s = 0$, $R_0 = a$ and $u_0 = U$ at $s = 0$. After non-dimensionalising we obtain $X_s = 1$, $X = Z = Z_s = 0$ and $R_0 = u_0 = 1$ at $s = 0$.

6.1.1 Steady-state solutions

The initial conditions are given by the solutions to the steady-state equations. Therefore we look for the steady-state solutions for equations (6.62), (6.64), (6.65) and (6.27). We

consider all variables to be functions of s only to give

$$(X_s Z_{ss} - X_{ss} Z_s)\left(u_0^2 - \frac{3}{Re}u_{0s} - \frac{1}{WeR_0}\right) - \frac{2}{Rb}u_0 + \frac{(X+1)Z_s - ZX_s}{Rb^2} = 0, \tag{6.66}$$

$$u_0 u_{0s} = -\frac{1}{We}\left(\frac{1}{R_0}\right)_s + \frac{(X+1)X_s + ZZ_s}{Rb^2} + \frac{3(R_0^2 u_{0s})_s}{ReR_0^2}, \tag{6.67}$$

$$\frac{u_{0s}}{2}R_0 + u_0 R_{0s} = 0 \tag{6.68}$$

and

$$X_s^2 + Z_s^2 = 1. \tag{6.69}$$

From equation (6.68) we can see $R_0^2 u_0 =$ constant. Using the conditions at the orifice, which are $R_0 = 1$ and $u_0 = 1$ at $s = 0$, as described in the previous section, we have

$$R_0^2 u_0 = 1. \tag{6.70}$$

We can substitute (6.70) into equations (6.66) and (6.67) to give

$$u_0 u_{0s} = -\frac{1}{We}\frac{u_{0s}}{2\sqrt{u_0}} + \frac{(X+1)X_s + ZZ_s}{Rb^2} + \frac{3}{Re}\left(u_{0ss} - \frac{u_{0s}^2}{u_0}\right) \tag{6.71}$$

and

$$(X_s Z_{ss} - X_{ss} Z_s)\left(u_0^2 - \frac{3}{Re}u_{0s} - \frac{\sqrt{u_0}}{We}\right) - \frac{2}{Rb}u_0 + \frac{(X+1)Z_s - ZX_s}{Rb^2} = 0. \tag{6.72}$$

Equations (6.71), (6.72) and (6.69) form a system of equations for the three unknowns X, Z and u_0. The boundary conditions at the orifice are $X = Z = Z_s = 0,\ u_0 = X_s = 1$ at $s = 0$, as described in the previous section. Downstream boundary conditions $u_0(\infty) = \infty$ and $R_0(\infty) = 0$ are required so that the jet accelerates. However in Decent *et al.* [12] they show that unless the Reynolds number is very low (or the Ohnesorge number is very large; typically much larger than 1) then the contribution from viscosity vanishes to the leading order terms in the trajectory when solved numerically. Therefore, these equations

simplify numerically to the inviscid steady-state equations and the inviscid and viscous solutions are indistinguishable numerically. In all experiments carried out the Reynolds number has been high enough to use the solutions to the inviscid steady state equations as the initial conditions here, as in chapter 5. This is discussed at length in Decent *et al.* [12]. Note that Decent *et al.* [12] had the same steady state, but only considered linear travelling waves.

6.1.2 Non-linear temporal solution

To find the temporal solution we only need to solve equations (6.64) and (6.65) since we are assuming a steady centreline therefore X and Z are assumed to be independent of t. This is the same approach that was used in chapter 5. (This assumption will be examined and verified in chapter 9.) The non-linear system to be solved is

$$u_{0t} + u_0 u_{0s} = -\kappa_s + \frac{(X+1)X_s + ZZ_s}{Rb^2} + \frac{3(R_0^2 u_{0s})_s}{ReR_0^2} \tag{6.73}$$

and

$$R_{0t} + \frac{u_{0s}}{2} R_0 + u_0 R_{0s} = 0 \tag{6.74}$$

where $\kappa = 1/WeR_0$. We replace the leading order curvature with the full curvature

$$\kappa = \frac{1}{We}\left(\frac{1}{R_0(1+\epsilon^2 R_0^2)^{1/2}} - \frac{\epsilon^2 R_{0ss}}{(1+\epsilon^2 R_{0s}^2)^{3/2}}\right)$$

otherwise the jet is unstable to infinitesimally short wave modes. This is also the case for straight jets [17], and inviscid curved jets (see chapter 5).

We solve this system using a finite difference method where the spatial grid is fixed and uniform and the time integration method is based on the Lax-Wendroff method as in section 5.3.

We denote $A = R_0^2$ so equations (6.73) and (6.74) can be written as

$$A_t + (Au_0)_s = 0 \tag{6.75}$$

and

$$u_{0t} + \left(\frac{u_0^2}{2}\right)_s = -\frac{1}{We}\frac{\partial}{\partial s}\left(\frac{4(2A + (\epsilon A_s)^2 - \epsilon^2 A A_{ss})}{(4A + (\epsilon A_s)^2)^{3/2}}\right) + \frac{(X+1)X_s + ZZ_s}{Rb^2} + \frac{3(Au_{0s})_s}{ReA}. \tag{6.76}$$

We solve equations (6.75) and (6.76) the same way as in section 5.3. Again, X and Z are held constant as the steady solutions. In our calculations the initial conditions are solutions to the inviscid steady state equations since all our experiments were carried out with sufficiently low viscosity liquids (with Ohnesorge number usually less than 1) that this is a good approximation. We impose periodic boundary conditions at the orifice

$$A(0,t) = 1, \quad u(0,t) = 1 + \delta \sin\left(\kappa \frac{t}{\epsilon}\right),$$

corresponding to a disturbance of frequency κ/ϵ and amplitude δ. (Note that we could change the initial conditions to be a perturbation of radius rather than velocity, though the above is probably the most realistic physically.)

Decent *et al.* [12] carried out a temporal stability analysis on a viscous jet. They found that the most unstable mode depends on the viscosity and is given by

$$\kappa^* = \frac{1}{2^{1/4}\sqrt{\sqrt{2} + 3Oh}} \tag{6.77}$$

where κ^* is the most unstable wavenumber. It is this formula that is used for κ in the above orifice disturbance.

In most of our experiments κ^* is calculated to be 0.7 to one significant figure; however in experiments involving the most viscous liquids $\kappa^* = 0.6$ to one significant figure.

6.1.3 Comparison of results using inviscid and viscous theories when $Re = \infty$

Figure 6.1 shows two simulations at break-up for an inviscid jet with $We = 70$ and $Rb = 10$. One simulation has been carried out using the inviscid theory described in chapter 5 with $K = 0.7$ and the other with the viscous theory with $Re = \infty$ and $\kappa = 0.7$. The simulations are qualitatively similar for both theories. Perturbations are convected along the length of the jet increasing in amplitude resulting in capillary pinch-off. A main drop is formed and a satellite drop is formed in front of the main drop demonstrating mode 2 break-up. The break-up lengths are very similar for both simulations.

Figure 6.2 shows two simulations at break-up for an inviscid jet with $We = 70$ and $Rb = 1$. One simulation has been carried out using the inviscid theory with $K = 0.7$ and the other with the viscous theory with $\kappa = 0.7$ and $Re = \infty$. In this case the simulations are qualitatively different. The simulation carried out with the inviscid theory is similar to the simulations in figure 6.1 except the wavelength of the perturbations is longer. The simulation carried out by the viscous theory using $Re = \infty$ shows mode 3 break-up. Elongated threads form between the main drops which will form satellite drops. The break-up length is much longer in the simulation using the viscous theory, even with $Re = \infty$.

In the inviscid case we solve equations (5.1) and (5.2) for u_0 and R_0. Neither of these equations contains rotation terms. For the viscous case we solve equations (6.73) and (6.74) for u_0 and R_0 and this system of equations does contain rotation terms in (6.73). The viscous theory and scaling presents a more accurate representation of the effects of rotation since the distinguished limit is different in that case. For large Rossby numbers the rotation rate is small so the effect of rotation is less.

Of course no real liquid is inviscid. The results here suggest that the rotation terms included in equations (6.73) and (6.74), but are missing in equations (5.1) and (5.2) will be important, even when Ohnesorge number is small, whenever Rossby number is small.

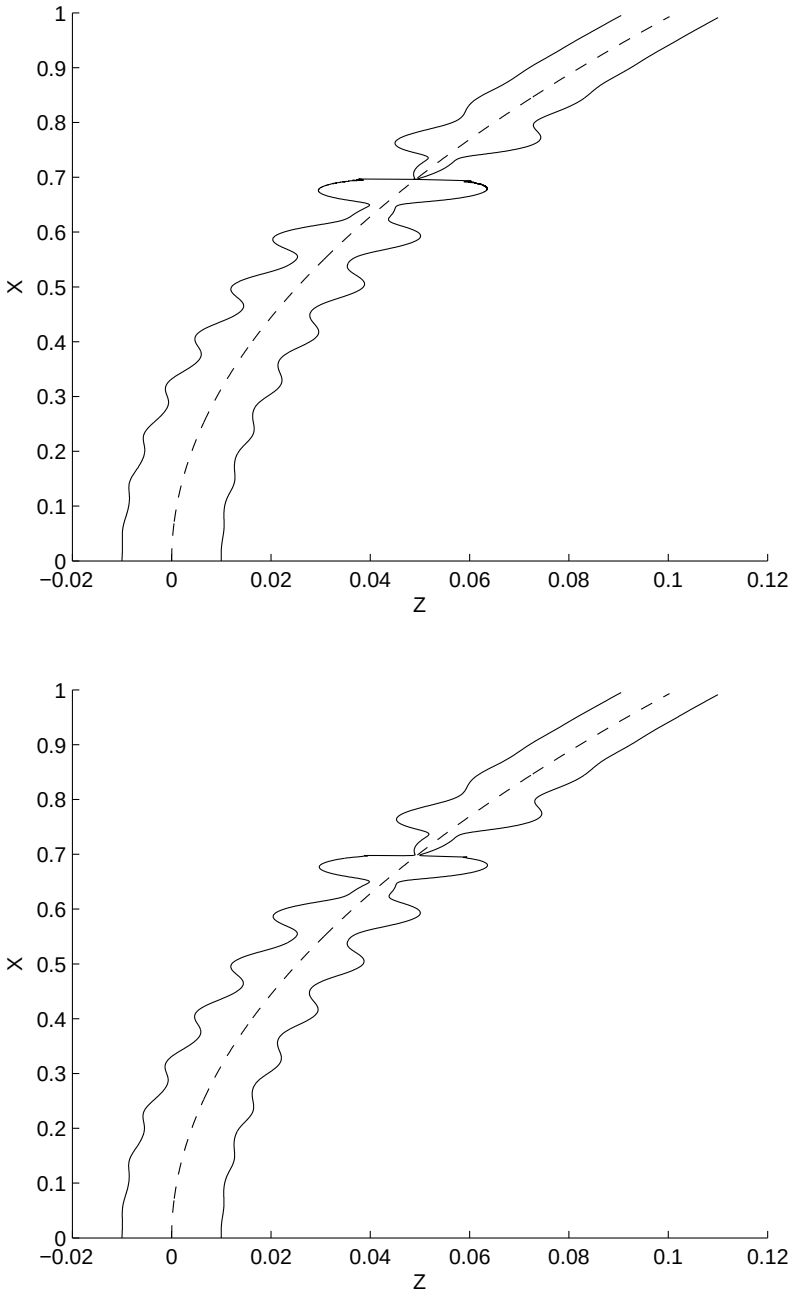

Figure 6.1: The simulation at the top is from the inviscid theory. The simulation at the bottom is from the viscous theory with $Re = \infty$. In both simulations $We = 70$ and $Rb = 10$.

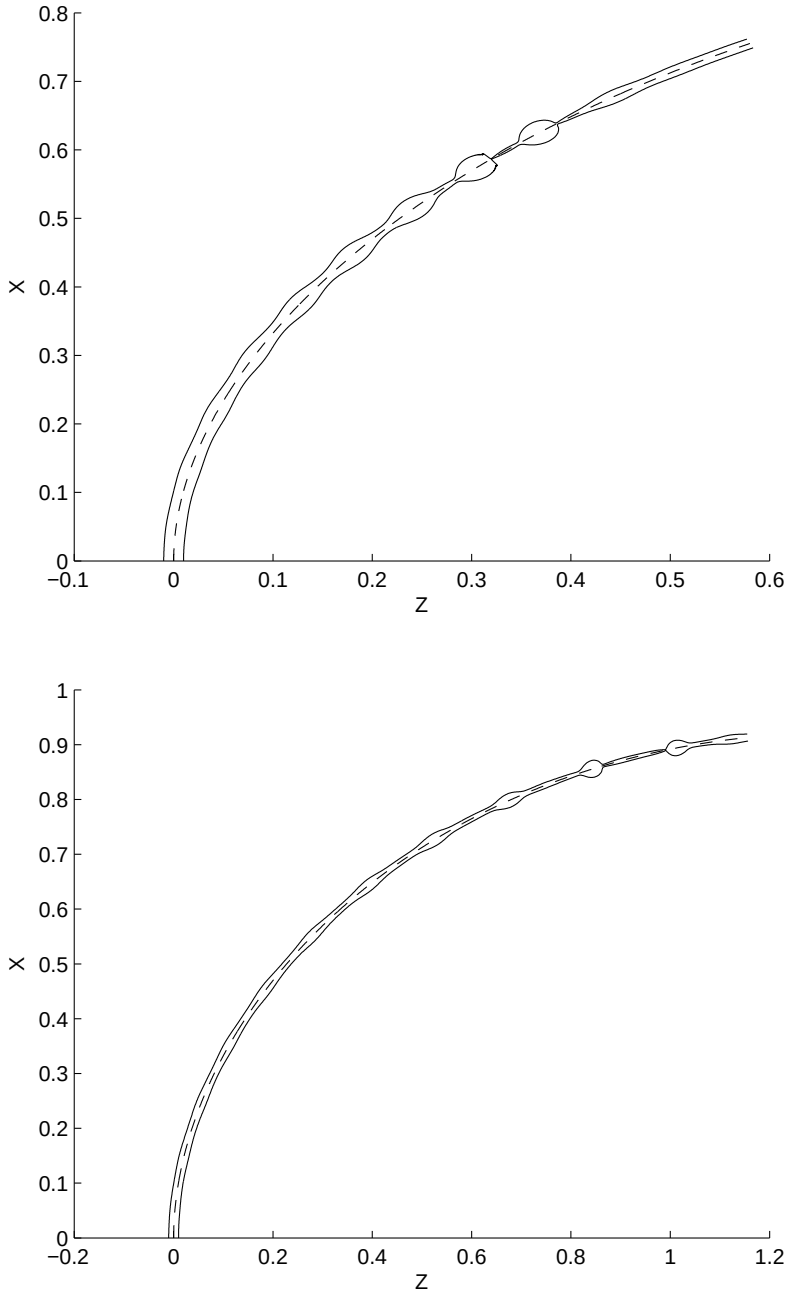

Figure 6.2: The simulation at the top is from the inviscid theory. The simulation at the bottom is from the viscous theory with $Re = \infty$. In both simulations $We = 70$ and $Rb = 1$.

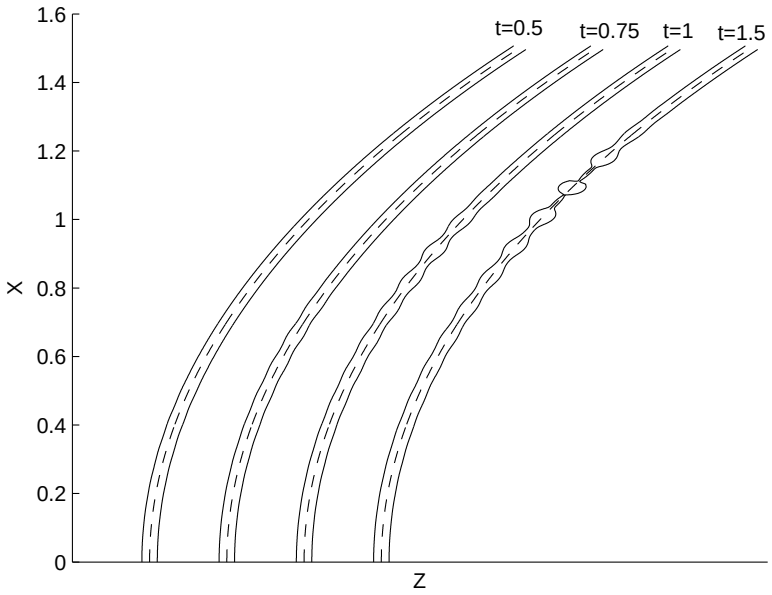

Figure 6.3: A jet with $Re = 3000$, $We = 50$, $Rb = 5$, $\delta = 0.001$, $\kappa = 0.7$ at times $t = 0.5,\ 0.75,\ 1$ and 1.5. The perturbations develop along the jet causing it to break-up at $t = 1.5$. The orifice is artificially shifted so that the jets at different times can be viewed more easily.

6.2 Results

6.2.1 Theoretical solutions

Figure 6.3 shows the evolution of a jet with $Re = 3000$, $We = 50$, $Rb = 5$, $\delta = 0.001$ and $\kappa = 0.7$. The spatial grid contains 3001 spaces, $ds = 0.001$ and $dt = 0.0001$. At $t = 0.5$ perturbations are beginning to develop on the surface of the jet. At $t = 0.75$ the amplitude of the perturbations increases and the perturbations are convected along the length of the jet. At $t = 1$ the amplitude of the perturbations increases still further and are convected further along the jet. We can see the beginning of capillary pinch-off. At $t = 1.5$ the jet finally breaks up and we see the formation of a main drop and two satellite drops either side of the main drop. The mode of break-up is mode 2.

Figure 6.4 shows the shape of the perturbations which are the variation in $R(s,t)$ along the arc-length s of the jet in figure 6.3. The horizontal axis is the arc-length s

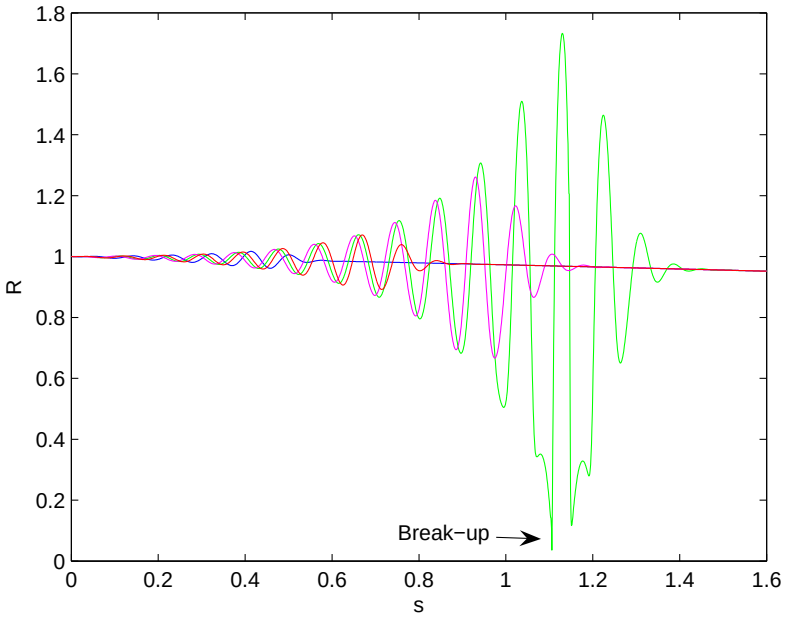

Figure 6.4: The perturbations travelling down the jet presented in figure 6.3. The blue line corresponds to $t = 0.5$, the red line to $t = 0.75$, the pink line to $t = 1$ and the green line to $t = 1.5$. The point which corresponds to the break-up of the jet has been highlighted.

and the vertical axis is the radius of the jet $R(s,t)$. We can see that at $t = 0.5$, $R(s,t)$ does not deviate much from the undisturbed radius. At $t = 0.75$, $R(s,t)$ deviates more from the undisturbed state and the deviation continues further along the length of the jet. At $t = 1$ the deviation of $R(s,t)$ from the undisturbed radius increases further. At $t = 1.5$ the jet breaks up. The point of break-up has been highlighted in figure 6.4 as the minimum of $R(s,t)$. It can be seen that $R(s,t)$ does not actually touch zero, and the break-up is chosen once this becomes 5% of the undisturbed radius. This is because there is a singularity in the equations at the break-up point [39]. Comparing figure 6.4 with figure 5.2 we can see there are considerably less numerical instabilities in 6.4 close to break-up.

Using this scaling we can predict main and satellite drop size using figure 6.4. The volume of the drops is obtained using a integral involving a volume of revolution,

$$V = \pi \int R_0^2 dt$$

over a wavelength at the break-up point. Then the radius of the resulting drop $\hat{R}$ can be found using

$$V = \frac{4}{3}\pi \hat{R}^3$$

since the drop will form a sphere.

When evaluating the volume of the drop we integrate over the wavelength before and after break-up. This gives us the volumes of two drops. We then calculate the radius of the two volumes by assuming the volume is spherical. The satellite drop corresponds to the smallest radius of these two drops.

6.2.2 Comparison between viscous theory and experiment

In this section we compare experimental results with results obtained using this theory. We choose three points within the pilot scale regime. In this case we have chosen $We = 47.15$, $We = 23.1$ and $We = 5.31$ (with the other parameters varying as appropriate).

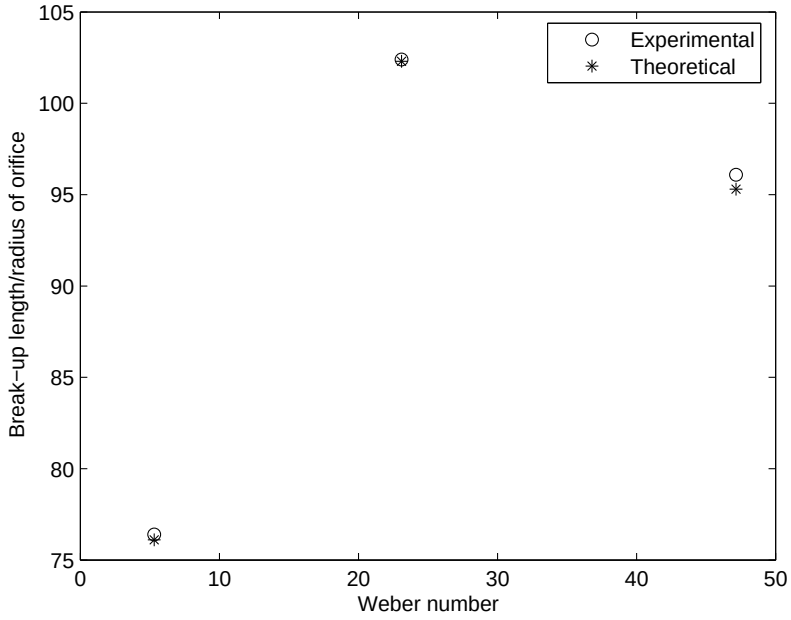

Figure 6.5: A plot comparing break-up lengths obtained experimentally and theoretically for $We = 5.31,\ 23.1$ and 47.15. The circles correspond to break-up lengths obtained from experiments and the stars correspond to break-up lengths obtained using the viscous theory, by fitting δ.

We choose κ so that (6.77) is satisfied. Using the theory we vary δ until we obtain a close match between experimental and theoretical values of the break-up length in each case. We used $\delta = 0.03$, $\delta = 0.008$ and $\delta = 0.00004$ respectively to achieve this fit in each case. We are able to obtain good agreement between experimental and theoretical results here by fixing δ in each case, unlike for the inviscid model in chapter 5. The results are presented in the form of a plot of Weber number against experimental and theoretical break-up length. This plot is given in figure 6.5. Therefore, in this case, δ is chosen so that the theoretical and experimental data match as best as possible in each of the three cases.

Using the same parameters and values of δ as in the previous paragraph we obtain the main and satellite drop sizes using the above fitted values for δ. The theoretical results are compared to the experimental results in figure 6.6. We can see that there is fairly good agreement between theory and experiment for the main drop sizes for all

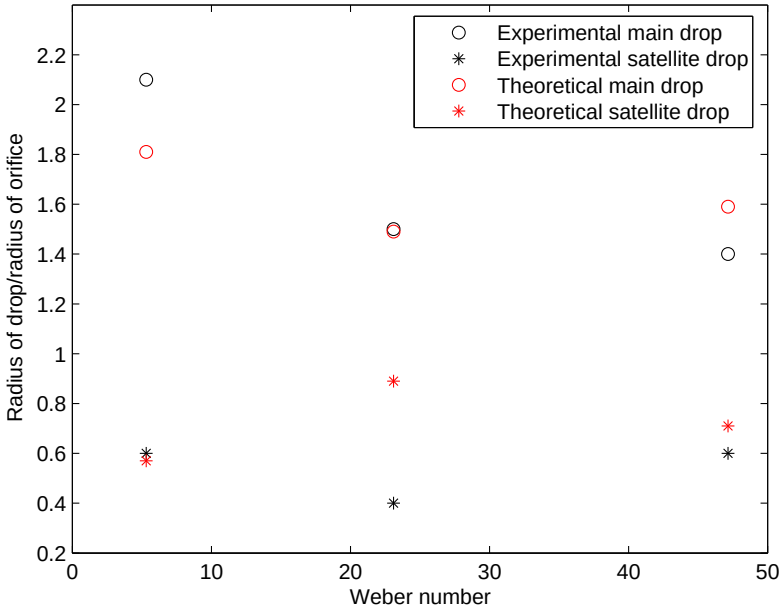

Figure 6.6: A plot comparing drop sizes obtained experimentally and theoretically. The black circles correspond to experimental main drop sizes. The red circles correspond to theoretical main drop sizes. The black stars correspond to experimental satellite drop sizes. The red stars correspond the drop sizes obtained experimentally. $We = 5.31$, 23.1 and 47.15.

the Weber numbers (the difference between experimental and theoretical main drop sizes ranges from 0-0.3 in non-dimensional units). There is also reasonable agreement between theory and experiment for satellite drop sizes (the difference between theoretical and experimental satellite drop sizes ranges from 0-0.5 in non-dimensional units).

The next step is to take the average value of δ from the above three values, in this case $\delta = 0.01268$, and re-calculate the main and satellite drop sizes from the simulations. We then compare the drop sizes obtained using this constant average value of δ with the drop sizes obtained in the experiments and the drop sizes obtained when we varied δ by fitting in each case. The results are presented in figure 6.7. The black and red markers are the same results as presented in figure 6.6. The blue circles represent the size of the main drops using the average value $\delta = 0.01268$ and the blue stars represent the size of the satellite drops obtained using the average value of $\delta = 0.01268$. We can see that the

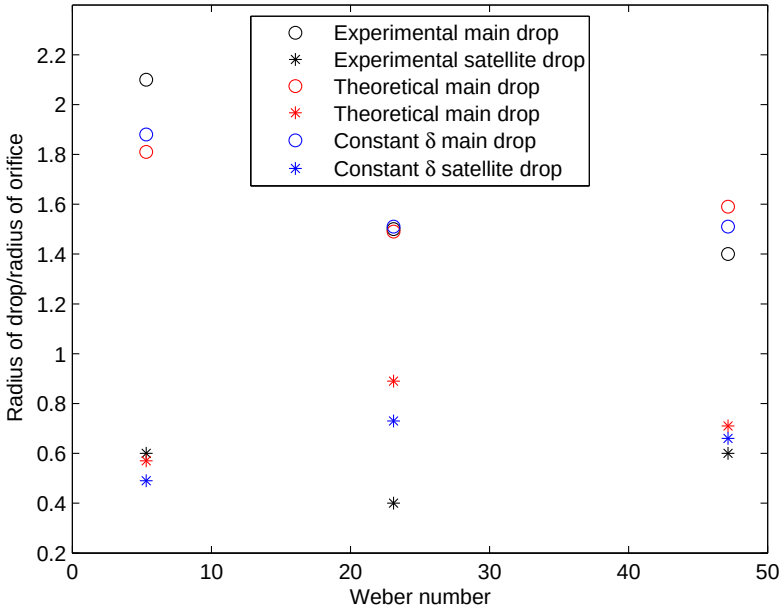

Figure 6.7: A plot comparing the results obtained in figure 6.6 with results obtained using a constant average value of $\delta = 0.01268$.

drop sizes obtained using a constant δ shows fairly good agreement with the drop sizes obtained experimentally and when δ was allowed to be fitted.

Figure 6.8 compares main and satellite drop sizes obtained both experimentally and theoretically for We=2.82, 5.02, 19.65 and 23.06 and $\delta = 0.01268$. These parameter values were all obtained on the pilot scale (again the other parameters are varied with each Weber number because of the interdependence of the parameters in the experiments). We can see that there is fairly good agreement between the experimental and theoretical drop sizes. The difference between the theoretical and experimental drop sizes varies from 0 to 0.3 in non-dimensional units.

These results show that even though the break-up length is highly dependent upon δ, which is usually unknown, fairly good agreement between theory and experiment can be found for drop sizes even if a typical rather than fitted value for δ is used in the theory in this case.

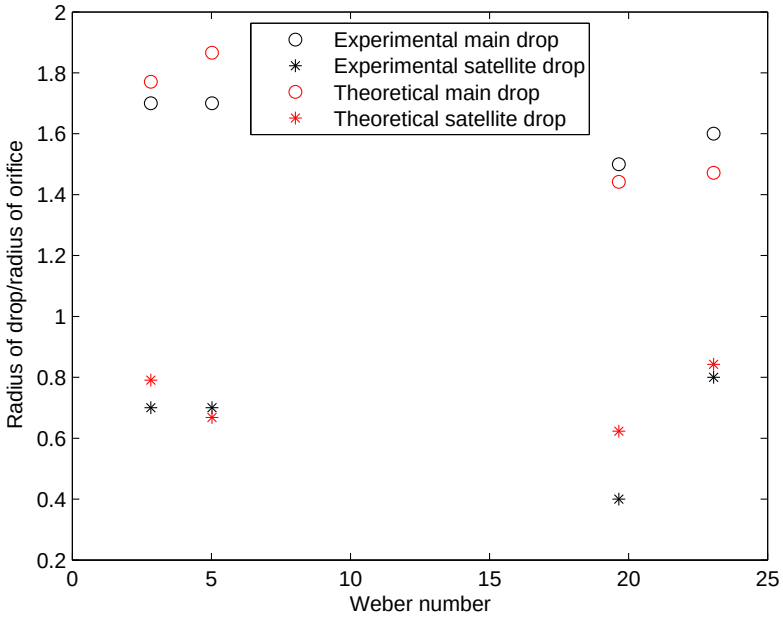

Figure 6.8: A plot comparing main and satellite drop sizes obtained theoretically and experimentally for $We = 2.82,\ 5.02,\ 19.65$ and 23.06. The theoretical drop sizes were obtained using a constant average value of $\delta = 0.01268$.

We have shown that reasonable agreement between experimental and the theoretical results can be achieved, giving us confidence in the theory. In the next section trends that the theory predicts will be examined. This enables us to determine how varying parameters affects drop sizes and break-up lengths. This cannot be easily ascertained from experiments because of interdependence of the parameters as already discussed. Theoretical results will be compared qualitatively to experimental results where possible but this will not be the aim of section 6.2.3 because the numerics are not always in the same parameter regimes as experiments.

6.2.3 Parametric study

In this section we extend the parametric study carried out in section 5.4.1 to include viscosity. Reynolds number is an additional parameter to be included.

Figure 6.9 compares the break-up length for different Weber numbers while Rossby number, Reynolds number and δ remain fixed. The spatial grid had 3001 spaces, $ds =$

0.0005, the temporal grid had 100,000 spaces and $dt = 0.00005$. The investigation was carried out using $We = 10,\ 20,\ 50,$ and 100, $Rb = 1$, $Re = 3000$ and $\delta = 0.01$. κ is chosen to satisfy (6.77). We can see that increasing the Weber number increases the break-up length dramatically. The break-up length increases from 40 to 170 in non-dimensional units. In figure 4.14 Weber number is plotted against experimental break-up length. The break-up length does increase with Weber number but the increase is not as dramatic as in the theoretical case. However experimentally we cannot vary Weber number and hold the other parameters fixed so this difference might be due to the effect of the other parameters in the experiments.

The result in figure 6.9 shows that Weber number has a strong effect on break-up length. The result in figure 5.3 where viscosity was neglected agrees with the result presented in figure 6.9.

Figure 6.10 compares Weber number with main and satellite drop sizes for $We = 10,\ 20,\ 50$ and 100. As Weber number increases the size of the satellite drop increases, and the difference in the size of the satellite drops is 0.3 in non-dimensional units. The size of the main drop decreases slightly, by 0.1 in non-dimensional units. It is difficult to compare figure 4.10 with figure 6.10. The information that can be gained from figure 4.10 is limited since within each Ohnesorge number, Weber number is varied by changing the rotation rate Ω, therefore Rossby number and Reynolds are varied too. In figure 4.10 the Rossby number varies from 0.5 to 1, and the Reynolds number varies from 430 to 3000. So figure 6.10 shows how drop size varies with Weber number for fixed rotation rate which is very difficult to do experimentally.

Figure 6.11 shows the break-up lengths for different Rossby numbers Rb= 0.8, 1, 2, 3 and 5, with Weber number, Reynolds number and δ constant ($We = 50$, $Re = 3000$ and $\delta = 0.01$). Break-up length increases substantially with decreasing Rossby number. The break-up length varies from 145 to 60 in non-dimensional units. From figure 4.15 there is generally a decrease in experimental break-up length with Rossby number within each

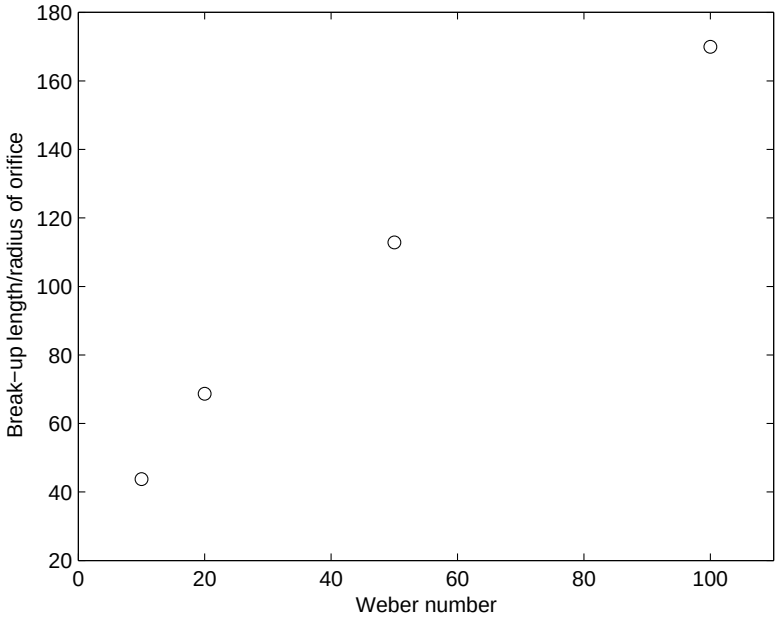

Figure 6.9: A plot of Weber number against break-up length. $We = 10,\ 20,\ 50$ and 100. $Rb = 1$, $Re = 3000$ and $\delta = 0.01$.

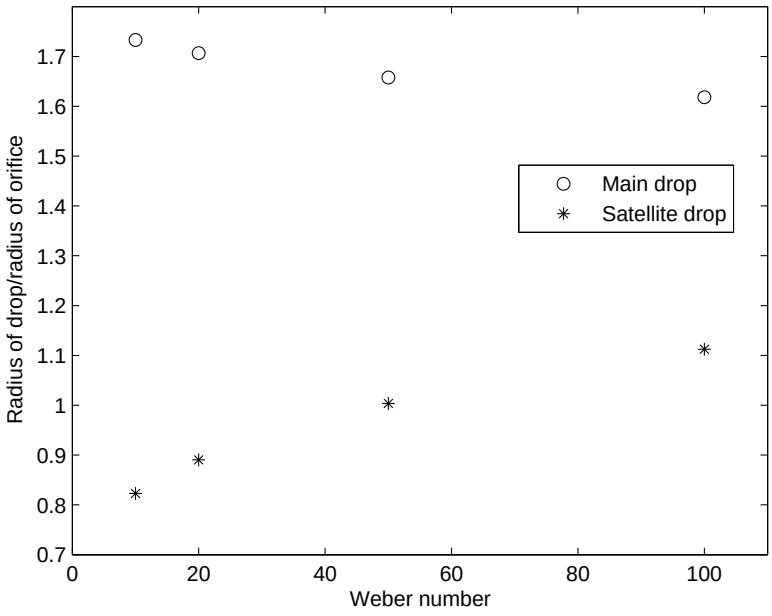

Figure 6.10: A plot showing Weber number against drop size for main and satellite drops. $We = 10,\ 20,\ 50$ and 100. $Rb = 1$, $Re = 3000$ and $\delta = 0.01$.

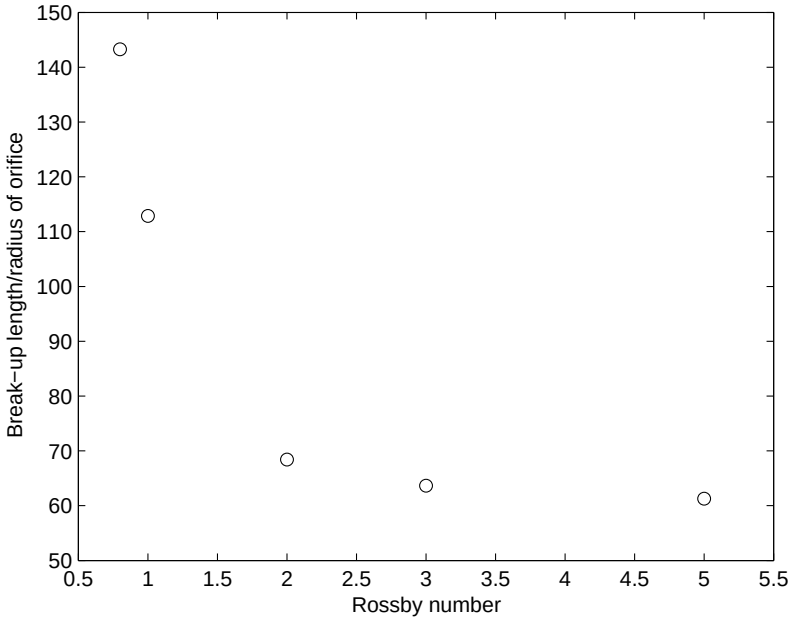

Figure 6.11: A plot showing Rossby number against break-up length. $Rb = 0.8,\ 1,\ 2,\ 3$ and 5. $We = 50$, $Rb = 1$, $Re = 3000$ and $\delta = 0.01$.

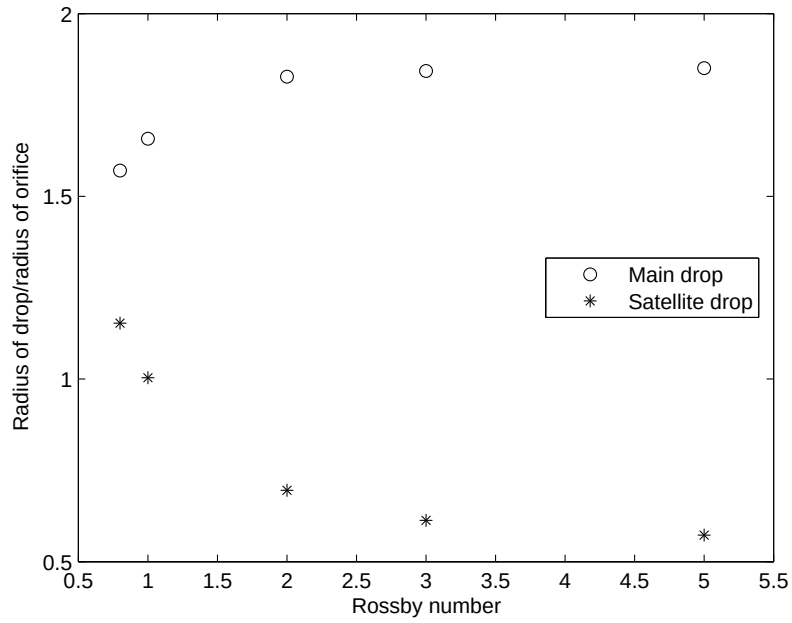

Figure 6.12: A plot showing Rossby number against drop size for main and satellite drops. $Rb = 0.8,\ 1,\ 2,\ 3$ and 5. $We = 50$, $Re = 3000$ and $\delta = 0.01$

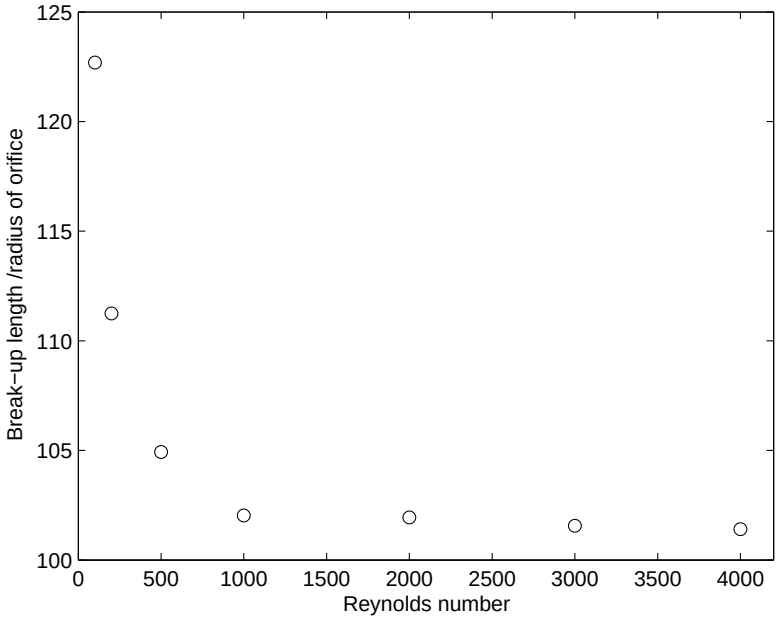

Figure 6.13: A plot of Reynolds number against break-up length, $We = 50$, $Rb = 1$ and $\delta = 0.01$. $Re = 4000,\ 3000,\ 2000,\ 1000,\ 500,\ 200$ and 100.

Ohnesorge number which agrees to some extent with the theoretical result qualitatively at least. In figure 5.5 we found that break-up length did not change much with Rossby number. However the viscous theory uses a different scaling which introduces more rotation terms into the problem. This makes Rossby number a more dominant parameter.

Figure 6.12 compares Rossby number with main and satellite drop size for $Rb = 0.8,\ 1,\ 2,\ 3$ and 5. The size of the main drop increases by 0.3 in non-dimensional units, and the size of the satellite drop decreases, by 0.5 in non-dimensional units, with increasing Rossby number. In figure 4.11 where Rossby number was plotted against experimental main and satellite drop size, we could not ascertain a conclusive trend. Experimentally we cannot easily vary Rossby number and keep the other parameters fixed. In figure 4.11 the Weber number varies from 10 to 70 and Reynolds number varies from 430 to 3000. The advantage of the results obtained in figure 6.12 is that we can see how drop size changes with Rossby number for fixed Weber number and Reynolds number.

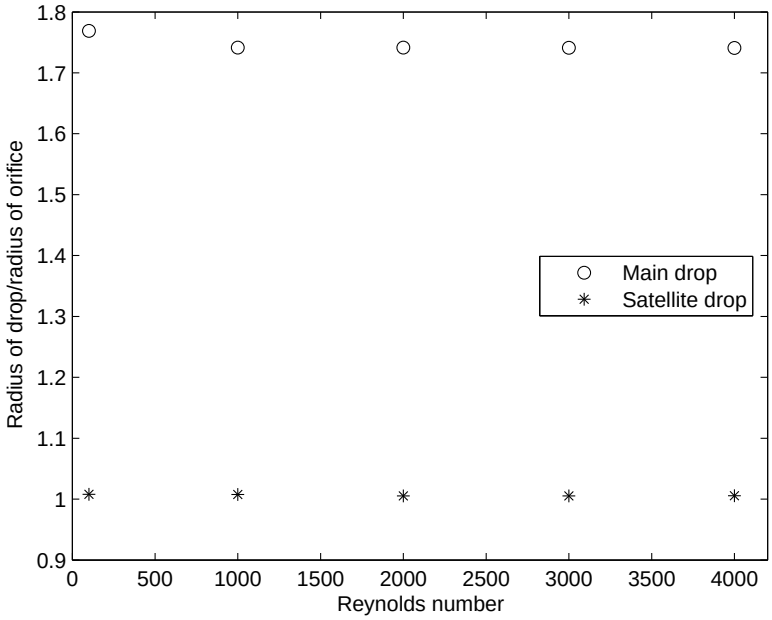

Figure 6.14: A plot showing Reynolds number against drop size for main and satellite drops. $Re = 4000,\ 3000,\ 2000,\ 1000$ and 100. $We = 50$, $Rb = 1$ and $\delta = 0.01$.

Figure 6.13 compares break-up lengths for different Reynolds numbers (Re= 4000, 3000, 2000, 1000, 500, 200 and 100). Here Weber number ($We = 50$), Rossby number ($Rb = 1$), and δ ($\delta = 0.01$) are all fixed. The break-up length increases markedly with decreasing Reynolds number. The break-up length varies from 101 to 123 in non-dimensional units. In figure 6.13 decreasing Reynolds number corresponds to increasing viscosity and also corresponds to increasing Ohnesorge number. From figures 4.14, 4.15, 4.16 and 4.17 we see that the break-up length is longer for larger Ohnesorge number. Larger Ohnesorge number corresponds to higher viscosity jets therefore the experimental results agree qualitatively with the theoretical result in figure 6.13.

Figure 6.14 compares the size of the satellite and main drops with Reynolds number ($Re = 4000,\ 3000,\ 2000,\ 1000$ and 100). We can see that Reynolds number has a negligible effect on the size of the main and satellite drops, the difference in main and satellite drop sizes is less than 0.1 in non-dimensional units. In figure 4.12, which showed Reynolds number against experimental main and satellite drop size, there was no relation

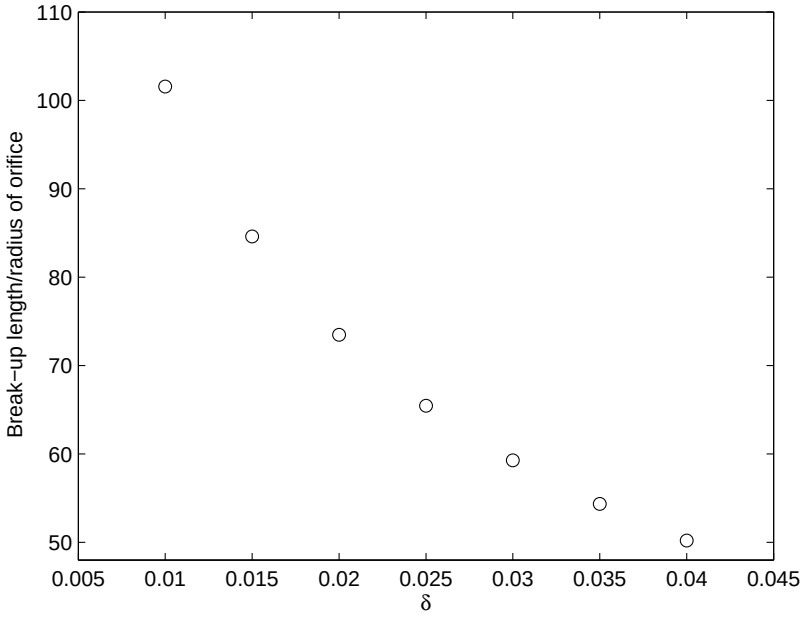

Figure 6.15: A plot of δ against break-up length. $We = 50$, $Rb = 1$ and $Re = 3000$. $\delta = 0.01,\ 0.015,\ 0.02,\ 0.025,\ 0.03,\ 0.035$ and 0.04.

between Reynolds number and main and satellite drop size. This is probably due to the influence of other parameters since we cannot vary Reynolds number and hold the other parameters constant experimentally. In figure 4.12 the Weber varies from 10 to 70 and the Rossby number varies from 0.5 to 1.

Figure 6.15 shows the break-up length for different values of δ with Rossby number, Weber number and Reynolds number held constant ($Rb = 1$, $We = 50$ and $Re = 3000$). The values of δ are 0.01, 0.015, 0.02, 0.025, 0.03, 0.035 and 0.04. The break-up length increases considerably with decreasing δ. The break-up length varies from 50 to 100 in non-dimensional units. This is similar to the result obtained when viscosity was neglected in section 5.4.1 (see figure 5.7) and is to be expected. Figure 6.16 shows the main and satellite drop sizes for different values of δ ($\delta = 0.01,\ 0.015,\ 0.02,\ 0.025,\ 0.03,\ 0.035$ and 0.04). δ has a negligible effect on drop size, the difference between main drop sizes is less than 0.1 in non-dimensional units and the difference in satellite drop sizes is also less than 0.1 in non-dimensional units. It is not possible to compare this part of the theoretical inves-

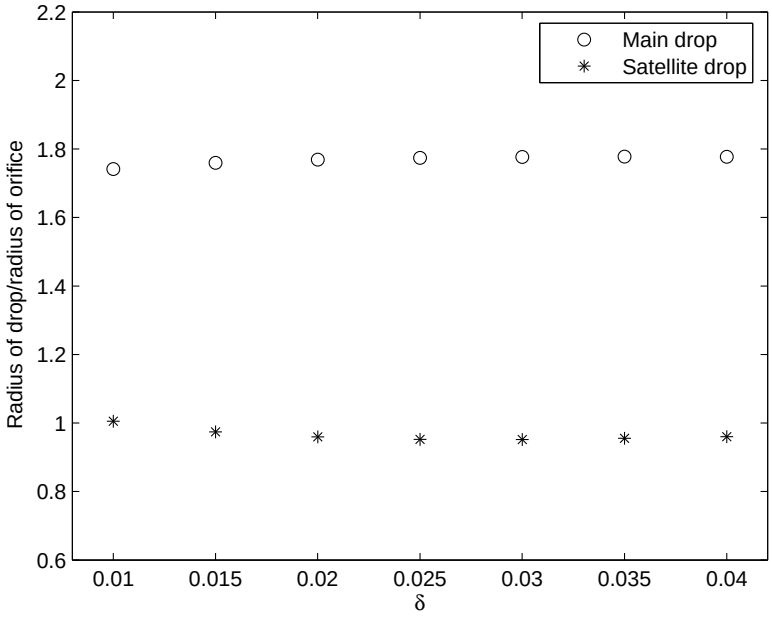

Figure 6.16: A plot of δ against drop size for main and satellite drops. $We = 50$, $Rb = 1$ and $Re = 3000$. $\delta = 0.01,\ 0.015,\ 0.02,\ 0.025,\ 0.03,\ 0.035$ and 0.04.

tigation to experimental results since there is no method of measuring δ experimentally.

6.3 Rossby number curves

The work in the previous section suggests that Rossby number has a greater effect on drop size than Weber number, Reynolds number or δ (though Weber number still has a fairly significant effect, especially on satellite drop size). The work presented in this section would be very difficult to undertake experimentally since we cannot vary one parameter while keeping the other parameters fixed. Figures 6.17, 6.18 and 6.19 are plots of main and satellite drop size against Rossby number for $Rb = 1,\ 2,\ 3$ and 5. In figure 6.17 different curves are produced for different Weber numbers, $We = 20,\ 30,\ 40$ and 50. Reynolds number and δ remain constant ($Re = 3000$, $\delta = 0.01$). The largest difference between the drop sizes for a particular Rossby number is 0.3 in non-dimensional units. This occurs for the satellite drops at $Rb = 1$. However at larger Rossby numbers the difference in main and satellite drop size with Weber number is much smaller. This suggests that Weber number has more effect upon drop size at low Rossby number.

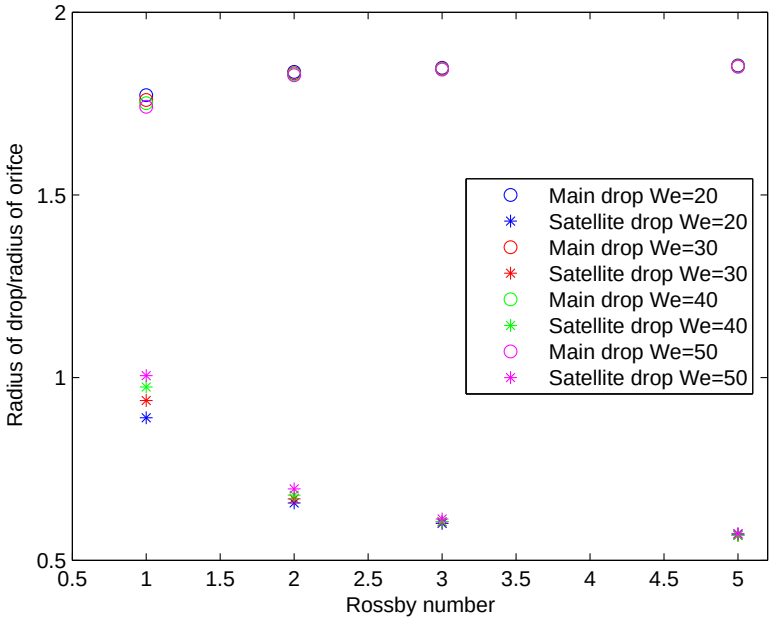

Figure 6.17: A plot of main and satellite drop size against Rossby number, $Rb = 1,\ 2,\ 3$ and 5, for different Weber numbers $We = 20,\ 30,\ 40$ and 50. $Re = 3000$ and $\delta = 0.01$.

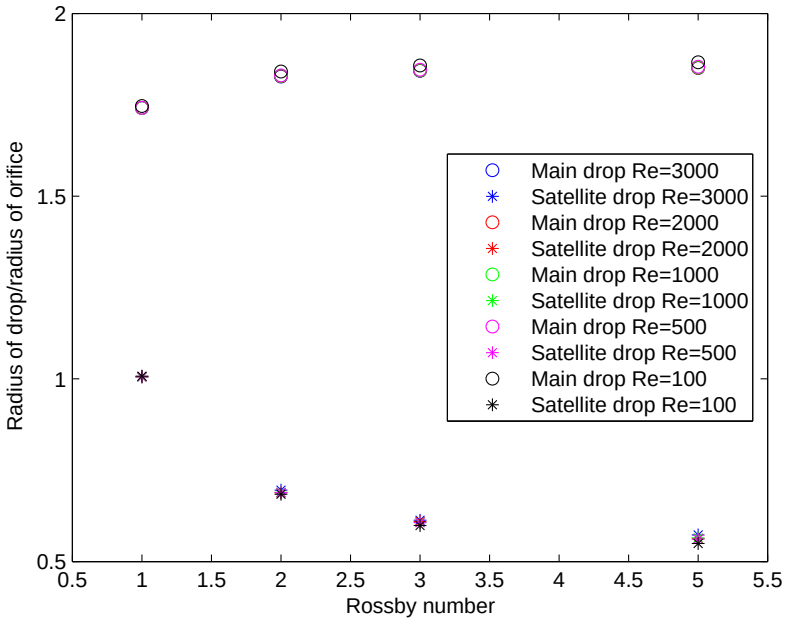

Figure 6.18: A plot of main and satellite drop size against Rossby number, $Rb = 1,\ 2,\ 3$ and 5, for different Reynolds numbers $Re = 100,\ 500,\ 1000,\ 2000$ and 3000. $We = 50$ and $\delta = 0.01$.

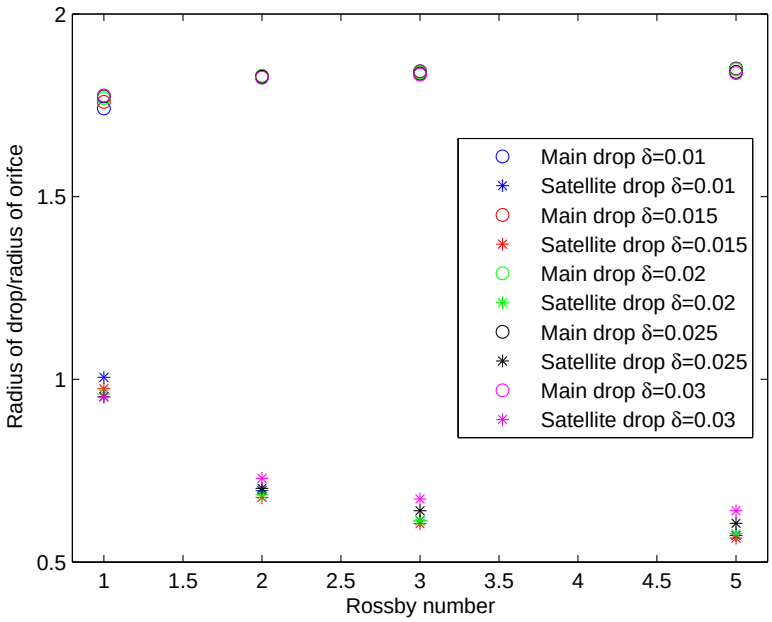

Figure 6.19: A plot of main and satellite drop size against Rossby number Rb = 1, 2, 3 and 5, for different values of δ, δ = 0.01, 0.015, 0.02, 0.025 and 0.03. $We = 50$ and $Re = 3000$.

In figure 6.18 curves are produced for different Reynolds numbers Re=100, 500, 1000, 2000 and 3000. Weber number and δ remain constant ($We = 50$ and $\delta = 0.01$). We can see that the difference in main and satellite drop size is negligible for each Rossby number (much less than 0.1 in non-dimensional units), this shows that Reynolds number has little influence on the drop size.

In figure 6.19 curves are produced for different values of δ, δ=0.01, 0.015, 0.02, 0.025 and 0.03. Weber number and Reynolds number remain constant ($We = 50$ and $Re = 3000$). δ has a negligible effect on main drop size within each Rossby number, the difference in main drop size is much less than 0.1 in non-dimensional units within each Rossby number. There is a small effect on satellite drop size, the greatest difference in satellite drop size within each Rossby number is 0.1 in non-dimensional units, which is small compared to the size of the drop.

6.4 Summary

In this chapter we have included viscosity in the model. We used a non-linear analysis in a similar way to chapter 5 but with a different scaling. This meant that rotation entered the problem in the equations of motion as well as in the initial conditions.

Experimental and theoretical break-up lengths were compared by varying δ until we obtained a good match between experimental and theoretical data. We did this for three cases and found that for each experimental break-up length a value of δ could be found that gave a theoretical break-up length that was an excellent match, this could not be done in chapter 5. Using the fitted value of δ in each case we calculated the main and satellite drop sizes. The agreement between experimental and theoretical drop sizes was reasonably good. Then the drop sizes were calculated again using a value of δ which was the average of the fitted values. Again we found reasonably good agreement between theoretical and experimental drop sizes. Drop sizes were calculated for a range of experimental parameters using the constant average value of δ. The theoretical drop sizes were compared to the experimental drop sizes. In all cases reasonable agreement was found. This shows we can choose a typical value of δ, provided it is of the correct order of magnitude, and obtain drop sizes that are in reasonable agreement with experimental results, which is useful since δ is usually unknown in experiments.

The parametric study carried out in chapter 5 was extended to include Reynolds number. In this parametric study Weber number, Rossby number and Reynolds number were assumed to be independent parameters. Experimentally we could not easily do this, so the theoretical work was able to give us information that could not be easily obtained experimentally. Trends in break-up length and drop sizes were examined. It was found that break-up length increases with increasing Weber number which agrees with the result in chapter 5. Increasing Rossby number caused the break-up length to decrease. In chapter 5 it was found that the break-up length only changed slightly with Rossby number. However the viscous theory incorporated more rotation terms and

therefore gave us more and better information. Also the result obtained from the viscous theory agreed with experimental results in chapter 4. Break-up length was found to increase with decreasing Reynolds number. Decreasing Reynolds number corresponds to increasing viscosity; viscous forces stabilise the jet so waves travel further before breaking the jet up. There is qualitative agreement with experimental results here. Break-up length increased with decreasing δ. This was expected since δ is the amplitude of the disturbance at the orifice. The greater the amplitude of the disturbance the sooner the jet will break-up. This agreed with the results from the inviscid theory in chapter 5.

Weber number, Rossby number, Reynolds number and δ were plotted against theoretical main and satellite drop sizes. It was found that Rossby number had a greater effect on drop size than Weber number, Reynolds number or δ.

Plots of Rossby number against main and satellite drop size were produced for different values of Weber number, Reynolds number and δ. It was found that at low Rossby number, Weber number affects drop size more than at high Rossby number. At $Rb = 1$ the difference in satellite drop was 0.3 in non-dimensional units, and the satellite drop size increased with increasing Weber number. The main drop size decreased with increasing Weber number by 0.1 in non-dimensional units. At high Rossby numbers, Weber number had a negligible effect on main and satellite drop size. Reynolds number had a negligible effect on drop size for all Rossby numbers. δ had a negligible effect on main drop size for all Rossby numbers, there was a greater effect on the size of the satellite drops where the difference in drop size was 0.1. But this is small compared to the size of the drop.

The major advantage of using the theory is that one parameter can be varied while the others are kept fixed. This enabled us to identify how each parameter influences break-up length and drop size. Experimentally we cannot easily vary one parameter while keeping the others constant therefore the trends can be influenced by other parameters.

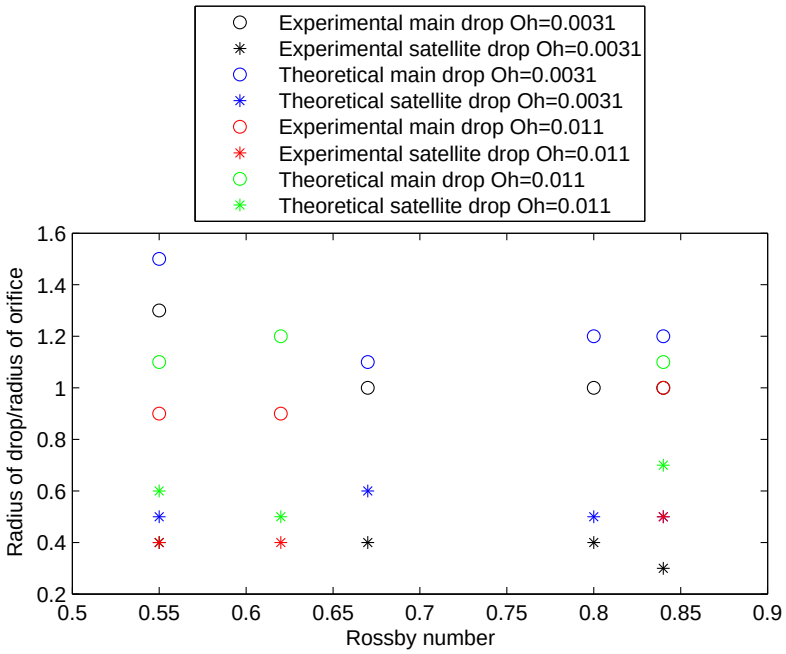

Figure 6.20: A plot of Rossby number against drop size. The red and black markers are the experimental data points plotted in figure 4.11. The blue markers are theoretical predictions for $Oh = 0.0031$ and the green markers are theoretical predictions for $Oh = 0.011$. At $Rb = 0.55$ the experimental satellite drop sizes are the same so the red and black star correspond to the same point. At $Rb = 0.84$ the red and blue star correspond to the same point and the experimental main drop sizes are the same so the black and red circle correspond to the same point.

Clearly further experimental and theoretical work is required to understand the interdependence of Rossby number, Reynolds number and Weber number in experiments, which is due to a complex flow inside the can. What has been shown here is that reasonable agreement between the theory and experiments can be achieved if experimental parameters are used in the theory. Also the behaviour of the drop sizes and jet break-up length have been examined with respect to the parameters (varied independently). While this is difficult to replicate within a single experimental set-up, it provides valuable physical insight into the problem. The parameter variation work also gives us an idea of how drop sizes and break-up lengths change.

Finally we demonstrate that it is possible to reproduce with reasonable accuracy experimental figures from chapter 4, using the theory, allowing for the interdependence of

the parameters in the experiments. Figure 6.20 shows figure 4.11 plotted with theoretical predictions for drop sizes, using $\delta = 0.01268$ (as a typical value), for comparison. For each data point Rossby number, Weber number, Reynolds number and Ohnesorge number are chosen to agree with the experimental values, so building in the interdependence of the parameters in the experiments. It can be seen there is reasonable agreement between theoretical and experimental data. The greatest difference in theoretical and experimental drop size is 0.3 in non-dimensional units.

It is also worth commenting that in experiments there is not just one wave that propagates down the jet, but a wavepacket. The most unstable mode constitutes the most common mode within this wavepacket, but there will be many other modes centred around this most unstable mode. It is this feature that gives rise to the distributions in drop sizes seen in experiments. This feature is difficult to replicate theoretically, but could be achieved by allowing the disturbance at the orifice to be equal to a Fourier series of a number of different wave modes with different frequencies. However this would introduce many more parameters into the model which would make the model less useful from a practical point of view and would be unlikely to provide any extra insight into the physics of the problem.

Chapter 7

Inclusion of gravity in the non-linear model

7.1 Introduction

Previously we have neglected gravity on the assumption that the can was rotating quickly, so the jets do not fall out of the horizontal plane significantly before the jet breaks into droplets. However if the can is rotating sufficiently slowly then the jet will fall significantly before it breaks up. The coordinate system used is similar to that in section 2.2, except there is an extra function $Y(s,t)$, as shown in figure 7.1. This function $Y(s,t)$ gives the vertical height of the jet's centreline relative to the centre of the orifice.

We will give an outline of some work described in Decent *et al.* [13] and Wallwork [41]. The inviscid case is considered. The model is written down as in section 2.2. The

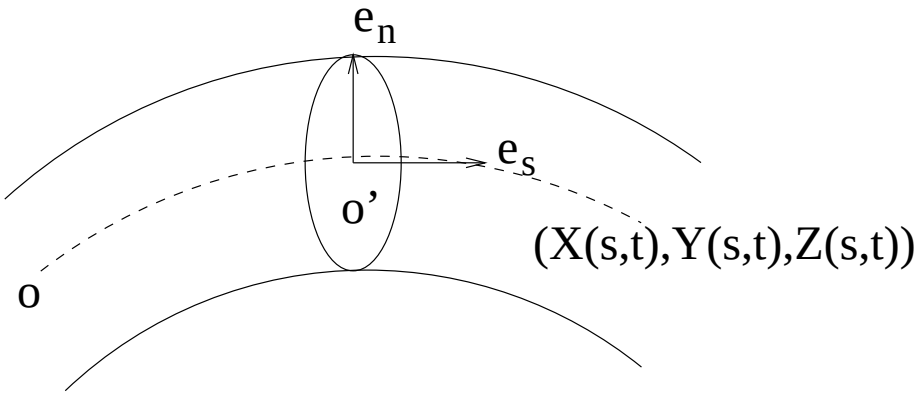

Figure 7.1: Definition sketch of the coordinate system

continuity equations and Euler's equations are

$$\nabla \cdot \mathbf{u} = 0 \tag{7.1}$$

and

$$\frac{\partial \mathbf{u}}{\partial t} + \mathbf{u} \cdot \nabla \mathbf{u} = -\frac{1}{\rho}\nabla p + \mathbf{g} - 2\boldsymbol{\omega} \times \mathbf{u} - \boldsymbol{\omega} \times (\boldsymbol{\omega} \times \mathbf{r}'). \tag{7.2}$$

The boundary conditions are the kinematic condition and the dynamic condition, namely

$$\frac{\partial f}{\partial t} + \mathbf{u} \cdot \nabla f = 0 \ \text{ on } \ n = R(s, \phi, t) \tag{7.3}$$

and

$$p = \sigma\kappa \ \text{ on } \ n = R(s, \phi, t), \tag{7.4}$$

where $\mathbf{g} = -g\mathbf{j}$ and g is the acceleration due to gravity. All other notation is the same as in section 2.2. An arc-length condition is required to close the system, namely

$$X_s^2 + Y_s^2 + Z_s^2 = 1. \tag{7.5}$$

Equations (7.1)-(7.5) are scaled using the following scalings,

$$\begin{gathered} \bar{u} = \frac{u}{U}, \ \ \bar{v} = \frac{v}{U}, \ \ \bar{w} = \frac{w}{U}, \ \ \bar{p} = \frac{p}{\rho U^2}, \ \ \bar{n} = \frac{n}{a}, \ \ \epsilon = \frac{a}{s_0}, \\ \bar{R} = \frac{R}{a}, \ \ \bar{s} = \frac{s}{s_0}, \ \ \bar{t} = \frac{tU}{s_0}, \ \ \bar{X} = \frac{X}{s_0}, \ \ \bar{Y} = \frac{Y}{s_0}, \ \ \bar{Z} = \frac{Z}{s_0}, \end{gathered} \tag{7.6}$$

where U is the exit speed of the jet, $R(s,t)$ is the radius of the jet, a is the radius of the orifice, Ω is the rotation rate of the can, ϵ is the aspect ratio which is small and s_0 is the radius of the can. The variables with the overbar correspond to non-dimensional quantities. Some lengthy equations were obtained and these are presented in Decent *et*

al. [13] and Wallwork [41]. Three non-dimensional groups were obtained, namely

$$F = \frac{U}{(s_0 g)^{1/2}}, \quad Rb = \frac{U}{\Omega s_0}, \quad We = \frac{\rho U^2 a}{\sigma},$$

which are Froude number, Rossby number and Weber number respectively. Dropping the overbars for simplicity and denoting $\mathbf{X} = X\mathbf{i} + Y\mathbf{j} + Z\mathbf{k}$ for the centreline of the jet, the steady solutions (see section 2.2) are found by posing asymptotic expansions, namely

$$\left.\begin{aligned} u &= u_0(s) + \epsilon u_1(s,n,\phi) + \cdots \\ v &= \epsilon v_1(s,n,\phi) + \epsilon^2 v_2(s,n,\phi) + \cdots \\ p &= p_0(s,n,\phi) + \epsilon p_1(s,n,\phi) + \cdots \\ R &= R_0(s) + \epsilon R_1(s,\phi) + \cdots \\ X &= X_0(s) + \epsilon X_1(s,t) + \cdots \\ Y &= Y_0(s) + \epsilon Y_1(s,t) + \cdots \\ Z &= Z_0(s) + \epsilon Z_1(s,t) + \cdots, \end{aligned}\right\} \tag{7.7}$$

with $w = 0$, so that the velocity at leading order is tangential to the centreline. For simplicity we write X_0, Y_0 and Z_0 as X, Y and Z respectively. Substituting (7.7) into the non-dimensional equations of motion some lengthy equations are obtained, and they are presented in Decent *et al.* [13].

The resulting equations were solved numerically subject to the initial conditions $X(0) = Y(0) = Y_s(0) = Z(0) = Z_s(0) = 0$ and $X_s(0) = R_0(0) = u_0(0) = 1$.

7.2 Non-linear inviscid analysis with gravity

Here we use use the scaling described in chapter 6 rather than chapter 5, so that it will be valid for small Rossby numbers as well as large Rossby numbers.

We consider the inviscid case. The model is written down as in Decent *et al.* [13]. The continuity equation and Euler's equations are used in the bulk namely

$$\nabla \cdot \mathbf{u} = 0 \tag{7.8}$$

and

$$\frac{\partial \mathbf{u}}{\partial t} + \mathbf{u} \cdot \nabla \mathbf{u} = -\frac{1}{\rho}\nabla p + \mathbf{g} - 2\boldsymbol{\omega} \times \mathbf{u} - \boldsymbol{\omega} \times (\boldsymbol{\omega} \times \mathbf{r}'). \tag{7.9}$$

The kinematic and dynamic conditions are used on the boundary, namely

$$\frac{\partial f}{\partial t} + \mathbf{u} \cdot \nabla f = 0 \ \text{ on } \ n = R(s, \phi, t) \tag{7.10}$$

and

$$p = \sigma\kappa \ \text{ on } \ n = R(s, \phi, t), \tag{7.11}$$

where $\mathbf{g} = -g\mathbf{j}$ and g is the acceleration due to gravity. Also the arc-length condition $X_s^2 + Y_s^2 + Z_s^2 = 1$ and the no flux conditions on the centreline $v = w = 0$ on $n = 0$ are required to close the system. The conditions at the orifice are given by $X = Y = Z = Y_s = Z_s = 0,\ X_s = 1,\ u = R = 1$ on $s = 0$. All other notation is the same as in section 2.2.1. Equations (7.8)-(7.11) are non-dimensionalised using the scalings in chapter 6. The same three non-dimensional groups were obtained as in the previous section, namely Froude number, Rossby number and Weber number.

We pose the asymptotic expansions

$$\left.\begin{aligned} u &= u_0(s,t) + (\epsilon n)u_1(s,t,\phi) + \cdots \\ v &= (\epsilon n)v_1(s,t,\phi) + (\epsilon n)^2 v_2(s,t,\phi) + \cdots \\ p &= p_0(s,t,\phi) + \epsilon p_1(s,t,\phi,n) + \cdots \\ R &= R_0(s,t) + \epsilon R_1(s,\phi,t) + \cdots \\ X &= X_0(s) + \epsilon X_1(s,t) + \cdots \\ Y &= Y_0(s) + \epsilon Y_1(s,t) + \cdots \\ Z &= Z_0(s) + \epsilon Z_1(s,t) + \cdots , \end{aligned}\right\} \tag{7.12}$$

with $w = 0$, so the velocity at leading order is tangential to the centreline. For simplicity we write X_0, Y_0 and Z_0 as X, Y and Z respectively. Substituting (7.12) into the non-dimensional equations of motion we obtain the following equations: at $O(\epsilon n)$ equation (7.8) is

$$v_1 = -\frac{u_{0s}}{2}. \tag{7.13}$$

The s-momentum equation becomes

$$u_{0t} + u_0 u_{0s} = -p_{0s} - \frac{Y_s}{F^2} + \frac{(X+1)X_s + ZZ_s}{Rb^2} \tag{7.14}$$

at $O(\epsilon)$. At $O(1)$ the n-momentum equation becomes

$$p_{0n} = 0 \tag{7.15}$$

and at $O(\epsilon)$ the n-momentum equation becomes

$$u_0^2\cos\phi(X_{ss}^2+Y_{ss}^2+Z_{ss}^2)^{1/2} = -p_{1n} + \frac{1}{F^2}\left(-\frac{Z_s(X_{ss}^2+Y_{ss}^2+Z_{ss}^2)^{1/2}}{\cos\phi(Y_{ss}Z_s - Z_{ss}Y_s) - X_{ss}\sin\phi}\right.$$
$$\left.+\frac{(\cos\phi(X_{ss}Z_s - Z_{ss}X_s) + Y_{ss}\sin\phi)(\sin\phi(Y_{ss}Z_s - Y_sZ_{ss}) + X_{ss}\cos\phi)}{(\cos\phi(Y_{ss}Z_s - Z_{ss}Y_s) - X_{ss}\sin\phi)(X_{ss}^2+Y_{ss}^2+Z_{ss}^2)^{1/2}}\right)$$
$$+\left(-\frac{2u_0Z_s}{Rb}+\frac{X+1}{Rb^2}\right)\frac{(\sin\phi(Y_{ss}Z_s - Y_sZ_{ss}) + X_{ss}\cos\phi)}{(X_{ss}^2+Y_{ss}^2+Z_{ss}^2)^{1/2}}$$
$$+\left(\frac{2u_0X_s}{Rb}+\frac{Z}{Rb^2}\right)\frac{(\cos\phi(Y_sX_{ss} - Y_{ss}X_s) - Z_{ss}\sin\phi)(\sin\phi(Y_{ss}Z_s - Y_sZ_{ss}) + X_{ss}\cos\phi)}{(\cos\phi(Y_{ss}Z_s - Z_{ss}Y_s) - X_{ss}\sin\phi)(X_{ss}^2+Y_{ss}^2+Z_{ss}^2)^{1/2}}$$
$$\left(-\frac{2u_0X_s}{Rb}+\frac{Z}{Rb^2}\right)\left(\frac{Y_s(X_{ss}^2+Y_{ss}^2+Z_{ss}^2)^{1/2}}{\cos\phi(Y_{ss}Z_s - Z_{ss}Y_s) - X_{ss}\sin\phi}\right). \tag{7.16}$$

At $O(1)$ the ϕ-momentum equation becomes

$$p_{0\phi} = 0 \tag{7.17}$$

and at $O(\epsilon)$ the ϕ-momentum equation becomes

$$-u_0^2\sin\phi(X_{ss}^2+Y_{ss}^2+Z_{ss}^2)^{1/2} = -\frac{1}{n}p_{1\phi} + \frac{1}{F^2}\left(\frac{\cos\phi(X_{ss}Z_s - Z_{ss}X_s) + Y_{ss}\sin\phi}{(X_{ss}^2+Y_{ss}^2+Z_{ss}^2)^{1/2}}\right)$$
$$+\left(-\frac{2u_0Z_s}{Rb}+\frac{X+1}{Rb^2}\right)\left(\frac{\cos\phi(Y_{ss}Z_s - Z_{ss}Y_s) - \sin\phi X_{ss}}{(X_{ss}^2+Y_{ss}^2+Z_{ss}^2)^{1/2}}\right)$$
$$+\left(\frac{2u_0X_s}{Rb}+\frac{Z}{Rb^2}\right)\frac{(\cos\phi(Y_sX_{ss} - X_sY_{ss}) - Z_{ss}\sin\phi)}{(X_{ss}^2+Y_{ss}^2+Z_{ss}^2)^{1/2}}. \tag{7.18}$$

The kinematic condition, equation (7.10) becomes

$$R_{0t} + u_0R_{0s} = nv_1 \ \text{ on } \ n = R_0(s) \tag{7.19}$$

at $O(\epsilon)$. Using the result from equation (7.13), equation (7.19) becomes

$$R_{0t} + u_0R_{0s} + \frac{u_{0s}R_0}{2} = 0. \tag{7.20}$$

Equation (7.11) which is the dynamic condition becomes

$$p_0 = \frac{1}{WeR_0} \tag{7.21}$$

at $O(1)$ and

$$p_1 = -\frac{1}{We}\left(-\frac{R_{1\phi\phi}+R_1}{R_0^2} + \cos\phi(X_{ss}^2+Y_{ss}^2+Z_{ss}^2)^{1/2}\right) \tag{7.22}$$

at $O(\epsilon)$. If we substitute (7.21) into equation (7.14) we arrive at

$$u_{0t} + u_0 u_{0s} = -\frac{Y_s}{F^2} - \frac{1}{We}\left(\frac{1}{R_0}\right)_s + \frac{(X+1)X_s + ZZ_s}{Rb^2} \tag{7.23}$$

At leading order the arc-length condition becomes $X_s^2 + Y_s^2 + Z_s^2 = 1$ and the no flux condition gives us $v_1 = 0$ on $n = 0$. Now consider $\sin\phi(7.16) + \cos\phi(7.18)$. This gives

$$\begin{aligned}\sin\phi p_{1n} + \frac{1}{n}\cos\phi p_{1\phi} = \frac{1}{(X_{ss}^2+Y_{ss}^2+Z_{ss}^2)^{1/2}}\left(\frac{1}{F^2}(X_{ss}Z_s - Z_{ss}X_s) - \frac{2u_0Y_{ss}}{Rb}\right.\\ \left.+\frac{X+1}{Rb^2}(Y_{ss}Z_s - Y_sZ_{ss}) + \frac{Z}{Rb^2}(Y_sX_{ss} - Y_{ss}X_s)\right) = G(s,t).\end{aligned} \tag{7.24}$$

The solution to equation (7.24) is of the form $p_1 = n\sin\phi G(s,t) + n\cos\phi H(s,t) + h(s,t)$. If we combine this result with equation (7.22) we obtain

$$n\sin\phi G(s,t) + n\cos\phi H(s,t) + h(s,t) = -\frac{1}{We}\left(-\frac{R_{1\phi\phi}+R_1}{R_0^2} + \cos\phi(X_{ss}^2+Y_{ss}^2+Z_{ss}^2)^{1/2}\right). \tag{7.25}$$

Equation (7.25) is a second order ordinary differential equation for R_1. As R_1 is periodic with period 2π it cannot contain terms such as $\phi\cos\phi$ or $\phi\sin\phi$. Therefore the inhomogeneous part of this differential equation must have zero coefficients so $G(s,t) = 0$ and

$$nH(s,t) + \frac{1}{We}(X_{ss}^2+Y_{ss}^2+Z_{ss}^2)^{1/2} = 0.$$

Therefore equation (7.24) yields

$$\frac{Z_s X_{ss} - Z_{ss} X_s}{F^2} - \frac{2Y_{ss}u_0}{Rb} + \frac{(X+1)(Y_{ss}Z_s - Z_{ss}Y_s)}{Rb^2} + \frac{Z(Y_s X_{ss} - Y_{ss}X_s)}{Rb^2} = 0 \quad (7.26)$$

and

$$H(s,t) = -\frac{1}{R_0 We}(X_{ss}^2 + Y_{ss}^2 + Z_{ss}^2)^{1/2}$$

so

$$p_1 = -\frac{n}{R_0 We}\cos\phi(X_{ss}^2 + Y_{ss}^2 + Z_{ss}^2)^{1/2} + h(s,t) \quad (7.27)$$

where $h(s,t)$ can be found at next order. Consider $\cos\phi(7.16) - \sin\phi(7.18)$ and we obtain

$$\left(u_0^2 - \frac{1}{R_0 We}\right)(X_{ss}^2 + Y_{ss}^2 + Z_{ss}^2) = -\frac{Y_{ss}}{F^2} + \frac{2u_0}{Rb}(X_s Z_{ss} - Z_s X_{ss}) + \frac{1}{Rb^2}((X+1)X_{ss} + ZZ_{ss}). \quad (7.28)$$

Equations (7.20), (7.23), (7.26), (7.28) and finally the arc-length condition $X_s^2 + Y_s^2 + Z_s^2 = 1$ form a system of five partial differential equations to be solved for the five unknowns X, Y, Z, u_0 and R_0, subject to the conditions at the orifice $X = Y = Y_s = Z = Z_s = 0$, $X_s = 1$, $u_0 = R_0 = 1$ on $s = 0$.

7.2.1 Non-linear temporal solution

As we are assuming a steady centreline, therefore X, Y and Z are functions of s only, we only need to solve equations (7.20) and (7.23) to find $u_0(s,t)$ and $R_0(s,t)$. This is the same assumption as used in chapters 5 and 6 (verified in chapter 9).

The non-linear system to be solved is

$$R_{0t} + u_0 R_{0s} + \frac{u_{0s} R_0}{2} = 0 \quad (7.29)$$

and

$$u_{0t} + u_0 u_{0s} = -\kappa_s - \frac{Y_s}{F^2} + \frac{(X+1)X_s + ZZ_s}{Rb^2} \quad (7.30)$$

where $\kappa = 1/WeR_0$.

Equations (7.26) and (7.28) and the arc-length condition combined with the steady versions of (7.29) and (7.30) which are

$$u_0 R_{0s} + \frac{u_{0s} R_0}{2} = 0 \tag{7.31}$$

and

$$u_0 u_{0s} = -\frac{Y_s}{F^2} - \frac{1}{We}\left(\frac{1}{R_0}\right)_s + \frac{(X+1)X_s + ZZ_s}{Rb^2} \tag{7.32}$$

are used to obtain the steady solutions. The steady solutions provide the initial condition of the flow. We solve the unsteady system using a finite difference method where the spatial grid is fixed and uniform and the time integration method is based on the Lax-Wendroff method as described in section 5.3.

We replace the leading order curvature in equation (7.30) with the full curvature

$$\kappa = \frac{1}{We}\left(\frac{1}{R_0(1+\epsilon^2 R_0^2)^{1/2}} - \frac{\epsilon^2 R_{0ss}}{(1+\epsilon^2 R_{0s}^2)^{1/2}}\right)$$

otherwise the jet is unstable to infinitesimally short wave modes. This is also the case for straight jets [17].

We denote $A = R_0^2$ so equations (7.29) and (7.30) can be written as

$$A_t + (Au_0)_s = 0 \tag{7.33}$$

and

$$u_{0t} + \left(\frac{u_0^2}{2}\right)_s = -\frac{1}{We}\frac{\partial}{\partial s}\left(\frac{4(2A + (\epsilon A_s)^2 - \epsilon^2 A A_{ss})}{(4A + (\epsilon A_s)^2)^{3/2}}\right) + \frac{(X+1)X_s + ZZ_s}{Rb^2} - \frac{Y_s}{F^2}. \tag{7.34}$$

The initial condition of the flow is given by the steady solutions of equations (7.26), (7.28), (7.31), (7.32) and the arc-length condition. We integrate forward in time from the initial conditions using equations (7.33) and (7.34) in the same way as described in

section 5.3. We impose periodic boundary conditions at the orifice

$$A(0,t) = 1, \quad u(0,t) = 1 + \delta \sin\left(\kappa \frac{t}{\epsilon}\right).$$

This corresponds to a disturbance of the exit velocity.

Wallwork [41] carried out a linear temporal stability analysis on a curved viscous jet. They found that the most unstable mode depends on the viscosity and is given by

$$\kappa^* = \frac{1}{2^{1/4}\sqrt{\sqrt{2} + 3Oh}} \tag{7.35}$$

where κ^* is the most unstable wavenumber. Equation (7.35) is used to calculate κ in the above orifice disturbance. For inviscid liquids, $\kappa^* = 0.7$ to one significant figure.

7.3 The viscous case

We now include viscosity in the above analysis. The model can be written down using the continuity equation and the Navier-Stokes equations, namely

$$\nabla \cdot \mathbf{u} = 0 \tag{7.36}$$

and

$$\frac{\partial \mathbf{u}}{\partial t} + \mathbf{u} \cdot \nabla \mathbf{u} = -\frac{1}{\rho}\nabla p + \nu \nabla^2 \mathbf{u} - 2\boldsymbol{\omega} \times \mathbf{u} - \boldsymbol{\omega} \times (\boldsymbol{\omega} \times \mathbf{r}') + \mathbf{g} \tag{7.37}$$

where $\mathbf{g} = -g\mathbf{j}$ and all other notation is the same as before. The equations on the free surface are given by the kinematic condition, the tangential stress condition and the normal stress condition. These equations are given in chapter 6 as (6.3), (6.4) and (6.5). The equations of motion are non-dimensionalised using the same scalings as in chapter 6 and four non-dimensional groups are obtained, Froude number, Rossby number, Reynolds number and Weber number. We pose the asymptotic expansions given in (7.12) and carry

out the same analysis as presented in section 7.2 and we obtain a system of five equations

$$R_{0t} + u_0 R_{0s} + \frac{u_{0s} R_0}{2} = 0, \tag{7.38}$$

$$u_{0t} + u_0 u_{0s} = -\frac{Y_s}{F^2} - \frac{1}{We}\left(\frac{1}{R_0}\right)_s + \frac{(X+1)X_s + ZZ_s}{Rb^2} + \frac{3(R_0^2 u_{0s})_s}{ReR_0^2}, \tag{7.39}$$

$$\frac{Z_s X_{ss} - Z_{ss} X_s}{F^2} - \frac{2Y_{ss} u_0}{Rb} + \frac{(X+1)(Y_{ss} Z_s - Z_{ss} Y_s)}{Rb^2} + \frac{Z(Y_s X_{ss} - Y_{ss} X_s)}{Rb^2} = 0, \tag{7.40}$$

$$\left(u_0^2 - \frac{1}{R_0 We}\right)(X_{ss}^2 + Y_{ss}^2 + Z_{ss}^2) = -\frac{Y_{ss}}{F^2} + \frac{2u_0}{Rb}(X_s Z_{ss} - Z_s X_{ss}) + \frac{1}{Rb^2}((X+1)X_{ss} + ZZ_{ss}), \tag{7.41}$$

and the arc-length condition $X_s^2 + Y_s^2 + Z_s^2 = 1$ for the five unknowns, X, Y, Z, u_0 and R_0. The conditions at the orifice are the same as in section 7.2, namely $X = Y = Y_s = Z = Z_s = 0$, $X_s = 1$, $u_0 = R_0 = 1$ on $s = 0$.

For the initial conditions we use the solutions to the steady-state equations in the inviscid case, namely equations (7.26), (7.28), (7.31) and (7.32) along with the arc-length condition. We could find the steady-state equations for the viscous case but Decent *et al.* [12] showed that unless Reynolds number was very small (or the Ohnesorge number was much greater than 1) the contribution from viscosity vanishes to the leading order terms in the trajectory. In all our experiments the Reynolds number has been high enough to use the solutions to the inviscid steady-state as the initial conditions. The solutions to the steady-state equations for the inviscid and viscous cases were compared numerically and found to be indistinguishable.

Only equations (7.38) and (7.39) need to be solved to find $u_0(s,t)$ and $R_0(s,t)$. We neglect equations (7.40), (7.41) and the arc-length condition since we are assuming a steady centreline therefore X, Y and Z are functions of s only. Again, this approach has been used in chapters 5 and 6, and will be verified in chapter 9.

The non-linear system to be solved is

$$R_{0t} + u_0 R_{0s} + \frac{u_{0s} R_0}{2} = 0 \tag{7.42}$$

and

$$u_{0t} + u_0 u_{0s} = -\kappa_s - \frac{Y_s}{F^2} + \frac{(X+1)X_s + ZZ_s}{Rb^2} + \frac{3(R_0^2 u_{0s})_s}{ReR_0^2}. \tag{7.43}$$

We replace the leading order curvature with the full curvature κ given in section 7.2.1 otherwise the jet is unstable to infinitesimally short wave modes. This system is solved using a finite difference method where the spatial grid is fixed and uniform and the time integration is based on the Lax-Wendroff method described in section 5.3.

We denote $A = R_0^2$ so equations (7.42) and (7.43) become

$$A_t + (Au_0)_s = 0 \tag{7.44}$$

and

$$u_{0t} + \left(\frac{u_0^2}{2}\right)_s = -\frac{1}{We}\frac{\partial}{\partial s}\left(\frac{4(2A + (\epsilon A_s)^2 - \epsilon^2 A A_{ss})}{(4A + (\epsilon A_s)^2)^{3/2}}\right) + \frac{(X+1)X_s + ZZ_s}{Rb^2} - \frac{Y_s}{F^2} + \frac{3(R_0^2 u_{0s})_s}{ReR_0^2}. \tag{7.45}$$

We solve equations (7.44) and (7.45) in the same way as in section 5.3. The initial conditions are given by the solutions of the steady-state equations described above. We impose the same periodic boundary conditions at the orifice, namely

$$A(0,t) = 1,\ u(0,t) = 1 + \delta \sin\left(\kappa \frac{t}{\epsilon}\right).$$

The most unstable wavenumber is given by equation (7.35). This is discussed in the previous section.

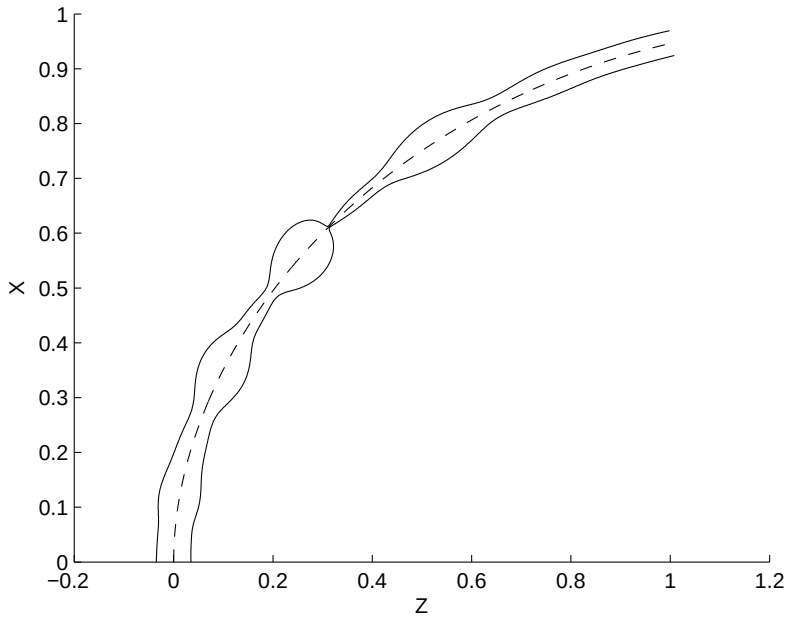

Figure 7.2: A simulation of a jet on the laboratory scale in the X-Z plane using the theory which includes gravity; $\delta = 0.1$, $F = 1.61$, $We = 28.88$, $Rb = 1.17$ and $Re = 140.2$.

7.4 Results

Figures 7.2 and 7.3 are simulations of a jet in the X-Z and X-Y planes respectively, carried out using the theory described above, including gravity. The parameters of the jet are $We = 28.88$, $Rb = 1.17$, $Re = 140.2$, $F = 1.61$ and $\delta = 0.1$ which are found within the laboratory scale regime. Figure 7.3 shows that the vertical drop of the jet in the Y-direction is small compared to the break-up length in this case. This suggests that gravity has little effect on this jet.

Figure 7.4 is a simulation of the same jet in figures 7.2 and 7.3 carried using the theory described in chapter 6, which includes viscosity but neglects gravity. Comparing figures 7.2 with figure 7.4 we can see that the simulations are qualitatively similar showing the same break-up mode; mode 2. The break-up lengths are also similar. Quantitative analysis of the effect of gravity on the break-up length is given in section 7.4.2.

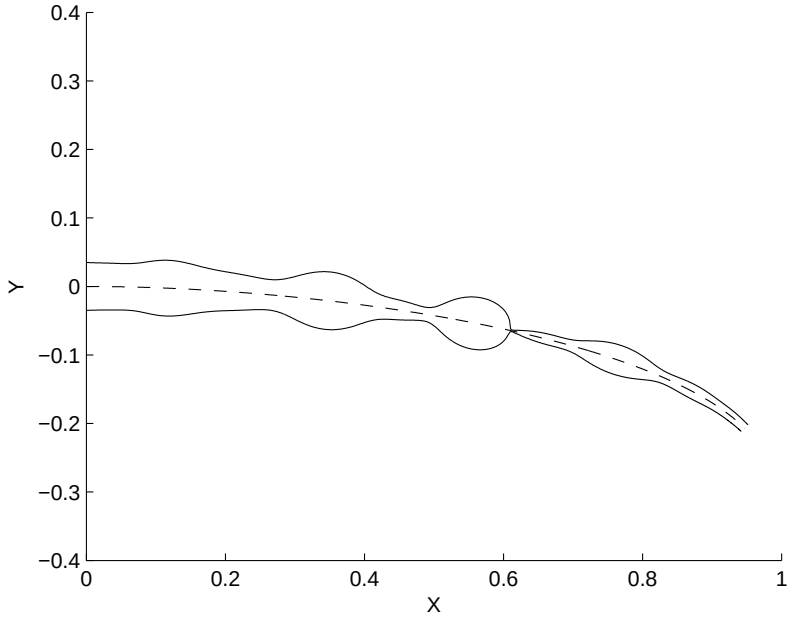

Figure 7.3: A simulation of a jet on the laboratory scale in the X-Y plane using the theory which includes gravity; $\delta = 0.1$, $F = 1.61$, $We = 28.88$, $Rb = 1.17$ and $Re = 140.2$.

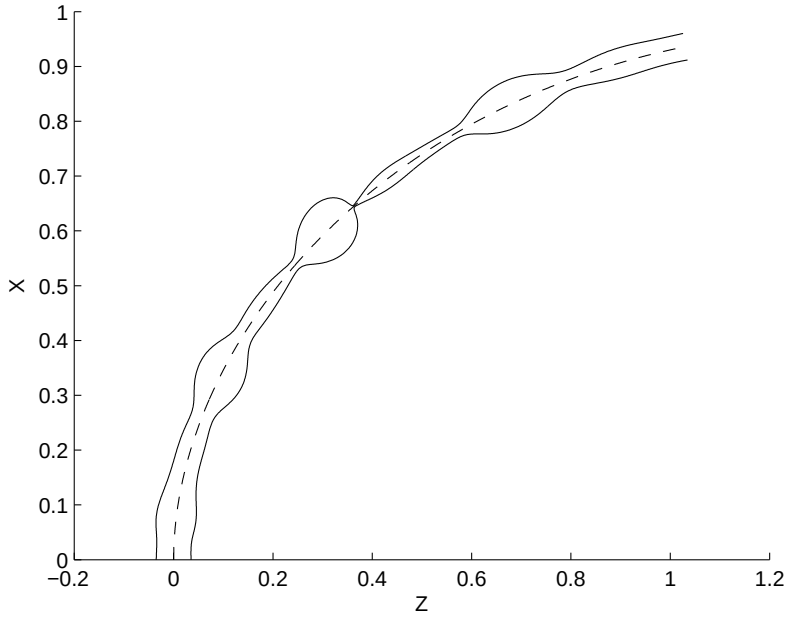

Figure 7.4: A simulation of a jet on the laboratory scale using the viscous theory from chapter 6; $\delta = 0.1$, $We = 28.88$, $Rb = 1.17$ and $Re = 140.2$.

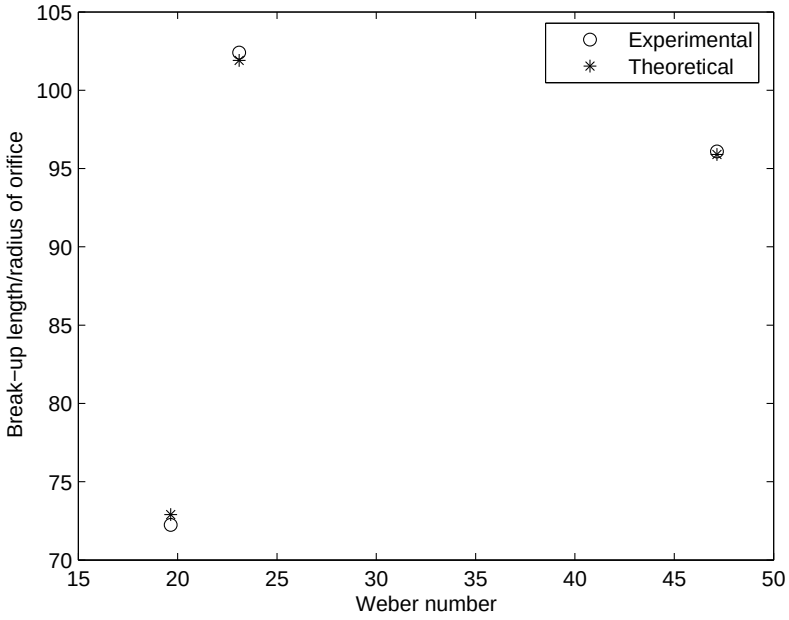

Figure 7.5: A plot comparing experimental and theoretical break-up lengths for $We = 19.65,\ 23.1$ and 47.15. The circles correspond to experimental break-up lengths. The stars correspond to break-up lengths obtained from using the theory described here including gravity and viscosity. It is these results that a fit for δ is obtained.

7.4.1 Comparison of theory and experiment

In this section we compare experimental and theoretical results in the same way as in section 6.2, but the theoretical results are obtained using the theory described above with the model incorporating both gravity and viscosity. Figure 7.5 is a plot which compares theoretical and experimental break-up lengths. The break-up lengths are plotted against Weber number for $We = 19.65$, $We = 23.1$ and $We = 47.15$ (with the other parameters varying as appropriate). As in section 6.2, δ is varied until the theoretical break-up length agrees with the break-up length obtained experimentally. The values of δ obtained to achieve this fit are 0.026, 0.009 and 0.0236 respectively. We are able to obtain good agreement between experimental and theoretical results here by fixing δ, as in chapter 6.

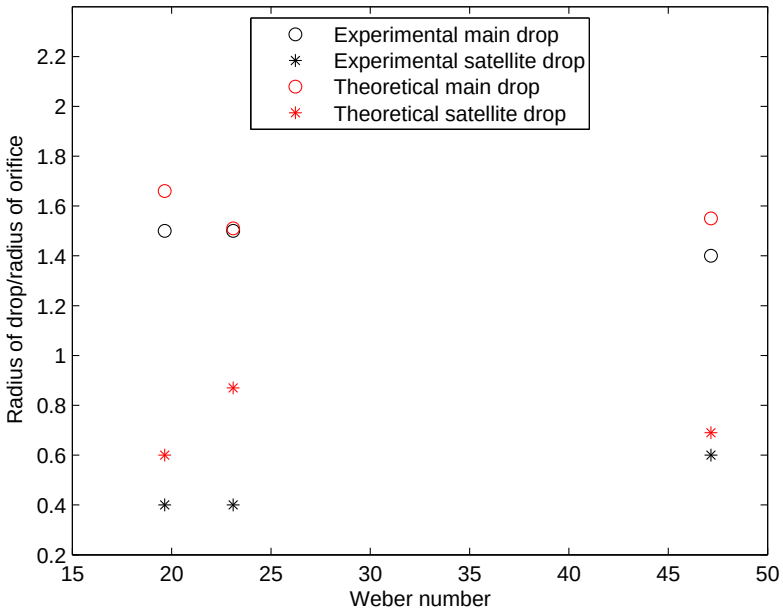

Figure 7.6: A plot comparing experimental and theoretical drop sizes for $We = 19.65,\ 23.1$ and 47.15. The black circles correspond to experimental main drop sizes and the red circles correspond to main drop sizes obtained from using the non-linear viscous gravity theory. The black stars correspond to satellite drop sizes obtained experimentally and the red stars correspond to satellite drop sizes obtained from the theory.

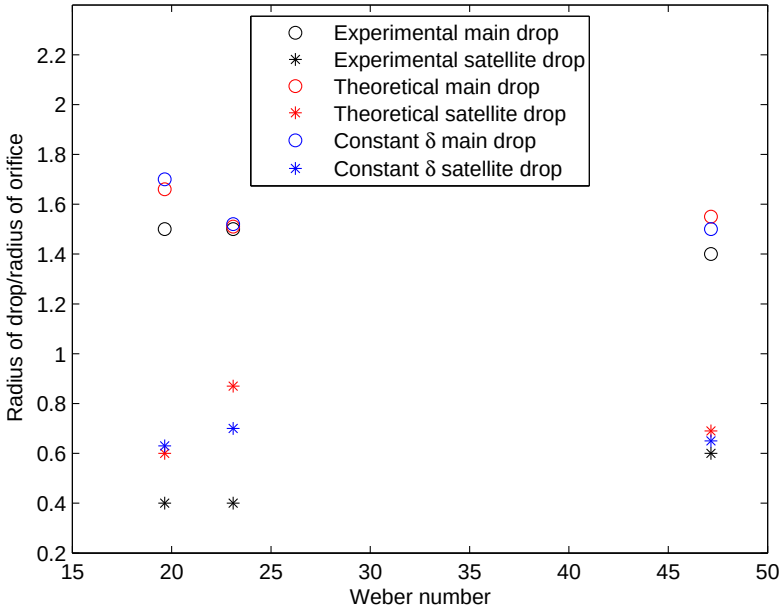

Figure 7.7: A plot comparing results in figure 7.6 with drop sizes obtained using $\delta = 0.01953$

Figure 7.6 compares theoretical and experimental drop sizes for main and satellite drops. The drop sizes are plotted against Weber number. Theoretical drop sizes are obtained using the same parameter values as in figure 7.5. We can see that for all Weber numbers there is fairly good agreement between experimentally and theoretically obtained main drop sizes. The difference between theoretically and experimentally obtained main drop sizes ranges from 0 to 0.2 in non-dimensional units. There is also reasonable agreement between theoretically and experimentally obtained satellite drop sizes. The difference between theoretically and experimentally obtained satellite drop sizes ranges from 0.1 to 0.5 in non-dimensional units.

As in chapter 6 we take the average value of δ, which in this case is 0.01953 and use the theory to obtain theoretical main and satellite drop sizes with the parameters used in figure 7.6. (Note that we get a different value for δ here primarily because we have used different values of Weber number in figures 6.5 and 7.5.) Figure 7.7 shows drop sizes obtained using the constant average value of δ along with the results presented in figure

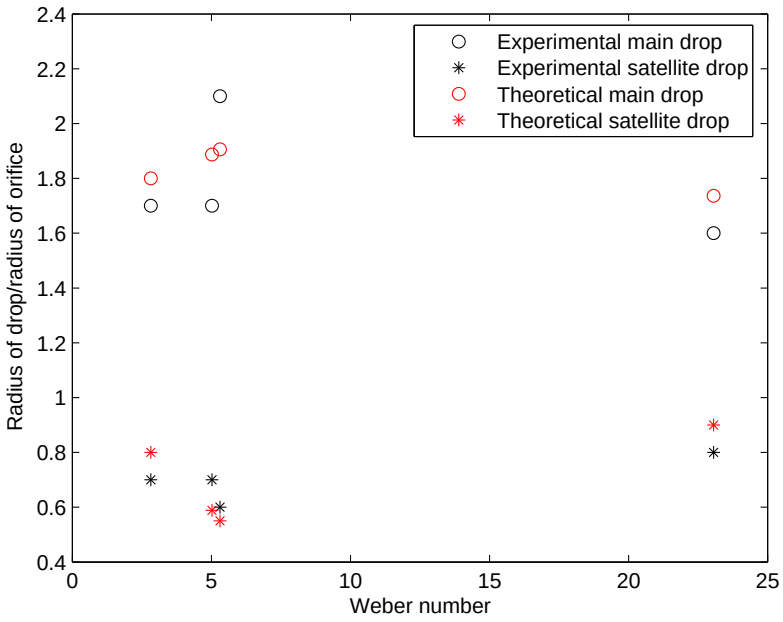

Figure 7.8: A plot comparing theoretically and experimentally obtained main and satellite drop sizes using the constant average value of $\delta = 0.01953$ for $We = 2.82,\ 5.02,\ 5.31$ and 23.06.

7.6. We can see that the drop sizes obtained using $\delta = 0.01953$ are similar to the drop sizes obtained using the values of δ required to match the theoretical and experimental break-up lengths. This is comparable to the result obtained in chapter 6 where viscosity was included and gravity was neglected. Therefore we can choose a typical value of δ and obtain a fairly accurate value for the drop sizes, provided δ is the correct order of magnitude.

Figure 7.8 compares theoretical and experimental drop sizes for main and satellite drops for $We = 2.82,\ 5.02,\ 5.31$ and 23.1. These parameter values were all obtained on the pilot scale (again the other parameter values were varied with each Weber number because of interdependence of the parameters in experiments). The theoretical drop sizes were obtained using the constant average value of δ, $\delta = 0.01953$. The agreement between the theoretical and experimental drop sizes is reasonably good. The difference between the experimental and theoretical drop sizes varies from 0 to 0.3 in non-dimensional units.

This is similar to the result obtained in chapter 6.

These results show that even though break-up length is highly dependent upon δ, which is usually unknown in experiments, fairly good agreement between theoretical and experimental drops sizes can be found if a typical rather than fitted value for δ is used in the theory.

We have shown that reasonable agreement between the experimental and the theoretical results can be achieved. In the next section trends that the theory predicts will be examined. This enables us to determine how varying parameters affects drop sizes and break-up lengths. This cannot be easily ascertained from experiments because of interdependence of the parameters as already discussed. Theoretical results will be qualitatively compared to experimental results where possible but this will not be the aim of section 7.4.2 because the numerics are not always in the same parameter regimes as experiments and because of the interdependence of the experimental parameters. Also we can examine the effect that Weber number, Rossby number and Froude number have on the trajectory of the jet.

7.4.2 Parametric study

In this section we extend the parametric study carried out in sections 5.4.1 and 6.2.3 by including gravity. We now include another parameter, Froude number F.

Figure 7.9 compares the break-up lengths of jets with different Rossby numbers ($Rb = 0.8,\ 1,\ 2,\ 3$ and 5) and constant Weber, Reynolds, Froude number and δ, ($We = 50,\ Re = 3000,\ F = 1$ and $\delta = 0.01$). Throughout this section κ is chosen to satisfy equation (7.35). Break-up length increases substantially with decreasing Rossby number. The break-up length varies from 110 to 65 in non-dimensional units. This is similar to the results obtained previously in figure 6.11 when viscosity was included but gravity was neglected. However the variation in break-up length here is not as large as in figure 6.11. Experimental work presented in figure 4.15 showed there is generally a decrease in break-up length with increasing Rossby number within each Ohnesorge number which

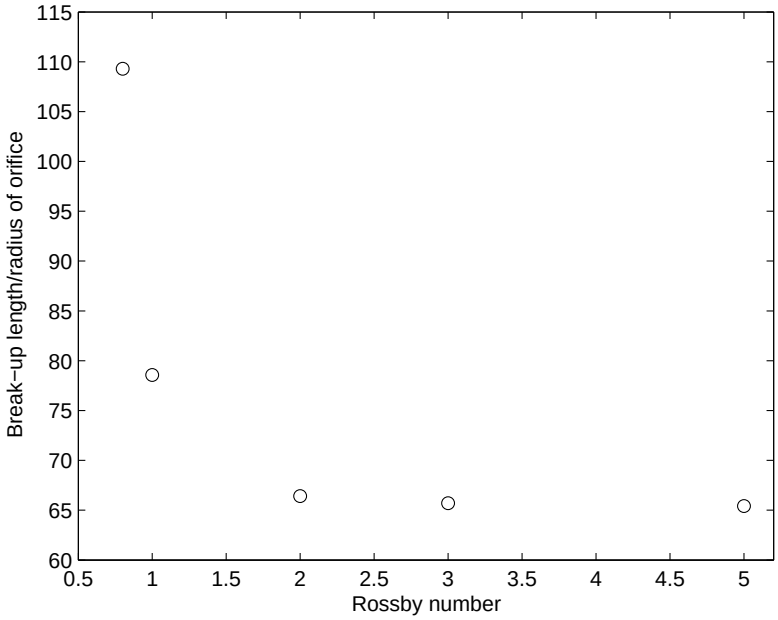

Figure 7.9: A plot of Rossby number against break-up length, $Rb = 0.8,\ 1,\ 2,\ 3$ and 5. $We = 50$, $F = 1$, $Re = 3000$ and $\delta = 0.01$.

agrees with the theoretical result to some extent, qualitatively at least. Results presented in figure 5.5 for the inviscid case found that break-up length did not change much with Rossby number. However in the theory presented here (as in the viscous theory) a different scaling is used which introduces more rotation terms into the problem. This makes Rossby number a more dominant parameter.

Figure 7.10 compares main and satellite drop sizes with Rossby number. We can see as Rossby number increases, the size of the satellite drop decreases by 0.3 in non-dimensional units and the size of the main drop increases by 0.1 in non-dimensional units. This is similar to the result obtained in figure 6.12 obtained using the viscous theory but neglecting gravity. However here we have less variation in main and satellite drop size. From experimental results presented in figure 4.11 we could not find a conclusive trend between Rossby number and drop size. Experimentally we cannot easily vary Rossby number while keeping the other parameters constant. In figure 4.11 the Weber number varies from 10 to 70, the Reynolds number varies from 430 to 3000 and the Froude number

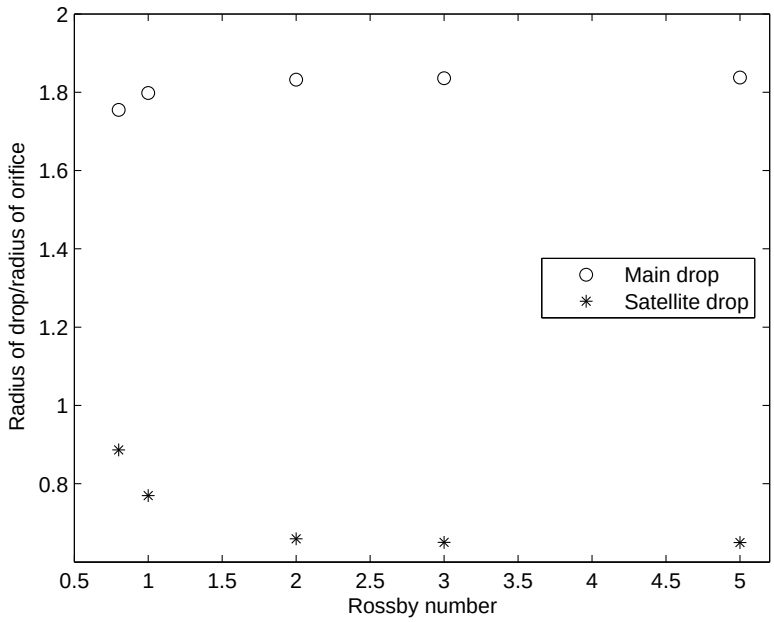

Figure 7.10: A plot of Rossby number against drop size, $Rb = 0.8,\ 1,\ 2,\ 3$ and 5. $We = 50$, $F = 1$, $Re = 3000$ and $\delta = 0.01$.

varies from 0.5 to 1.4. The advantage of the results presented in figure 7.10 is that we can see how drop sizes vary with Rossby number for fixed Weber number, Reynolds number and Froude number.

Figure 7.11 shows the trajectories of four jets with ($Rb = 0.8,\ 1,\ 2$ and 5) in the X-Y plane. Weber number, Reynolds number and Froude number are all fixed ($We = 50$, $Re = 3000$ and $F = 1$). At lower Rossby number the effects of rotation are greater. When the jet is near the orifice the rotational forces overcome the gravity forces. Further away the orifice influence of rotation is less and gravity forces become more dominant pulling the jet downwards.

Figure 7.12 shows the trajectories of the same four jets presented in figure 7.11 in the X-Y-Z space. We can see that at low Rossby number the jet coils more tightly. This agrees with the results presented in figure 5.6 where the trajectories are plotted neglecting gravity. Also we can see the trajectory falls less sharply in the X-Y plane at high Rossby number.

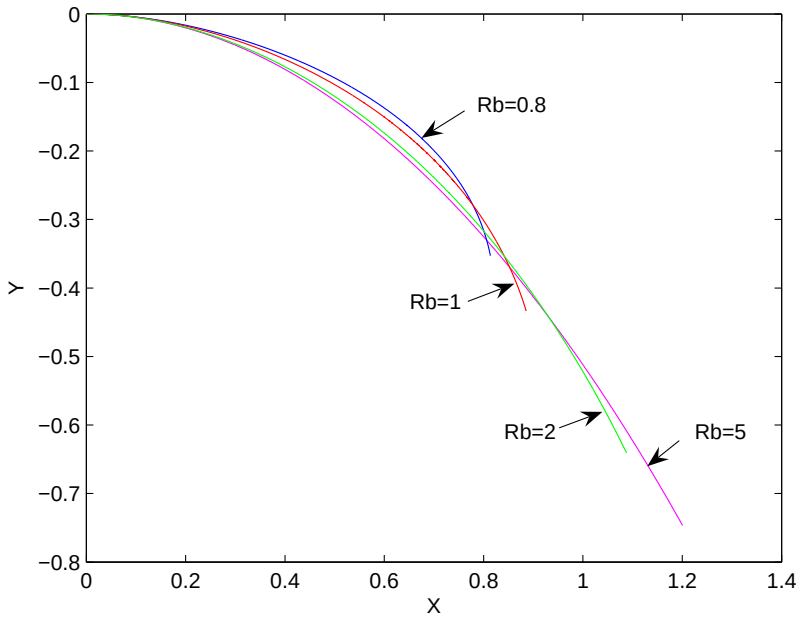

Figure 7.11: The trajectories of four jets in the X-Y plane with different Rossby numbers, $Rb = 0.8,\ 1,\ 2$ and 5, but with constant Weber, Reynolds and Froude numbers.

Figure 7.13 compares the break-up lengths of jets with different Weber numbers ($We = 20,\ 40,\ 50,\ 70$ and 100) but with constant Rossby, Froude and Reynolds numbers ($Rb = 1$, $F = 1$ and $Re = 3000$). Also the value of δ remains constant, $\delta = 0.01$. The break-up length of the jet increases substantially with increasing Weber number. The break-up length varies from 50 to 130 in non-dimensional units. This is similar to results presented in figures 5.3 where viscosity and gravity were neglected and 6.9 where gravity was neglected. The variation in break-up length is greater here than in figure 5.3 but less than in figure 6.9. Experimental results presented in figure 4.14 shows there is an increase in break-up length with increasing Weber number however the trend is weaker than in figure 7.13. Experimentally we cannot hold Weber constant while keeping the other parameters fixed so this difference might be due to the effects of other parameters.

Figure 7.14 shows that increasing Weber number causes the size of the main drop to decrease slightly, by less then 0.1 in non-dimensional units and the size of the satellite drop to increase, by 0.2 in non-dimensional units. This is similar to results obtained in

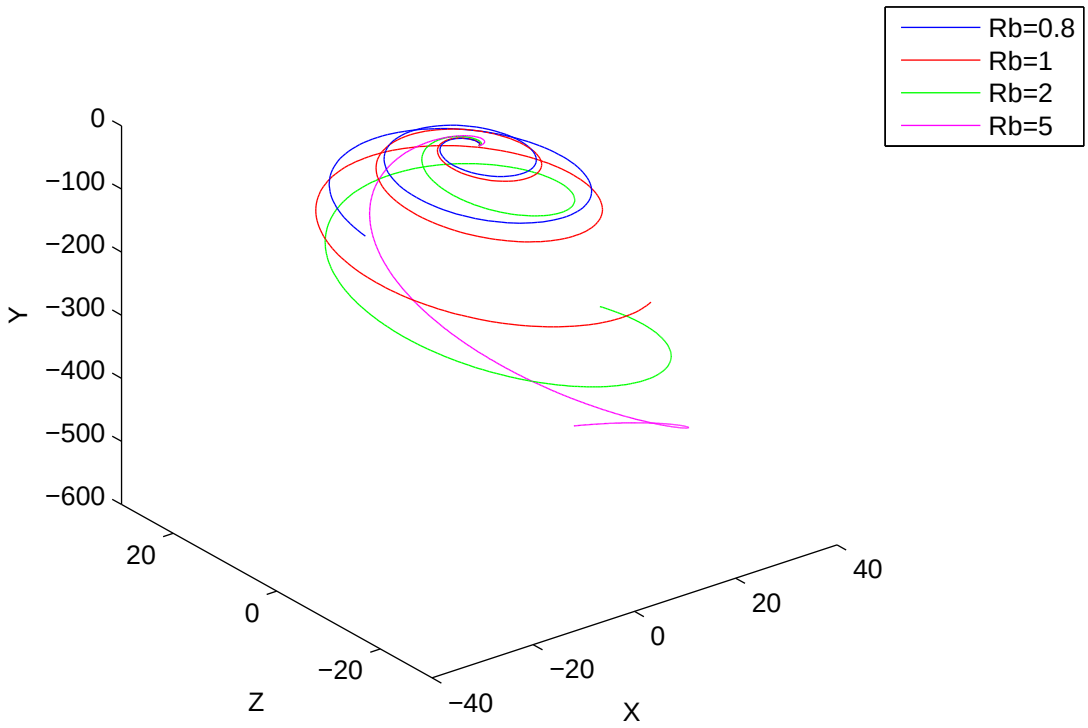

Figure 7.12: The trajectories of four jets in the X-Y-Z plane with different Rossby numbers, $Rb = 0.8,\ 1,\ 2$ and 5, but with constant Weber, Reynolds and Froude numbers.

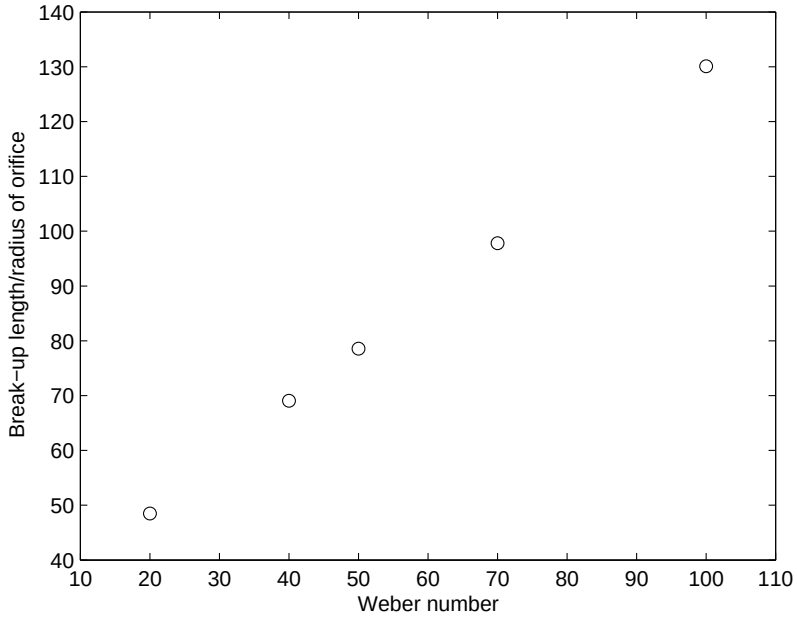

Figure 7.13: A plot of Weber number against break-up length for We = 20, 40, 50, 70 and 100. $Rb = 1$, $F = 1$, $Re = 3000$ and $\delta = 0.01$.

figure 6.10 where viscosity was included but gravity was neglected. However the variation in drop size here is less than in figure 6.10. It is difficult to compare figure 4.10 with figure 7.14. The information that can be gained from figure 4.10 is limited since within each Ohnesorge number, Weber number is varied by changing the rotation rate Ω, therefore Rossby number, Reynolds number and Froude number vary too. In figure 4.10 the Rossby number changes from 0.5 to 1, the Reynolds number changes from 430 to 3000 and the Froude number changes from 0.5 to 1.4. So figure 7.14 shows how drop sizes vary with Weber number for fixed rotation rate which is difficult to do experimentally.

Figure 7.15 shows the trajectories of three jets with Weber numbers We=20, 50 and 100 in the X-Y plane. We can see that decreasing Weber number causes the jet to become more curved. Decreasing Weber number corresponds to decreasing inertia. Therefore gravity is able to have more influence on the jet. Figure 7.16 shows the same trajectories as in figure 7.15 in the X-Y-Z space. We can see that the jets with lower Weber number coil more tightly than jets with higher Weber number. This agrees with

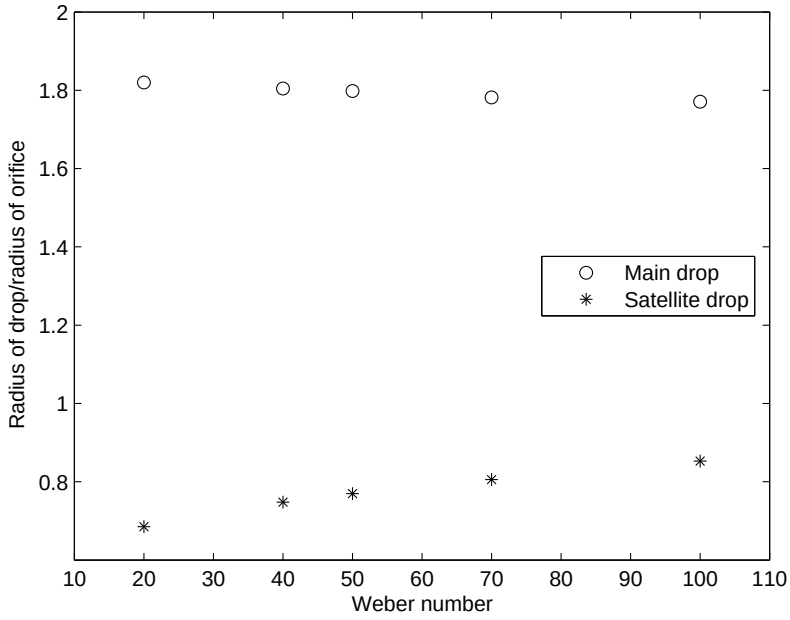

Figure 7.14: A plot of Weber number against main and satellite drop size for We = 20, 40, 50, 70 and 100. $Rb = 1$, $Re = 3000$ $F = 1$ and $\delta = 0.01$.

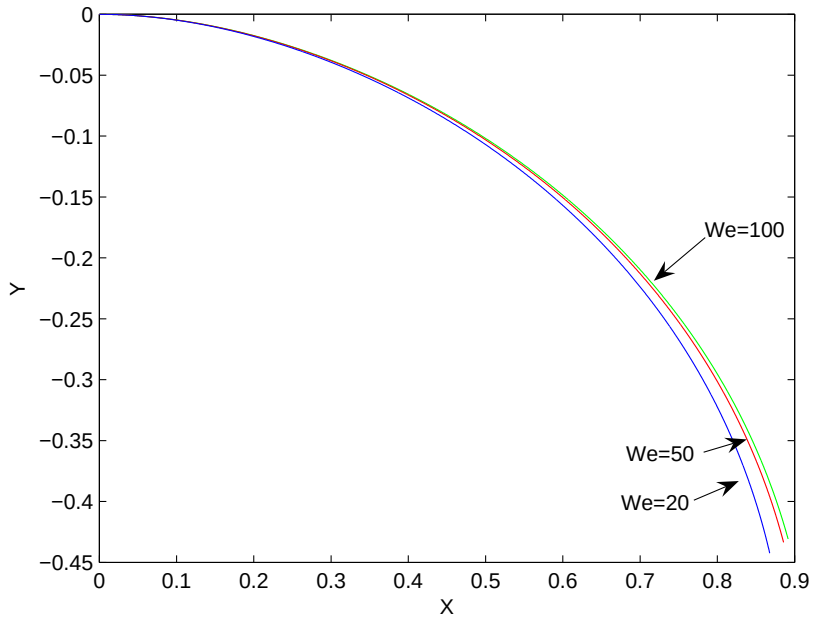

Figure 7.15: The trajectories of three jets with different Weber numbers (We = 20, 50 and 100) in the X-Y plane.

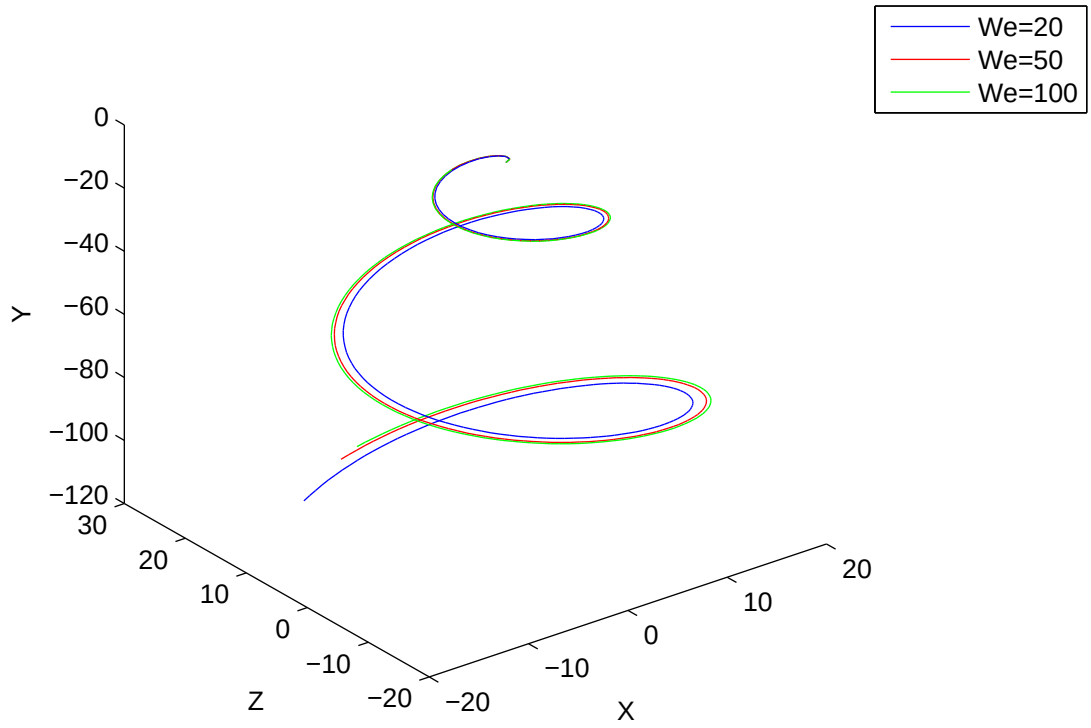

Figure 7.16: The trajectories of three jets with different Weber numbers (We = 20, 50 and 100) in the X-Y-Z space.

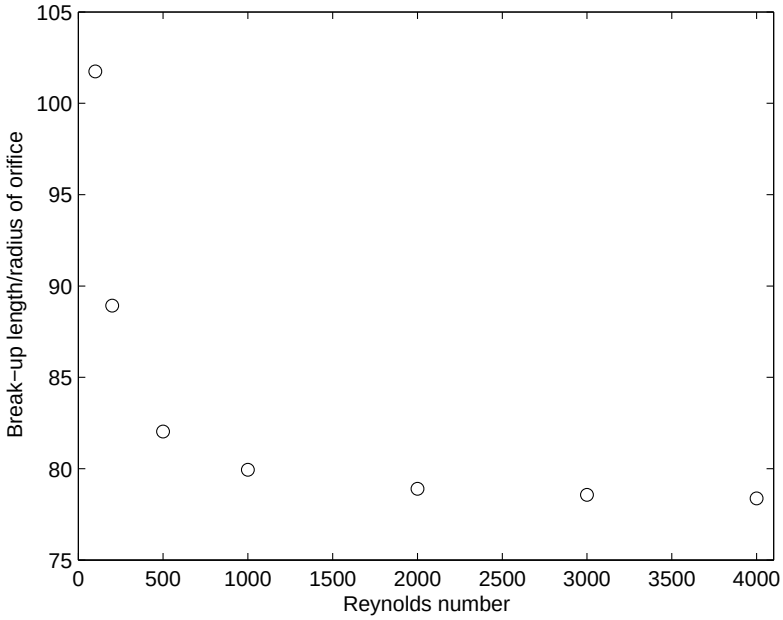

Figure 7.17: A plot of Reynolds number against break-up length. $We = 50$, $Rb = 1$, $F = 1$ and $\delta = 0.01$. $Re = 4000,\ 3000,\ 2000,\ 1000,\ 500,\ 200$ and 100.

results presented in figure 5.4 where the trajectories are plotted in the X-Z plane.

Figure 7.17 compares the break-up lengths of jets with different Reynolds number ($Re = 4000,\ 3000,\ 2000,\ 1000,\ 500,\ 200$ and 100) but with Weber number ($We = 50$), Rossby number ($Rb = 1$), Froude number ($F = 1$) and δ constant ($\delta = 0.01$). Decreasing Reynolds number causes the break-up length to increase considerably. The break-up length varies from 78 to 102 in non-dimensional units. This variation is similar to the variation obtained in figure 6.13 where viscosity is included but gravity is neglected. Experimental results presented in figures 4.14, 4.15, 4.16 and 4.17 showed that the break-up length was longer for higher Ohnesorge number. Larger Ohnesorge number corresponds to higher viscosity jets therefore the experimental results agree qualitatively with the result in figure 7.17.

Figure 7.18 shows Reynolds number against main and satellite drop size for Re=100, 1000, 2000, 3000 and 4000. Weber number, Froude number, Rossby number and δ are all constant ($We = 50$, $F = 1$, $Rb = 1$ and $\delta = 0.01$). Reynolds number has a negligible effect

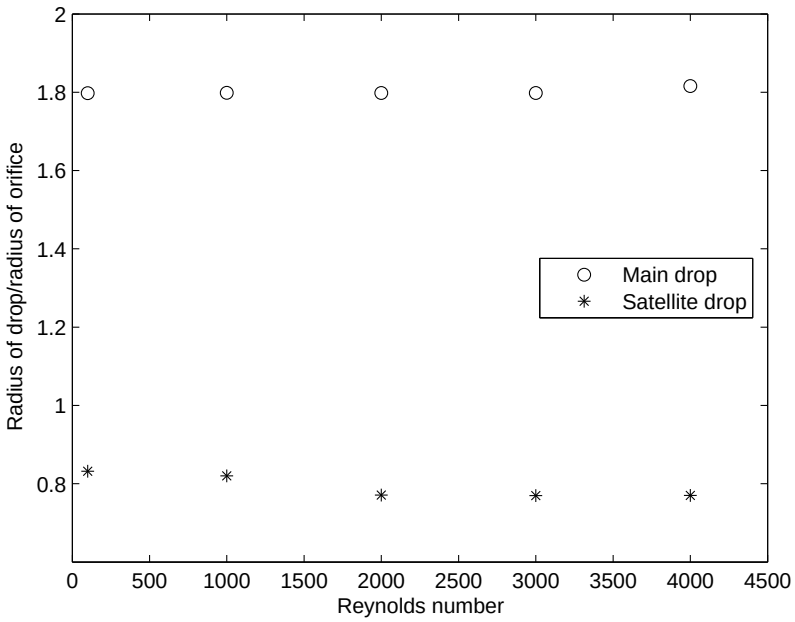

Figure 7.18: A plot of Reynolds number against drop size. $We = 50$, $Rb = 1$, $F = 1$ and $\delta = 0.01$. $Re = 4000,\ 3000,\ 2000,\ 1000$ and 100.

on the drop size, the difference in main drop size is less than 0.1 in non-dimensional units and the difference in satellite drop size is also less than 0.1 in non-dimensional units. This is similar to the results obtained in figure 6.14 where viscosity was included but gravity was neglected. In figure 4.12 there is no relation between Reynolds number and drop size. This is probably due to the influence of other parameters since experimentally we cannot vary Reynolds number and kept the other parameters fixed. In figure 4.12 the Weber number varies from 10 to 70, the Rossby number from 0.5 to 1 and the Froude number varies from 0.5 to 1.4.

Reynolds number has no effect on the trajectory of the jet. The reason for this is that viscosity does not appear in the leading order equations describing the trajectory, as discussed in section 6.2.3.

Figure 7.19 shows the break-up lengths of jets with different values of δ, (δ=0.01, 0.015, 0.02, 0.025, 0.03, 0.035 and 0.04) but the same Rossby, Weber, Froude and Reynolds number ($Rb = 1$, $We = 50$, $F = 1$ and $Re = 3000$). The break-up length

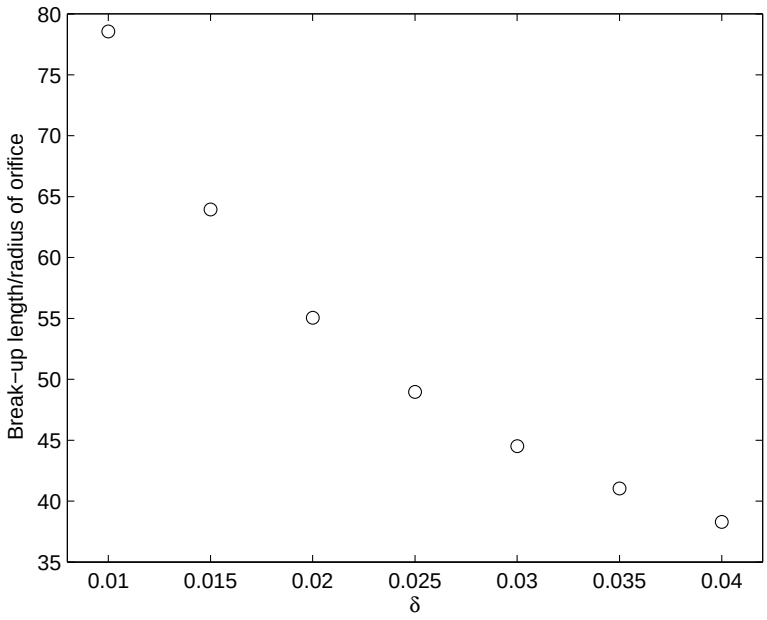

Figure 7.19: A plot of δ against break-up length. $We = 50$, $Rb = 1$, $Re = 3000$ and $F = 1$. $\delta = 0.01,\ 0.015,\ 0.02,\ 0.025,\ 0.03,\ 0.035$ and 0.04.

increases considerably with decreasing δ. The break-up length varies from 38 to 79 in non-dimensional units. This is to be expected and agrees with previous work presented in figures 5.7 where viscosity and gravity were neglected and 6.15 where gravity was neglected. However the variation in break-up length here is greater than in figure 5.7 but less than in figure 6.15.

Figure 7.20 shows main and satellite drop sizes against δ for δ=0.01, 0.015, 0.02, 0.025, 0.03, 0.035 and 0.04. The effect of δ on the drop size is negligible. For both main and satellite drops the difference in sizes is less than 0.1 in non-dimensional units. This agrees with work presented in figure 6.16 where viscosity was included but gravity was neglected. The comparison of these results with experimental data is difficult because we cannot measure δ.

Figure 7.21 compares the break-up length for jets with different Froude numbers ($F = 1$, 1.2, 1.5, 1.7 and 2), the same Weber ($We = 50$), Rossby ($Rb = 1$) and Reynolds number ($Re = 3000$) and the same value for δ ($\delta = 0.01$). Increasing the Froude number

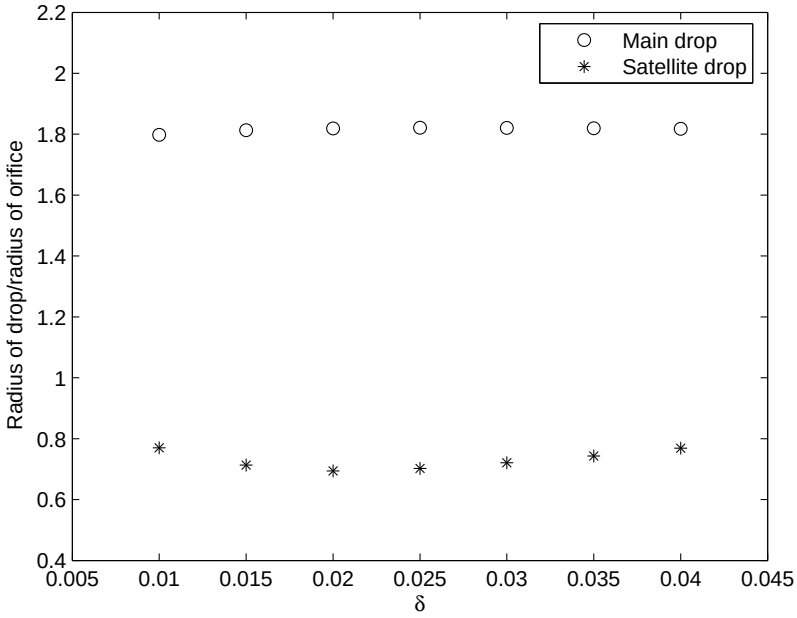

Figure 7.20: A plot δ against drop size. $\delta = 0.01,\ 0.015,\ 0.02,\ 0.025,\ 0.03,\ 0.035$ and 0.04 $We = 50$, $Rb = 1$, $Re = 3000$ and $F = 1$.

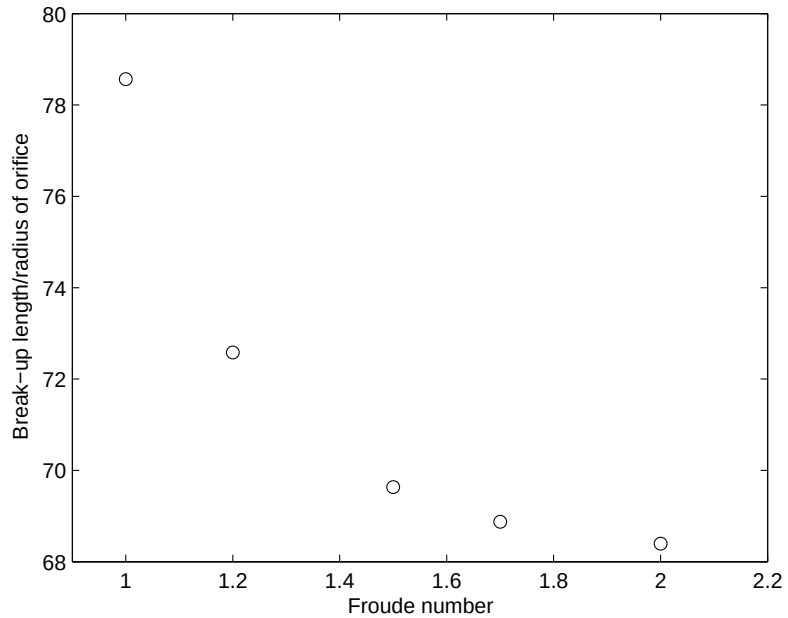

Figure 7.21: A plot of Froude number against break-up length. $F = 1,\ 1.2,\ 1.5,\ 1.7$ and 2. $We = 50$, $Rb = 1$, $Re = 3000$ and $\delta = 0.01$.

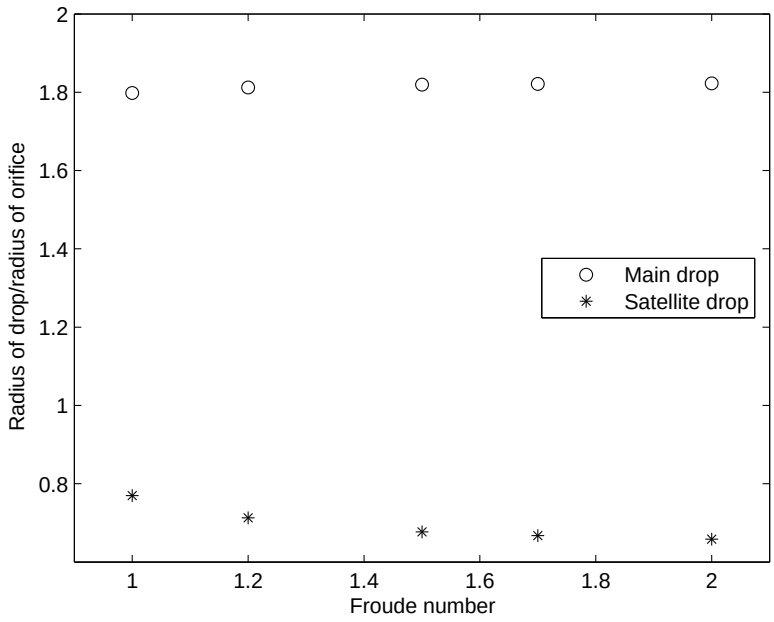

Figure 7.22: A plot showing Froude number against drop size for main and satellite drops. $F = 1,\ 1.2,\ 1.5,\ 1.7$ and 2. $We = 50$, $Rb = 1$, $Re = 3000$ and $\delta = 0.01$.

decreases the break-up length. This is a surprising result since experimental results presented in figure 4.17 seem to suggest that break-up length increases with increasing Froude number. However the theoretical result can be explained using spatial stability. Pages 278 and 279 of Decent *et al.* [13] show that decreasing the Froude number decreases the growth rate of the mode growing along the jet, therefore increasing the break-up length, so that figure 7.21 agrees with results of [13]. The results in this section show that the variation in break-up length with Froude number is less than the variation with Weber number, Rossby number, Reynolds number and δ. The discrepancy with the experimental results maybe due to other parameters having a stronger influence, since experimentally we cannot vary Froude number while holding the other parameters constant.

From figure 7.22 the effect of Froude number on main drop size was negligible. The difference in main drop size is less than 0.1 in non-dimensional units. There is a slight decrease in satellite drop size with increasing Froude number. However the difference in

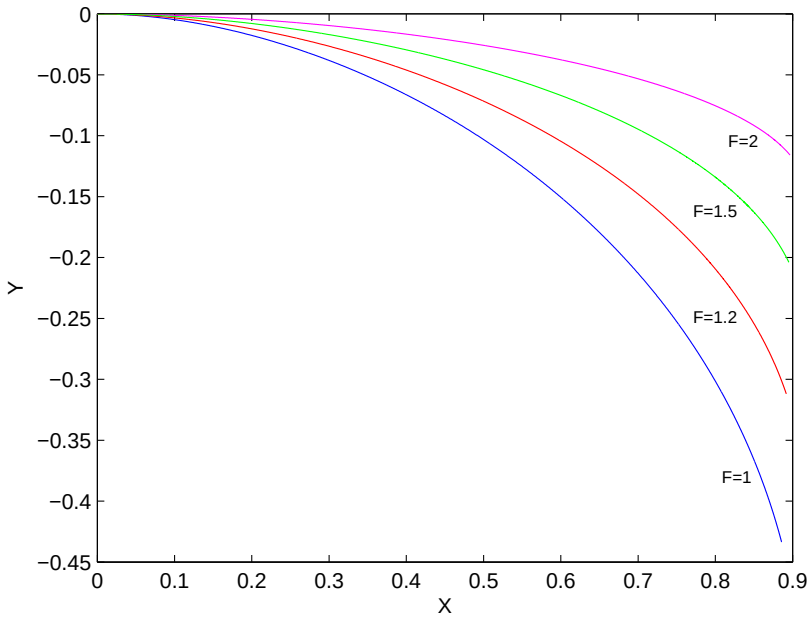

Figure 7.23: The trajectories of four jets with different Froude numbers (F = 1, 1.2, 1.5 and 2) and the same Weber and Rossby.

satellite drop size is less than 0.1 in non-dimensional units. We could not ascertain a conclusive trend between Froude and drop size experimentally but this is probably due to other parameters having more influence. In figure 4.13, Weber number varies from 10 to 70, Rossby number varies from 0.5 to 1 and Reynolds number varies from 430 to 3000.

Froude number had no effect on the trajectory in the X-Z plane. However from figure 7.23 we can see that decreasing the Froude number causes the jet to curve more in the X-Y plane. During experiments carried out by Partridge *et al.* [31] and Wong *et al.* [44] the jet was observed to fall out of the X-Z plane earlier for lower rotation rates. This is due to gravity having a greater effect at low Froude number, pulling the jet downwards. Figure 7.24 shows the trajectories of four jets in the X-Y-Z space. We can see that Froude number does not affect the jet in the X-Z plane, and the is jet falling out of the horizontal plane more for lower Froude number.

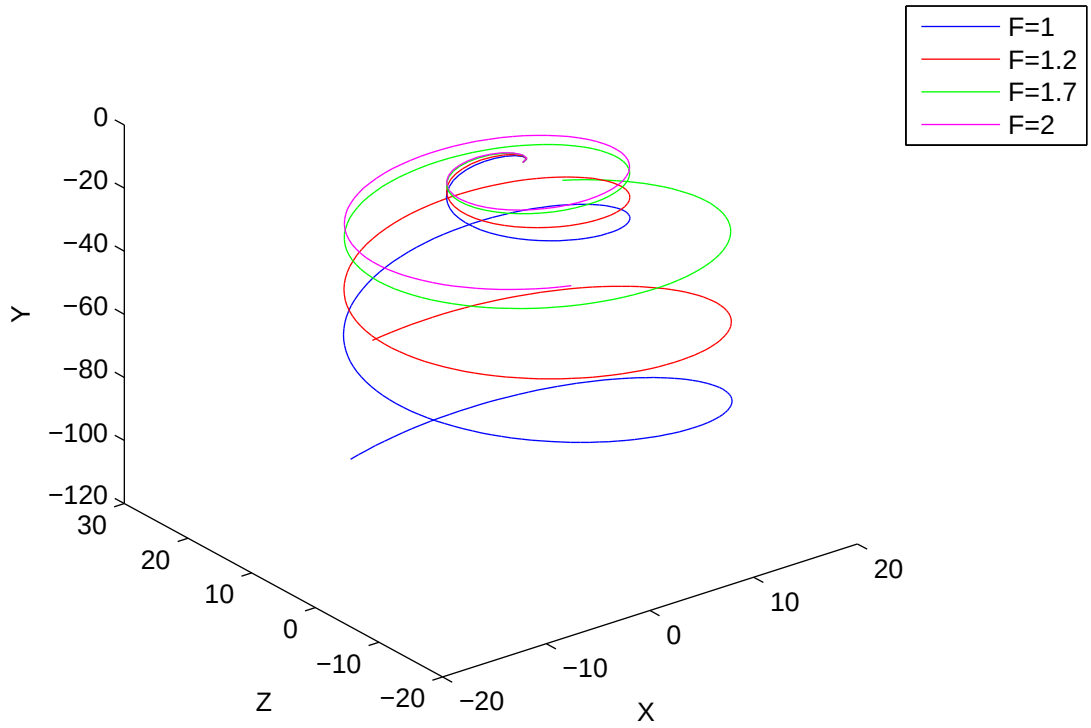

Figure 7.24: The trajectories of four jets with different Froude numbers (F = 1, 1.2, 1.7 and 2) and the same Weber and Rossby.

7.5 Comparison of drop sizes obtained using the viscous theory and the theory including gravity and viscosity

Table 7.1 compares normalised drop sizes obtained experimentally and theoretically, using the viscous theory and the theory including gravity and viscosity. Comparing the main drop sizes we can see that both theories give reasonable agreement with the experimental result with the difference in drop size varying from 0 to 0.3 in non-dimensional units.

The difference between theoretically and experimentally obtained satellite drops varies from 0 to 0.4 in non-dimensional units. Therefore there is reasonable agreement between theory and experiment and again both theories give similar agreement with experiment. (The drop sizes obtained using the viscous theory $\delta = 0.01268$ and the drop sizes obtained using the gravity theory $\delta = 0.01968$.)

Table 7.1: Table comparing main and satellite drop sizes obtained from pilot scale experiments, viscous theory and the theory including viscosity and gravity

We	Rb	Re	Experimental main drop	Experimental satellite drop	Viscous theory main drop	Viscous theory satellite drop	Gravity theory main drop	Gravity theory satellite drop
5.31	1.82	120.5	2.1	0.6	1.8	0.5	1.9	0.6
5.02	0.88	117.1	1.7	0.7	1.9	0.7	1.9	0.6
2.82	0.44	87.9	1.7	0.7	1.8	0.8	1.8	0.8
47.15	0.56	2251	1.4	0.6	1.5	0.7	1.5	0.7
23.06	0.546	435.1	1.6	0.8	1.7	0.8	1.7	0.9
23.1	0.588	1575	1.5	0.4	1.5	0.8	1.5	0.7
19.65	0.504	401.6	1.5	0.4	1.6	0.6	1.7	0.6

7.6 Comparison of inviscid, viscous and gravity theories

In this section we give a comparison of the three theories discussed in chapters 5, 6 and 7. In chapter 5 the non-linear inviscid theory is described. Viscosity and gravity are neglected. We found that the simulations gave mode 2 break-up and agreed qualitatively with experimental results. However we were unable to obtain drop sizes or match the break-up lengths obtained from the theory with the break-up lengths obtained experimentally because of the scaling used.

In chapter 6 a non-linear theory which includes viscosity but neglects gravity is described. The scaling used for this theory is different from the scaling used in the inviscid theory. This scaling meant that rotation entered the problem in the equations of motion and in the initial conditions rather than just the initial conditions as in the inviscid theory. The simulations can produce mode 3 break-up for low Rossby number even when $Re = \infty$ which corresponds to an inviscid liquid. Break-up lengths can be obtained which are in excellent agreement with experimental break-up lengths. Main and satellite drop sizes can be obtained that are in reasonably good agreement with experimentally obtained drop sizes. This shows that including viscosity in the problem gives more and better information. Also including viscosity is not difficult and does not require any extra computational effort.

Chapter 7 describes a theory which includes gravity and viscosity. The results from this theory are similar to the results from the viscous theory. Break-up lengths which are in very good agreement with experimental break-up lengths can be obtained. Drop sizes which are in reasonable agreement with experimental drop sizes can also be obtained. The only extra piece of information which can be obtained from the gravity theory is how far the jet falls in the vertical direction. Including gravity in the problem again does not require much more computational effort.

From this section we can see that the inviscid theory is missing some important information so it is better to use the viscous or gravity theories. However the gravity and

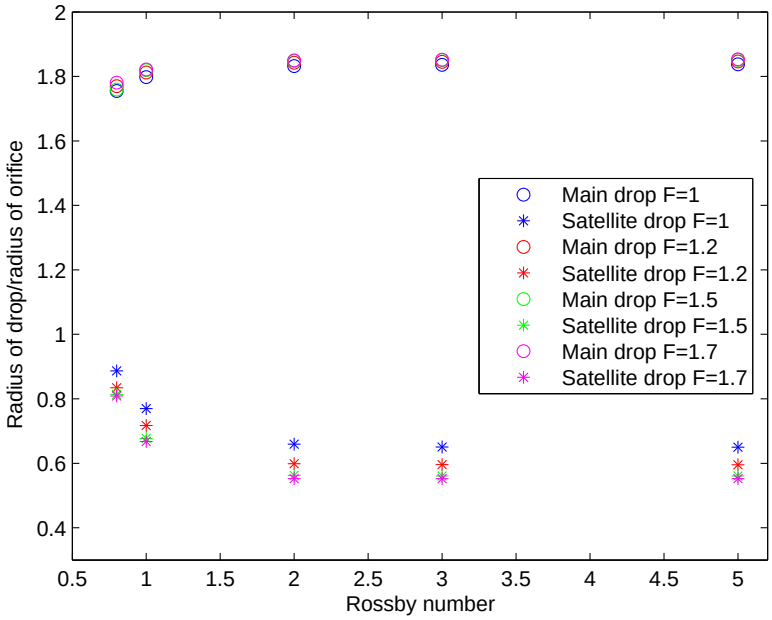

Figure 7.25: A plot of Rossby number against main and satellite drop size, Rb = 0.8, 1, 2, 3 and 5. For different Froude numbers F = 1, 1.2, 1.5 and 1.7. We = 50, Re = 3000 and δ = 0.01.

viscous theories yield similar results for break-up lengths and drop sizes.

7.7 Rossby number curves

Work in the previous section suggests that Rossby number has more effect on drop size than Froude number, Weber number, Reynolds number or δ (though Weber number still has a fairly significant effect, especially on satellite drop size). The work presented in this section would be very difficult to undertake experimentally since we cannot vary one parameter and keep the other parameters fixed easily. Figures 7.25, 7.26, 7.27 and 7.28 are plots of main and satellite drop size against Rossby number.

In figure 7.25 curves are produced for different Froude numbers F=1, 1.2, 1.5 and 1.7. Weber number, Reynolds number and δ are held constant (We = 50, Re = 3000 and δ = 0.01). The values of Rossby number are Rb=0.8, 1, 2, 3 and 5. We can see that Froude number has a small effect on main and satellite drop size for each Rossby number. The difference in size for main drops for each Rossby number is less than 0.1

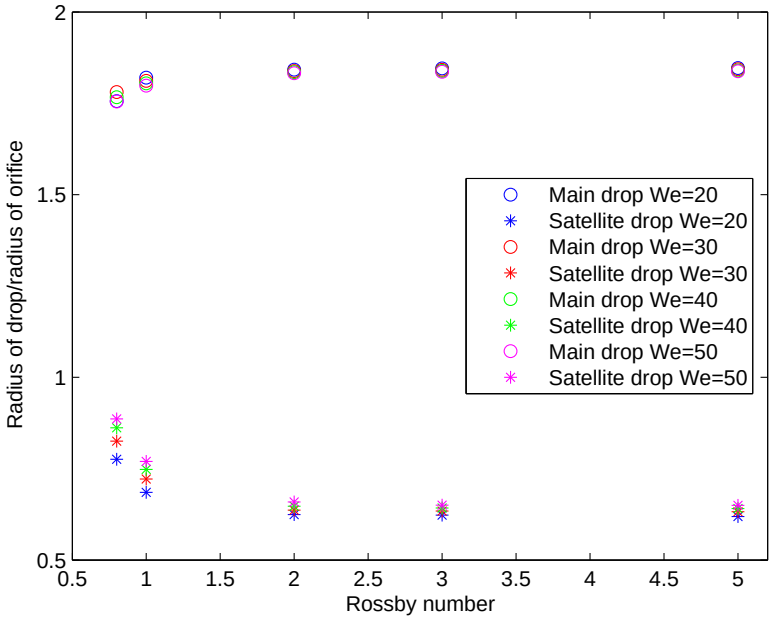

Figure 7.26: A plot of Rossby number against main and satellite drop size, Rb = 0.8, 1, 2, 3 and 5. For different Weber numbers We = 20, 30, 40 and 50. $F = 1$, $Re = 3000$ and $\delta = 0.01$.

in non-dimensional units. There is a greater effect on satellite drop size, however the greatest difference in satellite drop is still 0.1 in non-dimensional units. The size of the satellite drop decreases with Froude number.

In figure 7.26 curves are produced for different Weber numbers We=20, 30, 40 and 50. The values of Rossby number are Rb=0.8, 1, 2, 3 and 5. We can see that the greatest difference in main drop size for each Rossby number is 0.1 in non-dimensional units and the greatest difference in satellite drop size for each Rossby number is 0.2 in non-dimensional units. Weber number has more effect on drop size at low Rossby number. This is similar to the result obtained in figure 6.17.

In figure 7.27 curves are produced for different Reynolds numbers Re=100, 500, 1000, 2000 and 3000. Froude number, Weber number and δ are held constant ($F = 1$, $We = 50$ and $\delta = 0.01$). The values of Rossby number are Rb=1, 2, 3 and 5. We can see that Reynolds number has little effect on the drop size. The greatest difference in main

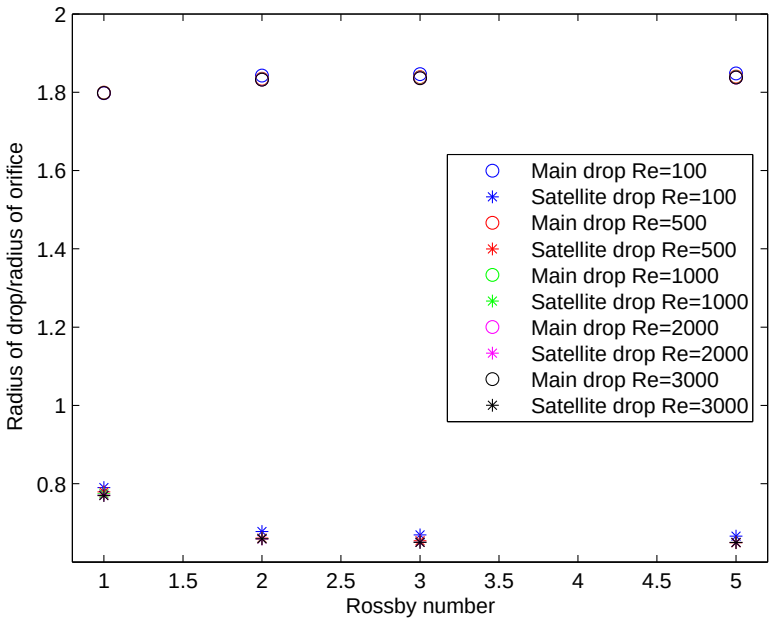

Figure 7.27: A plot of Rossby number against main and satellite drop size, Rb = 0.8, 1, 2, 3 and 5. For different Reynolds numbers Re = 100, 500, 1000, 2000 and 3000. $F = 1$, $We = 50$ and $\delta = 0.01$.

and satellite drop size for each Rossby number is less than 0.1 in non-dimensional units. This is similar to the result obtained in figure 6.18.

In figure 7.28 curves are produced for different values of δ (δ=0.01, 0.015, 0.02, 0.025 and 0.03). Froude number, Weber number and Reynolds number all remain constant ($F = 1$, $We = 50$ and $Re = 3000$). The values of Rossby number are Rb=1, 2, 3 and 5. We can see that δ does not affect the size of the main drop very much. The difference between the main drop size for each Rossby number is less than 0.1 in non-dimensional units. The greatest difference between satellite drop sizes for each Rossby number is 0.1 in non-dimensional units. This is similar to the result obtained in figure 6.19.

7.8 Summary

In this chapter we included gravity into the non-linear model. The same scaling as in chapter 6 was used so that rotation entered in the problem in the equations of motion as well as the initial conditions.

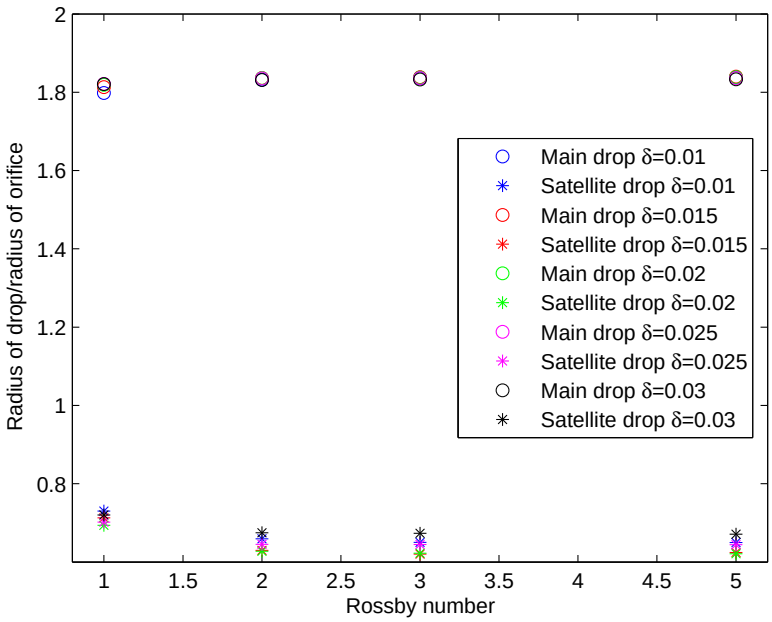

Figure 7.28: A plot of Rossby number against main and satellite drop size, $Rb = 1,\ 2,\ 3$ and 5. For different values of δ, $\delta = 0.01,\ 0.015,\ 0.02,\ 0.025$ and 0.03. $F = 1$, $We = 50$ and $Re = 3000$.

Experimental and theoretical break-up lengths were compared by varying δ until a match between the theoretical and experimental data was found. We did this for three cases and excellent agreement between experimental and theoretical break-up lengths could be found. Main and satellite drop sizes were calculated using the fitted value of δ in each case. Reasonably good agreement between theoretical and experimental drop sizes was obtained. A constant average value of δ was found and the drop sizes were calculated using this value of δ. Again reasonable agreement was found between experimental and theoretical data. Main and satellite drop sizes were calculated for different experimental parameters and again reasonable agreement between theoretical and experimental results was found. This shows that so long as δ is the correct order of magnitude we can obtain reasonably good agreement between experimental and theoretical results.

The parametric study carried out in chapters 5 and 6 was extended to include Froude number. In the study Weber number, Rossby number, Reynolds number and Froude number were assumed to be independent parameters. Experimentally this cannot

be done easily and so the theory can give us information that the experiments could not. Trends in break-up lengths and drop sizes were obtained. Trajectories of the jets in the X-Y plane and X-Y-Z space were obtained. Break-up length increases with increasing Weber number, decreasing Rossby number and decreasing Reynolds number. Break-up length decreases with increasing δ . These results agreed with results obtained in chapter 6. However the variation in break-up length was less than in chapter 6 suggesting that Froude number had some stabilising effect. Break-up length decreases with increasing Froude number; this agrees with work carried out by Decent *et al.* [13].

It was found that the trajectory of the jet falls out of the X-Z plane more for higher Rossby number, since higher Rossby number corresponds to lower rotation rate therefore the gravity forces have more effect on the jet, pulling it down. The jet coiled more tightly for lower Weber number. Jets with lower Weber number have less inertia and therefore can be coiled more tightly by the rotation. The jet fell out of the X-Z plane more for lower Froude number. The lower the Froude number the more effect gravity has on the jet causing the jet to fall out of plane more rapidly.

Weber number, Rossby number, Reynolds number, δ and Froude number were plotted against theoretical main and satellite drop size. It was found that Rossby number had a greater effect on drop size than Weber number, Reynolds number Froude number and δ. However the variation in drop size for Weber number and Rossby number was less than in chapter 6.

Plots of Rossby number against main and satellite drop size were obtained for different values of Weber number, Reynolds number, Froude number and δ. Froude number had a small effect on drop size for each Rossby number. The difference in main drop size was less than 0.1 in non-dimensional units. There was a greater effect on satellite drop size but the difference was still only 0.1 in non-dimensional units. Weber number had a greater effect on drop size at low Rossby number. At $Rb = 0.8$ the difference in drop size was 0.2 in non-dimensional units. The difference in main drop size was 0.1

in non-dimensional units. Reynolds number had a negligible effect on drop size. The difference in main and satellite drop size was less than 0.1 in non-dimensional units for each Rossby number. δ had a small effect on main and satellite drop size. The greatest difference in main drop size was less than 0.1 in non-dimensional units for each Rossby number and the difference in satellite drop size within each Rossby number was 0.1 in non-dimensional units.

The advantage of using the theory is that one parameter can be varied while the others are kept constant. This enables us to identify how each parameter influences break-up length and drop size. Experimentally we cannot easily vary one parameter while keeping the others constant.

Chapter 8

Insonification

8.1 Introduction

The difficulty in controlling drop formation is a major issue for industry, with satellites causing waste and adding to cost. Previous work on controlling liquid jet break-up has been carried out by Donelley and Glaberson [15] and Goedde and Yuen [21]. Donelley and Glaberson investigated liquid jets falling vertically under gravity. They found if the jet was left to break-up purely under capillary forces then main and satellite drops were obtained. They controlled water jet break-up using a loudspeaker. However for more viscous fluids they found that the loudspeaker alone had no effect on the jets. The sound waves could not overcome the viscous forces. Control was achieved by introducing a vibrating pin into the jet. This pin was attached to the loudspeaker so that the pin vibrated with the loudspeaker.

Goedde and Yuen [21] also investigated vertically falling liquid jets. They used electrical forces to generate perturbations on the surface of the jet. For more viscous jets however they had to use a pin attached to an electronic vibrator which was brought into contact with the jet, in a similar way to Donelley and Glaberson [15]. Again the electronic forces alone were unable to counteract the viscous forces.

We carried out experimental work on the pilot scale rig. A fully waterproof sub-aqua speaker was placed within the can as shown in figure 8.1. The speaker was connected to a personal computer and a sound wave was generated using signal generator software

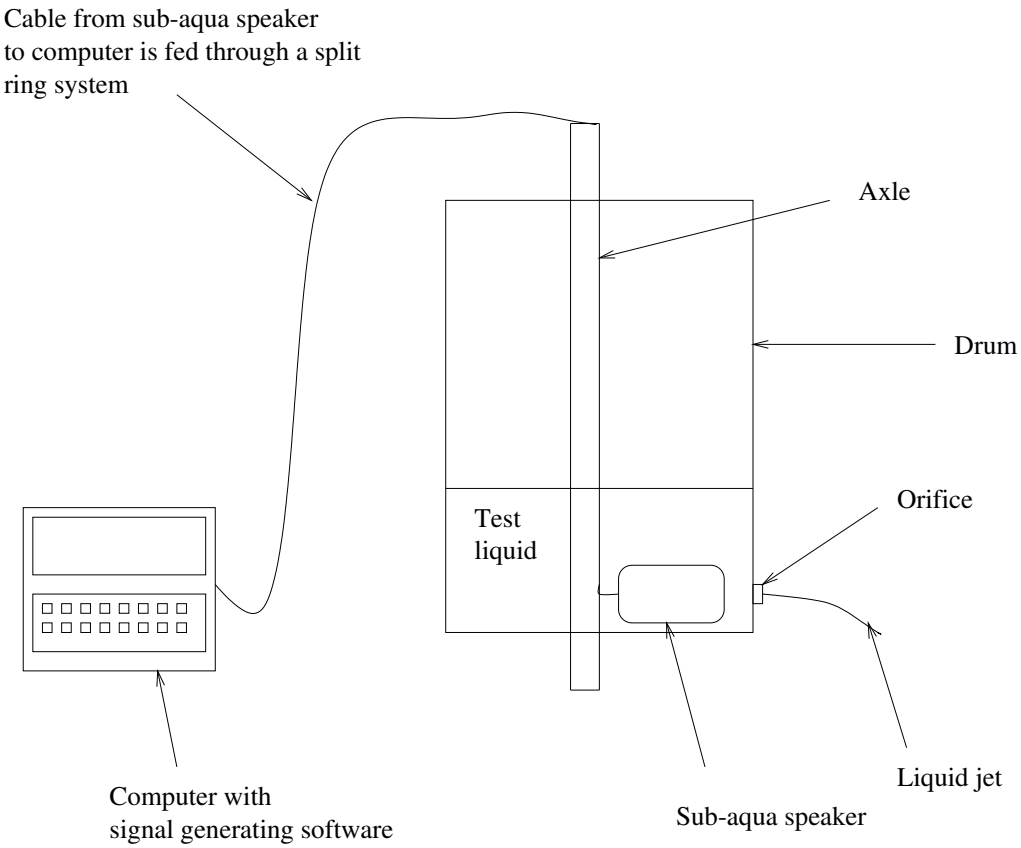

Figure 8.1: Sketch of the pilot scale rig with the sub-aqua speaker.

(Natch Engineering Sigjenny v0.989). The experimental method used was the same as in section 3.1. The drops were imaged using the high speed digital camera and analysed in the same way as described in section 3.1. The working fluid was water. The Rossby numbers of the experimental systems were $Rb = \infty,\ 7.01,\ 1.67$ and 1.12 (corresponding to rotational rates of 0, 1.28, 6.28 and 9.42 rad s^{-1} respectively). The aim was to control the disturbance that causes jet break-up and therefore drop formation, ultimately eliminating satellite drops.

8.2 Frequency of the sound wave

A linear temporal stability analysis on a curved viscous jet carried out by Decent *et al.* [12] showed that the most unstable mode depends on the viscosity and is given by

$$\kappa^* = \frac{1}{2^{1/4}\sqrt{\sqrt{2} + 3Oh}} \tag{8.1}$$

where κ^* is the most unstable wavenumber. If we consider the frequency associated with this most unstable linear wave, Decent *et al.* [12] showed that this was

$$\omega^* = \kappa^* u_0(s) \tag{8.2}$$

where ω^* is the non-dimensional frequency corresponding to the most unstable wavenumber. At the orifice, $s = 0$ and $u_0(s) = 1$ therefore equation (8.2) becomes

$$\omega^* = \kappa^*. \tag{8.3}$$

So in chapters 6 and 7 this is the frequency at the orifice corresponding to the most unstable wave which arises naturally without any additional vibration. Equation (8.3) is dimensionalised to give

$$f^* = \frac{U\kappa^*}{s_0} \tag{8.4}$$

Table 8.1: Parameter values obtained during the experiments and theoretically predicted values for κ^* and f^*.

Angular velocity [rad s^{-1}]	Exit velocity [ms^{-1}]	Rb	Re	We	Oh	κ^*	f* [Hz]
0	1.2033	∞	1800	30.17	0.0031	0.7048	5.9515
1.28	1.2785	7.01	1913	34.06	0.0031	0.7048	6.3234
6.28	1.4901	1.67	2229	46.26	0.0031	0.7048	7.369
9.42	1.5042	1.12	2251	47.15	0.0031	0.7048	7.4397

where f^* is the dimensional frequency corresponding to the most unstable mode at the orifice.

Table 8.1 gives the exit velocities and the dimensionless groups obtained experimentally, as well as the wavenumber and the dimensional frequency corresponding to the most unstable mode at the orifice for each system studied experimentally with insonification on the pilot scale rig. These are obtained from equations (8.1) and (8.4). From table 8.1, f^* has a small value in the range of 5.95-7.44 Hz. This gives us a starting point for our experiments.

The lowest frequency obtainable from the signal generator software is 10 Hz. Therefore the first set of experiments compare the drop size distributions without insonification with jets experiencing a sound wave of frequency 10 Hz. Figures 8.2, 8.3 and 8.4 show four drop size distributions for four different Rossby numbers: (a) $Rb = \infty$ (0 $rads^{-1}$), (b) $Rb = 7.01$ (1.28 $rads^{-1}$), (c) $Rb = 1.67$ (6.28 $rads^{-1}$) and (d) $Rb = 1.12$ (9.42 $rads^{-1}$). In figure 8.2 the blue line corresponds to no insonification and the red line corresponds to a jet experiencing a sound wave with frequency 10 Hz. It can be seen that insonification with a sound wave of 10 Hz has little effect on the drop size distributions at all Rossby numbers. A possible reason for this is that the amplitude of the sound wave was not large enough to affect the jet, despite the volume settings being at the maximum.

These experiments were repeated using a sound wave of 100 Hz. The drop size distributions are given in figure 8.3. The blue line corresponding to no insonification and the red line corresponding to a jet experiencing a sound wave of 100 Hz. At lower Rossby

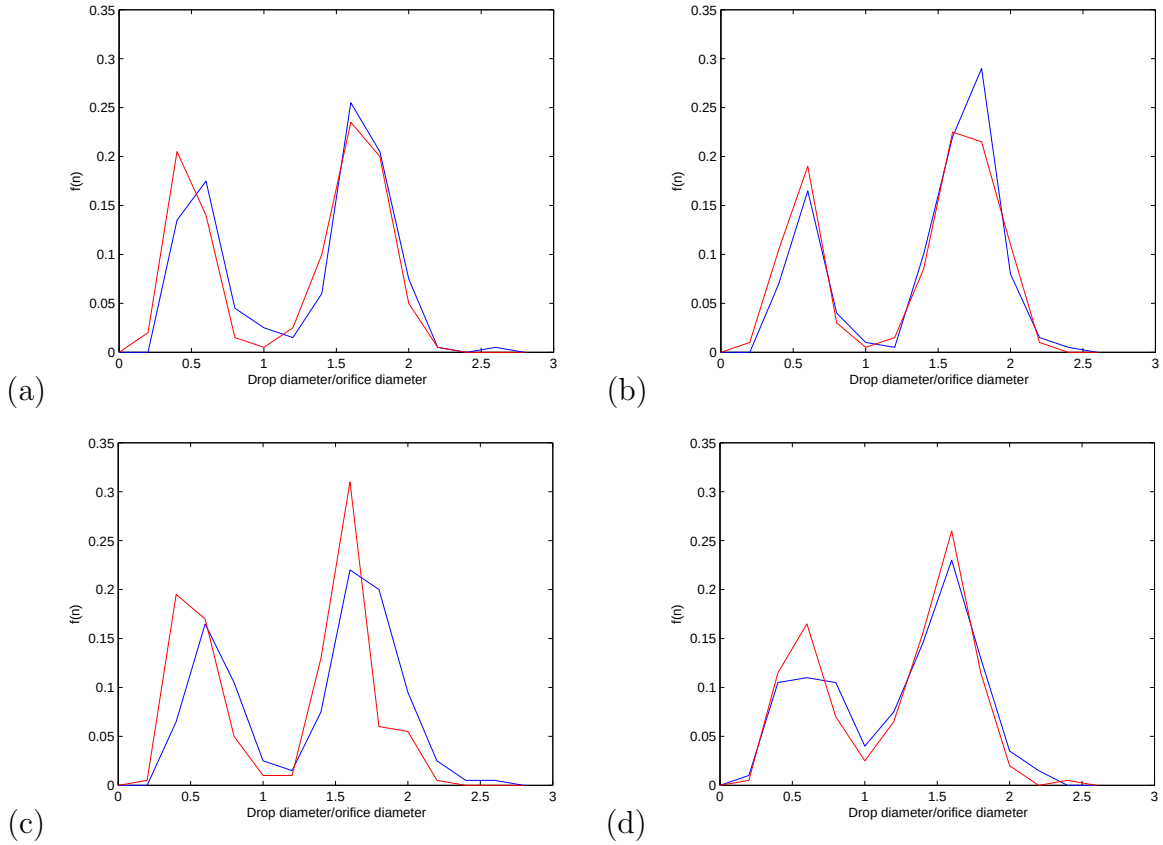

Figure 8.2: Four drop size distributions for four different Rossby numbers, ($Rb = \infty$, 7.01, 1.67 and 1.12) the blue line is the distribution for a jet experiencing no insonification and the red line corresponds to a jet subjected to a frequency of 10 Hz.

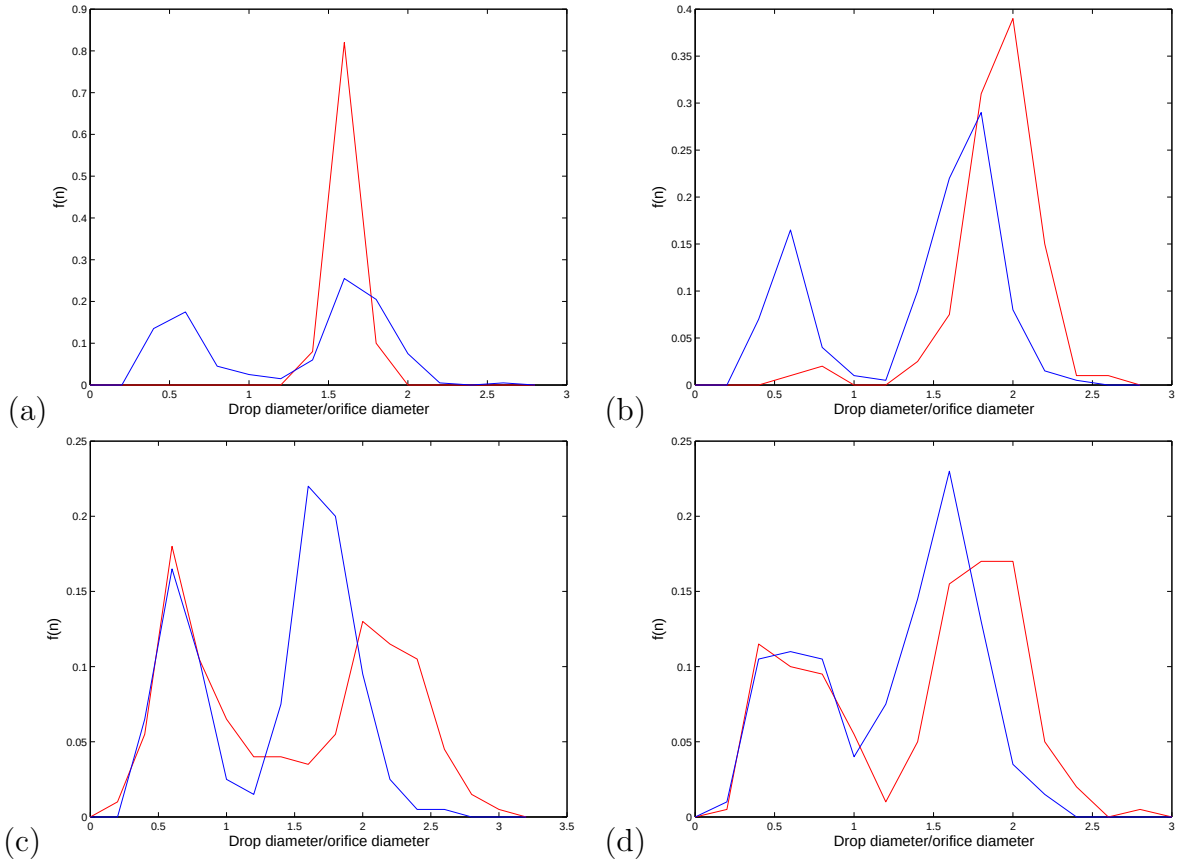

Figure 8.3: Drop size distributions for four different Rossby numbers ($Rb = \infty$, 7.01, 1.67 and 1.12). The red line corresponds to a jet being subjected to a sound wave with frequency 100 Hz and the blue line corresponds to a jet experiencing no insonification.

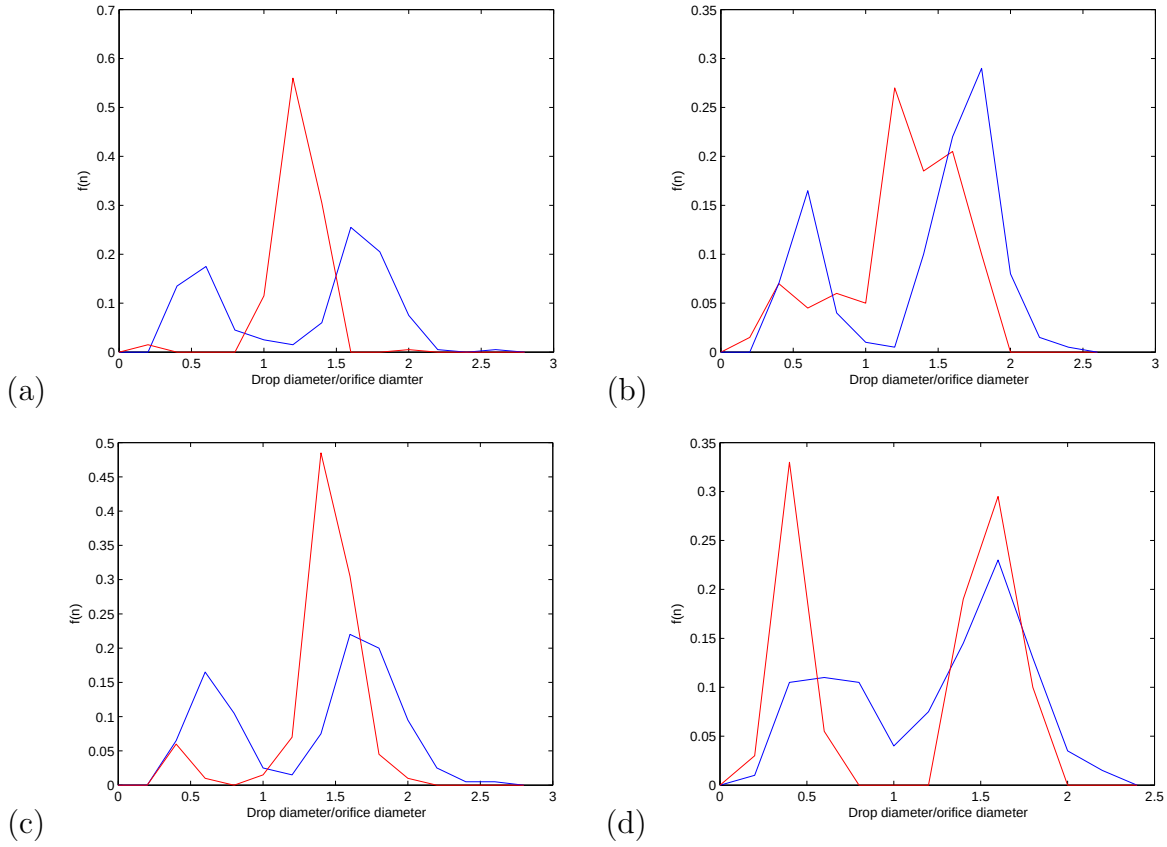

Figure 8.4: Four drop size distributions for four different Rossby numbers ($Rb = \infty$, 7.01, 1.67 and 1.12), the blue line is the distribution for a jet experiencing no insonification and the red line corresponds to a jet subjected to a frequency of 200 Hz.

numbers ($Rb = 1.67$ and $Rb = 1.12$) insonification produces a negligible effect on the satellite drops. At the higher Rossby numbers ($Rb = \infty$ and $Rb = 7.01$) insonification appears to reduce the number of satellite drops, particularly when $Rb = \infty$ where the satellite drops have been completely eliminated. The lower Rossby numbers correspond to higher rotation rates so it appears that at higher rotation rates the sound waves cannot overcome the increased rotational forces. Also at 100 Hz the volume of the sound wave is noticeably larger than at 10 Hz despite the volume settings being the same (because of the performance of the speaker). This means the amplitude of the sound wave is greater at 100 Hz than 10 Hz. This suggests a minimum amplitude of sound wave is required before insonification can be successful.

The experiments were repeated at 200 Hz. The drop size distributions are shown in figure 8.4. The blue line corresponds to no insonification and the red line corresponds the the jet experiencing a sound wave with frequency 200 Hz. At all Rossby numbers except $Rb = 1.12$, a significant number of satellite drops have been eliminated. At $Rb = \infty$ nearly all the satellite drops have been eliminated. At $Rb = 7.01$ a significant number of satellite drops have been eliminated. At $Rb = 1.67$ more satellite drops have been eliminated than with 100 Hz. At $Rb = 1.12$ insonification seems to be ineffective at eliminating the satellite drops. At higher rotation rates the higher rotational forces could be counteracting the effect of the insonification, and there would be increased influence from air resistance which could affect insonification. At $Rb = 1.12$, there are almost equal numbers of satellite and main drops showing that insonification did affect the jet even though the satellite drops were not eliminated. Again the volume of the sound wave with frequency 200 Hz was louder than the volume of the sound wave with frequency 100 Hz even though the volume settings were the same. This suggests the amplitude of the 200 Hz wave was greater than the amplitude of the 100 Hz wave.

Figures 8.5, 8.6, 8.7 and 8.8 show four experimental images with (a) no insonification, (b) insonification with 10 Hz, (c) insonification with 100 Hz and (d) insonification with 200 Hz. Figure 8.5 shows images of jets with $Rb = 1.12$. From figures 8.5(b) and (c) we can see 10 and 100 Hz insonification has little effect on the jet. From figure 8.5(d) a satellite drop is formed between the main drops, showing that at 200 Hz insonification does not eliminate satellite drops for $Rb = 1.12$, though insonification clearly has an effect.

Figure 8.6 shows images of jets with $Rb = 1.67$. From figure 8.6(b) insonification with 10 Hz has little effect on the jet since the drops are of non-uniform size. From figure 8.6(c) we can see the formation of satellite drops between the main drops suggesting that insonification at 100 Hz has been ineffective in eliminating satellite drops. From figure 8.6(d) we can see that a sound wave with a frequency of 200 Hz has more effect on the jet since the drops are of more uniform size and there is an absence of satellite drops.

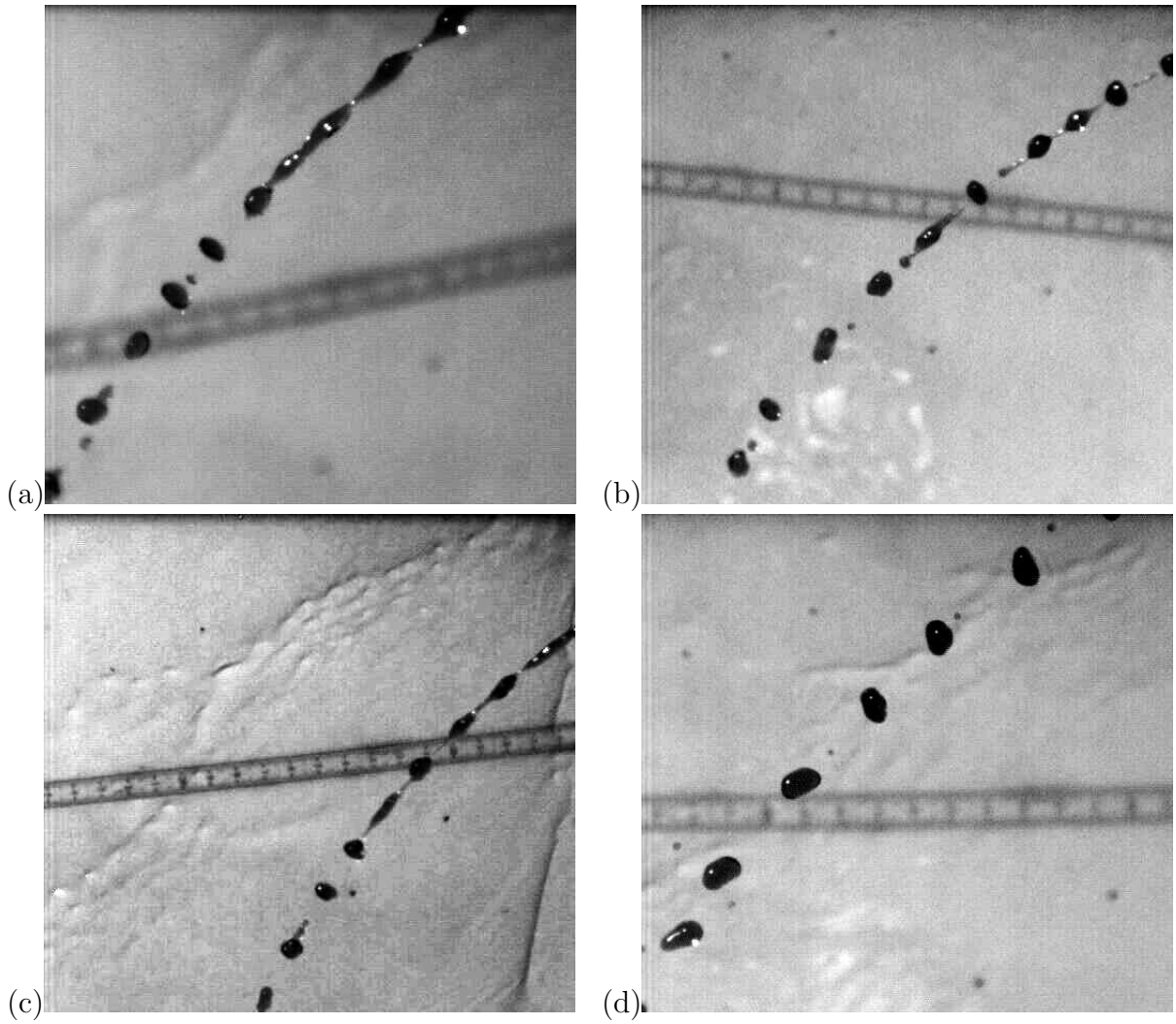

Figure 8.5: Four experimental images of jets with $We = 47.15$, $Rb = 1.12$ and $Re = 2251$.

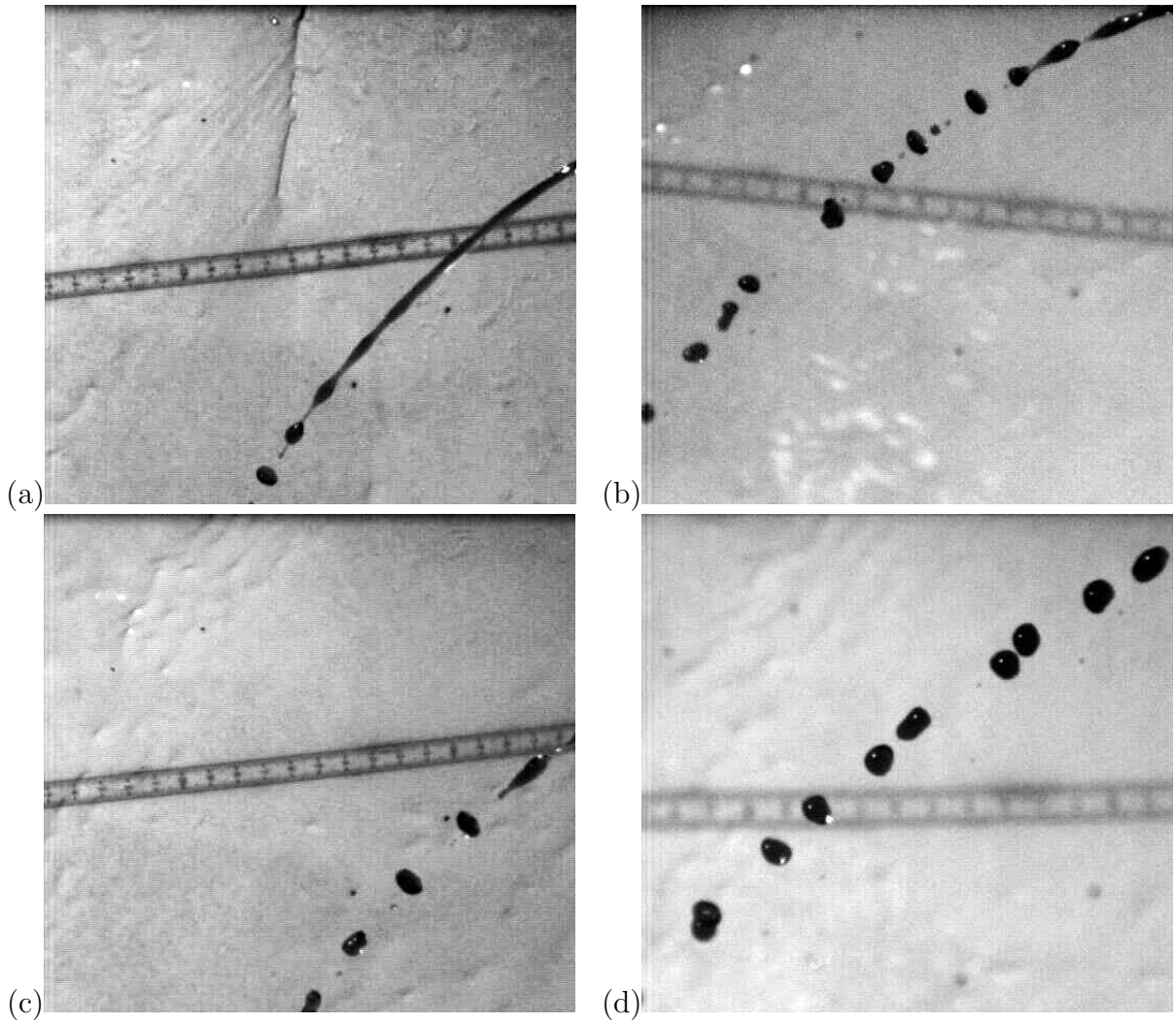

Figure 8.6: Four experimental images of jets with $We = 46.27$, $Rb = 1.67$ and $Re = 2229$.

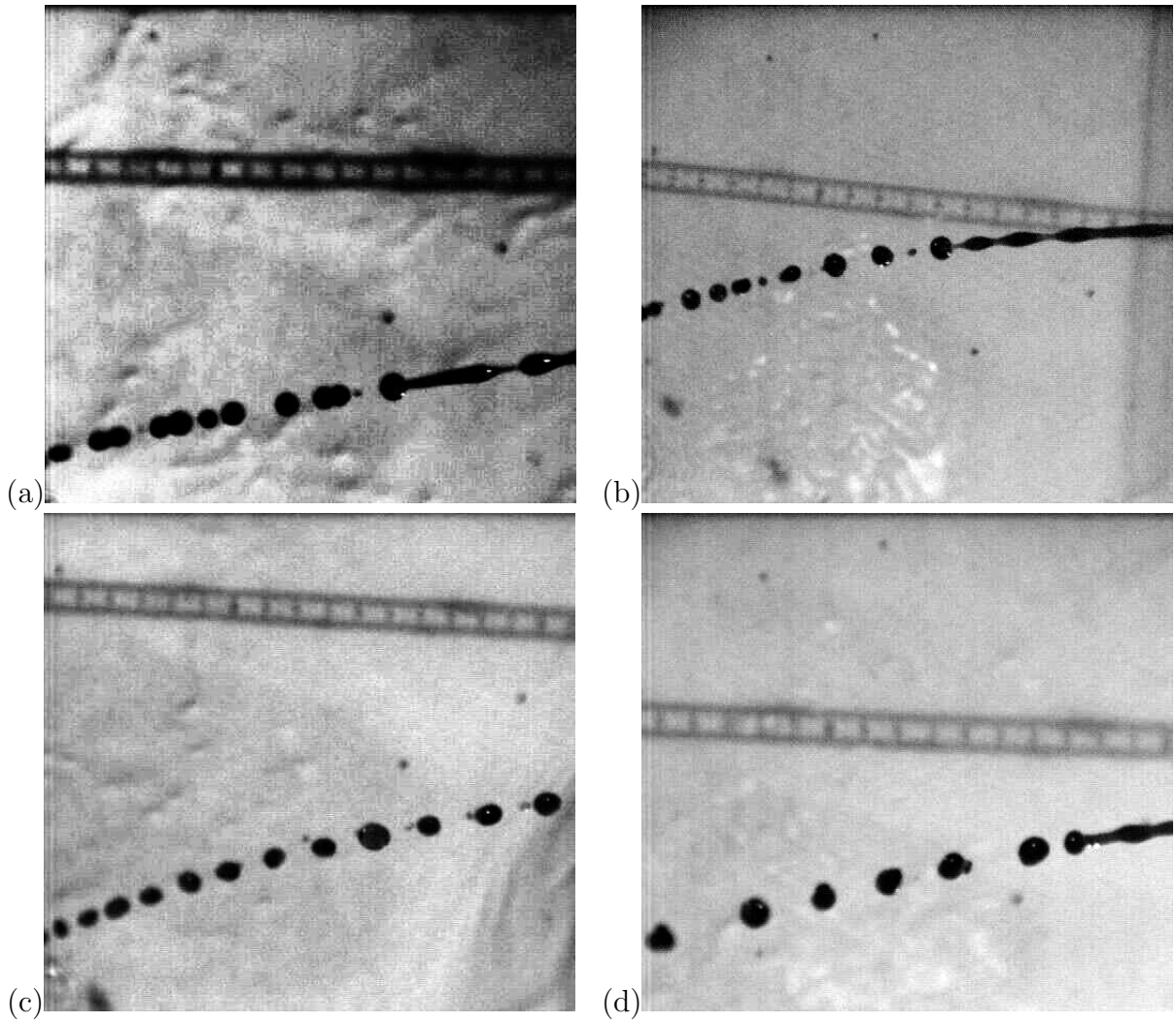

Figure 8.7: Four experimental images of jets with $We = 34.06$, $Rb = 7.01$ and $Re = 1913$.

These results can be confirmed from the drop size distributions shown above.

Figure 8.7 shows four experimental images of jets with $Rb = 7.01$. Comparing figures 8.7(a) and (b) we can see that a sound wave with frequency 10 Hz has negligible effect on the jet. However figures 8.7(c) and (d) show that sound waves of frequency 100 and 200 Hz have a considerable effect on the jet. In both cases almost all the satellite drops have been eliminated.

Figure 8.8 shows four experimental figures of jets with $Rb = \infty$. At 10 Hz insonification has a negligible effect. However with a sound wave of frequency 100 or 200 Hz

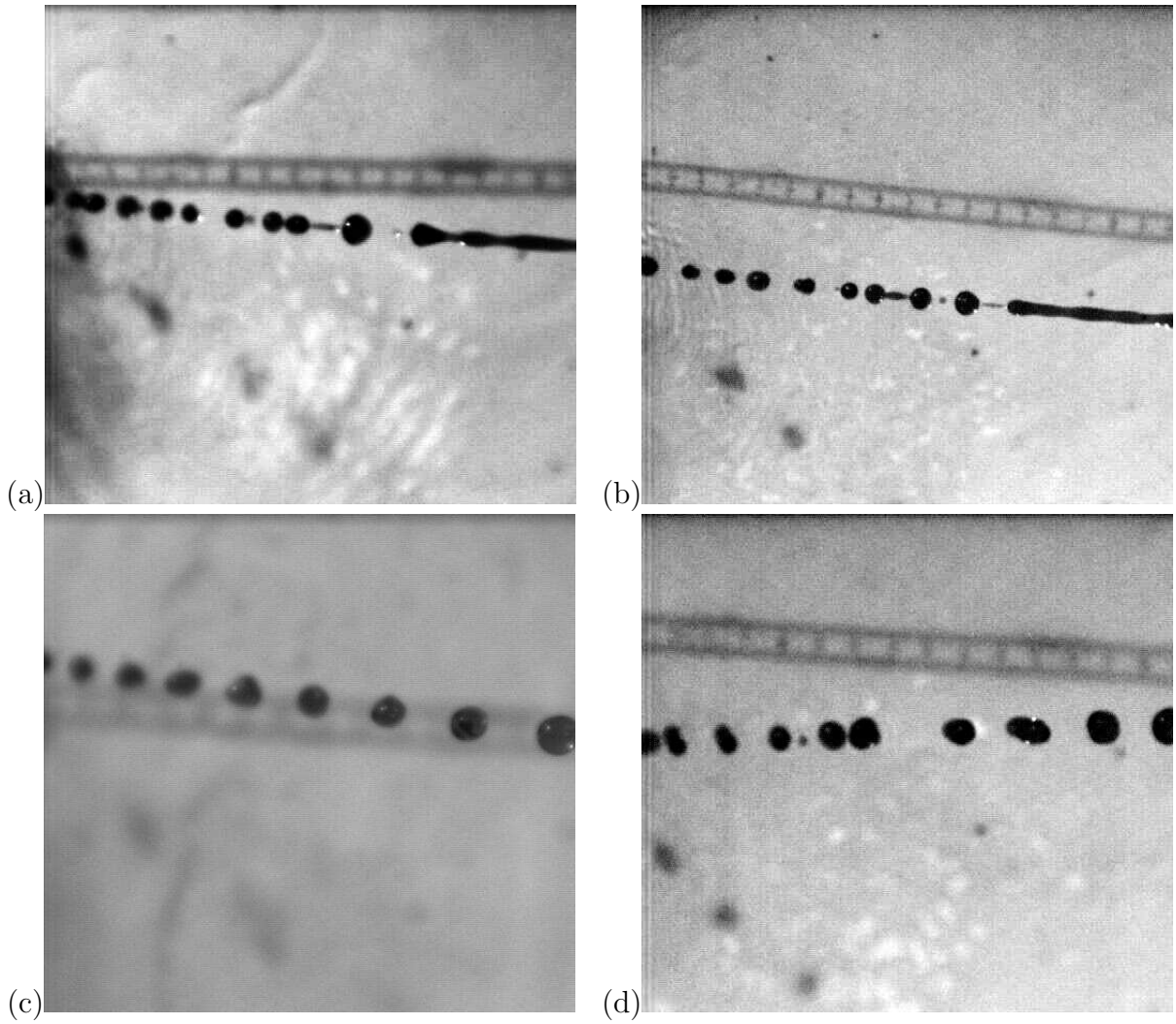

Figure 8.8: Four experimental images of jets with $We = 30.17$, $Rb = \infty$ and $Re = 1800$.

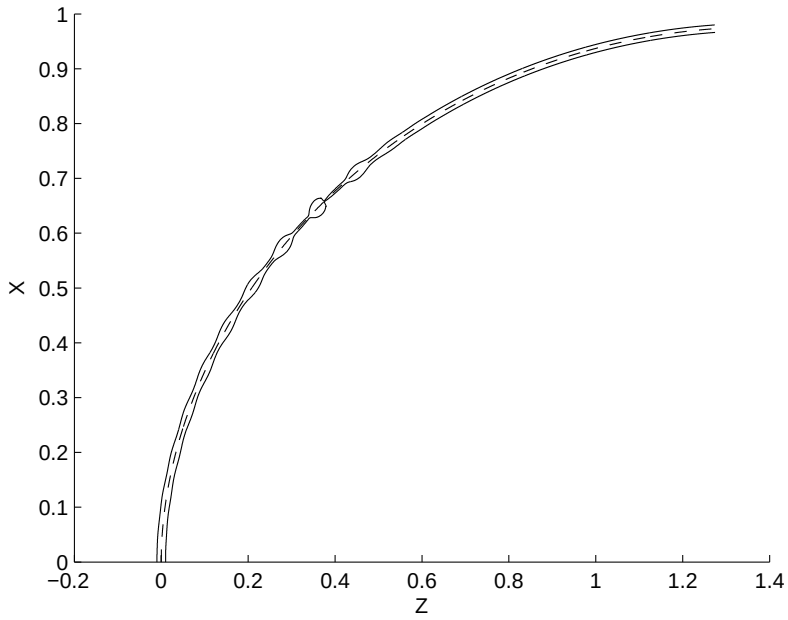

Figure 8.9: A simulation of a jet with $We = 47.15$, $Rb = 1.12$, $\delta = 0.01$ and $Re = 2251$. The jet is experiencing no insonification.

the effect of insonification is evident with the formation of more uniform sized drops.

8.3 Theory

In this section insonification is introduced into the non-linear analysis. The equations of motion are the same as the equations in chapter 6. Figure 8.9 is a simulation of a jet with $We = 47.15$, $Rb = 1.12$, $Re = 2251$ and $\delta = 0.01$. This jet is experiencing no insonification and the break-up mechanism is mode 2.

Figure 8.10 is a simulation of a jet with the same parameters as in figure 8.9. However this jet is experiencing a sound wave of 10 Hz. The conditions at the orifice have been modified to include another term representing the sound wave generated from the speaker given by

$$u(0,t) = 1 + \delta \sin\left(\frac{\kappa}{\epsilon}t\right) + \alpha \cos\left(\frac{\beta}{\epsilon}t\right). \tag{8.5}$$

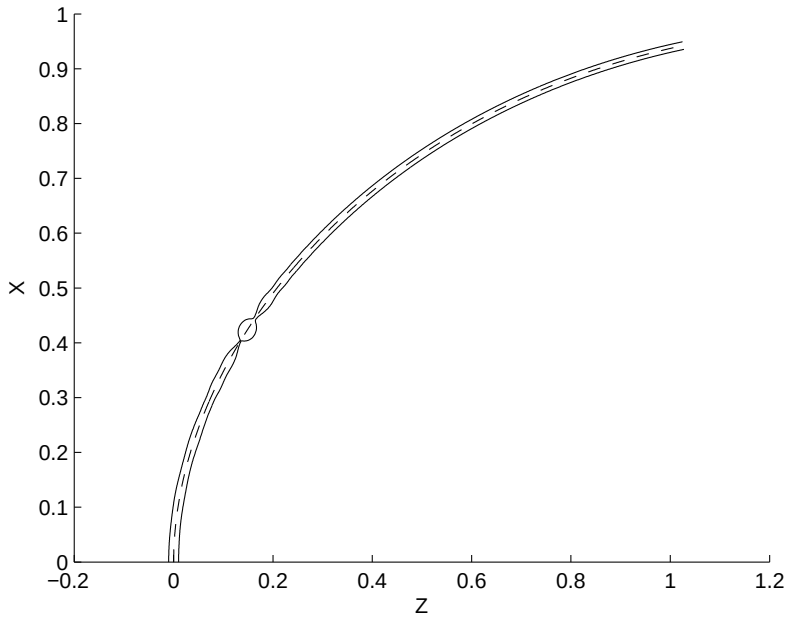

Figure 8.10: A simulation of a jet with $We = 47.15$, $Rb = 1.12$ and $Re = 2251$. The jet is experiencing a sound wave of 10 Hz, $\beta = 0.00947$, $\alpha = 0.1$ and $\delta = 0.01$.

We evaluate $\beta = 0.00947$ to give a non-dimensional wave frequency corresponding to 10 Hz. We are unable to calculate α which is the amplitude of the sound wave produced inside the liquid; however we know that the contribution from the sound wave is much greater than the most unstable mode (at least if the insonification is effective), therefore $\alpha >> \delta$ where δ is the magnitude of the most unstable mode at the orifice. So we choose $\alpha = 0.1$ since this makes α an order of magnitude larger than δ. We can see that the break-up mechanism is mode 1 with the formation of only one drop. The experimental results obtained in section 8.2 showed that insonification did not eliminate satellite drops in this parameter regime and the break-up mode was mode 2. This shows that at such low frequencies the sub-aqua speaker is producing a sound wave of insufficient amplitude at this frequency of 10 Hz.

Figure 8.11 is a simulation of a jet with the same parameter values as in figure 8.10 experiencing a sound wave of 10 Hz ($\beta = 0.00947$ in non-dimensional notation) but with $\alpha = 0.01$. This corresponds to a lower amplitude of sound wave. We can see that

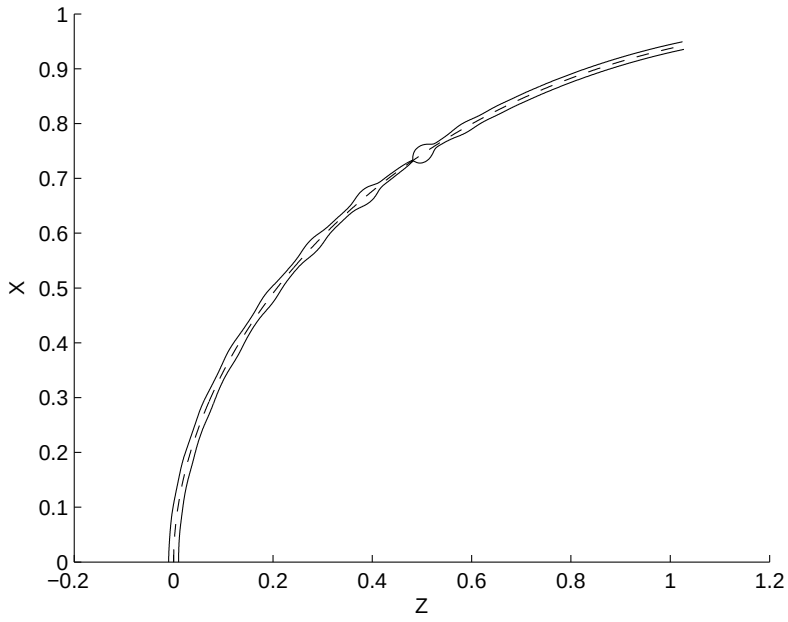

Figure 8.11: A simulation of a jet with $We = 47.15$, $Rb = 1.12$ and $Re = 2251$. The jet is experiencing a sound wave of 10 Hz, $\beta = 0.00947$, $\alpha = 0.01$ and $\delta = 0.01$.

insonification does not eliminate satellite drops when $\alpha = 0.01$ and the break-up mode is mode 2. This shows that the theory predicts a minimum amplitude of wave is required for insonification to successfully eliminate satellite drops which agrees with observations from the experiments.

It should be noted that the most unstable wave mode has wavenumber κ. This is the wave that grows most quickly as it travels downstream. The insonification frequency β that is excited will therefore have a lower growth rate as it travels downstream. For this wave to have an effect its initial amplitude α must be larger than the initial amplitude of the fastest growing mode.

Figure 8.12 shows the same jet as in figure 8.9 experiencing a sound wave of frequency 100 Hz, which corresponds to $\beta = 0.0947$, $\delta = 0.01$ and $\alpha = 0.1$. We can see that the break-up mode is again mode 1. Again experimentally we did not observe any effect from the sound wave and the break-up mode was mode 2, implying that experimentally the amplitude of the sound wave at 100 Hz was not large enough to eliminate satellite

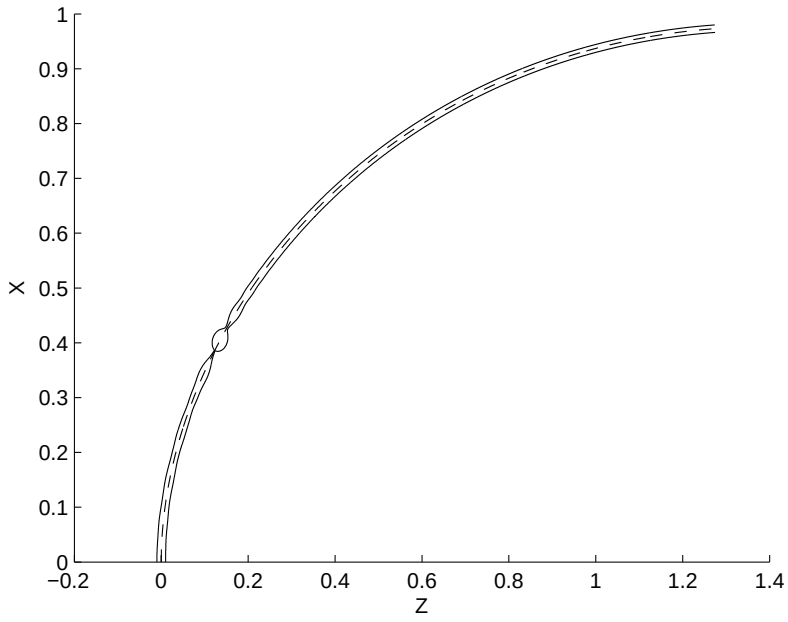

Figure 8.12: A simulation of a jet with $We = 47.15$, $Rb = 1.12$, $\alpha = 0.1$, $\delta = 0.01$ and $Re = 2251$. The jet is experiencing a wave with frequency 100 Hz. $\beta = 0.0947$.

drops for a jet with $Rb = 1.12$.

Figure 8.13 is a simulation of a jet with the same parameter values as the simulation presented in figure 8.12 experiencing a sound wave at 100 Hz ($\beta = 0.0947$ in non-dimensional notation) but with $\alpha = 0.01$. This corresponds to a lower amplitude of sound wave. Insonification at $\alpha = 0.01$ did not eliminate satellite drops and the break-up mode was mode 2.

Figure 8.14 shows the same jet as in figure 8.9 experiencing a sound wave of 200 Hz, $\beta = 0.189$. The break-up mode is mode 1 with only one main drop formed. Experimentally we found that satellite drops were not eliminated since the amplitude of the sound wave was not large enough to successfully eliminate satellite drops for a jet with $Rb = 1.12$.

Figure 8.15 is a simulation of a jet with the same parameter values as the simulation given in figure 8.14 experiencing a sound wave of 200 Hz but with $\alpha = 0.01$ which corresponds to a smaller amplitude than in figure 8.14. We can see when $\alpha = 0.01$

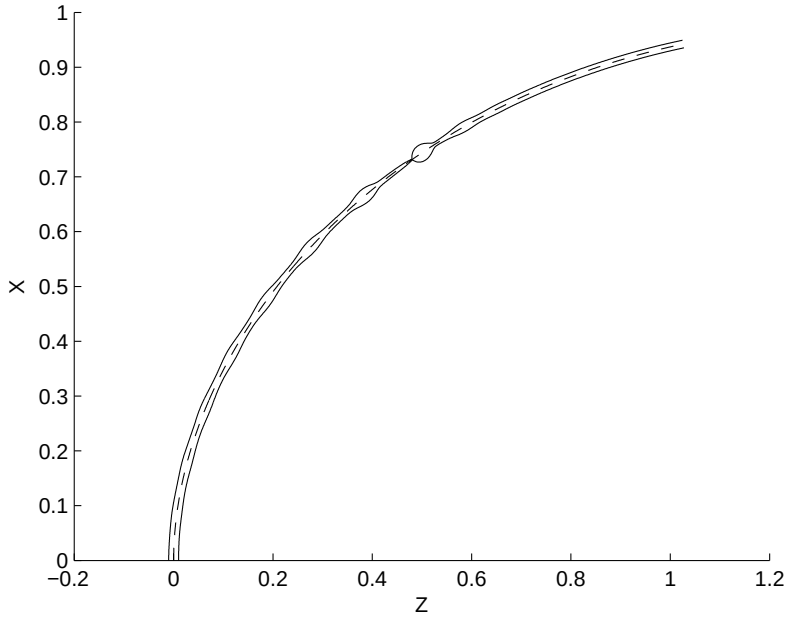

Figure 8.13: A simulation of a jet with $We = 47.15$, $Rb = 1.12$, $\alpha = 0.01$, $\delta = 0.01$ and $Re = 2251$. The jet is experiencing a wave with frequency 100 Hz. $\beta = 0.0947$.

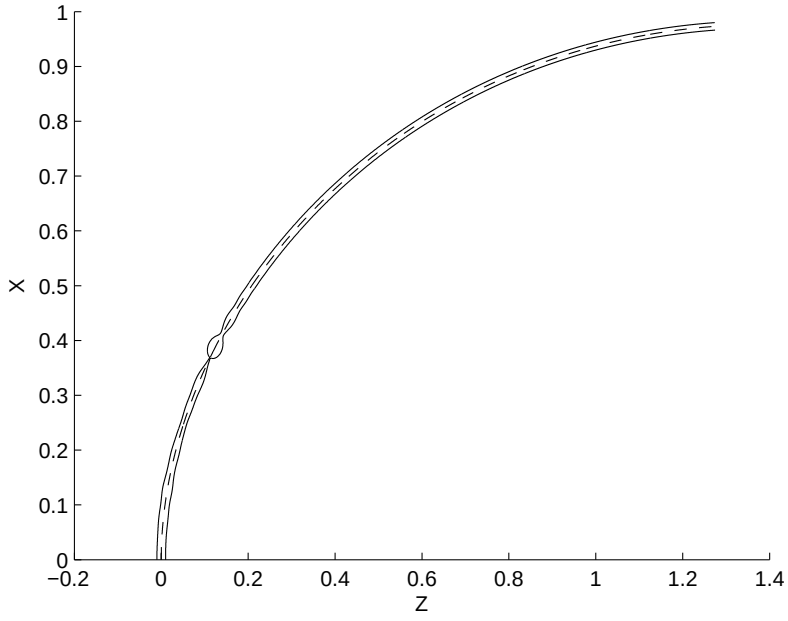

Figure 8.14: A simulation of a jet with $We = 47.15$, $Rb = 1.12$, $\alpha = 0.1$, $\delta = 0.01$ and $Re = 2251$. The jet is experiencing a sound wave with frequency of 200 Hz. $\beta = 0.189$.

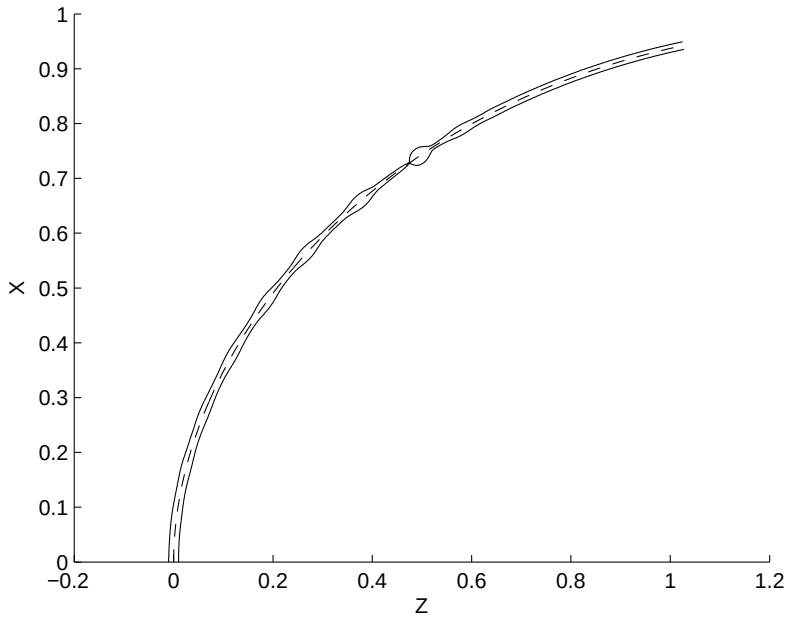

Figure 8.15: A simulation of a jet with $We = 47.15$, $Rb = 1.12$, $\alpha = 0.01$, $\delta = 0.01$ and $Re = 2251$. The jet is experiencing a sound wave with frequency of 200 Hz. $\beta = 0.189$.

insonification is ineffective at eliminating satellite drop and the break-up mode is mode 2, as in the experiments at this rotation rate.

The results in figures 8.10-8.15 are key results. They show that the theory predicts that insonification eliminates satellite drop formation providing the amplitude of the sound wave is large enough. The amplitude of the sound wave generated by the sub-aqua speaker was not large enough at these rotation rates to counteract the rotational forces at the frequencies used in the experiments. A possibility for further work is to repeat the experiments described earlier in this chapter with more sophisticated equipment.

Theoretical simulations presented in figures 8.10-8.15 were repeated for $Rb = \infty$, 7.01 and 1.67. Mode 1 break-up was always predicted when the jet experienced sound waves of 10, 100 and 200 Hz when $\alpha = 0.1$ and $\delta = 0.01$. Satellite drops were not eliminated when $\alpha = 0.01$ and $\delta = 0.01$, suggesting that experimentally we could always eliminate satellite drops in the experimental regimes providing the amplitude of the sound wave is large enough.

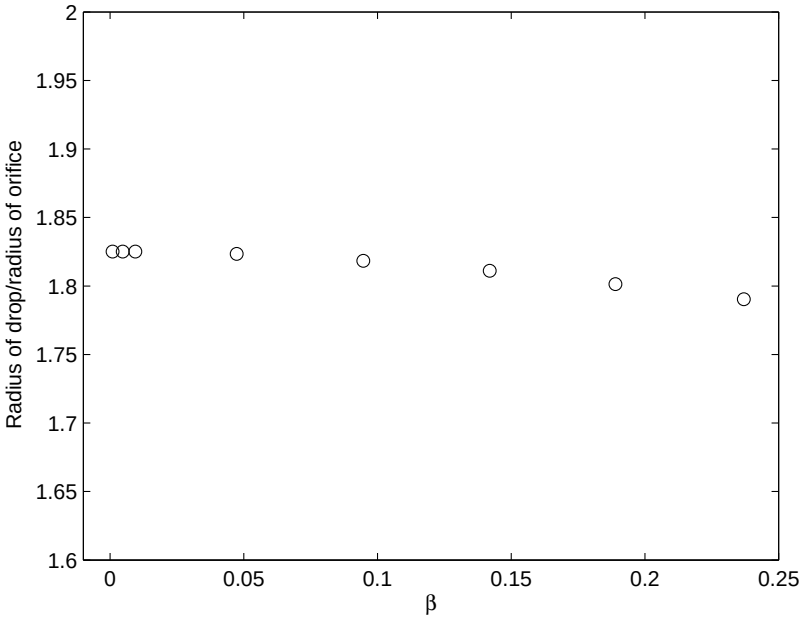

Figure 8.16: A plot showing drop size against β. $We = 47.15$, $Rb = 1.12$, $Re = 2251$, $\alpha = 0.1$ and $\delta = 0.01$.

The remaining part of this section will involve varying β outside of values used in experiments in order to find the limits of the effects of insonification and to obtain simulations outside of the experimental parameter regimes.

Figure 8.16 is a plot of β against drop size for $We = 47.15$, $Rb = 1.12$ and $Re = 2251$ when $\alpha = 0.1$ and $\delta = 0.01$. The values of β used are 0.000947, 0.004735, 0.00947, 0.04735, 0.0947, 0.142, 0.189 and 0.237. This corresponds to frequencies of 1, 5, 10, 50, 100, 150, 200 and 250 Hz. The plot corresponding to $\beta = 0.284$ (300 Hz) was not shown because at this frequency satellite drops begin to form. We can see for $\beta =$ 0.000947, 0.004735 and 0.00947 the drop size remains constant. However at larger β the drop size decreases slightly with increasing β (the difference in the drop sizes is 0.0348). Figures 8.2, 8.3 and 8.4 show that the main drop size does not change significantly with β for $Rb = 1.12$.

Figure 8.17 is a plot of β against drop size for the same parameter values and values of β as in figure 8.16 but with $\alpha = 0.01$. This corresponds to a lower amplitude sound wave

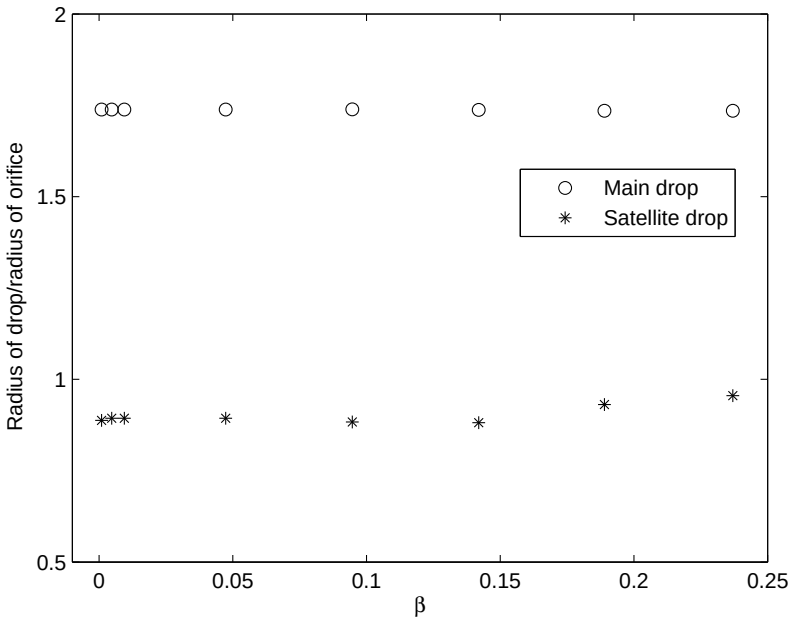

Figure 8.17: A plot showing drop size against β. $We = 47.15$, $Rb = 1.12$, $Re = 2251$, $\alpha = 0.01$ and $\delta = 0.01$. Circles correspond to main drops and stars correspond to satellite drops.

than in figure 8.16. We can see that at a lower amplitude satellite drops form and therefore insonification is ineffective. Also for $\beta = 0.000947,\ 0.0004735,\ 0.00947,\ 0.04735$ and 0.0947 the size of the main and satellite drops were constant. At higher values of β the size the main drop decreased slightly, which is similar to the result obtained when $\alpha = 0.1$, and the size of the satellite drop increases slightly.

Figure 8.18 is a plot showing β against drop size for $We = 34.06$, $Rb = 7.01$ and $Re = 1913$ when $\alpha = 0.1$ and $\delta = 0.01$. In this case the Rossby number is high and corresponds to a low rotation rate. The values of β are 0.00111, 0.00557, 0.0111, 0.0557, 0.111, 0.167, 0.223, 0.2786 and 0.334. This corresponds to frequencies of 1, 5, 10, 50, 100, 150, 200, 250 and 300 Hz. The plot corresponding to $\beta = 0.39$ (350 Hz) is not shown because at this frequency satellite drops begin to form. We can see that the drop size decreases slightly with increasing β. This is the same result obtained in figure 8.16.

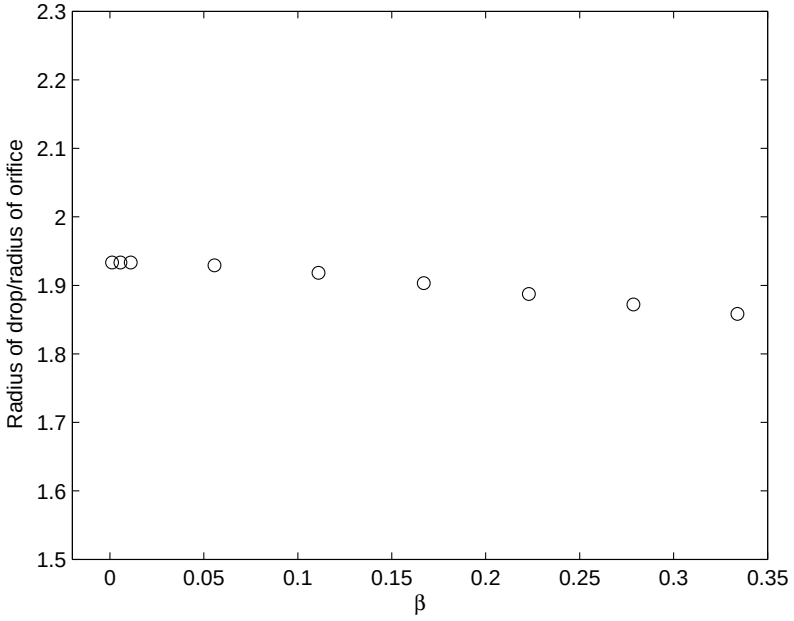

Figure 8.18: A plot showing drop size against β. $We = 34.06$, $Rb = 7.01$, $Re = 1913$, $\alpha = 0.1$ and $\delta = 0.01$.

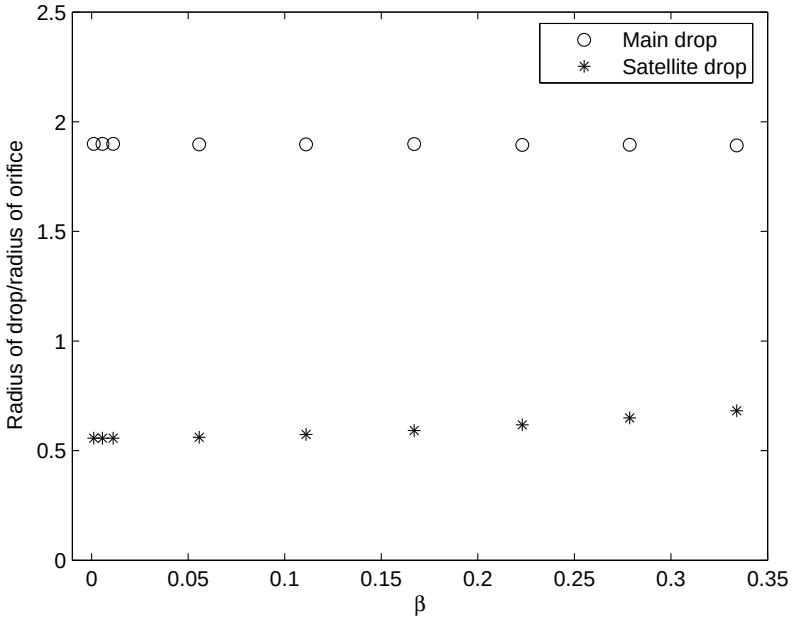

Figure 8.19: A plot showing drop size against β. $We = 34.06$, $Rb = 7.01$, $Re = 1913$, $\alpha = 0.01$ and $\delta = 0.01$. Circles correspond to main drops and stars correspond to satellite drops.

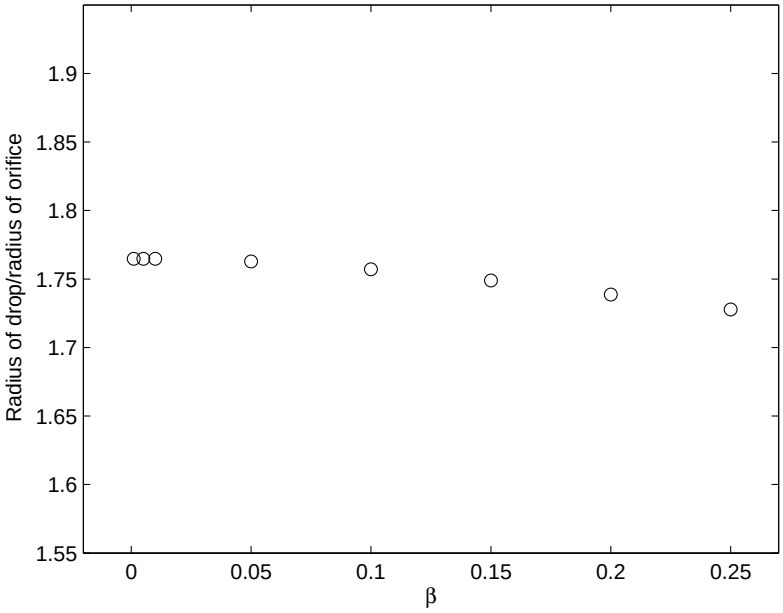

Figure 8.20: A plot showing drop size against β. $We = 100$, $Rb = 1$, $Re = 3000$, $\alpha = 0.1$ and $\delta = 0.01$.

Figure 8.19 is a plot of β against drop size for the same parameter values and values of β presented in figure 8.18 but with $\alpha = 0.01$ which corresponds to a lower amplitude sound wave. We can see that when $\alpha = 0.01$ satellite drops occur so insonification is ineffective. When $\beta = 0.00111,\ 0.00557$ and 0.0111 the size of the main and satellite drops remains constant. At higher values of β the size of the main drop decreases slightly, (this is similar to the result obtained when $\alpha = 0.1$) and the satellite drop size increases slightly. This result is similar to the results presented in figure 8.17.

Figure 8.20 shows a plot of β against drop size for a jet with $We = 100$, $Rb = 1$, $\alpha = 0.1$, $\delta = 0.01$ and $Re = 3000$. The values of β are 0.001, 0.005, 0.01, 0.05, 0.1, 0.15, 0.2 and 0.25. Satellite drops appeared at $\beta = 0.3$. We can see that the relationship between β and drop size is the same as the relationship obtained earlier in figures 8.16 and 8.18. The drop size remains constant for β=0.001, 0.005 and 0.01 and then decreasing slightly with increasing β.

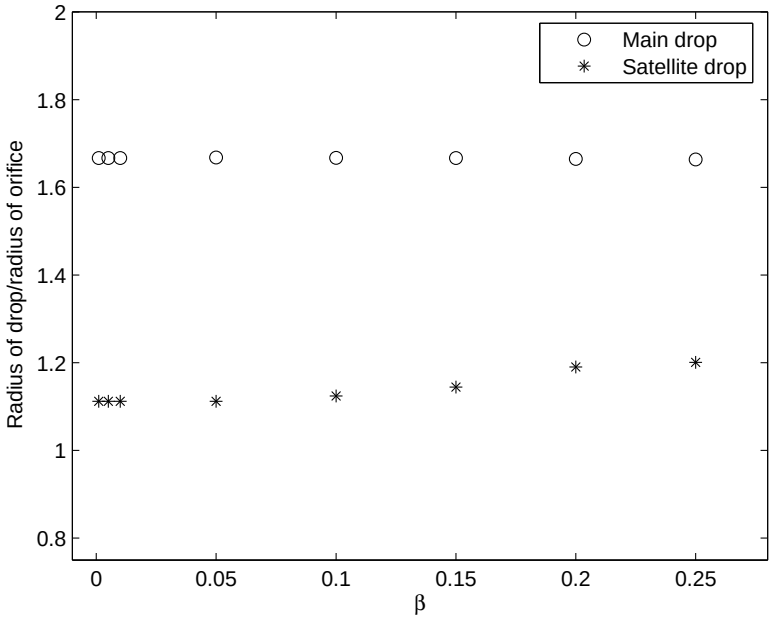

Figure 8.21: A plot showing drop size against β. $We = 100$, $Rb = 1$, $Re = 3000$, $\alpha = 0.01$ and $\delta = 0.01$. Circles correspond to main drops and stars correspond to satellite drops.

Figure 8.21 shows β against drop size for the same parameter values and the same values of β as in figure 8.20 but with $\alpha = 0.01$, corresponding to a lower amplitude of sound wave. When $\alpha = 0.01$ satellite drops are formed so insonification is ineffective. When β=0.001, 0.005 and 0.01 the size of the main and satellite drops remain constant, however at higher values of β the size of the main drop decreases slightly, (this is similar to the result obtained when $\alpha = 0.1$) and the size of the satellite drop increases slightly. This agrees with results presented in figure 8.17 and 8.19.

Figure 8.22 shows a plot of β against drop size for a jet with $We = 50$, $Rb = 1$, $\alpha = 0.1$, $\delta = 0.01$ and $Re = 100$. The values of β are 0.001, 0.005, 0.01, 0.05, 0.01, 0.15, 0.2 and 0.25, satellite drops appear at $\beta = 0.3$. The drop size remains constant for β=0.001, 0.005 and 0.01 but then decreases slightly with increasing β. This is the same relationship observed in figures 8.16, 8.18 and 8.20.

In figure 8.23 β is plotted against drop size. All the parameter values and the values of β are the same as in figure 8.22 but with $\alpha = 0.01$ corresponding to a lower amplitude

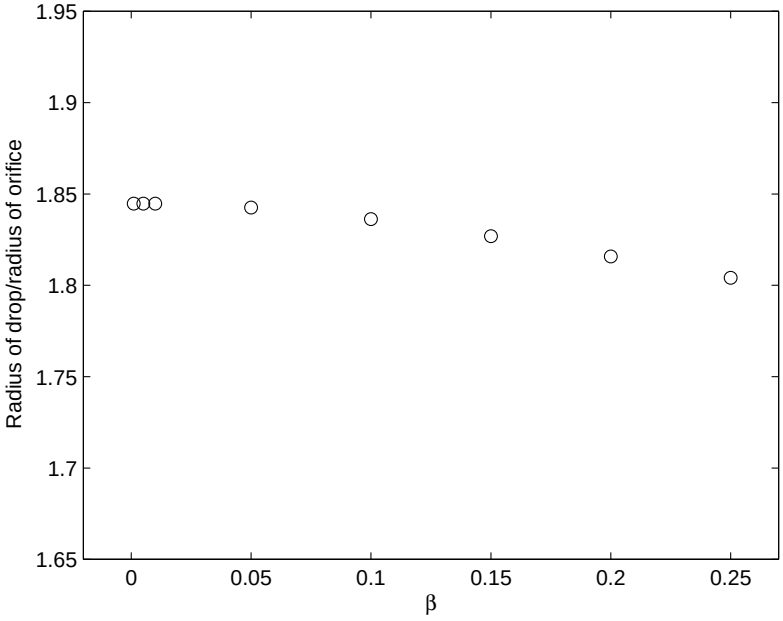

Figure 8.22: A plot showing drop size against β. $We = 50$, $Rb = 1$, $Re = 100$, $\alpha = 0.1$ and $\delta = 0.01$.

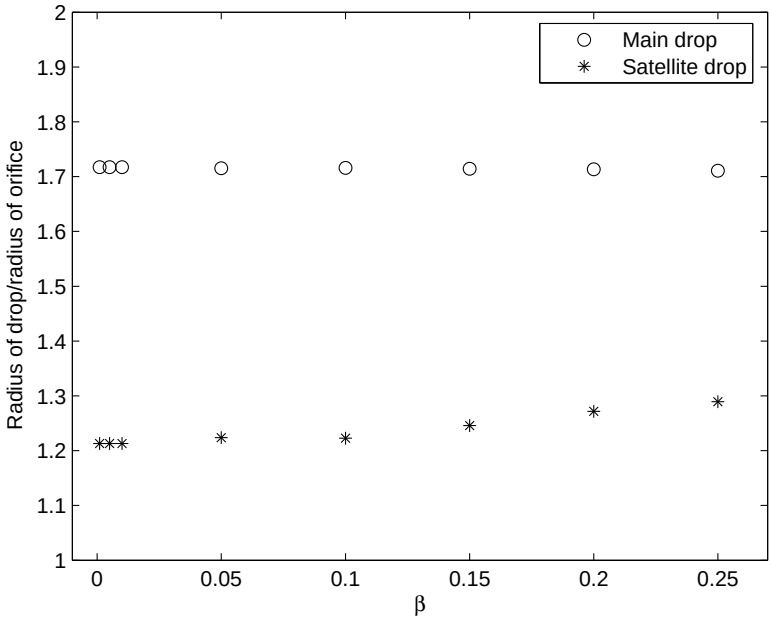

Figure 8.23: A plot showing drop size against β. $We = 50$, $Rb = 1$, $Re = 100$, $\alpha = 0.01$ and $\delta = 0.01$. The circles correspond to main drop sizes and the stars correspond to satellite drop sizes.

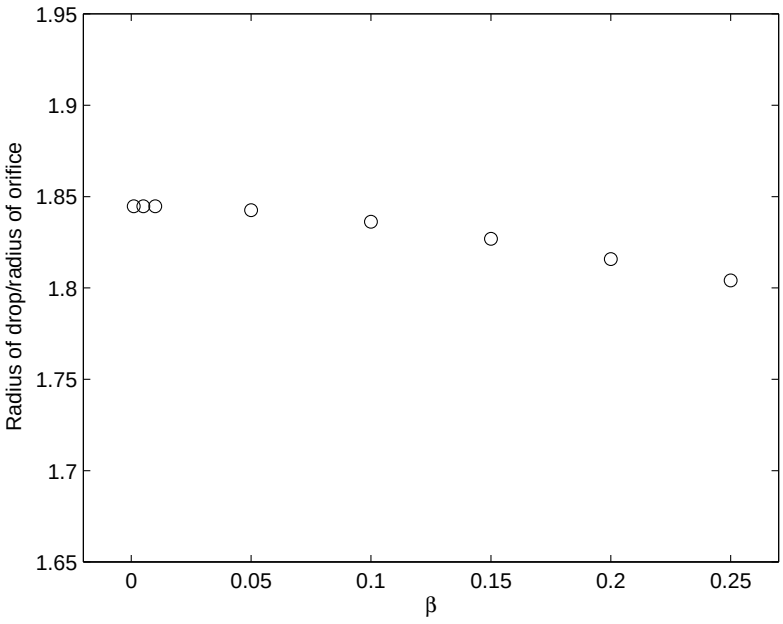

Figure 8.24: A plot showing drop size against β. $We = 5$, $Rb = 1$, $Re = 3000$, $\alpha = 0.1$ and $\delta = 0.01$.

sound wave. We can see that satellite drops occur therefore insonification has not been successful. At β=0.001, 0.005 and 0.02 the size of the main and satellite drops is constant, at higher values of β the size of the main drop decreases slightly, (this is similar to the result obtained when $\alpha = 0.1$) the size of the satellite drops increases slightly.

Figure 8.24 is a plot of β against drop size for a jet with $We = 5$, $Rb = 1$, $Re = 3000$, $\alpha = 0.1$ and $\delta = 0.01$. The values of β are 0.001, 0.005, 0.01, 0.05, 0.1, 0.15, 0.2, 0.25, 0.3 and 0.35. Satellite drops appeared at $\beta = 0.4$. At β=0.001, 0.005 and 0.01 the size of the main drop remains constant. At higher values of β the drop size decreases slightly. This agrees with results presented in figures 8.16, 8.18, 8.20 and 8.22.

Figure 8.25 is a plot of β against drop size for the same parameter values and the same values of β as in figure 8.24 but with $\alpha = 0.01$ which corresponds to a lower amplitude sound wave. We can see when $\alpha = 0.01$ satellite drops occur so insonification is ineffective. When β=0.001, 0.005, 0.01, 0.05, 0.1 and 0.15 the size of the main and satellite drops remain constant. At higher values of β the size of main drop decreases

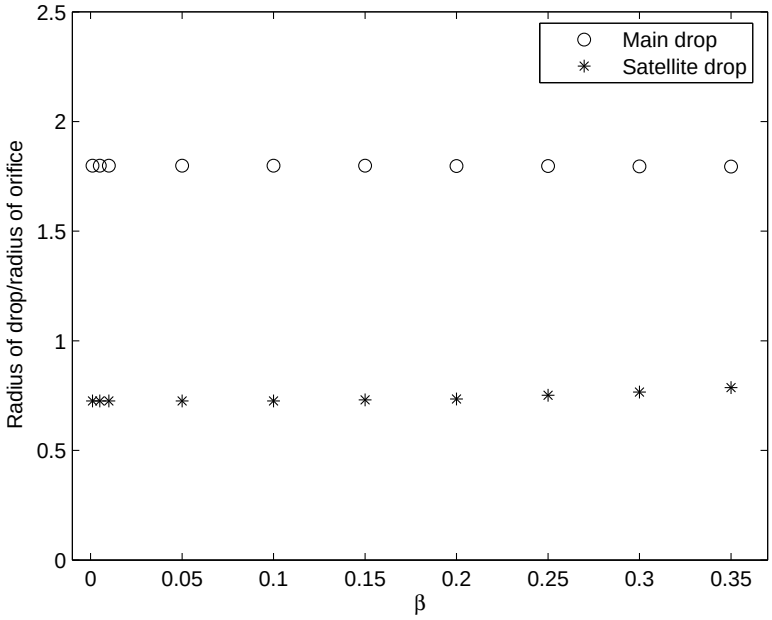

Figure 8.25: A plot showing drop size against β. $We = 5$, $Rb = 1$, $Re = 3000$, $\alpha = 0.01$ and $\delta = 0.01$. The circles correspond to main drop sizes and the stars correspond to satellite drop sizes.

slightly, (this is similar to the result obtained when $\alpha = 0.1$) and the size of the satellite drop increases slightly. This agrees with results presented in figures 8.17, 8.19, 8.21 and 8.23.

8.4 Break-up behaviour and α

Figures 8.26 and 8.27 are simulations of jets with parameter values obtained during insonification experiments carried out on the pilot scale rig. In figure 8.26 $We = 30.17$, $Rb = \infty$, $Re = 1800$ and the sound wave had a frequency of 200 Hz corresponding to $\beta = 0.237$. In the experiments insonification successfully eliminated almost all satellite drops and we obtained mode 1 break-up. In figure 8.27 $We = 46.27$, $Rb = 1.67$, $Re = 2229$ and the sound wave has a frequency of 10 Hz which corresponds to $\beta = 0.00956$. In the experiments insonification was unsuccessful and satellite drops were not eliminated. In both cases α is varied, so that $\alpha = 0,\ 0.01,\ 0.03,\ 0.05,\ 0.08$ and 0.1, to investigate the effect of increasing the amplitude of the sound wave on the break-up of the jet. (Note

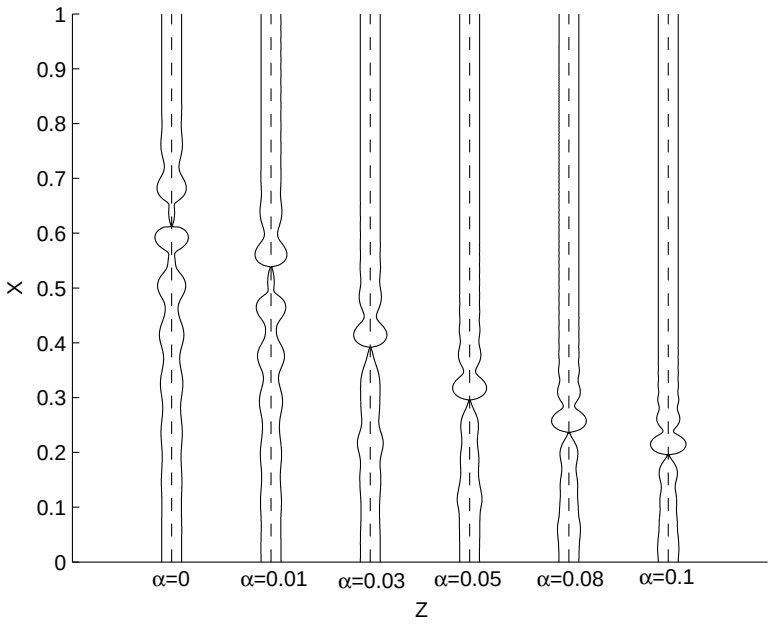

Figure 8.26: Simulations of jets with $We = 30.17$, $Rb = \infty$, $Re = 1800$ and $\delta = 0.01$. All the jets are experiencing a sound wave corresponding to $\beta = 0.237$. The amplitude of the wave in each case corresponding to $\alpha = 0,\ 0.01,\ 0.03,\ 0.05,\ 0.08$ and 0.1.

that $\alpha = 0$ corresponds to no insonification.) In both cases we choose $\delta = 0.01$.

In figure 8.26, when $\alpha = 0.01$ insonification has no effect the break-up mechanism and satellite drops are not eliminated. When $\alpha = 0.03$ the break-up mechanism has changed and no ligands form between the drops so no satellite drops can form. Therefore we have mode 1 break-up and insonification has been successful. At $\alpha = 0.05,\ 0.08$ and 0.1 satellite drops have been eliminated and mode 1 break-up is obtained. Note that increasing α decreases the break-up length. This was observed in experiments.

In figure 8.27 we can see that when $\alpha = 0.01,\ 0.03$ and 0.05 the break-up mechanism is similar to the break-up mechanism obtained when $\alpha = 0$, mode 2. However when $\alpha = 0.08$ the disturbances on the surface of the jet are very small leading to the possibility of mode 1 break-up. When $\alpha = 0.1$ we obtain mode 1 break-up.

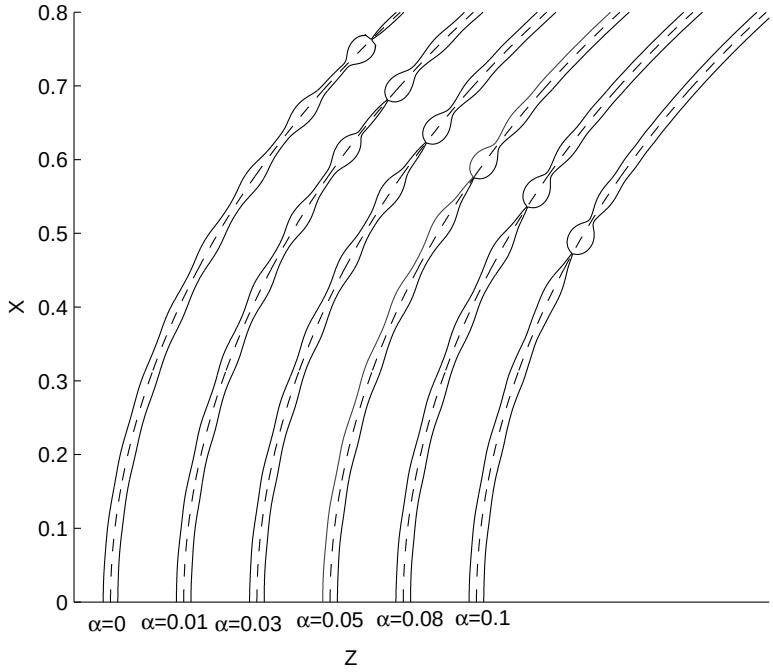

Figure 8.27: Simulations of jets with $We = 46.27$, $Rb = 1.67$, $Re = 2229$ and $\delta = 0.01$. All the jets are experiencing a sound wave corresponding to $\beta = 0.00956$. The amplitude of the wave in each case corresponding to $\alpha = 0,\ 0.01,\ 0.03,\ 0.05,\ 0.08$ and 0.1.

In figure 8.26, the amplitude of the sound wave required for effective insonification is lower than in figure 8.27. This seems to explain why we see better insonification at lower rotation rates in our experiments.

8.5 Summary

Experiments were carried out for four different Rossby numbers ($Rb = \infty$, 7.01, 1.12 and 7.01) with three different wave frequencies (10, 100 and 200 Hz). At 10 Hz insonification had a negligible effect on the drop size distributions at all the Rossby numbers. At 100 Hz insonification reduces the number of satellite drops at $Rb = 7.01$ and eliminates almost all the satellite drops at $Rb = \infty$ but there was a negligible effect at $Rb = 1.67$ and $Rb = 1.12$. At 200 Hz a significant number of satellite drops were eliminated at $Rb = \infty$, 7.01 and 1.67 but not at $Rb = 1.12$.

During the experiments the volume of the sound wave generated from the sub-aqua speaker was louder at 100 Hz than 10 Hz, and the volume of the sound wave was louder at 200 Hz than 100 Hz despite the volume setting being the same in all experiments. This suggested that the amplitude of the wave was larger at 200 Hz than 100 Hz and larger at 100 Hz than 10 Hz which implied a minimum amplitude of sound wave was required before insonification eliminates satellite drops.

These comments are fairly subjective since the human ear detects sound more easily at some frequencies than others and the ear does not have a uniform frequency response. However the numerics clearly point to a critical volume above which insonification is successful.

Lower Rossby number corresponded to higher rotation rates therefore there were greater rotational forces for the sound wave to overcome at lower Rossby number. So a larger amplitude of sound wave was required for insonification to be successful at lower Rossby numbers.

Theoretical studies showed that insonification was predicted to eliminate satellite drops successfully using a frequency of around 1 Hz up to 250-300 Hz for a range of parameters. This was encouraging since it means for further work we could design a more sophisticated experiment and therefore successfully eliminate satellite drops experimentally. The theoretical work was repeated for a lower amplitude sound wave and we found that insonification was unsuccessful. This showed that the theory predicted that a minimum amplitude of sound wave was required for satellite drops to be eliminated, which agrees with experimental results.

The theoretical studies were also carried out for parameter values that were not obtained in the experiments. We obtained similar results for all parameter values, the relationship between β (the non-dimensional frequency of the sound wave) and drop size was similar in all the cases considered and insonification was unsuccessful at $\alpha = 0.01$ but successful at $\alpha = 0.1$. Again the theory predicted that a minimum amplitude was required for insonification to be successful.

Simulations were carried out in two experimental parameter regimes; when insonification was successful and mode 1 break-up was obtained and when insonification was unsuccessful and the satellite drops were not eliminated. The amplitude of the sound wave was increased in each case. In the parameter regime where insonification was observed to be successful experimentally the onset of mode 1 break-up was predicted to occur at a lower amplitude than in the parameter regime where insonification was unsuccessful in experiments.

The theory in this chapter could be used to model forced mechanical vibrations at the orifice such as a vibrating pin. This is important since mechanical vibrations can produce oscillations with a greater amplitude than insonification, and could be used to control jet break-up in more viscous jets.

Chapter 9

Unsteady trajectory

9.1 Inviscid analysis

9.1.1 Introduction

In this subsection we give a brief overview of the non-linear inviscid analysis carried out by Părău *et al.* [34] for an unsteady trajectory. We consider long waves with wavelength $\lambda \sim s_0$ (so $\gamma \sim \epsilon$, see chapter 5), consider all variables to be dependent on long length and time scales only and pose all expansions in terms of ϵ as in chapter 6. We allow the centreline to be time-dependent so $X_t \neq 0$ and $Z_t \neq 0$. The expansions in v and w must now contain leading order terms to allow the centreline to move.

The model is written down using the continuity equation, Euler's equations, the kinematic condition and the dynamic condition. The full equations are given in Wallwork *et al.* [42].

We pose the following expansions

$$\left.\begin{aligned} u &= u_0(s,t) + (\epsilon n)u_1(s,\phi,t) + (\epsilon n)^2 u_2(s,\phi,t) + \cdots \\ v &= v_0(s,\phi,t) + \epsilon n v_1(s,\phi,t) + \cdots \\ w &= w_0(s,\phi,t) + \epsilon n w_1(s,\phi,t) + \cdots \\ R &= R_0(s,t) + \epsilon R_1(s,\phi,t) + \cdots \\ X &= X_0(s,t) + \epsilon X_1(s,t) + \cdots \\ Z &= Z_0(s,t) + \epsilon Z_1(s,t) + \cdots \\ p &= p_0(s,t) + \epsilon p_1(s,\phi,n,t) + \cdots \end{aligned}\right\} \tag{9.1}$$

and write $X_0 \to X$, $Z_0 \to Z$. From the kinematic condition we obtain

$$v_0(s,\phi,t) = (Z_s X_t - Z_t X_s)\cos\phi \tag{9.2}$$

at leading order. From the continuity equation we obtain

$$v_0 + \frac{\partial w_0}{\partial \phi} = 0 \tag{9.3}$$

at leading order. Substituting equation (9.2) into (9.3) and integrating gives

$$w_0(s,\phi,t) = -(Z_s X_t - Z_t X_s)\sin\phi. \tag{9.4}$$

Denoting $E = Z_s X_t - Z_t X_s$, the s-momentum equation gives

$$u_{0t} + E(Z_{st}X_s - X_{st}Z_s) + u_0 u_{0s} + u_0(X_s Z_{ss} - X_{ss}Z_s)E = -p_{0s} + \frac{2E}{Rb} + \frac{(X+1)X_s + ZZ_s}{Rb^2}. \tag{9.5}$$

at order ϵ. The n-momentum equation is

$$p_{1n} = -\cos\phi((E_t + u_0(X_{st}X_s - Z_{st}X_s) + Ev_1 + u_0E_s - (X_sZ_{ss} - X_{ss}Z_s)u_0^2 + \frac{2u_0}{Rb} \\ -\frac{1}{Rb^2}((X+1)Z_s - ZX_s)) - \sin\phi E(w_1 - v_{1\phi}). \tag{9.6}$$

at order ϵ. The ϕ-momentum equation is

$$p_{1\phi} = n\sin\phi(E_t + u_0(X_{st}Z_s - Z_{st}X_s) + Ev_1 + u_0E_s - (X_sZ_{ss} - X_{ss}Z_s)u_0^2 + \frac{2u_0}{Rb} \\ -\frac{1}{Rb^2}((X+1)Z_s - ZX_s)) - n\cos\phi Ew_1 + n\sin\phi Ew_{1\phi} \tag{9.7}$$

at order ϵ. Differentiating equation (9.6) with respect to ϕ gives

$$p_{1\phi n} = \sin\phi((E_t + u_0(X_{st}Z_s - Z_{st}X_s) + Ev_1 + u_0E_s - (X_sZ_{ss} - X_{ss}Z_s)u_0^2 + \frac{2u_0}{Rb} \\ -\frac{1}{Rb^2}((X+1)Z_s - ZX_s)) + \cos\phi Ev_{1\phi} + \cos\phi E(w_1 - v_{1\phi}) + \sin\phi E(w_{1\phi} - v_{1\phi\phi}) \tag{9.8}$$

and differentiating equation (9.7) with respect to n gives

$$p_{1n\phi} = \sin\phi((E_t + u_0(X_{st}Z_s - Z_{st}X_s) + Ev_1 + u_0E_s - (X_sZ_{ss} - X_{ss}Z_s)u_0^2 + \frac{2u_0}{Rb} \\ -\frac{1}{Rb^2}((X+1)Z_s - ZX_s)) + \cos\phi Ew_1 - \sin\phi Ew_{1\phi}. \tag{9.9}$$

Equating equations (9.8) and (9.9) gives

$$2w_{1\phi} - v_{1\phi\phi} = 0. \tag{9.10}$$

From the continuity equation, at order ϵ we have

$$u_{0s} + 2v_1 + w_{1\phi} + (X_sZ_{ss} - X_{ss}Z_s)(Z_sX_t - Z_tX_s) = 0. \tag{9.11}$$

Differentiating equation (9.11) with respect to ϕ we arrive at

$$2v_{1\phi} + w_{1\phi\phi} = 0. \tag{9.12}$$

From equations (9.10) and (9.12) we obtain

$$v_1(s,\phi,t) = a_1(s,t)\cos 2\phi + b_1(s,t)\sin 2\phi + c_1(s,t)$$

and

$$w_1(s,\phi,t) = -a_1(s,t)\sin 2\phi + b_1(s,t)\cos 2\phi + c_2(s,t)$$

where a_1, b_1, c_1 and c_2 are unknowns. From equation (9.11) we find

$$c_1(s,t) = -\frac{u_{0s}}{2} - \frac{(X_s Z_{ss} - X_{ss} Z_s)E}{2}. \tag{9.13}$$

From the kinematic condition, at order ϵ we obtain

$$R_{0t} + \frac{u_{0s}R_0}{2} + \frac{(X_s Z_{ss} - X_{ss} Z_s)ER_0}{2} + u_0 R_{0s} - R_{0s}(X_t Z_s + Z_t X_s) = 0 \tag{9.14}$$

and $a_1 = b_1 = 0$. From equation (9.6) we can write down an expression for p_1

$$\begin{aligned} p_1(s,\phi,t) = -n\cos\phi \Bigg(& E_t + u_0(X_{st}Z_s - Z_{st}X_s) - \frac{E}{2}(u_{0s} + (X_s Z_{ss} - X_{ss}Z_s)E) + u_0 E_s \\ & -(X_s Z_{ss} - X_{ss}Z_s)u_0^2 + \frac{2u_0}{Rb} - \frac{1}{Rb^2}((X+1)Z_s - ZX_s)\Bigg) - n\sin\phi E c_2 + p_{11}(s,t). \end{aligned} \tag{9.15}$$

From the dynamic condition we obtain

$$p_0(s,t) = \frac{1}{R_0 We} \tag{9.16}$$

at leading order and

$$p_1(s,\phi,t) = \frac{1}{We}\left(-\frac{R_{1\phi\phi}+R_1}{R_0^2} + \cos\phi(X_sZ_{ss} - X_{ss}Z_s)\right) \tag{9.17}$$

at order ϵ. Differentiating equation (9.16) and substituting into equation (9.5) we have

$$u_{0t}+E(Z_{st}X_s-X_{st}Z_s)+u_0u_{0s}+u_0(X_sZ_{ss}-X_{ss}Z_s)E = -\frac{1}{We}\left(\frac{1}{R_0}\right)_s+\frac{2E}{Rb}+\frac{(X+1)X_s+ZZ_s}{Rb^2}. \tag{9.18}$$

Equating (9.15) and (9.17), we have

$$\begin{aligned}\frac{R_{1\phi\phi}+R_1}{WeR_0^2} + p_{11}(s,t) - \cos\phi\Bigg[R_0\Bigg(E_t + u_0(X_{st}Z_s - Z_{st}X_s) - \frac{E}{2}(u_{0s} + (X_sZ_{ss} - X_{ss}Z_s)E) + u_0E_s \\ -(X_sZ_{ss} - X_{ss}Z_s)u_0^2 + \frac{2u_0}{Rb} - \frac{1}{Rb^2}((X+1)Z_s - ZX_s)\Bigg) + \frac{X_sX_{ss} - X_{ss}Z_s}{We}\Bigg] - \sin\phi R_0c_2 = 0.\end{aligned} \tag{9.19}$$

From equation (9.19) we impose the condition that R_1 is periodic in ϕ and therefore obtain $c_2 = 0$ (as we require $E \neq 0$) which gives

$$\begin{aligned}E_t + u_0(X_{st}Z_s - Z_{st}X_s) + E\left(-\frac{u_{0s}}{2} - (X_sZ_{ss} - X_{ss}Z_s)\frac{E}{2}\right) + u_0E_s \\ = (X_sZ_{ss} - X_{ss}Z_s)u_0^2 - \frac{2u_0}{Rb} + \frac{1}{Rb^2}((X+1)Z_s - ZX_s) - \frac{X_{ss}Z_s - X_sZ_{ss}}{R_0We}.\end{aligned} \tag{9.20}$$

We need to solve equations (9.20), (9.14), (9.18) and the arc-length condition subject to the initial and boundary conditions given in chapters 5 and 6. If X_0 and Z_0 are not time-dependent and s and t are replaced by $\bar{s}$ and $\bar{t}$ in derivatives of u_0 and R_0 equations (9.20), (9.14), (9.18) and the arc-length condition reduces at leading order to the system from section 5.1 namely, equations (5.1)-(5.4), as expected.

In the next section we present a method of finding $X(s,t)$ and $Z(s,t)$ by decomposing these terms into a steady and unsteady part.

9.1.2 Finding $X(s,t)$ and $Z(s,t)$

We assume $X(s,t)$ and $Z(s,t)$ are at leading order functions of s only with small terms added which are functions of s and t, so that

$$X(s,t) = \tilde{X}(s) + \hat{X}(s,t)$$

and

$$Z(s,t) = \tilde{Z}(s) + \hat{Z}(s,t),$$

where $\hat{X}$ and $\hat{Z}$ are small so we assume the centreline is almost but not quite steady. (Note that if this assumption is not justified then $\hat{X}$ and $\hat{Z}$ would become large. We shall see this does not happen.) Substituting these expansions into the arc-length condition $X_s^2 + Z_s^2 = 1$, we arrive at

$$\tilde{X}_s^2 + \tilde{Z}_s^2 = 1 \tag{9.21}$$

at leading order, and

$$\tilde{X}_s\hat{X}_s + \tilde{Z}_s\hat{Z}_s = 0 \tag{9.22}$$

at next order. Substitute these expansions into the definition of E given by

$$E = X_t Z_s - X_s Z_t, \tag{9.23}$$

and we have

$$E = \hat{X}_t\tilde{Z}_s - \tilde{X}_s\hat{Z}_t \tag{9.24}$$

at leading order. Differentiating equation (9.22) with respect to t we obtain

$$\tilde{X}_s\hat{X}_{st} + \tilde{Z}_s\hat{Z}_{st} = 0 \tag{9.25}$$

and differentiating equation (9.24) with respect to s gives

$$E_s = \hat{X}_{st}\tilde{Z}_s + \hat{X}_t\tilde{Z}_{ss} - \tilde{X}_{ss}\hat{Z}_t - \tilde{X}_s\hat{Z}_{st}. \tag{9.26}$$

Eliminating $\hat{Z_{st}}$ from equation (9.26) using equation (9.25) gives

$$E_s = \hat{X}_{st}\tilde{Z}_s + \hat{X}_t\tilde{Z}_{ss} - \tilde{X}_{ss}\hat{Z}_t + \frac{\tilde{X}_s^2\hat{X}_{st}}{\tilde{Z}_s}. \tag{9.27}$$

Eliminating $\hat{Z}_t$ from equation (9.27) using equation (9.24) gives

$$E_s = \hat{X}_{ts}\tilde{Z}_s + \hat{X}_t\tilde{X}_{ss} + \frac{\tilde{X}_s^2\hat{X}_{st}}{\tilde{Z}_s} - \tilde{X}_{ss}\left(\frac{\hat{X}_t\tilde{Z}_s - E}{\tilde{X}_s}\right). \tag{9.28}$$

Let $q = \hat{X}_t$ so equation (9.28) is

$$q_s + q\tilde{Z}_s\left(\frac{\tilde{Z}_{ss}\tilde{X}_s - \tilde{X}_{ss}\tilde{Z}_s}{\tilde{X}_s}\right) + \frac{\tilde{Z}_s\tilde{X}_{ss}E}{\tilde{X}_s} - E_s\tilde{Z}_s = 0. \tag{9.29}$$

By differentiating equation (9.21) with respect to s we can eliminate $\tilde{Z}_{ss}$ from (9.29) to give

$$q_s - \frac{\tilde{X}_{ss}}{\tilde{X}_s}q + \frac{\tilde{Z}_s\tilde{X}_{ss}E}{\tilde{X}_s} - \tilde{Z}_sE_s = 0. \tag{9.30}$$

Equation (9.30) is a first order ordinary differential equation which can be solved using the integrating factor $1/\tilde{X}_s$. We can write equation (9.30) as

$$\frac{d}{ds}\left(\frac{q}{\tilde{X}_s}\right) = \frac{E_s\tilde{Z}_s}{\tilde{X}_s} - \frac{\tilde{X}_{ss}\tilde{Z}_sE}{\tilde{X}_s^2} \tag{9.31}$$

which can be integrated to give

$$\frac{q}{\tilde{X}_s} = \int_0^s \left(\frac{E_sZ_{0s}}{\tilde{X}_s} - \frac{\tilde{X}_{ss}\tilde{Z}_sE}{\tilde{X}_s^2}\right) ds. \tag{9.32}$$

We can then integrate the first term under the integral by parts

$$\frac{q}{\tilde{X}_s} = \frac{E\tilde{Z}_s}{\tilde{X}_s} - \int_0^s E\left(\frac{\tilde{Z}_{ss}\tilde{X}_s}{\tilde{X}_s^2} - \frac{\tilde{X}_{ss}\tilde{Z}_s}{\tilde{X}_s^2} + \frac{\tilde{X}_{ss}\tilde{Z}_s}{\tilde{X}_s^2}\right) ds + c(t)$$

where $c(t)$ is function of t which will be determined. Therefore we have

$$q = E\tilde{Z}_s - \tilde{X}_s \int_0^s \frac{E\tilde{Z}_{ss}}{\tilde{X}_s} ds + c(t)\tilde{X}_s, \tag{9.33}$$

so

$$\hat{X}_t = E\tilde{Z}_s - \tilde{X}_s \int_0^s \frac{E\tilde{Z}_{ss}}{\tilde{X}_s} ds + c(t)\tilde{X}_s. \tag{9.34}$$

At $s = 0$, $E = E_s = 0$ therefore $c(t) = 0$. From equation (9.34) we have

$$\hat{X}_t = E\tilde{Z}_s - \tilde{X}_s \int_0^s \frac{E\tilde{Z}_{ss}}{\tilde{X}_s} ds. \tag{9.35}$$

By substituting (9.35) into equation (9.24) we arrive at

$$\hat{Z}_t = -E\tilde{X}_s - \tilde{Z}_s \int_0^s \frac{E\tilde{Z}_{ss}}{\tilde{X}_s} ds. \tag{9.36}$$

We substitute (9.35) and (9.36) into the left hand side of equation (9.20) and linearise the left hand side of equation (9.20) in E, since E is proportional to $\hat{X}$ and $\hat{Z}$. Replacing the X and Z terms on the right hand side of equation (9.20) with $\tilde{X}$ and $\tilde{Z}$, we arrive at

$$\begin{aligned} E_t + u_0\left(E_s - \frac{\tilde{X}_{ss}}{\tilde{Z}_s}\int_0^s \frac{E\tilde{Z}_{ss}}{\tilde{X}_s} ds\right) + u_0 E_s - \frac{E}{2}u_{0s} \\ = u_0^2 S - \frac{2}{Rb}u_0 + \frac{(\tilde{X}+1)\tilde{Z}_s - \tilde{Z}\tilde{X}_s}{Rb^2} - \frac{S}{WeR_0} \end{aligned} \tag{9.37}$$

This integro-partial differential equation in E is solved using finite differences. Then equations (9.35) and (9.36) can be used to find $\hat{X}$ and $\hat{Z}$.

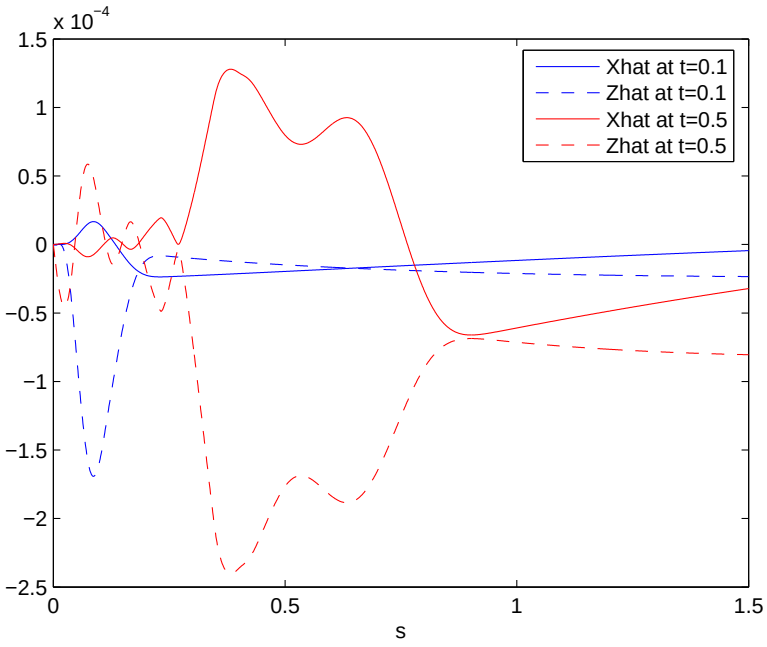

Figure 9.1: The deviation of the trajectory from the steady state at $t = 0.1$ and 0.5 for $We = 70$, $Rb = 1$ and $\delta = 0.1$.

9.1.3 Results

In this subsection we obtain the deviation of the centreline of the jet from its steady-state, namely $\hat{X}$ and $\hat{Z}$ for inviscid jets for $Rb = 1$ and $Rb = 10$. In figures 9.1 and 9.2 $\hat{X}$ and $\hat{Z}$ are plotted at $t = 0.1$ and $t = 0.5$ in non-dimensional units.

Figure 9.1 plots the arc-length s against $\hat{X}$ and $\hat{Z}$, the deviation of the trajectory from its undisturbed position for an inviscid jet with $We = 70$, $Rb = 1$ and $\delta = 0.1$. The maximum deviation is of order 10^{-4} which is small compared to $X_0(s)$ and $Z_0(s)$. Therefore the trajectory is approximately steady.

Figure 9.2 plots the arc-length against the deviation of the trajectory from the steady state for an inviscid jet with $We = 70$, $Rb = 10$ and $\delta = 0.1$. The maximum deviation of the centreline from the steady-state is of the order 10^{-5} which is again small compared to $X_0(s)$ and $Z_0(s)$ and is smaller than in figure 9.1. This is to be expected since when $Rb = 10$ there is less rotation than when $Rb = 1$ so we would expect the

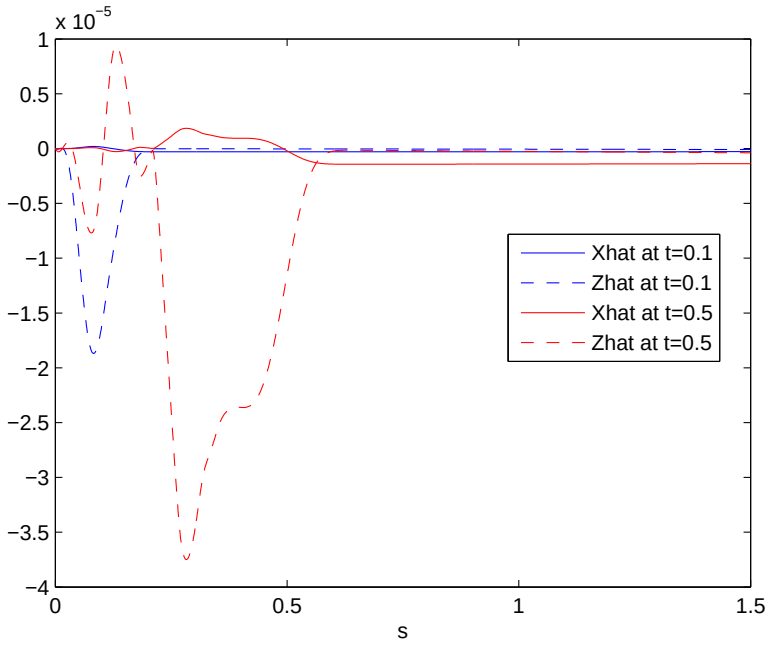

Figure 9.2: The deviation of the trajectory from the steady state at $t = 0.1$ and 0.5 for $We = 70$, $Rb = 10$ and $\delta = 0.1$.

deviation from the steady state to be less.

Figure 9.3 shows a simulation of an inviscid jet at $t = 0.1$ and $t = 0.5$, with $We = 70$ and $Rb = 1$. We can see the trajectory of the jet is almost exactly steady, which is expected. Simulations were carried out for other parameter values and the trajectory was always found to be steady for inviscid jets. This means that the assumption in chapter 5 for inviscid jets that the centreline is steady is a very good approximation.

9.2 Inclusion of viscosity when the centreline is time-dependent

In this section we include viscosity into the previous analysis. The model is written down using the continuity equation, the Navier-Stokes equations, the kinematic condition and the tangential stress conditions given in chapter 6. We denote $X_s Z_{ss} - X_{ss} Z_s$ as S and $X_t Z_s - Z_t X_s$ as E. We pose the same expansions given in (6.39) except v and w now have leading order terms such that,

$$v = u_0(s, \phi, t) + (\epsilon n) v_1(s, \phi, t) + (\epsilon n)^2 v_2(s, \phi, t) + \cdots$$

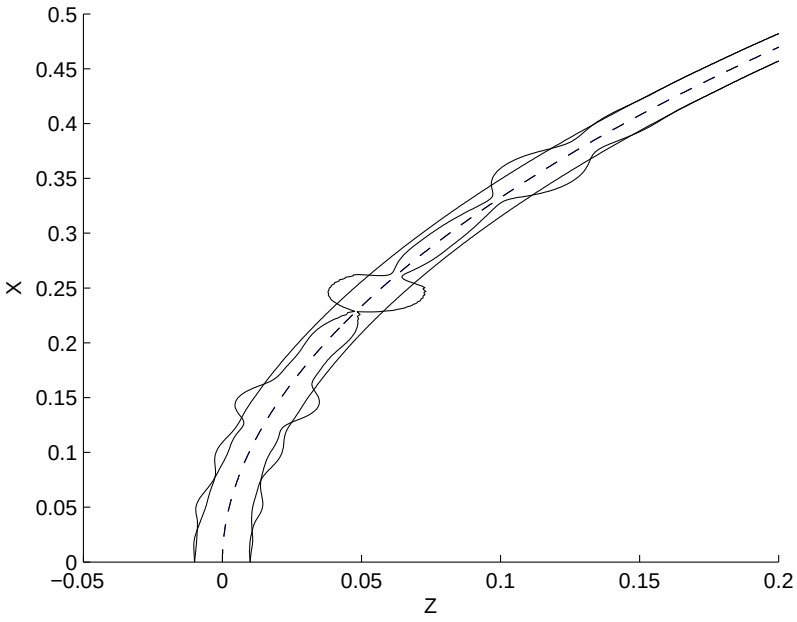

Figure 9.3: Simulation of an inviscid jet with $Rb = 1$, $We = 70$ and $\delta = 0.1$ at $t = 0.5$ and $= 0.1$.

and

$$w = w_0(s, \phi, t) + (\epsilon n) w_1(s, \phi, t) + (\epsilon n)^2 w_2(s, \phi, t) + \cdots .$$

We carry out the analysis in a similar way to chapter 6. From the kinematic condition, equation (6.32), we obtain

$$v_0(s, \phi, t) = E \cos \phi \tag{9.38}$$

at $O(1)$. From the tangential stress condition in the ϕ-direction (6.34) we have

$$R_0^3 v_{1\phi} = 0 \tag{9.39}$$

at $O(\epsilon)$ and

$$3R_0^2 R_1 v_{1\phi} + R_0^4 (w_2 + v_{2\phi}) - 2R_0^2 R_{1\phi} w_{1\phi} = 0 \tag{9.40}$$

at $O(\epsilon^2)$. From equation (9.39) we have

$$v_{1\phi} = 0. \tag{9.41}$$

From the continuity equation (6.26), we have

$$v_0 + \frac{\partial w_0}{\partial \phi} = 0 \tag{9.42}$$

at leading order,

$$u_{0s} + 2v_1 + w_{1\phi} + ES = 0 \tag{9.43}$$

at $O(\epsilon n)$ and

$$u_{1s} + 3v_2 + w_{2\phi} + (3v_1 + w_{1\phi})\cos\phi S - w_1 \sin\phi S = 0 \tag{9.44}$$

at $O((\epsilon n)^2)$. By substituting (9.38) into equation (9.42) and integrating we obtain

$$w_0(s, \phi, t) = -E \sin\phi. \tag{9.45}$$

By differentiating equation (9.43) and substituting (9.41) into the resulting equation we have

$$w_{1\phi\phi} = 0. \tag{9.46}$$

Therefore

$$w_{1\phi} = C$$

but since we require w_1 to be periodic in ϕ, $C = 0$. So $w_{1\phi} = 0$. This means equation (9.43) gives

$$v_1 = -\frac{u_{0s}}{2} - \frac{ES}{2} \tag{9.47}$$

and equation (9.40) gives

$$w_2 + v_{2\phi} = 0. \tag{9.48}$$

From the tangential stress condition in the s-direction (6.33) we have

$$u_1 = (u_0 S - E_s)\cos\phi \tag{9.49}$$

at leading order and

$$u_2 = \frac{3}{2}(u_{0s} + SE)\frac{R_{0s}}{R_0} + \frac{u_{0ss} + (SE)_s}{4} \tag{9.50}$$

at next order. Differentiating equation (9.48) with respect to ϕ we obtain

$$w_{2\phi} = -v_{2\phi\phi}.$$

We substitute this into equation (9.44) to give

$$v_{2\phi\phi} - 3v_2 = u_{1s} + 3v_1 \cos\phi S - w_1 \sin\phi S. \tag{9.51}$$

Substituting equations (9.47) and (9.49) into equation (9.51) we arrive at

$$v_{2\phi\phi} - 3v_2 = \cos\phi \left(u_0 S_s - E_{ss} - \frac{u_{0s}S}{2} - \frac{3S^2E}{2} \right) - w_1 S \sin\phi. \tag{9.52}$$

The particular solution to (9.52) is

$$v_2 = \frac{1}{4}\left(\frac{u_{0s}}{2}S - u_0 S_s + \frac{3}{2}ES^2 + E_{ss} \right)\cos\phi + \frac{w_1}{4}S\sin\phi \tag{9.53}$$

and we obtain

$$w_2 = \frac{1}{4}\left(\frac{u_{0s}}{2}S - u_0 S_s + \frac{3}{2}ES^2 + E_{ss} \right)\sin\phi - \frac{w_1}{4}S\cos\phi. \tag{9.54}$$

Using the n-momentum equation (6.30) we have

$$p_1 = \left(-E_t - u_0(X_{st}Z_s - Z_{st}X_s) - u_0 E_s + \frac{E}{2}(u_{0s} + SE) + u_0^2 S - \frac{2}{Rb}u_0 + \frac{(X+1)Z_s - ZX_s}{Rb^2} \right.$$
$$\left. + \frac{1}{Re}\left(E_{ss} - \frac{3}{2}ES^2 - \frac{5}{2}u_{0s}S - u_0 S_s \right) \right)\cos\phi + \left(\frac{S}{Re} - E \right) w_1 \sin\phi \tag{9.55}$$

at $O(\epsilon)$. From the normal stress condition, equation (6.35) we obtain

$$p_0 = -\frac{u_{0s} + SE}{Re} + \frac{1}{R_0 We} \tag{9.56}$$

at leading order and

$$R_0 p_1 - \frac{4}{Re} R_0 v_2 = \frac{1}{We}\left(-\frac{R_{1\phi\phi} + R_1}{R_0^2} + S\cos\phi\right) \tag{9.57}$$

at $O(\epsilon)$. Substituting equation (9.55) into equation (9.57) we obtain

$$\begin{aligned} -\frac{R_{1\phi\phi} + R_1}{We R_0^3} = \Bigg(&-E_t - u_0(X_{st}Z_s - Z_{st}X_s) - u_0 E_s + \frac{E}{2}(u_{0s} + SE) + u_0^2 S \\ &-\frac{2}{Rb}u_0 + \frac{(X+1)Z_s - ZX_s}{Rb^2} + \frac{1}{Re}(-3ES^2 - 3u_{0s}S) - \frac{S}{We R_0}\Bigg)\cos\phi - w_1 E\sin\phi. \end{aligned} \tag{9.58}$$

Since we require R_1 to be periodic in ϕ the coefficients of $\cos\phi$ and $\sin\phi$ must vanish, therefore

$$\begin{aligned} &E_t + u_0(X_{st}Z_s - Z_{st}X_s) + u_0 E_s - \frac{E}{2}(u_{0s} + SE) + \frac{3}{Re}ES^2 \\ &\quad = u_0^2 S - \frac{2}{Rb}u_0 + \frac{(X+1)Z_s - ZX_s}{Rb^2} - \frac{3}{Re}u_{0s}S - \frac{S}{We R_0} \end{aligned} \tag{9.59}$$

and

$$w_1 E = 0. \tag{9.60}$$

From equation (9.60) we have $w_1 = 0$. The s-momentum equation (6.29) becomes

$$\begin{aligned} &u_{0t} + E(Z_{st}X_s - X_{st}Z_s) + u_0 u_{0s} + 2u_0 ES - EE_s \\ &\quad = -p_{0s} + \frac{2}{Rb}E + \frac{(X+1)X_s + ZZ_s}{Rb^2} + \frac{1}{Re}(u_{0ss} + 4u_2 + (SE)_s) \end{aligned} \tag{9.61}$$

at $O(\epsilon)$. Substituting (9.50) and (9.56) into equation (9.61) we obtain

$$\begin{aligned} u_{0t} + E(Z_{st}X_s - X_{st}Z_s) + u_0u_{0s} + 2u_0ES - EE_s \\ = -\frac{1}{We}\left(\frac{1}{R_0}\right)_s + \frac{2}{Rb}E + \frac{(X+1)X_s + ZZ_s}{Rb^2} + \frac{3}{Re}\frac{(R_0^2(u_{0s}+SE))_s}{R_0^2}. \end{aligned} \tag{9.62}$$

The kinematic condition at order ϵ is

$$R_{0t} + \frac{u_{0s}}{2}R_0 + \frac{S}{2}ER_0 + u_0R_{0s} - R_{0s}(u_0 - X_tX_s - Z_tZ_s) = 0. \tag{9.63}$$

We need to solve equations (9.63), (9.62), (9.59) and the arc-length condition subject to the initial and boundary conditions given in chapter 6.

We assume $X(s,t)$ and $Z(s,t)$ are leading order functions of s only with small terms added that are functions of s and t

$$X(s,t) = \tilde{X}(s) + \hat{X}(s,t)$$

and

$$Z(s,t) = \tilde{Z}(s) + \hat{Z}(s,t)$$

so X and Z are almost but not quite steady. (If this assumption was not valid $\hat{X}$ and $\hat{Z}$ would become large with time; this does not happen.) Substituting into the arc-length condition $X_s^2 + Z_s^2 = 1$ we obtain

$$\tilde{X}_s^2 + \tilde{Z}_s^2 = 1 \tag{9.64}$$

at leading order, and

$$\tilde{X}_s\hat{X}_s + \tilde{Z}_s\hat{X}_s = 0 \tag{9.65}$$

at next order. Substituting $X(s,t)$ and $Z(s,t)$ into $E = Z_s X_t - Z_t X_s$ we have

$$E = \hat{X}_t \tilde{Z}_s - \tilde{X}_s \hat{Z}_t. \tag{9.66}$$

Differentiate equation (9.65) with respect to t, we obtain

$$\tilde{X}_s \hat{X}_{st} + \tilde{X}_s \hat{X}_{st} = 0 \tag{9.67}$$

and by differentiating equation (9.66) with respect to s we have

$$E_s = \hat{X}_{st} \tilde{Z}_s + \hat{X}_t \tilde{Z}_{ss} - \tilde{X}_{ss} \hat{Z}_t - \tilde{X}_s \hat{Z}_{st}. \tag{9.68}$$

Using (9.67) we can eliminate $\hat{Z}_{st}$ from equation (9.68), and we arrive at

$$E_s = \hat{X}_{st} \tilde{Z}_s + \hat{X}_t \tilde{Z}_{ss} - \tilde{X}_{ss} \hat{Z}_t + \frac{\tilde{X}_s^2 \hat{X}_{st}}{\tilde{Z}_s}. \tag{9.69}$$

$\hat{Z}_t$ can be eliminated from equation (9.68) using equation (9.66)

$$E_s = \hat{X}_{st} \tilde{Z}_s + \hat{X}_t \tilde{Z}_{ss} - \tilde{X}_{ss} \left(\frac{\hat{X}_t \tilde{Z}_s - E}{\tilde{X}_s} \right) + \frac{\tilde{X}_s^2 \hat{X}_{st}}{\tilde{Z}_s}. \tag{9.70}$$

Let $q = \hat{X}_t$ so we can re-write equation (9.70) as

$$q_s \left(\tilde{Z}_s + \frac{\tilde{X}_s^2}{\tilde{Z}_s} \right) + q \left(\tilde{Z}_{ss} - \frac{\tilde{X}_{ss} \tilde{Z}_s}{\tilde{X}_s} \right) + \frac{\tilde{X}_{ss} E}{\tilde{X}_s} - E_s = 0. \tag{9.71}$$

Equation (9.71) can be rearranged to give

$$q_s + q \tilde{Z}_s \left(\frac{\tilde{Z}_{ss} \tilde{X}_s - \tilde{X}_{ss} \tilde{Z}_s}{\tilde{X}_s} \right) + \frac{\tilde{Z}_s \tilde{X}_{ss} E}{\tilde{X}_s} - \tilde{Z}_s E_s = 0. \tag{9.72}$$

Using (9.64) we write equation (9.72) as

$$q_s - q\frac{\tilde{X}_{ss}}{\tilde{X}_s} + \frac{\tilde{Z}_s\tilde{X}_{ss}E}{\tilde{X}_s} - \tilde{Z}_sE_s = 0. \tag{9.73}$$

Equation (9.73) can be solved using the integrating factor $1/\tilde{X}_s$, therefore equation (9.73) can be written as

$$\frac{d}{ds}\left(\frac{q}{\tilde{X}_s}\right) = \frac{E_s\tilde{Z}_s}{\tilde{X}_s} - \frac{\tilde{X}_{ss}\tilde{Z}_sE}{\tilde{X}_s^2}. \tag{9.74}$$

After integrating equation (9.74) becomes

$$\frac{q}{\tilde{X}_s} = \int_0^s \left(\frac{E_s\tilde{Z}_s}{\tilde{X}_s} - \frac{\tilde{X}_{ss}\tilde{Z}_sE}{\tilde{X}_s^2}\right) ds. \tag{9.75}$$

We can integrate the first term on the right-hand side of equation (9.75) by parts and multiply both sides by $\tilde{X}_s$ to obtain

$$q = E\tilde{X}_s - \tilde{X}_s\int_0^s \frac{E\tilde{Z}_{ss}}{\tilde{X}_s}ds + b(t)\tilde{X}_s. \tag{9.76}$$

Using the conditions at the orifice, $E = E_s = 0$ at $s = 0$ we find $b(t) = 0$. Replacing q with $\hat{X}_t$ equation (9.76) becomes

$$\hat{X}_t = E\tilde{Z}_s - \tilde{X}_s\int_0^s \frac{E\tilde{Z}_{ss}}{\tilde{X}_s}ds. \tag{9.77}$$

Substituting (9.77) into equation (9.66) and using (9.64) we obtain

$$\hat{Z}_t = -E\tilde{X}_s - \tilde{Z}_s\int_0^s \frac{E\tilde{Z}_{ss}}{\tilde{X}_s}ds. \tag{9.78}$$

Substitute (9.77) and (9.78) into the left hand side of equation (9.59) and linearise the left hand side of equation (9.59) in E. Replacing the X and Z terms on the right hand

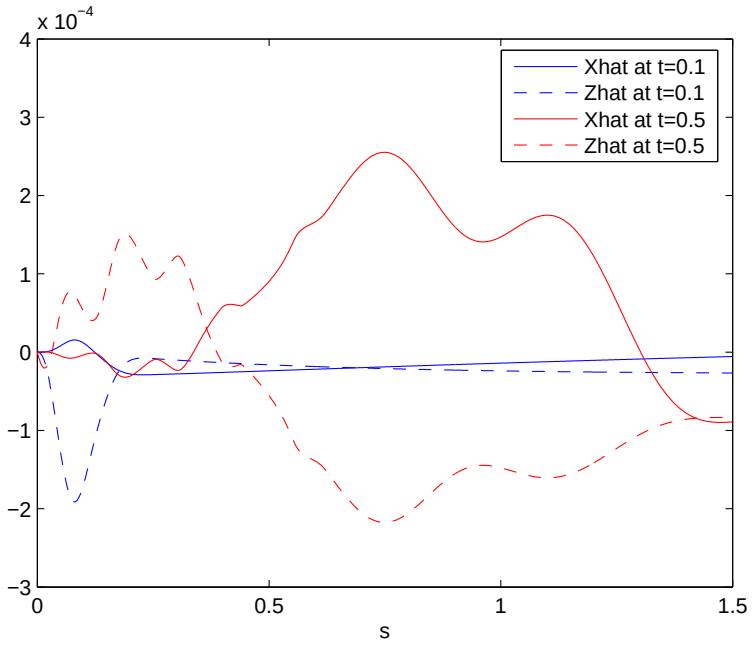

Figure 9.4: The deviation from the steady state for a jet with $We = 70$, $Rb = 1$, $Re = 100$ and $\delta = 0.1$ at $t = 0.1$ and $t = 0.5$.

side of equation (9.59) with $\tilde{X}$ and $\tilde{Z}$ we arrive at

$$E_t + u_0\left(E_s - \frac{\tilde{X}_{ss}}{\tilde{Z}_s}\int_0^s \frac{E\tilde{Z}_{ss}}{\tilde{X}_s}ds\right) + u_0E_s - \frac{E}{2}u_{0s} = u_0^2S - \frac{2u_0}{Rb} + \frac{(\tilde{X}+1)\tilde{Z}_s - \tilde{Z}\tilde{X}_s}{Rb^2} - \frac{3u_{0s}S}{Re} - \frac{S}{WeR_0}. \tag{9.79}$$

Equation (9.79) is an integro-partial differential equation in E that is solved using finite differences. Equations (9.77) and (9.78) can be used to find $\hat{X}$ and $\hat{Z}$.

9.2.1 Results

In this section we plot graphs similar to those presented in subsection 9.1.3 but for more viscous jets with $Re = 100$. All the other parameters are the same as in subsection 9.1.3. The deviation from the steady state is obtained for $t = 0.1$ and $t = 0.5$ in non-dimensional units.

Figure 9.4 is a plot of arc-length s against the deviation of the centreline from the steady-state, $\hat{X}$ and $\hat{Z}$ for a jet with $We = 70$, $Rb = 1$, $Re = 100$ and $\delta = 0.1$. The maximum deviation of the centreline is of the order 10^{-4} which is small compared to

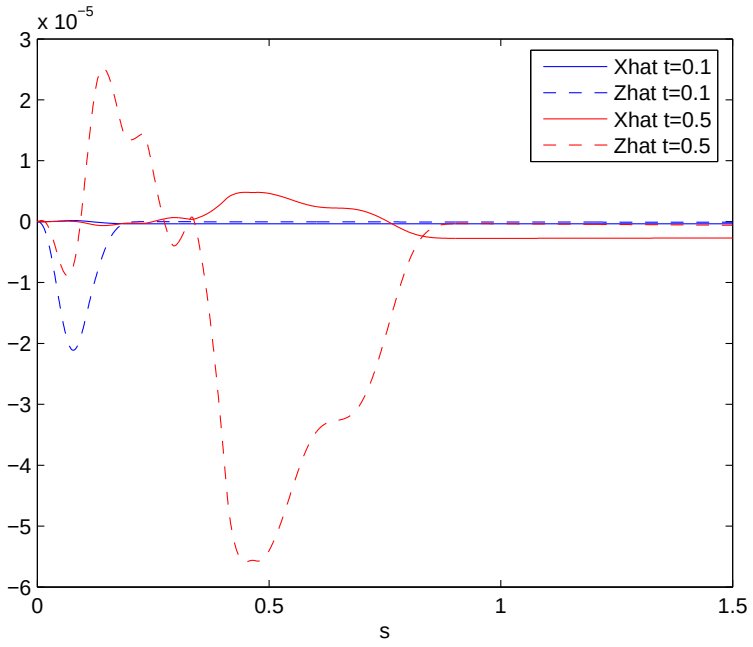

Figure 9.5: The deviation from the steady state for a jet with $We = 70$, $Rb = 10$, $Re = 100$ and $\delta = 0.1$ at $t = 0.1$ and $t = 0.5$.

$X_0(s)$ and $Z_0(s)$ therefore the centreline is approximately steady.

Figure 9.5 shows the deviation of the centreline from the steady-state plotted against arc-length for a jet with $We = 70$, $Rb = 10$, $Re = 100$ and $\delta = 0.1$. Again we can see that the maximum deviation from the steady-state is of the order of 10^{-5} which is small compared to $X_0(s)$ and $Z_0(s)$. This means that the trajectory of the jet is again approximately steady. The deviation from the centreline is smaller than in figure 9.5 when the Rossby number is 1. This was expected since at $Rb = 10$ the jet will have less rotation than at $Rb = 1$.

Figure 9.6 is a simulation of a jet with $We = 70$, $Rb = 1$, $Re = 100$ and $\delta = 0.1$ at $t = 0.1$ and $t = 0.5$ in non-dimensional units. The jet breaks up at $t = 0.5$ and the centreline is approximately steady as expected.

By comparing figures 9.1 and 9.2 with figures 9.4 with 9.5 we can see that the deviation of the trajectory from the steady state is greater for the more viscous jet. This suggests that at very high viscosity the centreline of the jet could become unsteady.

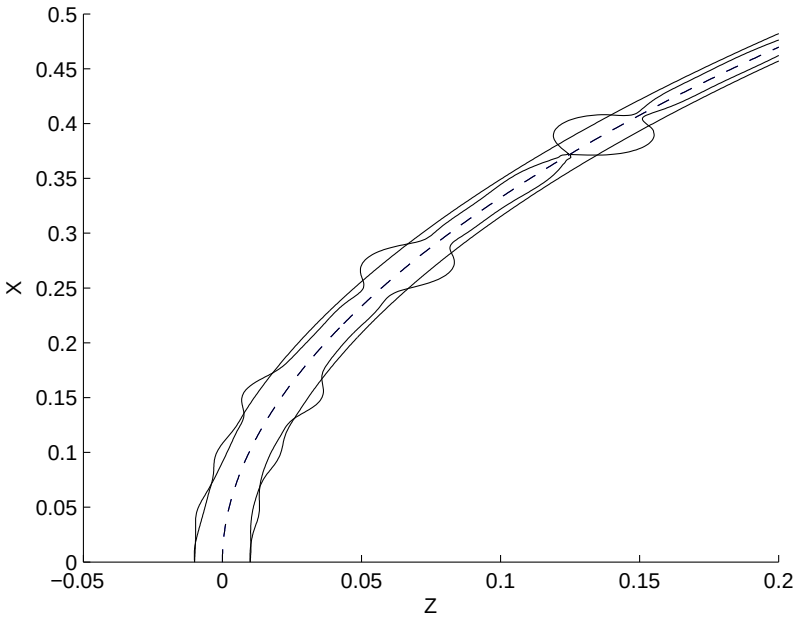

Figure 9.6: A simulation of a viscous jet with $We = 70$, $Rb = 1$, $Re = 100$ and $\delta = 0.1$ at $t = 0.1$ and $t = 0.5$.

This was observed in Wong *et al.* [44] as mode 4 break-up. However the numerics do not converge for mode 4 parameter values. This is probably because the instability mechanism appears to be 'absolute' rather than 'convective' for mode 4 since a wave is seen to propagate towards the orifice in mode 4. This is not covered by this theory.

9.3 Summary

In this section we have allowed the trajectory of the jet to become unsteady. We have calculated the deviation of the centreline from the steady-state for inviscid jet. We found that the deviation from the centreline was small compared to the steady-state solutions and therefore the centreline is approximately steady. We then calculated the deviation from the centreline for more viscous jets and again we found that the deviation from the centreline was small compared to the steady-state solutions. So the centreline of the jet is again approximately steady. This shows that our approximation that the trajectory of the jet is steady used in chapters 5 to 8 is valid.

However it was found that the deviation of the trajectory was greater for the more viscous jet. This suggests that the trajectory of the jet could become unsteady at very high viscosity. This was observed in laboratory scale experiments carried out by Wong *et al.* [44]. This is a possible area of future work and will be discussed in chapter 10.

Chapter 10

Conclusions and further work

The aim of this thesis was to extend the work on the behaviour of liquid jet break-up and drop formation of curved liquid jets to obtain a better understanding the problem on a scale closer to the industrial scale. This was done by carrying out experiments on a pilot scale and developing existing theories to include other parameters such as viscosity and gravity.

Novel insonification experiments were carried out in an attempt to control satellite drop formation. Insonification was also included in the theory. The trajectory of the jet was allowed to become time-dependent. The deviation of the trajectory from its steady-state was calculated and simulations of the jet were obtained in this more complicated situation.

10.1 Conclusions

In chapter 4 the results from the pilot scale experiments were discussed and compared to the laboratory scale experiments carried out by Wong *et al.* [44]. Of the four modes of break-up obtained on the laboratory scale, two were obtained on the pilot scale, mode 2 and mode 3. The modes were less well defined on the pilot scale with jets displaying characteristics of mode 2 breaking up in several places simultaneously. On the laboratory scale multiple break-up points were only observed in mode 3 and mode 4 break-up. Mode 1 break-up was not observed on the pilot scale, which could be due to external factors such as wind resistance or vibration of the rig. Mode 4 was also not observed on the pilot

scale; we were unable to carry out experiments within the mode 4 break-up regime on the pilot scale as we could not achieve high Rossby number, low Weber and low Reynolds number simultaneously.

Non-axisymmetric disturbances were observed on the pilot scale which were not seen on the laboratory scale and ligands between the main drops were observed to curve. This was not seen on the laboratory scale. This showed that wind resistance had a greater effect on the pilot scale than the laboratory scale.

Rotation rate was plotted against exit velocity. Exit velocity was found to increase with increasing rotation rate. This showed that the exit velocity in the rotating frame was dependent on the rotation rate. This meant that if the rotation rate was varied not only did the Rossby number change but the Weber number, Reynolds number and Froude number also changed. This demonstrated interdependence between the parameters.

Drop size distributions were obtained for mode 2, mode 3 and the mode 2/mode 3 boundary; these drop size distributions were compared to results obtained on the laboratory scale. All the drop size distributions obtained on the pilot scale were bi-modal corresponding to the formation of satellite and main drops. The drop size distributions were found to be similar to the drop size distributions obtained for mode 3 break-up obtained on the laboratory scale. This was unsurprising since mode 2 and mode 3 break-up were less well defined on the pilot scale.

Plots of experimentally obtained main and satellite drops and break-up lengths against Weber number, Rossby number, Reynolds number and Froude number were presented and some trends were found. However because of the interdependence of the parameters the physical insight that could be gained from these results was limited.

In chapter 5 an overview of the non-linear inviscid theory developed by Părău *et al.* [33, 34] was given. An attempt was made to compare experimental and theoretical break-up lengths. δ was varied until the difference between the theoretical and experimental break-up lengths was minimised. However a good match could not be found no matter

what value of δ was chosen. A parametric study was carried out where each of the parameters, Weber number, Rossby number and δ were varied. The break-up length increased with increasing Weber number. This was due to jets with higher Weber number having more inertia and therefore travelling further before breaking up. There was only a small change in break-up length with Rossby number. The break-up length increased with decreasing δ. This was expected since δ represents the amplitude of the disturbance at the orifice. The larger the value of δ, the sooner the jet will break-up.

The trajectory of the jet was plotted for different values of Weber and Rossby numbers. The trajectory of the jet curves more with decreasing Weber number. Decreasing the Weber number corresponds to less inertia therefore the jet curves less. The trajectory of the jet curved more with decreasing Rossby number. Decreasing the Rossby number corresponds to increasing the rotation rate therefore the jet curves more. These results agreed with experimental results obtained in Wallwork *et al.* [42].

In chapter 6 viscosity was included in the model. A different scaling was used which meant that rotation terms appeared in the equations of motion as well as the initial conditions. In the inviscid case rotation only entered the problem in the initial conditions. Theoretical and experimental results were compared and it was found that δ could be varied until the experimental and theoretical break-up lengths matched. Very good agreement between experimental and theoretical break-up lengths was found. Drop sizes were obtained using the same values of δ that were used to match the experimental and theoretical break-up lengths and fairly good agreement was found between experimental and theoretical drop sizes. Drop sizes for an average value of δ were also obtained and the agreement between experimental and theoretical results was still fairly good. This showed that we could choose a typical value of δ and reasonable agreement between theory and experiment could be obtained provided δ was of the correct order of magnitude. It should be pointed out that the break-up length is highly dependent upon δ. This perhaps is not so much of a concern since drop size prediction is more important in industry than break-up length prediction.

The parametric study was extended to include Reynolds number. It was ascertained that break-up length increases with increasing Weber number, this agreed with results obtained using the inviscid theory. The break-up length increased with decreasing Rossby number. Decreasing Rossby number corresponds to increasing rotation rate, therefore break-up length increased with increasing rotation rate. Using the inviscid theory the break-up length did not change much with Rossby number. However the viscous theory incorporated more rotation terms into the problem giving more and better information. It was shown that break-up length increases as Reynolds number decreases. Decreasing Reynolds number corresponds to increasing viscosity, therefore break-up length increased with increasing viscosity. This was due to the viscous forces stabilising the jet. Break-up length increased with decreasing δ. This was expected since δ is the amplitude of the disturbance at the orifice. The greater the amplitude of the disturbance the sooner the jet will break-up. This agreed with results obtained using the inviscid theory.

Weber number, Rossby number, Reynolds number and δ were plotted against theoretically obtained main and satellite drop sizes. Rossby number had more effect on drop size than Weber number, Reynolds number and δ. Weber number had more effect on drop size at low Rossby number and δ had more effect on satellite drop size than main drop size.

In chapter 7 gravity was included in the theory and the same investigations were carried out as for the viscous theory. Again we could choose values of δ so that theoretically obtained break-up lengths agreed with the experimental results. Theoretical drop sizes could be obtained that were in reasonable agreement with experimental results using the fitted value of δ or typical value of δ.

The parametric study was extended to include Froude number. The relationships between Weber number, Rossby number, Reynolds number and δ with break-up length were similar to the relationships obtained in chapter 6 where gravity was neglected. However the variation in break-up length was less than in chapter 6 suggesting that

Froude number had some stabilising effect on the jet. It was found that break-up length increases with decreasing Froude number. This result agreed with the linear work carried out by Decent *et al.* [13].

Weber number, Rossby number, Reynolds number, Froude number and δ were plotted against theoretically obtained main and satellite drop sizes. Rossby number had more effect on drop size than Weber number, Reynolds number and δ. However the variation in drop size with Weber number and Rossby number was less than in chapter 6 where gravity was neglected. Weber number had more effect on drop size at low Rossby number and δ and Froude number had more effect on satellite drop size than main drop size.

Using this theory we investigated how the trajectory of the jet changed with Rossby number, Weber number and Froude number. The trajectory of the jet fell out of the X-Z plane more for higher Rossby number. Higher Rossby number corresponds to lower rotation rate therefore gravity forces have more effect on the jet. The jet coils more tightly for lower Weber number. Jets with lower Weber number have less inertia therefore the jet coils more tightly as they are affected more by rotation. Jets with lower Froude number fall out of the X-Z plane more. At lower Froude number gravity has more effect on the jet. These results agreed with results in Wallwork [41].

The major advantage of using the theory is that the parameters can be separated and variations in break-up lengths and drops sizes can be found for each parameter. Experimentally it is very difficult to vary one parameter while keeping the others constant. This shows that we were able to obtain information from the theory that we were not able to gain experimentally, providing greater scientific input. When the experimental interdependence of parameters was included in the theory there was some agreement between experimental and theoretical results showing that the theory can be used to make predictions.

In chapter 8 we discussed experiments carried out with insonification, using sound waves of 10, 100 and 200 Hz for four different rotation rates ($Rb = \infty$, 7.01, 1.68 and 1.12). Insonification at all frequencies did not eliminate satellite drops for low Rossby numbers; however at high Rossby numbers insonification at 100 and 200 Hz did successfully eliminate satellite drops. The 10 Hz sound wave did not successfully eliminate satellite drops at any Rossby number.

During the experiments the volume of the sound wave generated from the sub-aqua speaker appeared to be louder at 100 Hz than 10 Hz and louder at 200 Hz than 100 Hz despite the volume settings being the same for all experiments. (This observation was simply by the human ear which does not have a uniform response to all frequencies.) This suggested a minimum amplitude of sound wave was required before insonification successfully eliminated satellite drops. Insonification was included in the theory and it was found that insonification was predicted to be successful over a range of frequencies from 1 to 300 Hz in and out of the experimental parameter regimes. This was encouraging since it meant that insonification could successfully eliminate satellite drops for a larger range of frequencies and experimental parameters if more sophisticated equipment was used. The theoretical investigations were repeated for a lower amplitude of sound wave and insonification was not successful. This suggests a minimum amplitude of sound wave was required before insonification was successful which agrees with the observations in the experiments.

A movie demonstrating successful insonification for $Rb = \infty$ can be found at http://web.mat.bham.ac.uk/L.Partridge.

In chapter 9 the trajectory of the jet was allowed to become time-dependent. We calculated the deviation of the centreline of the jet from its steady-state in the inviscid case for two different Rossby numbers, $Rb = 1$ and $Rb = 10$. The deviation from the steady-state was small in both cases so the centreline was approximately steady. The deviation was less for $Rb = 10$ which was expected since this corresponds to a lower

rotation rate. The deviation was also calculated for more viscous jets ($Re = 100$) for $Rb = 1$ and $Rb = 10$. Again the deviation was found to be small so the centreline was approximately steady. But there was more variation in the centreline in the more viscous case. This suggested that at very high viscosity the trajectory of the jet could become unsteady. This was observed in experiments carried out by Wong *et al.* [44] on the laboratory scale as mode 4 break-up.

10.2 Suggestions for further work

Future projects could or will involve examining the following projects.

10.2.1 Flow in the can

In chapter 4 it was ascertained that the exit velocity of the jet in the rotating frame was dependent on the rotation rate of the can. This meant that when the rotation rate was varied Rossby number, Weber number, Reynolds number and Froude number change therefore experimentally it was difficult to separate the parameters. This is indicative of complex flow in the can. The flow in the can could be imaged using particle image velocimetry (PIV). The flow in the can could be imaged at different rotation rates and we would be able to show how the rotation rate influences the exit velocity of the jet. This was attempted previously by Dr David Wong but further work is required.

Computational fluid dynamics (CFD) could also be carried out to determine $U = U(\Omega)$ theoretically by simulating the flow in the can. This would be a major piece of work which would give us insight into the interdependence of the parameters. In October 2006 an MPhil student started work in this area in the School of Mathematics at the University of Birmingham. Once an experimental or CFD formula for $U = U(\Omega)$ is obtained, this could be fed into the theory applied here.

10.2.2 Unsteady trajectories and mode 4 break-up

In chapter 9 the trajectory of the jet was allowed to become time-dependent. The deviation of the trajectory from its steady-state was calculated in inviscid and viscous cases.

In both cases the deviation from the steady-state was found to be small. Simulations of the jet were obtained and the trajectory was seen to be approximately steady as expected. However in the viscous case the deviation from the steady-state was found to be greater than in the inviscid case. This means that for very high viscosity jets the trajectory could become significantly unsteady. This was observed by Wong *et al.* [44] in experiments carried out on the laboratory scale as mode 4 break-up. The mechanism of mode 4 break-up is different to the other modes of break-up. In break-up modes 1 to 3 a wave propagates away from the orifice; this is known as a 'convective' instability. In mode 4 break-up the wave is observed to propagate back towards the orifice after the jet has ruptured as well as away from the orifice; this is known as an 'absolute' instability. The theories discussed in this thesis always assume the instability to be convective.

A suggestion for further work would be to develop a theory which incorporates absolute instabilities. An absolute instability theory would be very different to the theories presented in this work. It would require a major amount of work since the slender jet assumption probably would not be valid and the full equations of motion would need to be solved numerically.

10.2.3 Non-Newtonian liquids

In all the viscous analyses the fluid is considered to be Newtonian. This means the shear stress is proportional to the rate of strain and that the dynamic viscosity is the constant of proportionality. In the case of a non-Newtonian fluid the shear stress is not proportional to the rate of strain therefore the dynamic viscosity is not constant. There are several types of non-Newtonian fluids depending on how the dynamic viscosity behaves. Two examples are shear thinning where the viscosity of the liquid decreases with increasing rate of strain and shear thickening where the viscosity of the liquid increases with increasing rate of strain. The viscosity may be expressed as a power law. This would alter the equations of motion. A current PhD student is working on this problem at the University of Birmingham in the School of Mathematics. Experiments could also

be carried out using a non-Newtonian liquid, such as aqueous carboxymethylcelluose (cmc). This compound is available in the Department of Chemical Engineering and is a commonly used polymer in industry.

10.2.4 Lagrangian camera

All the experiments described in this thesis have been carried out using a stationary camera. Even though good quality images of break-up can be obtained with this camera, the evolution of the perturbations along the jet cannot be followed. A small lightweight camcorder was obtained by the School of Mathematics. The camera was attached to the side of the can and therefore could rotate with the can. The evolution of the wave propagating along the jet could be observed. Some preliminary experiments were carried out and a movie can be found at http://web.mat.bham.ac.uk/L.Partridge. Work would need to be carried out to improve the resolution of the images; however this would be a promising area of further work where further physical insight into jet break-up and drop formation could be obtained. However we felt that our static camera was fit for our purposes here.

10.2.5 Further work on insonification

In chapter 8 insonification experiments were carried out. Insonification successfully eliminated satellite drops at high Rossby numbers if a 100 or 200 Hz sound wave was used. However at 10 Hz insonification was unsuccessful at all Rossby numbers. The theory predicted that insonification could be successful over a range of frequencies for Rossby numbers within and outside of the experimental parameter regimes, provided that the amplitude of the sound wave was sufficiently large.

If more sophisticated equipment could be obtained it would be worth repeating the insonification experiments. We would expect insonification to successfully eliminate satellite drops for a larger range of frequencies and experimental parameters.

10.2.6 Air resistance modelling

From the pilot scale experiments it was observed that air resistance had more effect on jet break-up than on the laboratory scale. These effects could be incorporated into the theory by including air resistance into the equations of motion. Preliminary work carried out by a former MSci student in the School of Mathematics showed that the equations to be solved are formidable. This would be a major piece of work however valuable insights into the effects of air resistance could be obtained.

Bibliography

[1] M. Abromowitz and I.A. Stegun. *Handbook of mathematical functions, 9th edn.* Dover, 1970.

[2] J.N. Anno. *The mechanics of liquid jets.* Lexington Books, 1977.

[3] M.H.I. Baird and J.F. Davidson. Annular jets - I. *Chem. Eng. Sci.*, 17:467–472, 1962.

[4] G.K. Batchelor. *An introduction to fluid mechanics.* Cambridge University Press, 1967.

[5] J.B. Blaisot and S. Adeline. Instabilities on a free falling jet under an internal flow breakup mode regime. *Int. J. Multiphase Flow*, 29:629–653, 2003.

[6] D.B. Bogy. Drop formation in a circular liquid jet. *Ann. Rev. Fluid Mech.*, 11:201–229, 1979.

[7] D.M.A. Camelot, R.P.A. Hartman, J.C.M. Marijnissen, B. Scarlett, and D. Brunner. Experimental study of the jet break up for electrohydrodynamics atomisation of liquids in the cone-jet mode. *J. Aerosol Sci*, 30:976–977, 1999.

[8] K.C. Chaudhary and T. Maxworthy. The nonlinear capillary instability on a liquid jet. Experiments on satellite drop formation and control. *J. Fluid Mech.*, 96:287–297, 1980.

[9] K.C. Chaudhary and T. Maxworthy. The nonlinear capillary instability on a liquid jet. Part 2. Experiments on jet behaviour before droplet control. *J. Fluid Mech.*, 96:275–286, 1980.

[10] A.D.D. Craik. *Wave interactions and fluid flows.* Cambridge University Press, 1985.

[11] L.J. Cummings and P.D. Howell. On the evolution of non-axisymmetric viscous fibres with surface tension, inertia and gravity. *J. Fluid Mech.*, 389:361–389, 1999.

[12] S.P. Decent, A.C. King, M.J.H. Simmons, E.I. Părău, D.C.Y. Wong, and I.M. Wallwork. The trajectory and stability of a spiralling liquid jet: Part II. Viscous theory, 2004. Submitted to J. Eng. Math.

[13] S.P. Decent, A.C. King, and I.M. Wallwork. Free jets spun from a prilling tower. *J. Eng. Math.*, 42:265–282, 2002.

[14] F. Dias and J.-M. Vanden-Broeck. Flows emerging from a nozzle and falling under gravity. *J. Fluid Mech.*, 213:465–477, 1990.

[15] R. J. Donelley and W. Glaberson. Experiments on the capillary of a liquid jet. *Proc. R. Soc. London, Ser. A*, 290:547–556, 1966.

[16] J. Eggers. Universal pinching of 3d axisymmetric free-surface flow. *Phys. Rev. Lett.*, 71:3458–3460, 1993.

[17] J. Eggers. Nonlinear dynamics and breakup of free-surface flows. *Rev. Mod. Phys.*, 69:865–929, 1997.

[18] J. Eggers and T.F. Dupont. Drop formation in a one-dimensional approximation of the Navier-Stokes equations. *J. Fluid Mech.*, 262:205–221, 1994.

[19] M.V. Entov and A.L. Yarin. The dynamics of thin liquid jets in air. *J. Fluid Mech.*, 140:91–111, 1984.

[20] D.S. Finnicum, S.J. Weinstein, and K.J. Rushack. The effect of applied pressure on the shape of a two-dimensional liquid curtain falling under the influence of gravity. *J. Fluid Mech.*, 255:647–665, 1993.

[21] E.F. Goedde and M.C. Yuen. Experiments on liquid jet instabillity. *J. Fluid Mech.*, 40:495–511, 1970.

[22] D.R. Hide. *Handbook of chemistry and physics.* CRC Press, 2004.

[23] J.H. Hilbing and S.D. Heister. Droplet size control in liquid jet breakup. *Phys. Fluids*, 8:1574–1581, 1996.

[24] M.M. Hohman, M. Shin, G. Rutledge, and M.P. Brenner. Electro-spinning and electrically forced jets. I. Stability theory. *Phys. Fluids*, 13:2201–2220, 2001.

[25] J.B. Keller and M.L.Weitz. Upward 'falling' jets and surface tension. *J. Fluid Mech.*, 2:201–203, 1957.

[26] J.B. Keller, S.I. Rubinow, and Y.O. Tu. Spatial instability of a jet. *Phys. Fluids*, 16:2052–2055, 1973.

[27] T.A. Kowaleski. On the separation of droplets from a liquid jet. *Fluid Dynamics Research*, 17:121–145, 1996.

[28] S.P. Lin. *Breakup of liquid jets and sheets.* Cambridge University Press, 2003.

[29] S. Middleman. *Modeling of axisymmetric flows.* Academic Press, 1995.

[30] D.T. Papageorgiou and O. Orellana. Study of cylindrical jet breakup using one-dimensional models of the Euler equations. *SIAM J. Appl. Math*, 59:286–317, 1998.

[31] L. Partridge, D.C.Y. Wong, M.J.H. Simmons, E.I. Părău, and S.P. Decent. Experimental and theoretical description of the break-up of curved liquid jets in the prilling process. *Chemical Engineering Research and Design*, 83:1267–1275, 2005.

[32] W.H. Press, S.A. Teukolsky, W.T. Vetterling, and B.P. Flannery. *Numerical recipes in Fortran 77: The art of scientific computing; (Fortran numerical recipes, vol 1).* Cambridge University Press, 2001.

[33] E. Părău, S. Decent, A. King, M. Simmons, and D. Wong. Dynamic breakup and drop formation from a liquid jet spun from a rotating orifice: Part II. Theoretical. *Proceedings of FEDSM'03*, 2003.

[34] E. Părău, S.P. Decent, A.C. King, M.J.H. Simmons, and D.C. Wong. Nonlinear travelling waves on a spiralling liquid jet. Accepted in Wave Motion.

[35] J.I. Ramos. Upward and downward annular liquid jets: Conservation properties, singularities and numerical errors. *Appl. Math, Modelling*, 20:440–458, 1996.

[36] J.W.S. Rayleigh. On the stability of liquid jets. *Proc. Lond. Math. Soc.*, 10:4–13, 1878.

[37] F. Savart. Memoire sur la constitution des veines liquides lancees par des orifices circulaires en mince paroi. *Ann. Chim. Phys*, 53:337–374, 1833.

[38] R.M.S.M. Schulkes. Dynamics of liquid jets revisited. *J. Fluid Mech.*, 250:635–650, 1993.

[39] Y.D. Shikhmurzaev. Coalescence and capillary breakup of liquid volumes. *Phys. Fluids*, 12:2386–2396, 2000.

[40] J.-M. Vanden-Broeck and J.B. Keller. Jets rising and falling under gravity. *J. Fluid Mech.*, 124:335–345, 1982.

[41] I.M. Wallwork. *The trajectory and stability of a spiralling liquid jet.* PhD thesis, The University of Birmingham, UK, 2002.

[42] I.M. Wallwork, S.P. Decent, A.C. King, and R.M.S.M. Schulkes. The trajectory and stability of a spiralling liquid jet: Part I. Inviscid theory. *J. Fluid Mech.*, 459:43–65, 2002.

[43] C. Weber. Zum zerfall eines Flüssigkeitsstrahles. *Z. Agnew. Math. Mech.*, 11:136–154, 1931.

[44] D. Wong, M. Simmons, S. Decent, E. Părău, and A.C. King. Break-up dynamics and drop size distributions created from spiralling liquid jets. *Int. J. Multiphase Flow*, 30:499–520, 2004.

[45] D. Wong, M. Simmons, A. King, S. Decent, and E. Părău. Dynamic breakup and drop formation from a liquid jet spun from a rotating orifice: Part I. Experimental. *Proceedings of FEDSM'03*, 2003.

[46] Y. Zhu, H.N. Oguz, and A. Prosperetti. On the mechanism of air entrainment by liquid jets at the free surface. *J. Fluid Mech.*, 404:151–177, 2000.